The Electrochemistry of Titanium Corrosion

By

James J. Noël

A Thesis

Submitted to the Faculty of Graduate Studies

in Partial Fulfillment of the Requirements

for the Degree of

Doctor of Philosophy

Department of Chemistry

University of Manitoba

Winnipeg, Manitoba

THE UNIVERSITY OF MANITOBA

FACULTY OF GRADUATE STUDIES

*****

COPYRIGHT PERMISSION PAGE

The Electrochemistry of Titanium Corrosion

BY

James J. Noël

A Thesis/Practicum submitted to the Faculty of Graduate Studies of The University of Manitoba in partial fulfillment of the requirements of the degree of

Doctor of Philosophy

Abstract

This Thesis describes investigations of the corrosion resistant behaviour of titanium and several α-phase Ti alloys, in aqueous solutions, under conditions relevant to buried titanium nuclear waste containers. A range of electrochemical and *ex situ*, post-electrochemistry analyses were used to study the nature, growth, breakdown, and dissolution of oxide films on Ti, the absorption of hydrogen, and the influence of dilute alloying components.

These experiments support published work suggesting the passive film on titanium is composed of TiO_2 with a rutile-like packing density; however, when grown in aqueous solution, significant amounts of hydrogen are incorporated into the oxide in the form of Ti-OH and bound water molecules. On alloy materials containing Ti-noble metal intermetallic precipitates, the passive film seems to be discontinuous, presumably because it does not form as well over exposed intermetallic particles as it does over grains of titanium. The exposed particles are believed to catalyze the cathodic half-reaction and reinforce passivity by anodically polarizing the alloy.

The passive oxide film on titanium can be penetrated by dissolution in strongly acidic solution. It appears that catalysis of the hydrogen evolution reaction by exposed intermetallic particles or spontaneously formed titanium hydride anodically polarizes the metal, thereby limiting the amount of corrosion. The data presented here also support published claims that the passive oxide undergoes mechanical breakdown induced by increasing temperatures above 60-70°C. Thermally induced film breakdown was found to be a necessary, but insufficient, condition for the initiation of crevice corrosion on Ti. The nature of the electrolyte species present was found to play an important role in crevice corrosion initiation.

The semiconducting passive oxide film helps protect the underlying titanium from absorption of electrolytic hydrogen at potentials positive of its flat band potential. At lower potentials, band bending results in electronic degeneracy, an increase in electrical conductivity, oxide reduction, incorporation of hydrogen into the oxide, and eventually hydrogen ingress into the metal.

This work focuses on understanding the underlying physical and chemical reasons for the empirically observed corrosion and hydrogen absorption properties of titanium and its alloys that have evolved into practical guidelines for industrial service conditions.

Extended Abstract

This Thesis describes investigations of the corrosion resistant behaviour of titanium and several of its dilute α-phase alloys in aqueous solutions under conditions (temperature, pH, solution composition, *etc.*) expected to be relevant to titanium alloy containers buried in a nuclear fuel waste disposal vault. A range of electrochemical experiments (open circuit potential, polarization, electrochemical impedance spectroscopy, coupled electrode crevice corrosion and combined electrochemistry/neutron reflectometry measurements) and post-electrochemistry, *ex situ* analyses (X-ray photoelectron spectroscopy, hydrogen extraction, optical microscopy, and Auger electron spectroscopy) were used to study the nature and growth of the passive oxide film on titanium, its breakdown and dissolution, the absorption of hydrogen into the titanium, and the influence of dilute alloying components on some of these behaviours. The major conclusions are mentioned briefly below.

The data generated in these experiments support published papers that suggest the passive film on titanium is composed of TiO_2 with a rutile-like packing density; however, when grown in aqueous solution, significant amounts of hydrogen are incorporated into the oxide in the form of Ti-OH and bound water molecules. On alloy materials containing Ti-noble metal intermetallic precipitates, the passive film seems to be discontinuous, presumably because it does not form as well over exposed intermetallic particles as it does over grains of titanium. This observation helps explain the enhanced corrosion resistance of these alloys over unalloyed titanium –the exposed particles are believed to

catalyze the cathodic half-reaction and reinforce passivity by anodically polarizing the alloy.

The passive oxide film on titanium can be penetrated by dissolution in acidic solution. This requires a pH less than ~1 in deaerated HCl solution at room temperature. It appears that catalysis of the hydrogen evolution reaction by exposed intermetallic particles, or even by titanium hydride spontaneously formed at the metal surface, anodically polarizes the metal under some circumstances, thereby limiting the amount of corrosion occurring. The data presented here also support published claims that the passive oxide undergoes mechanical breakdown induced by increasing temperatures above 60-70°C. The underlying cause of the breakdown was suggested to be crystallization of the passive film from an amorphous state. Thermally induced breakdown of the passive film was found to be a necessary, but not sufficient, condition for the initiation of crevice corrosion on Ti. The nature of the electrolyte species present, in particular the type of anion, was found to play an important role in crevice corrosion initiation.

The passive oxide film was found to help protect the underlying titanium from absorption of electrolytic hydrogen at potentials positive of a certain threshold potential. This threshold potential was found to be close to the flat band potential of the semiconducting oxide film. The experimental results suggest that, at potentials below the threshold, band bending in the semiconductor results in electronic degeneracy, accompanied by an increase in the electrical conductivity of the oxide, oxide reduction, incorporation of hydrogen into the oxide, and eventually hydrogen ingress into the metal.

This work focuses on understanding the underlying physical and chemical reasons for many of the empirically observed corrosion and hydrogen absorption properties of titanium and its alloys that have evolved into practical guidelines for the industrial service conditions of these materials.

Acknowledgements

The author wishes to thank Dave Shoesmith for his help and guidance, endless stream of ideas, lectures on the Theory of Theories, and putting up with being tripped on the hockey rink.

The author is grateful for the participation of Dr. Hymie Gesser, the project supervisor.

Thank you to Brian Ikeda for working closely with the author on this project, participating in many detailed and winding discussions, and providing budgetary support.

Thanks are due to Zin Tun for patiently instructing the author in neutron scattering techniques, his painstaking care in aligning the spectrometer, and helping to run the experiments and analyze the data.

The author humbly acknowledges the valuable contributions to this work (some great and some small) made by the following individuals: Paul Crosthwaite, Mike Quinn, Jim Betteridge, Steve Ryan, Grant Bailey, Cyril Clarke, Neil Miller, Andy Gerwing, Cindy Litke, Leslie Strandlund, Greg Kasprik, Ian Muir, Rod McEachern, David Jobe, Peter Taylor, Dennis Leneveu, Jack Cahoon, Jeff Knight, Louis David, Stan, Chum, Stu Halley, Elmer Volpel, Brian Morash, Steve Cribbs, Marg McDowall, Lawrence Johnson, Sham Sunder, Roger Dutton, Merle Brown, Jerry Smith, Jim Cafferty, Lesa Cafferty, Darcey Doering, John Root, Mike Montaigne, Larry McEwan, Mel Potter, Glen McRae, Mike Maguire, John Scully, Steven Yu, Zaven Altounian, Philip Chiu, Fridolin Ting, Marcus

Csaky, Mark Soth, Jeff Fingler, Nadine Lambe, Theresa Chan, Jason Penner, Laurie Kingsmill, Kevin Jackson, Marilyn Kovari, Pearl Murphy, Siegrun Meyer, George Montgomery, David Haworth, Karen Clay, Dan Bizzotto, Jocelyn Richer, David Mancey, Lorne Stolberg, Monique Chenier, and Patricia Noël.

AECL provided funding for this work.

Dedicated to

Patricia, my wife,

and our children,

Amanda, John, and David

Table of Contents

List of Figures

List of Tables

Abbreviations and Symbols

ADC ..... Analogue-to-Digital Converter
AES ..... Auger Electron Spectroscopy
BE ..... Binding Energy
CANDU ..... Canadian Deuterium Uranium Reactor
CNFWMP ..... Canadian Nuclear Fuel Waste Management Program
DVM ..... Digital Volt Meter
E_g ..... Bandgap Energy
E_F ..... Fermi Level
E_{fb} ..... Flat Band Potential
E_{oc} ..... Open Circuit Potential
EDTA ..... Ethylenediaminetetraacetic Acid
EELS ..... Electron Energy Loss Spectroscopy
EIS ..... Electrochemical Impedance Spectroscopy
ERA ..... Elastic Recoil Detection Analysis
FAIT ..... Field-Assisted Ion Transport
FRA ..... Frequency Response Analyzer
FWHM ..... Full Peak Width at Half-Maximum Intensity
$[H]_c$ ..... Critical Hydrogen Concentration for Brittle Cracking
HAR ..... Hydrogen Absorption Reaction
HER ..... Hydrogen Evolution Reaction
HIC ..... Hydrogen-Induced Cracking
IPE ..... Inverse Photoemission Spectroscopy
J_H ..... Rate of Hydrogen Redistribution
KE ..... Kinetic Energy
LEED ..... Low Energy Electron Diffraction
LEIS ..... Low Energy Ion Scattering
MEED ..... Medium Energy Backscattered Electron Diffraction
PC ..... Personal Computer
PEM ..... Photoelectrochemical Microscopy
PTFE ..... Poly(tetrafluoroethylene)
R_{CG} ..... Rate of Crack Growth
R_{HA} ..... Rate of Hydrogen Absorption
$\Re_{PB}$ ..... Pilling Bedworth Ratio
RBS ..... Rutherford Backscattering Spectroscopy
RDS ..... Rate-Determining Step
RED ..... Reflection Electron Diffraction
SCE ..... Saturated Calomel Electrode
SERS ..... Surface-Enhanced Raman Spectroscopy
SLD ..... Scattering Length Density
SSIMS ..... Static Secondary Ion Mass Spectrometry
STM ..... Scanning Tunneling Microscopy
TEM ..... Transmission Electron Microscopy

Ti-2 ..... ASTM Grade-2 Titanium (Commercial Purity)
Ti-12 ..... ASTM Grade-12 Titanium (Ti-0.8Ni-0.3Mo)
Ti-16 ..... ASTM Grade-16 Titanium (Ti-0.05Pd)
Ti-0.1Ru ..... Experimental Titanium-Ruthenium Alloy
UHV ..... Ultra-High Vacuum
XAS ..... X-ray Absorption Spectroscopy
XPS ..... X-ray Photoelectron Spectroscopy

1 Introduction

1.1 Motivation and approach

1.1.1 Background

This work was done largely in support of the Canadian Nuclear Fuel Waste Management Program (CNFWMP). An encyclopedic disquisition on nuclear fuel waste disposal can be found in AECL's "Environmental Impact Statement on the Concept for Disposal of Canada's Nuclear Fuel Waste" [1] and the nine primary references listed therein. Only a brief summary of how the waste disposal concept relates to this project will be given here.

The nuclear fuel waste disposal concept put forth in the CNFWMP involves burial of solid fuel waste in sealed metallic containers 500-1000 m deep within the granitic rock of the Canadian Shield. Due to the deleterious radiological and chemical effects of some components of the fuel waste on living organisms, it is desirable that nuclear fuel waste be isolated from the "biosphere" for extremely long periods[1]. Four barriers to the escape of the waste are incorporated in the disposal concept: the waste form; the container; the buffer, backfill and vault seals; and the "geosphere". It has been proposed that the waste form be discarded CANDU reactor fuel bundles consisting of uranium dioxide (UO_2) pellets in Zircaloy[2] tubes. This waste form is highly insoluble and should retain contaminants under expected waste vault conditions. The container, proposed to be either titanium (Ti) or copper (Cu), would isolate the waste form from the groundwater.

---

[1] After 500 years the activity of the radioactive waste would decrease by a factor of 200 000 [1]. Other desirable containment periods ranging from 100 to 1 000 000 years have been discussed elsewhere [5].

[2] A zirconium-based alloy containing small amounts of Sn, Fe, Cr, and Ni [6].

This requires a container with suitable mechanical stability and corrosion resistance. The combination of buffer (bentonite clay and sand), backfill (crushed rock, clay and sand) and vault seals (grouts, clays and concretes) should help control the chemical environment within the vault and inhibit ground water movement into and out of the disposal vault, thereby reducing container corrosion, waste form dissolution, and contaminant transport. Finally, the "geosphere", the surrounding bulk of granitic rock, is intended to act as another barrier to groundwater movement as well as a protection from natural events and human intrusion [1].

1.1.2 Objectives

This Thesis describes some of the studies undertaken to evaluate the corrosion properties of Ti and some of its dilute alloys. While this work is intended to explore the corrosion behaviour of Ti, not to justify a particular choice of nuclear waste disposal container material, the corrosion phenomena investigated and the range of experimental conditions employed were limited to those that would be relevant to a Ti container in the conceptual waste disposal vault. As such, portions of this Thesis provide either underlying or direct support for investigations of the suitability of Ti or its dilute alloys as materials for the construction of nuclear fuel waste disposal containers.

1.1.3 Strategy

The expected conditions in the proposed disposal vault [2] would, initially, be warm ($T \leq 100°C$) and oxidizing, due to nuclear reactions continuing within the fuel waste, and air introduced into the vault during container emplacement, respectively. The buffer material adjacent to the exterior surfaces of the containers may remain dry for some

period, but would eventually saturate with groundwater. The groundwater is expected to be a chloride-containing solution of pH 7-9. Ultimately, the vault conditions are expected to evolve to cool (ambient temperature) and anoxic, as radioactive decay processes within the waste subside and the available oxidants are exhausted by container corrosion and by reaction with minerals and organic material in the backfill. The restricted mass transport conditions established by the buffer, backfill, vault seals and geosphere would severely inhibit the replenishment of oxidants in the waste vault. Appropriate engineering design can ensure the mechanical stability of containers at the time of burial; hence the lifetimes[1] of Ti containers would ultimately be limited by corrosion. Under the projected vault conditions, the corrosion processes most likely to determine the lifetimes of Ti containers are general or uniform corrosion, crevice corrosion, and hydrogen-induced cracking (HIC) [2].

Therefore, in keeping with the objectives of this work (Section 1.1.2), experiments were performed in aqueous solutions, most containing dissolved chloride ions, at pH values from 9 to < 1 (the latter representing conditions expected to develop during localized corrosion [3]), at temperatures from 20 to 100°C, on specimens of Ti and a number of Ti alloys containing low levels of alloying constituents. These experiments were designed to investigate general corrosion, crevice corrosion, and hydrogen absorption by Ti, the latter being a prerequisite for container failure by HIC. Some aspects of the properties of the passive film on Ti were also investigated since the passive film influences the rate and extent of these corrosion processes.

[1] The container lifetime is the period between the time of emplacement in the disposal vault and the moment of container failure (*i.e.*, penetration or rupture).

Electrochemical techniques were employed for much of this research since they are largely compatible with the phenomena under study (corrosion is an electrochemical redox reaction), and, in view of Faraday's Law [4], provide a direct measure of the rates and the extent of redox reactions. The nature of the passive film on Ti was probed by electrochemical impedance spectroscopy (EIS). Where possible, independent techniques were used to complement electrochemical measurements. Such analyses yielded information on the composition (X-ray photoelectron spectroscopy (XPS), Auger electron spectroscopy (AES), neutron reflectometry), structure (Auger depth profiling, neutron reflectometry, optical microscopy), and oxidation states (XPS) at Ti surfaces, and the presence of absorbed hydrogen (vacuum degassing, optical microscopy, neutron reflectometry). This combination of approaches was intended not only to quantify the corrosion processes under study but to provide underlying physical and chemical insight.

1.1.4 Scope

The remainder of Section 1 contains a summary of the known corrosion behaviour of Ti in aqueous solution, followed by a review of the literature on passive oxide films on Ti and their properties. A description of published work on hydrogen evolution and hydrogen absorption is offered as background material to the hydrogen absorption studies presented later. Section 2 documents the procedures used to obtain the results presented and discussed in the Section 3. These include open circuit potential measurements, polarization curves, EIS, XPS, neutron reflectometry, crevice corrosion initiation, and hydrogen absorption measurements. The experimental results are presented and discussed in Section 3. This Section is organized by experimental technique, but attempts

are made to link complementary evidence from different techniques together. Finally, the conclusions drawn from this research are summarized in Section 4. Section 4 also attempts to connect the series of smaller revelations from these seemingly disparate experiments into a coherent thesis of the electrochemistry of titanium corrosion. References to published literature listed in Section 5.

Unless specifically indicated otherwise, all potentials[1] herein are reported with respect to the saturated calomel electrode (SCE).

[1] These are all potential *differences* between the system of interest and the reference electrode since electrochemical potentials are reported on a relative, rather than an absolute, scale.

1.2 Aqueous electrochemistry of titanium

1.2.1 Attributes of titanium

Titanium, named for the Titans of Roman mythology, is the ninth most abundant element in the Earth's crust [7, 8]. Ti does not occur on Earth in native metallic form; instead, it is found in concentrated form in deposits of rutile (TiO_2), ilmenite ($FeTiO_3$), and sphene ($CaTiSiO_5$) and in less-concentrated form in most igneous rocks, iron ores, and the sediments derived from them [7, 8]. It has also been detected in living organisms, meteorites, lunar rock samples, and class-m stellar spectra [8]. Discovered in 1791 by W. Gregor and named in 1795 by M.H. Klaproth, Ti possesses some unusual physical and chemical properties that make it very useful in a broad range of applications [7, 8]. A list of some of the important characteristics of Ti is given in Table 1.2.1-a.

Ti metal was first prepared in pure form (99.9%) in 1910 by Hunter, who heated titanium tetrachloride ($TiCl_4$) with sodium in a steel bomb, but it remained a laboratory curiosity until 1946 when Kroll developed the commercial production method of reducing $TiCl_4$ with magnesium. This process is still in use for producing commercial grade Ti; higher-purity Ti is produced by decomposing the iodide [8].

Ti is an important structural material due to its combination of low density, high strength and ability to withstand extremes of temperature. It can be as strong as steel but 45% lighter, or twice as strong as aluminum while only 60% heavier. These features have led to its widespread application in the aerospace industry [9].

Table 1.2.1-a Characteristics of Titanium

Characteristic	Value	Reference
Atomic Number	22	[8]
Atomic Weight	47.867	[8]
Specific Gravity	4.54 @ 20°C	[8]
Melting Point	1668°C	[8]
Boiling Point	3287°C	[8]
Valence	0, 2, 3, 4	[8]
Colour	lustrous silvery metal	[7, 8]
Form (T < 880°C)	hexagonal close-packed (α)	[8]
Form (T > 880°C)	cubic close-packed (β)	[8]
Specific Resistivity	3×10^{-6} Ω·cm @ 20°C	[7]
Stable Isotopes	46-50	[8]
Radioactive Isotopes	39-45, 51-58	[8]
Superconductivity Temperature	0.53 K	[8]
Standard Reduction Potential[1]		[8]
$Ti^{2+} + 2e^- \leftrightarrow Ti$	-1.63 V *vs.* SHE	
$Ti^{3+} + e^- \leftrightarrow Ti^{2+}$	-2.0 V *vs.* SHE	
$TiO_2 + 4H^+ + 4e^- \leftrightarrow Ti + 2H_2O$	-0.86 V *vs.* SHE	
$Ti(OH)^{3+} + H^+ + e^- \leftrightarrow Ti^{3+} + H_2O$	0.06 V *vs.* SHE	

Ti is an extremely reactive element. It burns in air and is the only element to burn in nitrogen. Bare metallic Ti reacts strongly with water and hydrogen. This reactivity has been used advantageously in metallurgical processes where Ti is added as a deoxidizer or denitrogenizer [7] and in ultra high vacuum pumping where titanium sublimation pumps are used as an oxygen getters.

In many common situations however, this high reactivity actually functions to protect the metal from oxidation. Exposed to oxygen or water, Ti surfaces quickly react to form an oxide that is thin, compact, strongly adherent, and highly insoluble. (The properties of

[1] Kelly [10] warned that the solution chemistry and speciation of Ti are so poorly understood that even the best of the standard half-cell reduction potentials recorded for the aqueous Ti must be used with caution.

the oxide are discussed at length in Section 1.3.) The thin passive oxide formed then protects the metal from further chemical attack, including that by water, oxygen, moist chlorine, chloride ions, organic acids and dilute mineral acids [8, 9]. The high reactivity ensures that any mechanical damage to the passive oxide will rapidly repair itself. Thus, Ti, covered by the thin oxide, is highly resistant to gas-phase oxidation and aqueous corrosion, giving it application in many situations where a high level of resistance to chemical reaction is desired, such as in desalination plants, ships, biological implants, kraft mills, chlor-alkali plants, and other aggressive industrial environments. The variety of industrial applications employing Ti, the amount of Ti in service, and the rates and causes of failure of Ti components are the subject of a recent report [9].

1.2.2 Introduction to titanium corrosion

The electrochemical response of Ti in aqueous solutions falls somewhere between that of the true valve metals (*e.g.*, Zr, Nb, Ta) and that of the active-passive metals (*e.g.*, Fe, Co, Ni, Cr). In particular, its oxide film formation resembles that of valve metals, while its corrosion is similar to corrosion of active-passive metals. In defining the bounds of his review of the electrochemical behaviour of Ti [10], Kelly noted that, in aqueous solutions, Ti displays four different types of behaviour. They are:

1.) "active" behaviour –a state in which the metal can be oxidized at a relatively high rate, forming Ti(III) ions in solution.

2.) "passive" behaviour –a state in which the metal is covered by a titanium oxide film and can be oxidized only very slowly, resulting in production of Ti(IV) ions in solution or thickening of the film.

3.) "active-passive" behaviour –a transitional state between the active and passive states in which metal oxidation is somewhat impeded by the incomplete state of surface passivation.

4.) "hydrogen evolution" –a cathodic behaviour that occurs in conjunction with active corrosion of Ti, or when Ti is polarized to sufficiently low potentials, either by an externally impressed current or through electrical contact with another actively corroding metal (*i.e.*, galvanic coupling).

Which particular behaviour is spontaneously exhibited at a given time depends on the duration of exposure, pH, temperature, solution composition, material composition, and other factors [10]. The current-potential response of titanium in acidic aqueous solution is illustrated schematically in Figure 1.2.2-a. From the Figure one can see how the polarization response of Ti can be divided into the four distinct regions described by Kelly: the hydrogen evolution, active, active-to-passive transition, and passive regions.

The cathodic (*i.e.*, reduction) current that flows when a titanium electrode is polarized to a potential within the hydrogen evolution region represents the consumption of electrons by the hydrogen evolution reaction (HER) and a related process, the absorption of hydrogen into the metal. It should be noted, however, that the hydrogen evolution region as depicted in Figure 1.2.2-a is an artificial designation applied for convenience in describing the polarization behaviour of Ti. In reality, the HER also takes place at potentials throughout the active and active-to-passive transition regions. Indeed, as may be apparent in the following discussions, it is probably a mistake to consider the active and active-passive behaviours on Ti as being separate from the production of hydrogen.

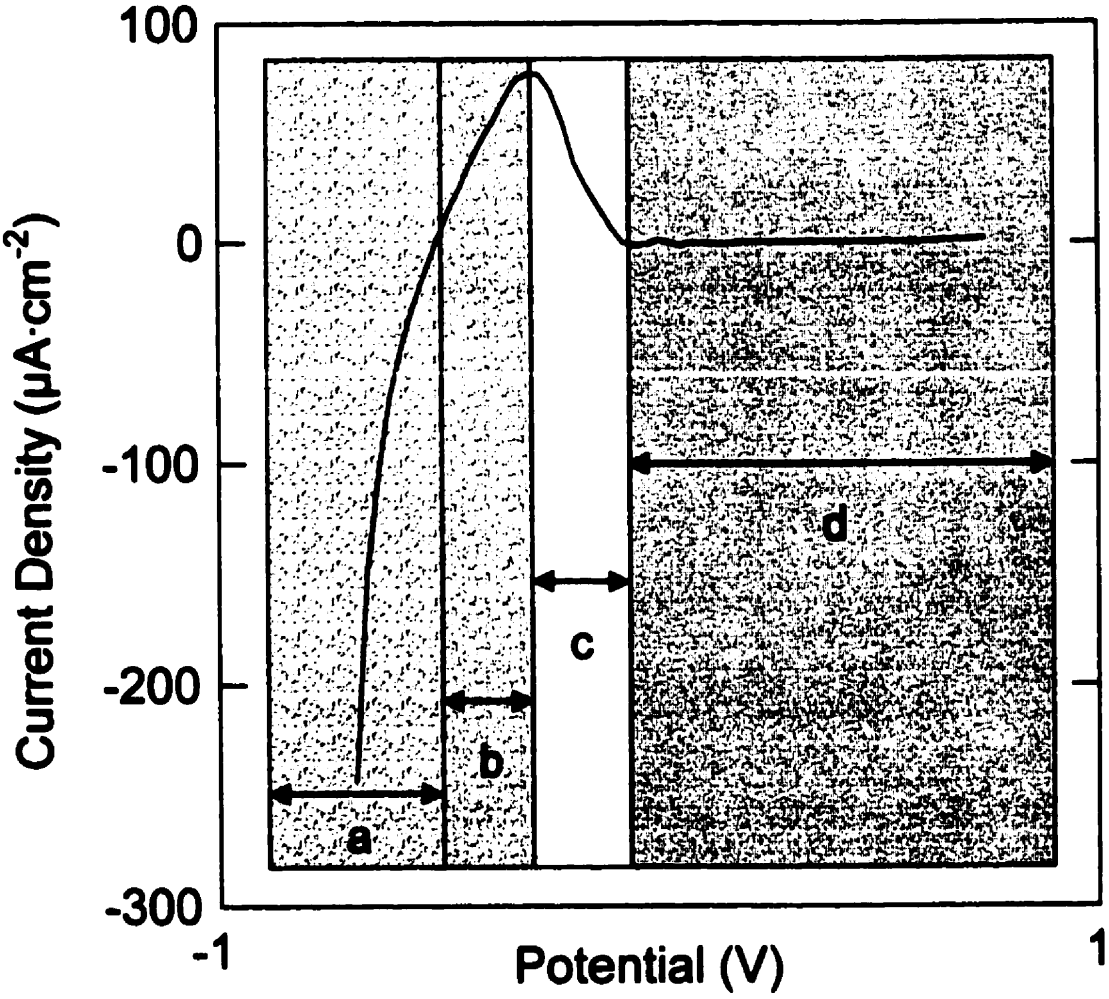

Figure 1.2.2-a Schematic illustration of the current-potential relationship for Ti in acidic aqueous electrolyte indicating the different behavioural ranges: (a) hydrogen evolution region, (b) active region, (c) active-to-passive transition, (d) passive region. Units indicated on the axes are intended to add perspective to the illustration; they do not represent accurate positioning of the current-potential curve.

The relatively low anodic current densities (a few $\mu A \cdot cm^{-2}$ or less) displayed by Ti when polarized to potentials within the passive region indicate a very low rate of metal oxidation to produce Ti(IV) ions that may dissolve into solution or participate in oxide film thickening [10]. That the corrosion rate can be very low under such strongly oxidizing conditions is a major advantage for Ti over many other structural metals. This remarkable corrosion resistance of the highly reactive metal depends entirely on the properties of the thin passive oxide film present on the metal surface under these conditions.

The remaining two regions from Figure 1.2.2-a, the active and active-to-passive transition regions, represent the potential range where Ti is most susceptible to corrosion damage in acidic aqueous environments (although corrosion damage also occurs, along with hydrogen damage, in the hydrogen evolution region). The behaviour demonstrated in these two regions has been thoroughly reviewed by Kelly [10].

Rather than cover the breadth of the vast titanium literature superficially, Kelly restricted his review to a detailed and critical discussion of the active and active-passive states, suggesting that a critical review of the passive state would be a useful undertaking for someone else. Therefore, in this Section, the active and active-passive states will be covered in a synopsized fashion to provide appropriate background for the discussion of the experiments involving surface activation, crevice corrosion, hydrogen evolution, and hydrogen absorption reported herein. The literature dealing with the passive state deserves more detailed coverage to support the conclusions and hypotheses generated from the current studies and, therefore, is reported in detail in Section 1.3. Hydrogen

evolution and absorption, which were only briefly mentioned in Kelly's review, are discussed in Section 1.4.

1.2.3 Active region and active-to-passive transition

Active behaviour is not exhibited by Ti under all conditions, even when it is polarized to a potential corresponding to what is shown as the active region in Figure 1.2.2-a. In order for Ti to manifest active behaviour, its ubiquitous passive film must be penetrated, either chemically or mechanically, and then the exposed surface must be maintained under appropriate conditions (potential, pH, temperature, dissolved oxygen concentration, and others [10]) so that repassivation does not occur. For Ti, the latter requirement demands a fairly aggressive environment; in deaerated aqueous chloride solutions at 30°C the maximum pH for which a stable active state exists is about 2.3 [11].

The active region and active-to-passive transition can be characterized as shown in Figure 1.2.3-a. As the potential is increased from the lower potential limit of the active region, the anodic current density, and therefore the metal dissolution rate, increases to a maximum, called the critical current density, I_m, at the "passivation potential", E_m [12]. The passivation potential defines the boundary between the active region and the active-to-passive transition. As the potential is increased beyond E_m, the anodic current decreases and metal dissolution slows until the active-to-passive transition gives way to the passive region beyond the "Flade potential" [12].

The effect of having this active-passive maximum in the anodic dissolution rate is that the dissolution rate will be very low if the electrochemical potential at the Ti surface is either much lower than the lower limit of the active dissolution region or higher than the Flade

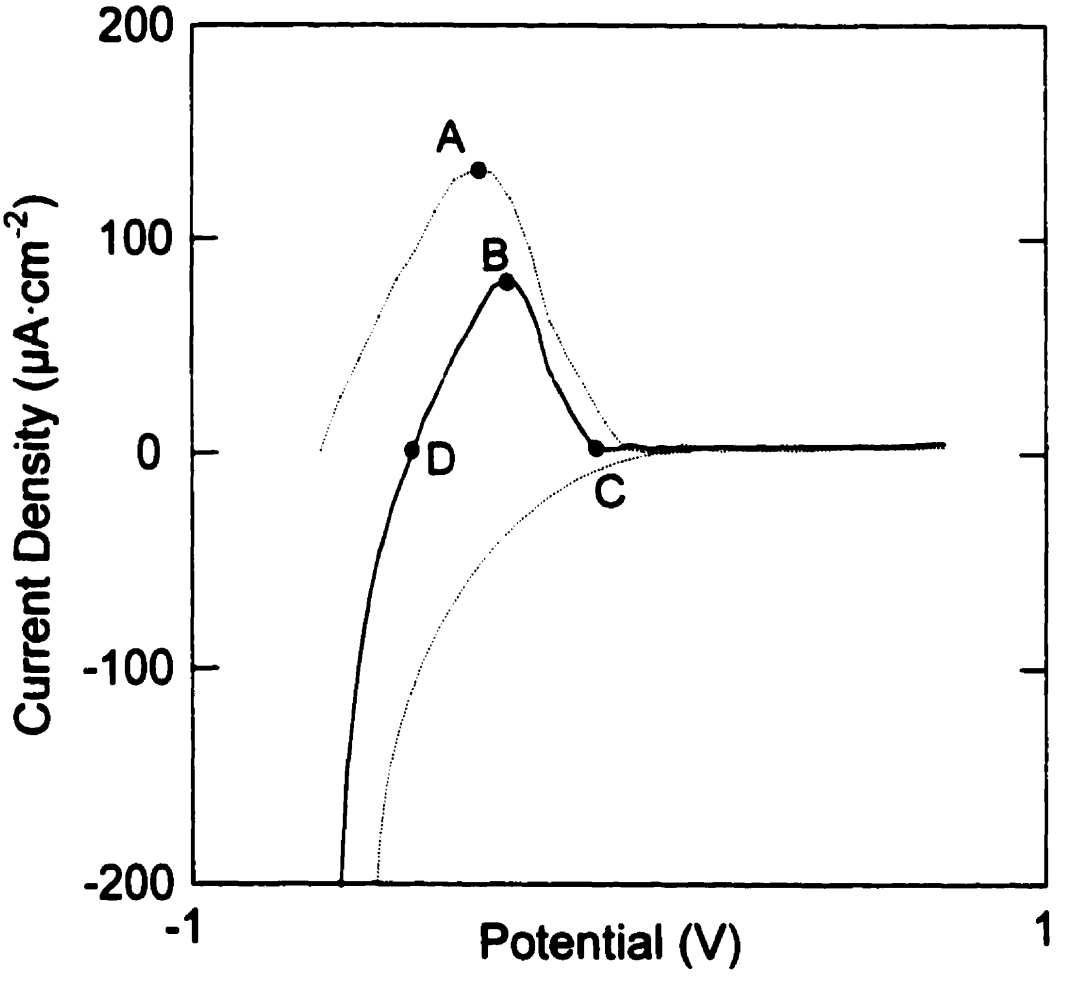

Figure 1.2.3-a Schematic illustration of the current-potential relationship for Ti in acidic aqueous electrolyte indicating how the partial currents due to the Ti dissolution and proton reduction reactions (dotted curves) combine to yield the observed net current (solid curve). Significant points on the curves include: (A) the point at which the Ti dissolution rate is at a maximum ($E_{m,d}$, $I_{m,d}$), (B) the measured current peak, defined by the passivation potential and critical current density for passivation (E_m, I_m), (C) the Flade potential, and (D) the open circuit or corrosion potential, E_{oc}. As in Figure 1.2.2-a, the units indicated on the axes are provided to add perspective only.

potential. Furthermore, under freely corroding conditions (*i.e.*, without an externally applied potential), the net current on the metal must be zero so that charge is conserved, and the electrochemical potential of the metal must adopt a value at which this condition is satisfied, that is, a potential at which the partial currents due to the oxidation and reduction half-reactions occurring on the surface are equal in magnitude. This is called the corrosion potential, or, more generally, the open circuit potential, E_{oc}. Therefore, if the associated cathodic reaction that drives metal dissolution has a reversible potential greater than the Flade potential and occurs at a rate higher than $I_{m,d}$ at $E = E_{m,d}$ (where $I_{m,d}$ represents the maximum partial current due to metal dissolution and $E_{m,d}$ the potential at which this maximum partial current is achieved), then E_{oc} will be spontaneously driven into the passive region (the only point at which the anodic and cathodic partial currents could be equal in magnitude) and the metal dissolution rate will be exceedingly low [13].

Kelly's review article [10] describes in detail the chemical characteristics of Ti in the active and active-to-passive states. A brief summary is presented here. There exist three common schools of thought regarding the state of the surface in the active and active-to-passive transition regions. Some researchers have suggested that the surface is covered by a phase oxide, a thinner version of the passive film, while others insist that only an adsorbed monolayer of oxygen species covers the surface under these conditions. A third group considers the active and active-to-passive transition region surfaces to be covered by a surface hydride. Kelly [10] convincingly dispels the idea of a phase oxide on active and active-to-passive titanium surfaces, but acknowledges that, under some

circumstances, the presence of a hydride phase on the metal is undeniable. The evidence for an adsorbed monolayer of oxygen species in many cases is strong. However, "bare" Ti, or Ti covered by adsorbed water does not appear to be an option since one would expect to observe Tafel behaviour[1] under these conditions, as is observed on other water-covered active metals such as Fe. Anodic Tafel behaviour is not observed on Ti.

Throughout the active region and most of the active-to-passive transition (up to $E = E_m + 0.13\,\mathrm{V}$), Ti dissolves exclusively as Ti(III) ions. Only at the high-potential end of the active-to-passive transition are Ti(IV) ions released from the corroding metal. Stirring has no effect on the dissolution rate in the active and active-to-passive transition regions, indicating that the corrosion reactions are activation-controlled, as opposed to mass transport-controlled. The value of E_m is independent of the temperature, while I_m increases with increasing temperature ($\log(I_m) \propto -\frac{1}{T}$). The apparent activation energy for Ti dissolution is $57.3\,\mathrm{kJ \cdot mol^{-1}}$ in $1\,\mathrm{mol \cdot dm^{-3}}$ HCl and $59.9\,\mathrm{kJ \cdot mol^{-1}}$ in $0.5\,\mathrm{mol \cdot dm^{-3}}$ H_2SO_4 [10].

Passive Ti spontaneously activates in deoxygenated chloride and sulphate solutions at pH values less than 2.3 and 3.0, respectively, at 30°C. Both E_m and I_m are pH-dependent, but to determine the correct functional relationship, E_m and I_m must be corrected for the simultaneously occurring HER. When such a correction is made, yielding the new values $E_{m,d}$ and $I_{m,d}$, the following relationships apply [10]:

[1] Tafel behaviour is indicated by a linear relationship between the potential and the logarithm of the current density, extending over several orders of magnitude of current density change.

$$\frac{\partial \log I_{m,d}}{\partial pH} = -\frac{2}{3} \qquad \textbf{(1.2.3-a)}$$

$$\frac{\partial \ln I_{m,d}}{\partial E_{m,d}} = \frac{F}{2RT} \qquad \textbf{(1.2.3-b)}$$

$$\frac{\partial E_{m,d}}{\partial pH} = -\frac{4}{3}\frac{(2.303)RT}{F} \qquad \textbf{(1.2.3-c)}$$

In addition, the lower potential limit of the active region remains nearly constant while the Flade potential decreases with increasing pH. The existence of these relationships involving small whole number ratios and multiples of the mechanistically significant parameter $\frac{RT}{F}$ must be accounted for in any reasonable mechanism proposed [10].

Many mechanisms for active dissolution have been put forth, some of which account for the relationships expressed above, some of which do not, and therefore cannot be considered valid proposals. Many of these have been formulated based on *thermodynamic* considerations that suggest what is *possible*, rather than the *kinetic* data, which determine what actually *happens*. Kelly [10] wittily refers to this common failure to reconcile thermodynamics with kinetics as "The Great Nernstian Hiatus".

As in any corrosion reaction, the oxidation half-reaction on the freely corroding metal is driven by an electrochemically equivalent amount of reduction, taking place on the same surface or one electrically connected to it, to maintain a charge balance. As mentioned previously, one of the great corrosion advantages of active-passive metals such as Ti is that, if the cathodic half-reaction is strong enough at potentials corresponding to the

active region, the only potentials at which this charge balance can be maintained between the anodic and cathodic half-reactions fall within the passive region.

One of the extraordinary features of Ti is that its active region corrosion product (Ti(III)) can transform itself into an effective corrosion inhibitor (Ti(IV)) in the same solution, in contact with the corroding electrode, without any special manipulation. Small concentrations of Ti(IV) have been shown to induce repassivation of active Ti. The mechanism by which Ti(IV) can effect repassivation appears to be that it acts as an additional oxidant, strengthening the cathodic half-reaction and pushing E_{oc} into the passive region as described above [14, 15]. The interesting feature of this process is that the Ti(IV) that aids repassivation can be produced by the oxidation, at passive areas of a piece of Ti undergoing localized corrosion, of Ti(III) ions produced at actively corroding areas on the *same* piece of metal. The effect has been termed autopassivation. Autopassivation can also occur in any electrolyte-coupled active-passive Ti system; that is, a system in which active-state and passive-state Ti surfaces are located in the same body of electrolyte (such as exists during localized corrosion).

Active dissolution of Ti under uniform corrosion conditions in sulphate solutions is significantly faster than it is in chloride solutions. The difference has been attributed to the stronger ability of sulphate to complex Ti ions. Ti(III) is very weakly complexed by chloride (less than 5% $[Ti(H_2O)_5Cl]^{2+}$ in 1.0 $mol \cdot dm^{-3}$ HCl]). Ti(IV) is complexed more strongly by chloride than is Ti(III), but sulphate complexes are stronger still, the dominant Ti(IV) species in sulphate solutions being $Ti(OH)_3HSO_4$. In perchlorate solutions up to

1.5 mol·dm^{-3}, Ti(IV) was found to exist entirely as $[Ti(OH)_2]^{2+}$ and $[Ti(OH)_3]^{+}$ species [10].

Autopassivation, on the other hand, is more difficult in chloride solutions than in sulphate. Kelly reported that it takes 10.5 times as large a concentration of Ti(IV) ions to passivate an active Ti surface in 1.0 mol·dm^{-3} HCl than it does in 0.5 mol·dm^{-3} H_2SO_4. It also requires 10-100 times as long to generate the concentration of Ti(IV) required for autopassivation in the HCl solution (due to the lower corrosion rate), suggesting that autopassivation should be much less likely to occur in chloride media. This means that chloride should function to promote localized corrosion, which it is known to do.

1.2.4 Crevice corrosion

Crevice corrosion is an insidious form of corrosion that occurs in cracks and gaps between adjacent metal surfaces, or spaces between metals and other solid materials that hinder mass transport. Crevice corrosion, like pitting, is a type of occluded cell corrosion, *i.e.*, corrosion occurs on an area of the metal surface that is exposed to a volume of solution that has stagnated and developed aggressive local chemical conditions due to restrictions in mass transport [10]. A schematic diagram of the processes involved in crevice corrosion on Ti is given in Figure 1.2.4-a.

The lifetime of a corroding crevice can be divided into three phenomenological phases: initiation, propagation, and repassivation [16]. Initiation requires that sufficiently aggressive chemical conditions (*e.g.*, low pH, low concentration of dissolved oxygen) develop within the crevice that the passive oxide film is penetrated and the underlying metal can achieve an active state.

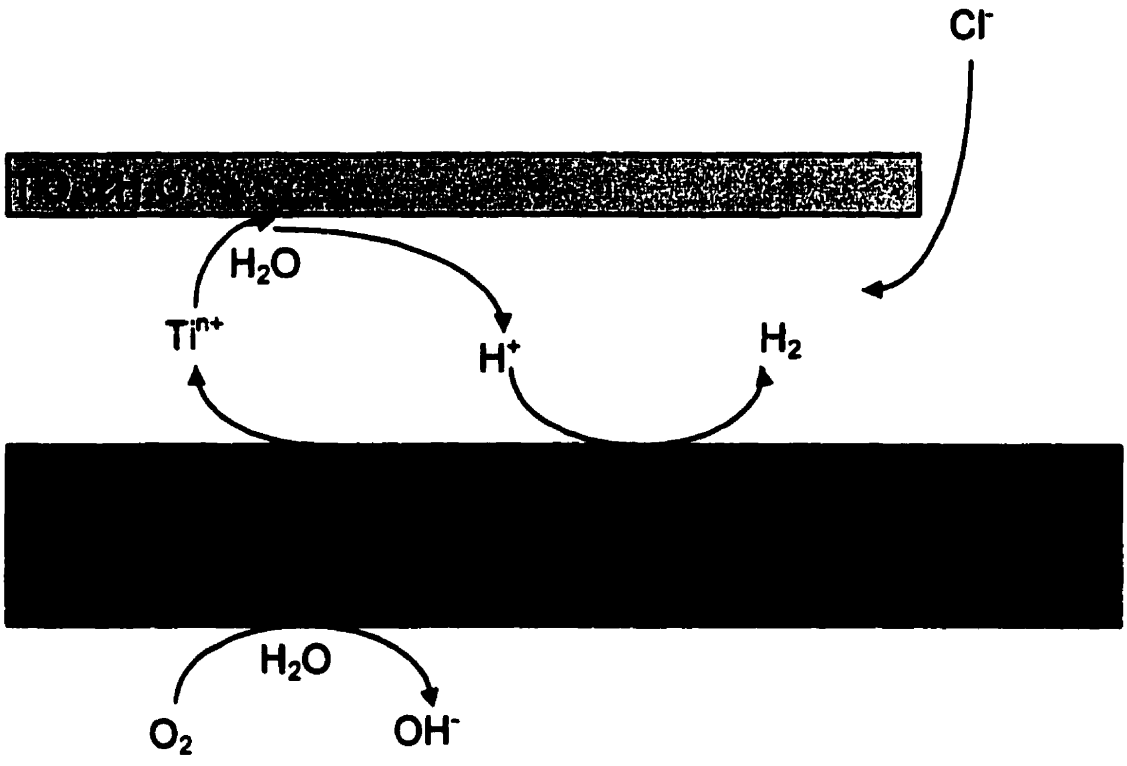

Figure 1.2.4-a Schematic depiction of crevice corrosion and the chemical processes involved. Metal oxidation within the crevice is driven by oxygen reduction on the crevice exterior. Metal dissolution is followed by cation hydrolysis, which results in precipitation of corrosion product deposits and acidification of the crevice interior. Once the crevice anolyte pH is low enough, metal oxidation can also couple to proton reduction within the crevice. This is a self-sustaining reaction, producing more protons by cation hydrolysis while other protons are reduced in driving corrosion. The proton reduction reaction leads to hydrogen gas evolution and hydrogen absorption by the metal. Autopassivation by Ti(IV) species is a possibility if active and passive sites coexist within the occluded area.

Propagation, *i.e.*, the continuation and spread of crevice corrosion, requires that part of the metal be maintained in an active state (which, in turn, requires specific conditions of pH and potential, as described in Section 1.2.3) and part of it be supplied with oxidant. This oxidant can be oxygen or another oxidizing species that is reduced on the passive surfaces of the metal in areas outside of the occluded region, or it can be protons that are generated within the occluded region by hydrolysis of metal ions and reduced to hydrogen within the crevice interior.

Repassivation occurs when the chemical conditions or electrochemical potential required for active behaviour [10, 17] can no longer be maintained within the crevice, and a passive oxide film is re-grown on the corroding surfaces. This could happen as a result of: increased mass transport within the crevice (*e.g.*, due to an increase in the crevice gap dimensions), which would cause an increase in the local pH, oxygen ingress within the occluded region, or a change in the potential drop at the metal/solution interface; an increase in the rate of the cathodic reaction, which could generate anodic protection (*e.g.*, autopassivation by Ti(IV) as described above in Section 1.2.3); decreased availability of oxidant; or other factors.

While this division of the overall crevice corrosion process into initiation, propagation, and repassivation phases is convenient for descriptive purposes (and these phases must occur in sequence for a given point within a crevice), initiation, propagation, and repassivation can take place simultaneously at different points within a corroding crevice throughout its lifetime.

The chemical conditions within a corroding crevice on Ti have been notoriously difficult to measure due to the small volumes of solution and awkward geometries involved and the strongly adherent, insoluble corrosion product deposits produced, yet some attempts have been made using microelectrodes [3, 10]. These investigations showed the depletion of dissolved oxygen within the crevice after immersion in aerated solution and the development of crevice pH values below 1.0 before crevice corrosion initiation in electrolytes having bulk pH values near neutral. Although the crevice corrosion studies were performed at elevated temperatures (T > 70°C), these observations are consistent with the statement in Section 1.2.3 that, at T = 30°C, pH values less than about 2.3 and 3.0 are required for spontaneous activation of Ti in deaerated chloride and sulphate solutions, respectively [10], (although the required conditions were even more severe) and with the known ability of dissolved oxygen to maintain passivity on Ti. The depletion of oxygen within the crevice results from oxygen reduction coupled to metal oxidation, combined with the restricted mass transport conditions that inhibit replenishment of the dissolved oxygen from the bulk solution outside the crevice [10].

Similarly, acidification within the crevice occurs as a result of metal oxidation followed by hydrolysis of the metal cations; for example:

$$Ti^{4+} + 2H_2O \rightarrow [Ti(OH)_2]^{2+} + 2H^+ \qquad \textbf{(1.2.4-a)}$$

or

$$Ti^{4+} + 4H_2O \rightarrow Ti(OH)_4 + 4H^+ \qquad \textbf{(1.2.4-b)}$$

The local acidity is maintained by the meagre mass transport into and out of the crevice [10].

It is interesting to note that the two cathodic half-reactions that drive crevice propagation, oxygen reduction and proton reduction, have different influences on the crevice pH. Oxygen reduction takes place on the passive exterior surfaces of a corroding crevice, and in neutral solution creates basic reaction products;

$$O_2 + 2H_2O + 4e^- \rightarrow 4OH^- \qquad \textbf{(1.2.4-c)}$$

Proton reduction can take place on the interior surfaces of a corroding crevice, which are exposed to acidic solution;

$$2H^+ + 2e^- \rightarrow H_2 \qquad \textbf{(1.2.4-d)}$$

and

$$H^+ + e^- \rightarrow H_{abs} \qquad \textbf{(1.2.4-e)}$$

where H_{abs} refers to a hydrogen atom absorbed into the metal matrix[1]. Taken alone, reaction **1.2.4-c** would increase the pH of the bulk solution outside the crevice, while reactions **1.2.4-d** and **1.2.4-e** would result in an increase in pH within the crevice.

One must recall, however, that reduction reactions are always coupled to an electrically equivalent set of oxidation reactions to maintain a charge balance. In this case, proton reduction reactions **1.2.4-d** and **1.2.4-e** would be coupled to metal oxidation reactions,

[1] Hydrogen absorption by Ti will be covered in Section 1.4.

also occurring within the crevice, which lead to proton-producing hydrolysis reactions such as **1.2.4-b**. The amounts of proton production and consumption by these coupled redox reactions are equivalent. Thus, the proton reduction reaction can drive metal dissolution without affecting the crevice pH. One could imagine this cycle continuing until the Ti was completely consumed; however, in practice, there are some losses of protons by mass transport out of the crevice, the rates and yields of hydrolysis reactions may change during the crevice lifetime, and, as mentioned above, other processes may also lead to repassivation.

The oxygen reduction reaction (**1.2.4-c**) would also be coupled to metal oxidation reactions that lead to proton-producing hydrolysis reactions within the crevice. Due to the spatial separation, however, the pH increase due to oxygen reduction on the crevice exterior would not immediately neutralize the acidity produced by metal hydrolysis within the crevice, and the crevice interior would be acidified [10]. Therefore, if a small amount of oxygen reduction occurs, just enough to balance proton loss from the crevice and maintain the acidic pH, significant corrosion damage could be done by the redox cycle involving the coupling of metal oxidation to proton reduction within the crevice. In fact, the amount of proton reduction within corroding crevices has been measured and found to account for ~80-90% of the damage occurring during periods of crevice corrosion on Ti [18-22]. In other words, the amount of corrosion observed was 5-10 times the amount directly attributable to the available oxygen (according to Faraday's law).

Finally, in order to maintain charge neutrality in the crevice (where a net oxidation takes place, generating an excess of cationic species in solution), some ionic current must flow

between the bulk solution and the crevice anolyte. This is accomplished, at least in part, by migration of anions (*e.g.*, chloride or sulphate) into the crevice [3, 10, 16]. The number of anions required would become quite large for a rapidly propagating crevice. Thus, the crevice anolyte would become a highly concentrated, dense solution [23]. The solution chemistry of Ti in highly concentrated, acidic, saline solutions at elevated temperatures is not well known. It should be noted, however, that the activity coefficient for HCl increases with increasing chloride concentration above ~0.5 $mol \cdot dm^{-3}$ [24], suggesting that the anolyte solution within a propagating crevice could be remarkably aggressive.

Of equal importance to crevice propagation as the aggressive chemical conditions is the maintenance within the crevice of potentials that fall within the active region for Ti (the extent of the active region itself being determined by the chemical conditions) [10, 17]. While the potential developed on Ti surfaces exposed to oxygenated solution, including those on the crevice exterior, tends to be high (*i.e.*, within the passive potential range), lower, active region potentials can be established within the crevice due to the combination of current flow and impedance between the crevice interior and exterior. This impedance can result from a combination of oxide film resistance, solution resistance increased by the narrow crevice geometry, film capacitances, *etc.*

On planar electrodes uniformly corroding in homogeneous bulk solution, the anodic and cathodic half-reactions proceed at immediately adjacent locations on the surface. The surface must therefore adopt a single potential at which the rates of the two half-reactions are electrochemically equal, since there is no significant impedance and therefore no

potential drop between the anodic and cathodic sites. In crevice corrosion (and other forms of localized corrosion), the significant physical separation of anodic and cathodic sites on the metal surface and the ability to maintain differing solution compositions at each allow the metal to adopt a different potential at each site, provided that the overall reduction rate is still equal to the total oxidation rate.

An extensive series of crevice corrosion studies has already been conducted on Ti for the express purpose of predicting the longevity of Ti nuclear fuel waste containers under Canadian waste disposal vault conditions, including the evaluation of the effects of: temperature; oxygen concentration; solution composition and pH; radiation fields; material composition, impurities, and microstructure; heat treatment and welding; applied potential; crevice tightness; exposure time; and anode-to-cathode area ratios [2, 16, 19-22, 25-37]. The major conclusions of these studies will be summarized below, along with information from a[1] good general review of crevice corrosion on Ti [38, 39].

1.2.4.1 Temperature

The susceptibility of Ti alloys to crevice corrosion generally increases with increasing temperature. It is widely accepted [40] that crevice corrosion will not initiate on Ti at temperatures lower than ~70°C, regardless of pH or solution chemistry (except in a few very extreme cases) [38]. These generalizations are solidly based on empirical observations gathered from extensive field and laboratory experience with Ti and its alloys and are used as practical "rules of thumb" [40]; less effort has been put into

[1] The singular is used here, as this is one review published in two parts.

understanding the fundamental bases for these observations.

Such broad generalizations cannot be made concerning crevice corrosion *propagation*. Ikeda *et al.* [22] found that, once initiated, crevice corrosion on Grade-2 Ti[1,2] propagated at a rate that strongly depended on temperature, following an Arrhenius-type relationship over the temperature range 30-150°C. The corrosion damage appeared to localize at lower temperatures and become more general within the occluded area at higher temperatures [20]. On Ti-12[3] the crevice corrosion rate was much less dependent on temperature.

In spite of the temperature dependence of the crevice corrosion propagation rate, the amount of corrosion damage was ultimately determined by the amount of oxygen available for consumption, and not the corrosion rates. The Arrhenius relationship displayed by Ti-2 suggested a single interfacial reaction step with an activation energy of ~55 $kJ \cdot mol^{-1}$ was rate-controlling, and the authors took this as evidence that the crevice corrosion rate was controlled by the kinetics of the oxygen reduction reaction [22].

The repassivation tendencies of the two alloys were also found to be very different; Ti-2 continued to crevice corrode at temperatures down to ambient[4] if the temperature was lowered gradually enough[5], while Ti-12 repassivated at temperatures $\leq 70°C$, regardless

[1] Grade-2 Ti is a Ti material of commercial purity.

[2] For ease of notation, throughout this Thesis Grade-n Ti will be shortened to Ti-n, where n represents the ASTM grade classification. For example, ASTM Grade-2 Ti will be shortened to Ti-2.

[3] Ti-12 is an alloy containing a nominal 0.8 wt.% Ni and 0.3 wt.% Mo.

[4] At room temperature, crevice corrosion could not be sustained indefinitely and ceased after ~100 h. Examination of the corroded surfaces showed increased localization of attack with decreasing temperature, propagation becoming limited to a few sites around the periphery of the crevice [20].

[5] According to Schutz [38], a rapid temperature reduction quenches active crevices on Ti-2.

of the cooling rate, and even if oxygen was still available outside the crevice to drive the corrosion reaction [20, 22, 38]. Once temperature-induced repassivation of crevice corrosion on either material occurred, crevice corrosion could not be revived by re-heating the system to 105°C [20].

From both the propagation and repassivation data it was concluded that the differences between the behaviours of Ti-2 and Ti-12 indicated that the crevice corrosion of Ti-2 is controlled primarily by environmental factors, whereas that of Ti-12 is governed predominantly by properties of the material itself [20].

1.2.4.2 Oxygen concentration

Oxygen in solution is required for the propagation of crevice corrosion on Ti. Ikeda *et al.* found that crevice corrosion could be easily initiated in oxygenated solutions, but when they attempted to initiate crevice corrosion on Ti-2 in deaerated solution, very little crevice corrosion was observed [16]. McKay and Mitton [19] suggested that the overall crevice corrosion propagation rate on Ti-2 was rate-limited by oxygen diffusion. The propagation rate decayed logarithmically as the oxygen in a closed system was consumed by the corrosion reactions. Ikeda *et al.* [29] found a half-order dependence of the crevice corrosion propagation rate on the dissolved oxygen concentration and suggested that the crevice corrosion rate was controlled by the kinetics of the oxygen reduction reaction [22].

The extent of crevice corrosion propagation on Ti-2 (*i.e.*, the amount of corrosion damage to the metal), however, was determined to depend not on the oxygen concentration, but

on the total amount of oxygen available for consumption [2, 22]. Ikeda *et al.* showed that crevice corrosion propagation on Ti-2 ceased when the available oxygen was depleted, but, for a limited time after the cessation of crevice corrosion, the corrosion reaction within the oxygen-starved crevice could be revived by adding more oxygen (i.e., the crevice was only dormant, not repassivated, and crevice corrosion propagation would recommence if re-supplied with oxidant) [16, 20, 35].

The period during which crevice corrosion could be re-started appeared to terminate when a sudden increase in the artificially creviced electrode potential occurred [2, 22, 29] such that it approached the potential of a freely corroding non-creviced Ti electrode in the same solution. After the appearance of this feature, further additions of oxygen only increased the creviced electrode potential, signifying the presence of a passive system; no rekindling of crevice corrosion propagation occurred[1] [2, 29]. The authors interpreted this feature as the crevice's repassivation signature, probably indicating the neutralization of the low pH within the crevice and the formation of a passive oxide layer on the previously corroding surfaces [16, 34, 35].

The effects of oxygen concentration on the propagation rate of crevice corrosion on Ti-12 were recently reported [37]. While the initial propagation rate increased with increasing oxygen concentration, the steady-state crevice corrosion rate and the total extent of corrosion damage were independent of the oxygen concentration. The propagation period before repassivation occurred decreased in length with increasing oxygen concentration.

[1] In fact, crevice corrosion could only be re-started by increasing the temperature even further and re-initiating the attack, presumably at previously uncorroded sites [B.M. Ikeda, private communication].

On Ti-12, crevice corrosion did not continue to propagate until all the available oxygen was consumed; instead, repassivation occurred after crevice corrosion propagated to a very limited degree [2, 35, 37]. Similar to Ti-2, the repassivation signature involving the sudden increase in the creviced electrode potential was observed on Ti-12 along with a simultaneous cessation of crevice corrosion [2].

The extent of crevice corrosion of Ti-12 was not controlled by the amount of oxidant available as it was on Ti-2. The published accounts of oxygen effects on crevice corrosion of Ti-2 and Ti-12 support the statement in Section 1.2.4.1 that crevice corrosion of Ti-2 is controlled primarily by environmental factors, whereas that of Ti-12 is governed predominantly by properties of the material itself [20].

1.2.4.3 Solution composition and pH

Crevice corrosion of Ti is only known to occur in solutions containing chloride, bromide, iodide, fluoride, or sulphate [38]. The effects of many other solution species on Ti crevice corrosion have been investigated [2, 37, 38]. Non-oxidizing cations have insignificant effects on crevice corrosion, with the exception of Mg^{2+}, Ca^{2+}, Zn^{2+}, and Al^{3+}, which may hydrolyze, yielding very low pH values and aggravating localized pitting-type corrosion within the corroding crevice [37, 38]. Oxidizing cationic species and other species that depolarize the cathodic reaction can dramatically stimulate crevice corrosion initiation and propagation[1] [38]. Oxidizing anionic species may diffuse or migrate into corroding crevices, inhibiting crevice corrosion attack [38], presumably by

[1] Because they are encountered nearly universally, oxygen and H^+ effects on crevice corrosion are discussed separately from other solution species.

causing repassivation of the interior surfaces of the occluded region. Other species, such as carbonate and sulphate, tend to suppress crevice corrosion, possibly by complexing Ti cations and preventing their acid-producing hydrolysis, by buffering the pH directly, or by lowering the critical Ti^{4+} concentration required for autopassivation [10] in the case of SO_4^{2-}, and by simple pH buffering in the case of CO_3^{2-} [2]. The observation that SO_4^{2-} suppresses crevice corrosion to a greater degree than does CO_3^{2-} suggests that pH buffering is not as effective as complexation and/or autopassivation in controlling crevice corrosion [2].

Exposure of the corrodant solution to crushed glass suppressed initiation and propagation of crevice corrosion on Ti and enhanced repassivation [2]. The effect was attributed to dissolved silica, but no suggestions regarding the mechanism of corrosion inhibition were offered. Table 1.2.4.3-a lists some of the solution species tested and their effects on Ti crevice corrosion.

The effects of chloride on Ti crevice corrosion have been studied in greater detail [27, 33]. Although the extent and rate of crevice corrosion were said not to be particularly dependent on the chloride concentration [2], some interesting influences were noted [27]. On Ti-2, the extent of crevice corrosion decreases with increasing chloride concentration [27]. This trend is unusual for corrosion reactions and was thought to be a consequence of either a diminished potential difference between the metal surfaces of the crevice interior and exterior, or an elevated pH in the crevice interior caused by complexation of Ti cations by chloride anions, preventing acid production by cation hydrolysis [27, 37]. Crevice corrosion attack was found to be more uniform within the occluded region at the

highest chloride concentrations, an observation that may support the former explanation; however, the crevice corrosion-suppressing influence of other Ti-complexing anions (*e.g.*, SO_4^{2-}) supports the latter [2, 27, 37]. Ikeda *et al.* felt that the complexation hypothesis was the more likely of the two explanations offered.

Table 1.2.4.3-a Solution Species and Their Effects on Crevice Corrosion [10, 37, 38]

Effect	Little influence	Hydrolyze, causing attack	Accelerate attack	Inhibit attack	Permit initiation
Species	Na^+, K^+, NH_4^+	Ca^{2+}, Mg^{2+}, Zn^{2+}, Al^{3+}	Fe^{3+}, Cu^{2+}, Ni^{2+}, Ti^{4+}, Ce^{4+}, Sn^{4+}, VO_2^+, Te^{4+}, Te^{6+}, Se^{4+}, Se^{6+}, Hg^{4+}, Pt^{2+}, Pt^{4+}, Pd^{2+}, Ru^{3+}, Ir^{3+}, Rh^{3+}, Au^{3+}, Cl_2, H^+, O_2	*Ti^{4+}, OCl^-, ClO_3^-, ClO_4^-, NO_3^-, $Cr_2O_7^{2-}$, MoO_4^{2-}, $S_2O_3^{2-}$, VO_4^{3-}, VO_3^-, IO_3^-, WO_4^-, silica, SO_4^{2-}, CO_3^{2-}	F^-, Cl^-, Br^-, I^-, SO_4^{2-}

* If produced inside the crevice, Ti^{4+} may cause autopassivation [10] (see Section 1.2.3).

For materials that resist crevice corrosion, such as Ti-12, or Ti-2 alloys containing high levels of Ni and Fe impurities [37], increasing the chloride concentration increases the likelihood of crevice corrosion initiation and the extent of propagation up to a concentration of ~2-3 mol·dm^{-3} [27, 35]; however the extent of corrosion damage decreases for more concentrated solutions. It would appear that the chloride increases the corrosion of these resistant materials by enhancing the initiation stage, but at high concentrations results in a lower extent of propagation, perhaps for the same reason that crevice corrosion propagation decreases with increasing chloride concentration on Ti-2.

As with most corrosion reactions, the pH has a large influence on the crevice corrosion of Ti. The emphasis in this summary is on the bulk solution pH, since the pH of the crevice interior is established and maintained by the corrosion reactions quite separately from that of the solution bulk. Decreasing the bulk solution pH strongly increases susceptibility to crevice corrosion [38], probably by enhancing the rate of the oxygen reduction reaction by lowering the potential and by increasing the conductivity of the passive oxide film through film thinning and increasing the number density of electronic defects such as Ti^{3+} [27]. Ti-12 and the noble metal alloys are much more resistant than Ti-2 in this regard [38, 40]. At very low pH values, the ability to maintain different solution chemistries inside and outside the crevice is lost and only uniform corrosion proceeds. At the other end of the scale, crevice corrosion on Ti in chloride media is stifled at pH values above 10.5 [38].

1.2.4.4 Radiation fields

The influence of radiation fields on the crevice corrosion of Ti was a consideration in investigations of Ti as a candidate material for nuclear fuel waste containers [16, 25, 35, 37]. For intact fuel waste containers, radiation would emanate from within the containers, and any crevice corrosion would occur on the exterior of the container walls. Thus, to influence crevice corrosion, radiation would first have to penetrate the Ti metal (~6 mm in the case of the proposed containers); therefore the radiation effects studied were limited to those caused by gamma (γ) radiation, the only type emitted by nuclear fuel waste that is capable of penetrating 6 mm of Ti.

The influence of γ-rays on Ti crevice corrosion appears limited to their ability to produce corrosion-influencing radiolytic species in solution; direct effects of this radiation on the metal are small [16]. γ-Radiolysis of water produces oxidizing species, such as $OH^{\bullet}$, H_2O_2, and O_2, and a corresponding amount of reducing species, such as $H^{\bullet}$, $e^-_{(aq)}$, and H_2 [16] (where the "$^{\bullet}$" symbol signifies a radical species and $e^-_{(aq)}$ represents an electron in the aqueous phase).

In experiments with Ti-2, Ikeda and co-workers [16, 35, 41] found that the radiolytic production of oxidizing species within the crevice could inhibit crevice corrosion. When crevice corrosion was initiated in the presence of γ-radiation at dose rates of 4 $Gy \cdot h^{-1}$ or more, crevice repassivation occurred before the available oxygen in the system was depleted[1] [2], limiting the extent of corrosion damage. Application of γ-radiation to actively propagating crevices did not cause them to repassivate before the available oxygen was depleted; however, an immediate decrease in the propagation rate was observed [16]. Ikeda *et al.* concluded that γ-irradiation enhanced the crevice corrosion resistance of Ti-2, but that the overall influence was small [37].

1.2.4.5 Material composition, impurities and microstructure

The crevice corrosion resistance of Ti is strongly influenced by the presence of certain alloy components and even minor impurities [38]. Alloying and impurity effects on the uniform corrosion of Ti materials are discussed in detail in Section 1.2.5; the elements

[1] In the absence of radiation, crevice corrosion propagation on Ti-2 normally proceeded until the available oxygen was consumed (see Section 1.2.4.2).

that promote passivation of Ti under uniform corrosion conditions in hot reducing acids similarly enhance Ti crevice corrosion resistance [38]. These elements can significantly expand the range of temperatures and pH values in which crevice corrosion can be avoided [38] or help limit the extent of crevice corrosion by inducing repassivation [37]. For example, Schutz [42] found that the bulk solution pH and temperature ranges where crevice corrosion is possible on unalloyed Ti (Ti-1 and Ti-2: $pH \leq 8$, $T \geq 65°C$) were significantly improved by alloying with Ni and Mo (Ti-12: $pH \leq 3$, $T \geq 70°C$) or with Pd or Ru (Ti-7, Ti-11, Ti-16, Ti-17 and Ti-0.1Ru[1]: $pH \leq 1$, $T \geq 80°C$). The crevice corrosion advantages of Ti-12 over Ti-2 were also noted by McKay [21, 32].

For experiments conducted on Ti-2, Ti-12, and Ti-16, the extent of crevice corrosion damage was found to increase in the order [37]:

Ti-16	<<	Ti-12	<	Ti-2	<	Ti-2	<	Ti-2
(Ti-Pd)		(Ti-Ni-Mo)		(high Fe, high Ni)		(high Fe, low Ni)		(low Fe, low Ni)

Microstructural effects on crevice corrosion propagation have also been studied [43, 44]. It is somewhat difficult to separate microstructural influences on Ti corrosion from compositional effects, since the distribution of grain sizes and the existence of different crystallographic phases are, in part, consequences of the presence and levels of alloying elements or impurities. The effects of material microstructure are not well understood; however, a number of structure-related observations have been made.

[1] Ti-7, Ti-11, Ti-16, and Ti-17 are all Pd-containing alloys and Ti-0.1Ru represents an experimental Ti alloy containing 0.1 wt.% Ru.

Ikeda *et al.* [44] noted that Ti-2 materials with larger grain sizes have generally poorer crevice corrosion resistance than those with smaller grain sizes; however, they pointed out that the grain size is associated with the purity of the material, the smaller-grained material usually containing higher levels of (potentially corrosion-inhibiting) impurities. They also found that other factors could override the grain size rule-of-thumb and make smaller-grained material more susceptible to crevice corrosion attack than larger-grained specimens.

Hall *et al.* [43] used heat treatments to vary the microstructure of Ti-12 specimens. They found three titanium phases that were significant to the corrosion process: α, β, and Ti_2Ni. The corrosion rate was low when the ratio of β-phase to Ti_2Ni was low, or when the β-phase contained high levels of Ni and was present without Ti_2Ni. High general corrosion rates were observed when significant amounts of β-phase and Ti_2Ni were present together or on α/β materials after long annealing periods that caused the β-phase to be depleted of Ni. Ikeda *et al.* [44] noted that the presence of martensitic, twinned, and highly deformed crystal structures in Ti-2 can lead to varied and unpredictable corrosion behaviour. These structures were found to be associated with areas of high Fe content.

Overall, it seems that the corrosion behaviour of Ti is highly sensitive to very small concentrations of alloying elements and trace impurities. Many of these act to enhance the corrosion resistance. The role of the microstructure in determining the corrosion performance is much less clear and is complicated by the interdependence of the microstructure and the composition.

1.2.4.6 Heat treatment and welding

Heat treatments and welding can change the material microstructure, introduce impurities, and move impurities and alloying elements within the microstructure [43, 45-47]. Since the influence of the material microstructure, and that of some of the impurities (such as Fe), are poorly understood (see Sections 1.2.4.5 and 1.2.5), it follows that the effects of heat treatment and welding are not well defined. Ikeda *et al.* [45] found that their welded Ti-2 specimens were slightly less susceptible to corrosion than the original metal. In experiments on welded T-35 (commercial purity) titanium in 8 mol·dm^{-3} HCl, Caprani *et al.* [46] also found that the welded metal had superior corrosion resistance compared to samples of the original material. They attributed this resistance to the inhibitory effect of oxygen present in the metal (introduced during welding).

In contrast to the welding, the heat treatments applied by Ikeda *et al.* [45] sometimes had unexpectedly severe deleterious effects on the crevice corrosion resistance of Ti-2. Based on the results of transmission electron microscopy (TEM), Ikeda *et al.* concluded that the high rates of localized attack they observed were a consequence of enriching the Fe content of the grain boundaries and the formation of highly corrosion-susceptible martensitic structures. Fukuzuka *et al.* [47] also observed increased corrosion attack on heat-treated electrodes of commercial purity Ti for cases in which the heat treatments resulted in the concentration of Fe in the grain boundaries or the production of a martensitic acicular alpha titanium phase.

It is apparent that, before an understanding of the relationship between crevice corrosion susceptibility and heat treatments or welding can be achieved, awareness of the influences

of composition and microstructure, and the connections between the two, will be required.

1.2.4.7 Applied potential

According to Schutz [38], anodic polarization intensifies crevice corrosion initiation by promoting crevice acidification through increased metal oxidation within the crevice, and the subsequent metal ion hydrolysis. This subject does not appear to have been widely investigated experimentally. Satoh *et al.* [48] observed faster initiation of crevice corrosion on commercially pure Ti when more positive potentials were applied. McKay [21, 32] and McKay and Mitton [19] noted that initiation had already taken place before they polarized their artificial crevices on Ti-2 and Ti-12. Sridhar and Dunn [49], working with Type 304L stainless steel and Alloy 825 found that after application of anodic polarization to artificial crevices, current flow was observed before any pH change could be detected. They acknowledged, however, that they may not have been able to monitor the pH close enough to the sites of initiation, which were expected to be in the narrowest regions of the crevice (metal contact points at surface asperities).

It is clear, however, that once crevice corrosion has been initiated on Ti, the externally applied potentials can have a dramatic effect on its propagation [19, 21, 32], even though, due to the very high electrical resistivity generated by the restricted crevice geometry, the externally applied potential has little influence on the actual potential in the deeper reaches of the crevice (beyond a very short distance from the crevice mouth) [19]. It was proposed [19, 21, 32] that anodic polarization of the crevice exterior, combined with the ohmic potential drop due to the highly resistive crevice geometry, results in a spatial zone

near the crevice mouth over which the local potential falls within the active dissolution region for Ti. Rapid corrosion occurs in this zone, and the acidity created by hydrolysis of the dissolved Ti cations lowers the pH of the crevice interior. Although the ohmic resistance of the crevice prevents the applied potential from influencing the local potential deep within the crevice interior, the low pH allows crevice corrosion to proceed without the exchange of significant current between the innermost regions of the crevice and the crevice mouth or crevice exterior (*i.e.*, crevice corrosion becomes an autocatalytic, proton-driven reaction at crevice interior depths beyond the range of external potential influence).

Crevice corrosion did not occur on commercial purity Ti under applied potentials in the -0.4 V range [48], although it was noted that total cathodic protection against crevice corrosion may not be possible under the most severe conditions [38]. The rate of crevice corrosion on Ti-2 increased strongly with increasing applied potential in the range -0.36 V to over 0.8 V [19, 21, 32, 48]. McKay [21] observed a critical potential ($\sim -0.57 \pm 0.020$ V) for crevice corrosion on Ti-2. He claimed that at potentials below this critical value crevice corrosion deactivation, rather than repassivation, occurred. McKay also stated that the effect of applying potentials externally was equivalent to changing the concentration of oxygen in galvanically coupled crevice corrosion experiments.

Experiments with Ti-12 [21, 50] also showed an increase in the crevice corrosion propagation rate with increasing potential, except that the absolute rates were lower on Ti-12 than on Ti-2 and the extent of corrosion damage was limited by repassivation of the

Ti-12 material at potentials in the lower end of the polarization range. The corroding crevice on Ti-12 did not repassivate at an applied potential of 0.44 V in 1.0 mol·dm^{-3} NaCl solution at 150°C [21], an effect that McKay attributed to a lower crevice pH at the more positive potentials. However, passivation *did* take place under these conditions in 5.0 mol·dm^{-3} NaCl solution.

1.2.4.8 Crevice characteristics

The characteristics of the crevice itself include such things as the crevice geometry and tightness or gap width, the metal surface condition, the type of crevice former (the material pressed against the metal surface to generate the occluded region), and the anode-to-cathode area ratio. These can have a profound effect on the ability of crevice corrosion to initiate and propagate on Ti.

The crevice gap width determines the volume of solution in the occluded region per unit surface area, and therefore the amount of each species required to influence the internal crevice chemistry. The gap width also controls the ease with which species can enter and exit the occluded region, and affects the electrical resistivity between sites within and exterior to the crevice. In general, tighter crevices have a higher susceptibility to crevice corrosion than more open surfaces [38, 48, 49]. On titanium, where very tight crevices are required for crevice initiation, the crevice gap width is determined by the finishes on the adjacent surfaces and their hardnesses, since the contact points between the adjacent surfaces are the surface asperities, and these can be deformed when pressed together in some cases. Therefore, flat, smooth-polished Ti surfaces suffer enhanced susceptibility to crevice corrosion compared to rough (*e.g.*, ground or sandblasted) surfaces [38], and

crevices formed between Ti and soft, easily deformable materials such as Teflon or dimethacrylate initiate crevice corrosion more readily than metal-to-metal crevices [48].

Other aspects of the Ti surface condition can also be important. For example, thermal oxidation of metal surfaces (in air, $T > 400°C$) affords significant protection against crevice corrosion initiation, but anodically oxidized surfaces have a crevice corrosion susceptibility similar to that of pickled surfaces [38, 51].

There is also concern that the crevice former material, in addition to its influence on the crevice tightness, can participate chemically in the crevice corrosion reaction in some cases, especially if the crevice former contains free halides, or can hydrolyse or decompose to produce free halides or acid halides, particularly fluoride [39].

The importance of unintentional crevice formers on crevice corrosion of buried Ti nuclear waste containers has been reviewed [2]. Plausible crevice formers examined included compacted clay buffer material, hydrothermally formed deposits, embedded iron particles, closure welds, and bio-films. Of these, crevice corrosion has only been observed under hydrothermally formed deposits and embedded iron particles[1]. Crevice

[1] This phenomenon is termed "smeared-iron surface pitting" [2].

corrosion in unclosed welds or under compacted buffer material or biofilms [52] could not be ruled out, although initiation and sustained propagation in *any* of these situations were considered unlikely.

A danger with most forms of localized corrosion is that coupling a small anodic surface with a large surface area cathode can result in a very high local corrosion rate. Ikeda *et al.* [45] found that the extent of crevice corrosion on Ti-2 was limited by the amount of oxygen available to drive corrosion, and not by the anode-to-cathode area ratio. On Ti-12, however, smaller anode-to-cathode area ratios resulted in increased corrosion damage; the corrosion rate appeared to be similar, but repassivation delayed, at smaller anode-to-cathode area ratios.

1.2.5 Alloying effects

Since many of the experiments reported in this Thesis involve direct comparisons of the behaviour of different Ti alloys exposed to the same conditions, a discussion of the known effects of alloying on the corrosion of Ti is essential. Small additions of alloying elements can have dramatic influences on the electrochemistry of Ti. Fortunately, the basis for many of these effects has been reasonably well established through the work of a number of scientists, beginning with Stern and Wissenberg in 1959 [53].

Stern and Wissenberg reasoned that alloying could be used to generate passivity on Ti in two ways: by inhibiting the anodic half-reaction, or by enhancing the cathodic half-reaction. Specifically, alloying with elements that could induce a decrease in the critical anodic current density (I_m) or the passivation potential (E_m) would make it easier for the cathodic half-reaction to exceed a current of $I_{m,d}$ at the potential $E_{m,d}$ and drive E_{oc} into

the passive region (see Section 1.2.3 and Figure 1.2.3-a). Alternatively, alloying with elements that catalyze the cathodic half-reaction, either by increasing the exchange current density or decreasing the cathodic Tafel slope, would also make it easier for the cathodic half-reaction to drive E_{oc} into the passive region by exceeding a current of $I_{m,d}$ at $E_{m,d}$. Alloying to enhance the cathodic reaction rate for this purpose has been termed "cathodic modification" [54].

In either case, it is necessary that the solution contain a redox system with a reversible potential more noble (*i.e.*, higher) than the Flade potential. The H^+/H_2 couple satisfies this condition on Ti. This cathodic route to passivity must be approached with caution however, because if the kinetics of the cathodic half-reaction are enhanced, but not enough to exceed $I_{m,d}$ at $E_{m,d}$, the corrosion rate of the alloy will also be increased [53]. This is the case for binary Ti-C alloys containing particles of titanium carbide (TiC), a material on which the cathodic polarization curve in 10% H_2SO_4 at 100°C is "enhanced" over that of Ti, but still intersects the anodic polarization curve of Ti in the active region. Consequently TiC particles cannot effect passivation of the base Ti metal in the alloy under these conditions [55], but instead enhance corrosion.

In other cases, the concentration of the alloying element intended to increase the cathodic kinetics may be too low to ensure immediate passivation of the alloy. However, if the alloying element resists corrosion and has low solubility in the corrosion-causing medium, dissolution of the base metal may enrich the alloy surface to the level at which the catalysis of the proton reduction reaction can drive the passivation process [53, 56].

Most published accounts of improved corrosion resistance by alloying Ti have concentrated on cathodically modifying alloying additions, especially noble metals [42, 43, 53-69], although several have discussed inhibition of the anodic (Ti dissolution) reaction and stabilization of the passive film [53, 59, 69-72].

Alloying elements that have been suggested to induce passivity of Ti by cathodic modification include Pt [53, 56, 57, 62], Pd [42, 53, 55-57, 60-63, 65, 66], Ni [43, 58, 64, 68], Mo [59], Ru [42, 53, 54, 56, 57, 60, 62], Re [53, 56], Fe [67], Ir [53, 62], Os [53], Rh [53], and Au [53]. Their relative effectiveness is roughly in the same order as their hydrogen overvoltages and exchange current densities for hydrogen [53]. This relationship between effectiveness and exchange current densities, along with the high corrosion resistance or immunity of most of these elements, make it possible to produce very good cathodically modified alloys on a commercial scale. Were it not for the very small amounts of precious metals (< 1% by weight in many cases [53]) required to achieve corrosion resistance, these alloys would be too expensive[1] to be widely used as structural materials [54, 60].

The extraordinary ability of these metals to catalyze the cathodic reactions on the alloy is thought to be based on the large difference in exchange current densities for hydrogen between these elements and Ti. The exchange current densities for hydrogen [12] on some of these pure metals in ~1 $mol \cdot dm^{-3}$ H_2SO_4 are approximately (in $A \cdot cm^{-2}$): Pd (1×10^{-3}), Pt (8×10^{-4}), Rh (3×10^{-4}), Ir (2×10^{-4}), Ni (6×10^{-6}), and Au (4×10^{-6}). By

[1] Even at a Pd concentration of only 0.15% by weight, Ti-7 is roughly twice the price of unalloyed Ti, solely due to its Pd content [60].

contrast, the exchange current density for hydrogen on Ti in ~1 mol·dm^{-3} H_2SO_4 is only about 6×10^{-8} A·cm^{-2}. Thus, it is readily apparent that only a small fractional coverage of the alloy surface by particles of the pure elements listed above would greatly increase the overall exchange current density for hydrogen on the alloy [53]. For example, a 0.1% surface coverage of Ti by Pd might be expected to boost the exchange current density for hydrogen by as much as three orders of magnitude. Usually, though, cathodically modifying alloy elements are not found as particles of the pure element in the alloy. Rather, when present in greater amounts than are soluble in the Ti matrix, they form intermetallic compounds with the Ti and these precipitate as particles of separate intermetallic phases, often in grain boundaries and triple points within the alloy.

A theory of how proton reduction is catalyzed on alloys and why the alloys sometimes display hydrogen overpotentials characteristic of the alloying element, rather than the base metal, has been published by Ezaki *et al.* [73]. Their theory is based on calculations of the electronic structure of transition metal alloy clusters. They concluded that, generally, if the alloying element is more electronegative than the base metal, charge transfer due to bond formation results in excess electron density near the alloying element, providing preferable sites for proton discharge and hydrogen reduction behaviour more characteristic of the alloying element. If the alloy element is less electronegative than the base metal then electron transfer takes place in the opposite direction, the preferred discharge sites are located close to base metal atoms, and the hydrogen reduction properties of the base metal tend to prevail. The predictions of their theory conflicted with their experimental observations that the hydrogen overpotential on Ti was increased by alloying with V, Cr, and Mn, and decreased by alloying with Fe, Co,

Ni and Cu; all of these metals have lower hydrogen overpotentials than Ti and all but Mn[1] are more electronegative than Ti [74].

Stern and Wissenberg [53] measured the corrosion rates of dilute Pt- and Pd-containing alloys in boiling HCl and H_2SO_4 solutions, as a function of noble metal concentration, to determine the concentrations of Pt or Pd that would yield optimum corrosion performance. They found an exponential drop in the corrosion rates as the noble metal concentration increased in the range 0 to 0.05% by weight. The corrosion rates decreased by up to ~2.5 orders of magnitude over this range. Above ~0.1% Pt or Pd by weight[2], no further gains in corrosion protection were realized up to a concentration of about 2 wt.% (the upper concentration limit of the study). These results were later reproduced by Sedriks [57].

Schutz [42, 60] and Sedriks [57] investigated the corrosion resistance of Ru-containing alloys and found that they offered corrosion protection comparable to Pd alloys, except that roughly twice as much Ru by weight[3] was required to achieve a similar suppression of the corrosion rate[4] [42]. The explanation given for the lower potency of Ru compared with Pt or Pd was that Ru has a higher overvoltage for proton reduction and a less noble corrosion potential.

---

[1] The electronegativities of Ti and Mn were both reported to be 1.5 [74].

[2] This is still well below the solubility limit of either element in the Ti matrix.

[3] This corresponds to roughly twice as much Ru in terms of mole fraction as well, since Pd and Ru have very similar atomic weights (106.4 *versus* 101.7, respectively [8]).

[4] This still represents a cost savings of ~45% [54] over the equivalent Pd-containing alloy, since Ru costs about 1/7 as much as Pd [54] [42].

Though not proven to be necessary, surface enrichment in the alloying element seems to be seen as a prerequisite to the establishment of cathodic modification on dilute Ti alloys. As described above, it would not seem unreasonable that very small concentrations of certain alloying elements could enhance the kinetics of the hydrogen reduction reaction by orders of magnitude over pure Ti. Thus, enrichment may not be a necessity, at least not in all cases.

For those who accept that enrichment is necessary, the mechanism by which cathodically modifying elements become enriched and achieve stability on the alloy surface is in dispute; there are two schools of thought. Some researchers suggest that the ability to create and maintain the necessary surface coverage of alloying elements to generate this cathodic modification effect is dependent on the relatively low corrosion susceptibility of most of these metals. As noble or corrosion resistant metals, these elements are not prone to oxidize or dissolve in corrosive aqueous media and, therefore, if present on the alloy surface in insufficient amounts to afford corrosion resistance initially, will become enriched as the Ti matrix dissolves, leaving behind intermetallic compounds containing the alloying elements. In fact, the presence of noble metal containing intermetallic particles on a Ti alloy surface should even *accelerate* the surface enrichment of these same particles by enhancing the rate of active Ti dissolution until the surface coverage is great enough to drive repassivation of the Ti (*i.e.*, until "cathodic modification" occurs) [13, 42, 53, 54, 56, 60, 63, 68].

Scientists following the second school of thought have suggested that the alloying element is released into solution as intermetallic compounds (*e.g.*, Ti_2Ni) dissolve.

Subsequently, it is electrodeposited[1] as a layer of the pure element at existing cathodic sites on the same corroding surface, thereby increasing the coverage of the surface by the alloying element [43, 57, 58, 75]. The basis for claiming that this mechanism occurs was provided by some atomic absorption measurements and photometric tests that indicated traces of Ru and Ni ions were present in solution after exposure of Ti-Ru [57] and Ti-Ni [58] alloy specimens, respectively, to boiling acid solutions. This evidence, coupled with the observation that cathodic modification could also be achieved by adding 10 ppm of Ni ions to a boiling acid solution containing an unalloyed Ti coupon [58], has been used to justify the dissolution-electrodeposition mechanism.

Several papers have used mass transport and concentration arguments, as well as measurements of cathodic kinetics on intermetallic compounds, to dispute the possibility or the necessity of significant alloy metal electrodeposition [54, 63, 68]. In one particularly elegant demonstration, Glass [68] showed that galvanic coupling of unalloyed Ti to a separate Ti_2Ni electrode could induce passivity on unalloyed Ti, which was lost again if the Ti_2Ni electrode was uncoupled.

Thus, it has been shown that, under certain conditions, it is possible to cause repassivation of Ti by either the electrodeposition [58] or the galvanic coupling [68] route. Enrichment by preferential dissolution of the Ti from the matrix has not been clearly demonstrated.

[1] The word used in the literature references to this process is "reprecipitated", however this implies a solubility effect. The process as described requires an electrochemical reduction reaction, rather than a local supersaturation.

Regardless of the mechanism by which surface enrichment of cathodically modifying elements *actually* takes place, or even *whether* enrichment is necessary, it has been clearly demonstrated that cathodic modification leading to repassivation of Ti does occur on alloy materials. In addition, the mechanism of surface enrichment may not be the same for each type of alloy. Ni ions in solution have been generated by corrosion of Ti-Ni alloys [58]; however, the absence of Pd ions in solution after corrosion of Ti-Pd alloys has also been noted [55, 63].

While cathodic modification offers greatly increased resistance to active corrosion of Ti, and the alloying additions are often small enough not to significantly influence the mechanical and physical properties of the material [60, 61], there are some caveats as well. Cathodically modified alloys sometimes suffer higher passive corrosion rates than unalloyed Ti [55, 56, 58, 61, 66, 68, 76] and increased hydrogen absorption efficiencies[1] [54, 58, 62, 77]. Externally applied currents or galvanic coupling resulting in cathodic polarization of the alloy may also increase the corrosion rates of cathodically modified alloys, since they may drive the potential into the active dissolution region. Although anodic currents may not be observed under these conditions, high rates of metal oxidation can occur at these sub-passive potentials; the oxidation current is simply masked by the cathodic currents resulting from even higher rates of reduction reactions on the same surface [53, 64, 76] (recall that the observed current is the sum of the anodic and cathodic partial currents, as shown in Figure 1.2.3-a). Finally, surface spalling or

[1] For aggressive conditions, except cathodic polarization, the absolute amount of hydrogen absorption is generally lower on the cathodically modified alloys since these suffer less active corrosion and therefore generate less hydrogen.

peeling may also occur under conditions of cathodic polarization, due to surface hydride formation resulting in embrittlement and stresses arising from the volume expansion from metal to hydride [54]. Pd-containing alloys appear to be more susceptible in this regard than those containing Ru [54, 57].

Inhibition of the anodic reaction on Ti lowers the critical current density for passivation (I_m). This is a very different approach to achieving passivity on Ti than the cathodic modification approach. In fact, as will be discussed below, the two approaches can be used in combination to enhance the ability of Ti alloys to passivate. Alloying elements that suppress the Ti dissolution reaction tend to be those that yield adherent, insoluble oxide compounds, such as Mo, Nb, Cr, W, Zr and Ta [59, 69, 70, 72, 78, 79].

Marcus [79] noted two ways in which alloying elements could act to inhibit anodic dissolution of active-passive alloys, namely by improving the thermodynamic stability of the metal or that of the oxide. Based on a plot of the heat of adsorption of oxygen on the pure elements *versus* the metal-metal bond energy, Marcus identified two groups: "passivity promoters" and "dissolution moderators" or "blockers". Passivity promoters, which include Ti and Cr, are elements that have a high metal-oxygen bond strength and a relatively weak metal-metal bond; the latter facilitates oxidation and the formation of a three-dimensional oxide layer, which requires the breaking of metal-metal bonds, while the former increases the stability of the passive oxide film formed. Dissolution moderators or blockers, including Mo, Nb, Ta, W, and Zr [72, 78, 79], have high metal-metal bond strengths, in addition to strong metal-oxygen bonds. Having strong metal-metal bonds increases the activation barrier for metal dissolution, while the strong metal-

oxygen bonds promote passive film stability, as they do for the passivity promoters described above. For example, Ti-Mo alloys containing 18-67 at.% Mo showed corrosion rates four orders of magnitude lower than those of pure Ti in 12 mol·dm^{-3} HCl solution [78]. These effects of alloying were well covered in a recent Ph.D. thesis [72], in particular for Ti-Nb and Ti-Zr alloys.

In practice, it appears that none of these elements is capable on its own of limiting Ti dissolution enough that the hydrogen reduction reaction on Ti can drive the potential into the passive region, unless present in relatively high concentrations. Mo on its own as an alloying element is capable of passivating Ti if it is present in intermediate concentrations (~5-30%) [59, 64, 69], however, the passivating action of Mo in this case may be a combination of anodic suppression and cathodic modification [59, 70]. For other elements, and for alloys containing lower concentrations of Mo it appears that complementary additions of cathodically modifying and anodically suppressing elements are effective in promoting passivation of dilute alloys [69] (*e.g.*, ternary alloys such as Ti-12 (Ti-0.8Ni-0.3Mo), Ti-Pd-Mo, or Ti-Pd-Cr).

Unfortunately, the passive corrosion rates on Ti alloys that resist active dissolution can be higher than that on unalloyed Ti [59, 78]. The susceptibility of some of these alloy additions, such as Mo and Cr, to transpassive dissolution results in conversion of the oxide to a more "TiO_2-like" structure at high anodic potentials, which renews the passivity [59], although Tomashov *et al.* [69] reported continuous transpassive dissolution for a Ti-15 wt.% Mo alloy.

The influence of Fe on the corrosion of Ti has been the subject of some controversy [16, 33, 44, 80-82]. Fe is a common impurity in commercial Ti materials and its concentration is not carefully controlled during production [44]. Cotton [80] claimed that the presence of Fe was detrimental to the corrosion resistance of Ti, but others [81] found it normally had an insignificant effect, and still others [16, 33, 82] perceived it to be beneficial[1]. A more recent investigation by Ikeda *et al.* [44] determined that attendant Ni impurities may have been responsible for the controversy over the influence of Fe on Ti corrosion. Ni is another poorly controlled contaminant of commercial Ti that tends to accompany Fe[2]. The latter authors found that, when present with Ni in intermetallic particles, Fe suppressed crevice corrosion of Ti, but when distributed more dilutely in β-phase crystals or altered microstructural features such as martensitic or twinned structures, Fe offered anodic sites at which crevice corrosion propagated preferentially.

As discussed above, alloying can have a very strong effect on the ability of Ti to undergo active corrosion. With respect to crevice corrosion, in which active dissolution within the occluded region is driven by reduction of oxidant both within the crevice and on passive surfaces exterior to the crevice, the positive effects of alloying have also been noted. For example, Schutz [42] found that the bulk solution pH and temperature ranges where crevice corrosion is possible on unalloyed Ti (Ti-1 and Ti-2: $pH \leq 8$, $T \geq 65°C$)

[1] In general, they agreed that Fe does represent a danger to Ti materials since it can act as an easy entry point for hydrogen, which can embrittle Ti.

[2] Ironically, Tsujikawa and Kojima [82] observed an apparent similarity between the effects of Fe and Ni on Ti corrosion and noted that Ni seemed to behave like Fe.

were significantly improved by alloying with Ni and Mo (Ti-12: pH ≤ 3, T ≥ 70°C) or with Pd or Ru (Ti-7, Ti-11, Ti-16, Ti-17 and Ti-0.1Ru: pH ≤ 1, T ≥ 80°C).

1.3 Passive oxide films

1.3.1 Introduction

The underlying reason for the very existence of metallic Ti in most common environments is that it rapidly and spontaneously forms an oxide film with exceptional stability and properties that allow it to effectively isolate the metal from the environment. Hence, titanium's corrosion resistance and ability to resist hydrogen absorption are dependent on the properties of this protective film. Some of the attributes of bulk Ti oxides are listed in Table 1.3.1-a; however, some of the features of thin oxide films on Ti (such as crystallinity [83-91]) can differ significantly from those of the bulk oxides and warrant further discussion.

The following sections review published work regarding the nature of thin oxide films on Ti in terms of their composition, structure, formation, removal, and reactivity.

1.3.2 Composition

One of the most commonly used techniques for investigating the chemical composition of oxide films on Ti has been X-ray photoelectron spectroscopy (XPS) [84, 92-97]. The relative binding energies (BE) and full peak widths at half-maximum intensities (FWHM) for Ti in the 0, +2, +3, and +4 oxidation states, and in titanium hydride, have been determined from the XPS spectra of standard Ti-containing materials [98]. Such values are used in comparison with experimental spectra to determine the composition of sample surfaces.

Table 1.3.1-a Some Attributes of Bulk Ti Oxides

Polymorph	Attribute	Value	Reference
Brookite	Crystal structure	rhombic	[8]
(TiO_2)	Colour	white	[8]
	Indices of refraction	2.585, 2.586, 2.741	[8]
	Specific gravity	4.17	[8]
	Melting point	1825°C	[8]
Anatase	Crystal structure	tetragonal	[8]
(TiO_2)	Colour	brown-black	[8]
	Indices of refraction	2.554, 2.493	[8]
	Specific gravity	3.84	[8]
	Melting point	1840°C	[99]
Rutile	Crystal structure	tetragonal	[8]
(TiO_2)	Colour	colourless	[8]
	Indices of refraction	2.616, 2.903	[8]
	Specific gravity	4.26	[8]
	Melting point	1830-1850°C	[8]
	Boiling point	2500-3000°C	[8]
TiO	Crystal structure	prismatic	[8]
	colour	yellow-black	[8]
	Specific gravity	4.93	[8]
	Melting point	1750°C	[8]
	Boiling point	>3000°C	[8]
Ti_2O_3	Crystal structure	trigonal	[8]
	Colour	violet-black	[8]
	Specific gravity	4.6	[8]
	Melting point	decomposes at 2130°C	[8]

Unfortunately, XPS results have not yielded an entirely clear picture of the film composition. Most authors agree that XPS profiles of oxide films formed on Ti in various aqueous solutions indicate that the outer portions of the film contain Ti almost exclusively in the +4 oxidation state [84, 92-94, 96, 97], but the location and amount of Ti in reduced states (Ti(II) and Ti(III)) is somewhat less certain. In some XPS investigations, minor amounts of Ti(III), and sometimes Ti(II), were observed on oxide surfaces [94, 96, 97], while in others, significant amounts were observed only after Ar^+ ion sputtering [84, 92, 93]. Unfortunately, because the electrodes in all these works had

been transferred from solution to XPS vacuum through the ambient air, and some were exposed to oxygenated solution [94, 96], one cannot say whether or not the presence of Ti almost exclusively as Ti(IV) on the electrode surfaces was simply a result of oxygen exposure. The one study in which the electrodes were exposed only to deaerated electrolyte in the cell and inert atmosphere during transfer reported the presence of Ti(III) and Ti(II) in nearly equal amounts with Ti(IV) at or near the electrode surface [95]. This work by Armstrong and Quinn acknowledges that the Ti(III) and Ti(II) may lie below a surface layer containing only Ti(IV) since XPS probes a finite depth into the surface[1]. In this case, the probed depth was calculated to be about 18 Å [95]. Armstrong and Quinn [95] found that by anodizing their electrode to more positive potentials up to 3 V, they could reduce the amounts of Ti(III) and Ti(II) observable in the sample surface. Beyond +3 V, Ti(III) and Ti(II) were eliminated.

By combining XPS analysis and Ar^+ ion sputtering, researchers have generated compositional depth profiles of the oxide film on Ti [84, 92, 93, 95]. Such profiles all indicate that the amounts of Ti(III) and Ti(II) increase with increasing sputter time. This result has been interpreted as indicating that reduced Ti states exist near the metal/oxide interface, sometimes directly below an overlayer of Ti(IV) oxide [84, 93, 95]. In fact, Armstrong and Quinn [95] found Ti(III) and Ti(II) below the layer of Ti(IV) oxide created by anodization at potentials greater than +3 V. Vallet *et al.* [92] dispute this interpretation, claiming the presence of reduced Ti states is an artifact of ion

[1] Since the X-rays used to generate the measured photoelectrons penetrate the sample to significant depths, the depth probed by XPS is limited by the photoelectron escape depth and the angle between the surface and the electron detector.

bombardment. They tried to support this argument by pointing out that they observed Ti only in the +4 oxidation state in anodized films probed to a depth of 70 Å by angle-resolved XPS, but subsequently observed Ti(III) and Ti(II) in the same films after 30 s of sputtering at a rate of 100 Å·min^{-1} (as calibrated against a Ta_2O_5 standard). However, the depth probed by the latter XPS measurements was stated to be 45-50 Å. Taken together with the sputtered depth of perhaps 50 Å (30 s x 100 Å·min^{-1}), the depth into the film probed after sputtering exceeded the 70 Å from the original surface in which no Ti(III) or Ti(II) were observed. Thus, it is possible that reduced Ti states existed in the sample all along, at depths greater than 70 Å, but were only observable after the overlayer of Ti(IV) oxide had been thinned by sputtering, in agreement with the other depth profiling accounts [84, 93, 95]. The possibility that Ti(III) and Ti(II) states were sputtering- or electron beam-induced artifacts was also considered by Armstrong and Quinn [95] but dismissed because they were able to observe Ti(III) and Ti(II) in XPS spectra that were taken without prior exposure of the samples to electron or ion beams. Also, their experience showed that TiO_2 is stable to the X-ray beam for several hours, and "experimental conditions were chosen to minimize the possibility of such an artifact". They did acknowledge, however, that some of the XPS signal attributed to Ti(II) may have been due to titanium carbide, which has the same $Ti_{2p3/2}$ BE as TiO, but further stated that the carbon content of the surface, as indicated by the C_{1s} band, was insufficient to account for all of the signal attributed to Ti(II).

Using TiO_2 single crystals [100-102] and powders [103] researchers have consistently demonstrated by XPS [100], electron energy loss spectroscopy (EELS) [101, 102], low energy ion scattering (LEIS) [100], static secondary ion mass spectrometry (SSIMS)

[102], X-ray absorption spectroscopy (XAS) [103], and inverse photoemission spectroscopy (IPE) [101] that Ar^+ ion bombardment, such as is used in depth profiling, causes preferential removal of O atoms from the oxide and reduction of Ti cations to Ti(III) and Ti(II) (but not Ti(0)). Furthermore, XAS [103] and low energy electron diffraction (LEED) [100] results indicate that Ar^+ ion beams also destroy long range order in TiO_2 crystals, although medium energy backscattered electron diffraction (MEED) [100] revealed that local ordering was still present.

As indicated above, increasing the anodization potential has the effect of reducing the amount of Ti(III) and Ti(II) observable on the film surface, up to a potential of 3 V [95]. Armstrong and Quinn [95] have argued that anodization does not eliminate Ti(III) and Ti(II) but rather thickens the Ti(IV) overlayer. XPS has been used quantitatively [93, 96] to determine the ratio of oxygen to titanium atoms (N_O/N_{Ti}) in oxides formed on Ti. Thierry *et al.* [96] recorded a value of N_O/N_{Ti} of 2.2, which they claimed was not significantly different from the theoretical value for TiO_2. Shibata and Zhu [93] examined oxides grown at a number of temperatures between 303 K and 353 K as a function of depth from the surface and found N_O/N_{Ti} to be approximately 2 in the outer levels of the oxide, decreasing to almost 1 after long sputtering times, with a mean value of 1.6. In addition, N_O/N_{Ti} values measured after a given sputter time, including the unsputtered surface, were higher for oxides grown at higher temperatures, with a difference of about 0.2 between films grown at 303 K and 353 K.

Examination of the O_{1s} band in the XPS spectra revealed that, while most of the oxygen present in the film was associated with metal oxides, a small component associated with

water or OH from the hydrated metal also existed [84, 93-96], perhaps as $TiO(OH)_2$ or TiOOH. Depth profiling work [93] and angle-resolved XPS [96] have indicated that the small water/OH component is localized in the outermost part of the oxide films. The distinction between bound water and hydrated metal by XPS appears difficult, and these components have been dealt with as a single combined contribution [84, 96].

Again using XPS quantitatively, Shibata and Zhu [84] determined the ratio of oxygen atoms associated with water or OH to those associated with metal oxide ($N_{O(OH)}/N_{O(Ti\text{-}O)}$) as a function of temperature from 303 K to 353 K, and as a function of film formation potential between 0 and 9 V (Ag/AgCl) at 303 K. A slow, steady increase in the value of $N_{O(OH)}/N_{O(Ti\text{-}O)}$ from 0.1 to 0.25 was observed for films grown at 1.5 V (Ag/AgCl) as the temperature was increased from 303 K to 333 K. At temperatures of 343 K and higher, a marked jump in the value of $N_{O(OH)}/N_{O(Ti\text{-}O)}$ took place, and by 353 K it reached 0.8. The effect of increasing the film formation potential was to reduce sharply the value of $N_{O(OH)}/N_{O(Ti\text{-}O)}$ from 0.3 to 0.1 over the range 0-1 V (Ag/AgCl), then much more gradually from 0.1 to 0.08 from 2 V to 9 V (Ag/AgCl). Thierry *et al.* [96] found that addition of hydrogen peroxide (H_2O_2) in millimolar amounts to the aqueous solutions in which their films were grown increased the amount of incorporated water/OH and broadened the depth of the film in which it was found.

Anodic oxide films on Ti have also been studied *in situ* by ellipsometric techniques [85, 104]. Blackwood *et al.* [104], growing anodic films on Ti by linear sweep voltammetry, noticed an irreversible change in the optical constants of the substrate at the anodic end of the formation scan, while those of the film remained unchanged. To account for this

observation, they proposed the formation of a layer of non-stoichiometric lower oxides between the outer TiO_2 and the metal. They rationalized this suggestion by noting the dubiousness of an abrupt junction between Ti and TiO_2, given the range of known non-stoichiometric lower oxides potentially formed by Ti, and, in view of the known properties of the lower non-stoichiometric titanium oxides, selected optical constants for this layer corresponding to those of a semi-metal. Theoretical curves calculated from this model were found to simulate the experimental data, even when a very thin (0.5 nm) non-stoichiometric lower oxide film was inserted between Ti and TiO_2. Further evidence for the existence of a hydrated oxide layer at the anodic film/solution interface, possibly $TiO_2 \cdot (H_2O)_{1.4}$ or $TiO_{0.6}(OH)_{2.8}$, was presented from the ellipsometric results of Ohtsuka *et al.* [85].

The results of both ellipsometric studies [85, 104] are supported by Rutherford backscattering spectroscopy (RBS) work [105]. The RBS analysis required the addition of hydrated surface layers to the film model to improve the fit to the experimental data. Although hydrogen is not directly observable by RBS, its presence was inferred from its effects on the apparent stopping power of the matrix and a significant over-stoichiometry in the surface layers of the oxide (probably from water and OH species) [105]. Elastic recoil detection analysis (ERA) was used to confirm the hydrogen content of the oxide.

At the oxide metal interface, RBS clearly showed a broad transition region with decreasing oxygen concentration between the outer oxide and the "bulk" titanium metal. Unfortunately, RBS does not distinguish between what might be a lower oxide of Ti and what could be simply a region containing large amounts of oxygen dissolved in Ti [105].

Auger electron spectroscopic (AES) characterization of thin oxide films on Ti revealed oxygen deficient films [95, 106]. Healy and Ducheyne [106] reported inhomogeneous surface coverage by interspersed regions of stoichiometric TiO_2 and sub-stoichiometric oxides on untreated Ti fibres, changing to nearly stoichiometric TiO_2 after passivation in 40% HNO_3. Armstrong and Quinn [95], by contrast, determined a N_O/N_{Ti} ratio of about 1.6 on all Ti specimens tested, including samples that had never been exposed to solution and some that had undergone anodization up to 2 V. Depth profiling by Ar^+ ion sputtering alternated with AES yielded large decreases in N_O/N_{Ti}. Again the authors noted the possibility that the observed changes could be an artifact caused by the known preferential sputtering effect discussed above, but dismissed it on the basis that they selected low power densities during sputtering to minimize this effect, as tested on a TiO_2 standard.

Attempts to analyze oxide films on Ti in solution by Raman scattering have had limited success. Ohtsuka *et al.* [86] were able to observe films grown by anodizing Ti for 1 h at potentials greater than 7 V (RHE) but observed no Raman bands *in situ* on films grown at lower potentials. Other researchers [90, 91] reported seeing no Raman bands *in situ* for films grown at potentials less than +80 V, although they used much shorter oxidation times (30 s). For all of the observed films, Raman spectra indicated a TiO_2 composition. At potentials less than 6.8 V, Ohtsuka *et al.* [86] recorded *ex situ* Raman spectra in air that again indicated TiO_2, but Pankuch *et al.* [91] observed a small amount of Ti_2O_3, coexisting with the TiO_2, by surface enhanced Raman scattering (SERS) *in situ*, in the potential range -1.4 V to +0.1 V. No O-H stretching vibrations were observed to support the presence of hydrated oxide species. When considering these results, however, one

must keep in mind that only compounds with sufficiently intense Raman-active bands can be observed. Also, in order to prepare the electrode for SERS, silver particles were electroplated on its surface. Such a treatment could result in reduction of the oxide and in compositional changes, especially in the outer surface layers where the hydrated oxide may be expected. The silver coating also limited the potential range over which the analysis could be performed, since anodic silver oxidation occurred at potentials positive of 0.1 V [91]. Air oxidation could also be a factor in the *ex situ* results of Ohtsuka *et al.* [86].

In situ neutron reflectometry measurements of anodic films in acidic solution have indicated a composition of TiO_2 [107, 108]. No hydrogen was observed in the films, in spite of the particular sensitivity of the technique for hydrogen.

The presence of non-stoichiometry in TiO_2 should be revealed in the optical and electronic properties of the films, and these were explored by D.C. conductivity [109], photoconductivity [109], electrochemical impedance spectroscopy (EIS) [97, 110], and scanning tunnelling microscopy (STM) [109] measurements. The electronic defects in the oxide films were found to be due to interstitial Ti^{3+} ions and oxygen vacancies, and the density of the donor states was determined. The EIS capacitance measurements of da Fonseca *et al.* [97] indicated donor densities of 2.5×10^{20} cm^{-3} to 7.5×10^{20} cm^{-3}, decreasing with increasing potential, over the film formation range 0-2 V; McAleer and Peter's values were comparable at 2×10^{19} cm^{-3} [110]. Photoconductivity measurements indicated no oxygen vacancies, while STM measurements of the surface density of states suggested 5% vacancies [109]. These latter results were rationalized using DC

conductivity calculations, which indicated that a level of 9% oxygen vacancies is insufficient to create an impurity band, leaving instead a variety of localized states which would act as trapping centres, impeding conduction in the films.

In summary, the composition of thin oxide films on Ti in aqueous solution remains the subject of some controversy; however, it is clear that the main constituent of all the films is TiO_2. In addition, it seems likely that within the TiO_2 matrix there exist some reduced metal cations and non-stoichiometry, probably due to the presence of interstitial Ti^{3+} ions and oxygen vacancies, rather than a separate phase.

1.3.3 Structure

Bulk titanium dioxide, TiO_2, may exist in amorphous form or in one of three polymorphic crystal structures: rutile, anatase, or brookite[1] (listed here in order of decreasing thermodynamic stability at room temperature) [111]. The oxide films on Ti may be either amorphous or crystalline depending on their rates of formation and their thermal history. Native passive films and anodic films grown under fast-growth conditions at low temperatures on Ti (and other passive metals such as Al, Ta, and Nb) are generally considered amorphous [83]. Growth of crystalline oxide can be encouraged by very low film growth rates [83, 112-116] while crystallization can be induced in amorphous oxide films by application of appropriate stimuli such as heat or very positive potentials (> 4-8 V) [83-91, 117].

[1] See Table 1.3.1-a.

Slowly grown anodic TiO_2 films have been found to grow "partially epitaxially" (with a high degree of rotational freedom about one axis) on the underlying Ti metal [83, 111-115]. "Slow" growth conditions are achieved for potentiodynamic sweep rates of $\leq 0.2\ mV \cdot s^{-1}$, or applied current densities $\leq 3\ \mu A \cdot cm^{-2}$ [115], although currents up to $2\ mA \cdot cm^{-2}$ have been used to achieve similar results [83]. The crystalline oxides obtained have been claimed to be all rutile by some authors [112, 113, 115], but a mixture of rutile and anatase, or just anatase, depending on the substrate surface crystallography, by others [111].

Photoelectrochemical microscopy (PEM) images [112, 113, 115], reflection electron diffraction (RED) [112, 113, 115], and transmission electron microscopy (TEM) [115] showed oxide structures that were uniform over entire substrate grains but dependent on substrate grain crystallography, highlighting the grain structure of the underlying Ti. Neighbouring grains on the same surface sometimes showed a more random oxide orientation. The preferred orientation of the rutile crystals was [110] normal to the substrate surface. This seems to conflict with the results of Wiesler *et al.* [111], who saw smaller crystallites (rutile ~ 40 Å and anatase ~ 80-100 Å), aligned in a different epitaxial arrangement, by X-ray scattering.

The authors of the latter paper [111] (one of whom (W.H. Smyrl) also participated in the PEM, RED, and TEM studies) acknowledged this discrepancy and offered four possible explanations: differences in oxide thicknesses; different surface pretreatments; effects of electron beam damage or heating; or differences in crystallography, since the latter studies were carried out on single crystals while the former employed polycrystalline Ti.

In all cases, the epitaxially grown oxide crystals were larger than those grown by fast potential sweep or potential step growth techniques. It was suggested [115] that anodic oxide films on Ti initially grow by a nucleation and growth mechanism and that grain-to-grain differences in oxide crystallization result from differences in the nucleation rates and oxide growth rates on grains of different crystallographic orientation.

"Native" passive films and rapidly grown anodic films at temperatures below 330 K and potentials less than about 4-8 V have generally been considered amorphous by scientists examining them by optical microscopy [87], photocurrent spectroscopy [89, 110], TEM [84, 117], ellipsometry [87], SERS [91], and normal Raman scattering [84, 86, 90]. Controversy arises here, too, since others have observed crystalline oxide (rutile) in rapidly grown anodic films by RED and TEM [112, 113, 115], although they saw more amorphous-looking patterns prior to etching these surfaces. As pointed out by Wiesler *et al.* [111], this uncertainty is partly due to a lack of appropriate structural probes with which to examine the films. A suitable structural probe should be surface-sensitive enough that the signal from the thin film is not overshadowed by that from the bulk metal beneath, yet not so surface-sensitive that it does not penetrate the whole film. Traditional structural probes suffer the former problem, others, such as RED, the latter. TEM *is* suitable for examining thin oxide films, but is a destructive *ex situ* technique that requires potentially structure-altering sample preparation and may be prone to electron beam-induced structural changes. The other techniques mentioned above (photocurrent spectroscopy, ellipsometry, SERS, and normal Raman scattering) are all non-structural probes from which structural conclusions are drawn by inference from optical properties (*i.e.*, band gaps, indices of refraction, and vibrational band broadening). Kozlowski *et al.*

[115] counter the inferences from optical measurements by suggesting that a very thin crystalline film might also exhibit electronic properties generally associated with amorphous materials. The latter authors *do* agree, however, that less long range order is present in films grown at higher oxidation rates [112-115].

The application of heat or sufficiently high potentials to oxide films on Ti is widely known to induce drastic changes in their properties [83-91, 110, 112, 117-119]. The exact nature of these changes and the conditions required to trigger them are still the subject of some debate. Those who accept the formation of an initially amorphous oxide film contend that the film undergoes a breakdown and crystallization process [83-91, 110, 117-119]. Those who viewed the oxide as always crystalline claimed that heating resulted in no structural changes [112] because there were no corresponding changes in the diffraction patterns they recorded. They did, however, observe changes in the oxide photoresponse, which they attributed to changes in the donor distribution within the film; application of a 10 V potential to the film [115] generated an additional well-defined ring in the RED pattern, which the authors suggested was an indication of secondary oxide phases (but not anatase).

"Breakdown crystallization" [119] of anodic oxide films has been observed for other passive metal systems, including Al [119], Ta [119, 120], and Nb [120]. Breakdown crystallization has been found to occur on Ti at applied potentials in the 4-8 V range [84-87, 89, 110, 117, 119], or at temperatures greater than 333 K [84], in a wide variety of solutions.

In some cases, breakdown crystallization potentials as high as 12-80 V have been reported [90, 91, 118]. It has been suggested [89] that these discrepancies arise from the effect of formation time (crystal growth tends to occur over time by a field-assisted annealing process, see Section 1.3.4), and the different sensitivities of electron diffraction and photoelectrochemical methods. The latter methods are able to observe an Urbach tail, Poole-Frenkel behaviour, development of a direct bandgap, and changes in quantum efficiency before changes in the diffraction pattern become evident. It has been noted that the apparent breakdown crystallization potential depends on the solution composition [89, 90, 110, 119, 121], current density [83, 88, 122], oxide film thickness [118, 121], and time [89, 90, 110, 118]. After the breakdown crystallization has occurred, the crystallized oxide has been observed to have a crystallography corresponding to anatase [84, 86, 90, 91, 118, 119] for potential-induced crystallization, and a mixture of rutile and anatase for thermally induced crystallization [84]. At very high potentials (>110 V) some rutile formation was observed with the anatase [88, 90, 91].

Some gross morphological changes have also been observed to coincide with the breakdown crystallization. It has been reported that as breakdown crystallization begins, the surface develops a "cratered" appearance [85, 86, 119], and that after breakdown crystallization it is "wrinkled" or "cracked" [84-86, 110, 119, 123]. Mikula *et al.* [88] noted a colour change to dull grey and a decrease in surface reflectivity after breakdown crystallization The mechanism of transformation from amorphous to crystalline films and possible breakdown modes giving rise to such changes in surface texture [121] are discussed in the following section on film formation.

1.3.4 Film formation and breakdown crystallization

The formation of a passive film happens spontaneously upon exposure of Ti to oxidants such as air or water. Even in deaerated solution, a pH ≤ 3 is required if spontaneous passivation is to be avoided, as shown by the Pourbaix (potential-pH) diagram [124] and other experimental studies [10]. Even under these acidic conditions, anodic film formation passivates the metal if potentials positive of about -0.3 V are applied [10]. Several general overviews of metal passivation are available in the literature [120, 125, 126].

In contrast to the disagreement on the composition and structure of oxide films on Ti, it is generally accepted [85, 87, 89, 95, 96, 104, 105, 110, 114, 121, 127, 128, 130, 131] that anodic oxide film growth on Ti occurs by a field-assisted ion transport mechanism[1] [120, 132], first suggested by Cabrera and Mott [133]. In fact, an understanding of the film growth mechanism may help explain some of the apparent discrepancies in the reports of film composition and structure.

Imagine a freshly exposed Ti surface reacting with a source of oxygen (H_2O, O_2, etc.) in direct contact with the metal surface. As the first thin continuous layer of oxide is formed (perhaps by a two-dimensional nucleation and growth mechanism [115]), it immediately becomes a physical barrier separating the two reactants [126] (*i.e.*, the source of Ti is found on the metal side of the oxide layer, the source of oxygen on the other). This, of course, inhibits further oxidation of the metal. In order for oxidation to continue, that is,

[1] Oxide film growth by solid-state processes should be distinguished from the accumulation of oxide deposits by dissolution-reprecipitation reactions [83].

for the oxide film to thicken, the two components of the film, Ti and O, must come together. This requires that one or both be transported through the existing surface oxide. This process is further complicated by interfacial reactions at the metal/oxide, oxide/solution, or oxide/gas interfaces that convert the reactant sources (Ti metal, H_2O, O_2, *etc.*) into species suitable for transport through the oxide (*e.g.*, Ti^{4+}, O^{2-}, OH^-). In addition, whatever film thickening does occur serves to enhance the barrier to further oxidation [120]. Thus, oxide film growth is largely controlled by the solid-state properties of the film itself. These properties will be discussed in detail in this section.

Although oxide film growth may occur on Ti exposed to oxidants in the gaseous, solution or solid states, for the purpose of this Thesis, only the film growth occurring on Ti immersed in solution will be considered. In this case, as stated above, the growth mechanism is widely thought to be field-assisted ion transport (FAIT). A concise description of the FAIT[1] process is as follows: if an anodic current is applied to the oxide-coated metal, it causes an electrostatic field to be established in the oxide (or increases the field already present) thereby driving metal cations or oxygen anions through the film and producing continued film growth [120].

Since the ionic conductivity of the oxide dominates its growth [120], and, as will become apparent, also influences the film composition and structure, it is worthwhile to describe the FAIT mechanism in some detail. Let us begin by considering an ideal system composed of a continuous, homogeneous, parallel-sided, defect-free, crystalline oxide

[1] Interestingly, *fait* is the French word for "makes".

film on a metal surface in solution. The reality for many metals, in fact, is not far from this idealized description [120].

In the absence of an electric field across, or a concentration gradient within, the oxide, the potential energy of a mobile ion should vary with distance within the oxide as shown schematically by the solid line in Figure 1.3.4-a. This picture was drawn assuming a positively charged interstitial mobile ion, but a similar treatment is roughly adaptable to the movement of any kind of defect [120]. In this model an ion would require sufficient thermal energy to mount a barrier of height W in order to reach the next site. According to kinetic theory, the proportion of ions possessing sufficient energy to make the jump is given by $\exp\left(\frac{-W}{k_B T}\right)$, where k_B is Boltzmann's constant, and T is the absolute temperature. It is assumed that the application of an electric field, $\overline{E}$, would reduce the potential energy barrier from W to $W - qa\overline{E}$ for ions moving with the field and increase the barrier from W to $W + qa\overline{E}$ for ions moving against the field, where q is the charge on the mobile ion and a is the distance between adjacent potential energy minima and maxima (assuming symmetrical sites and a periodic structure). The effect of the electric field is illustrated schematically by the dashed line in Figure 1.3.4-a.

The movement of ions of charge q from one local potential minimum to the next (a distance of $2a$) can be expressed as a current flow. Assuming that the mobile ions make "attempts" to cross the inter-site barrier at a frequency ν [120] (ν could be a phonon frequency [132]), and defining n to be the number density of mobile ions at a point in the oxide, then the current density flowing *with* the field would be

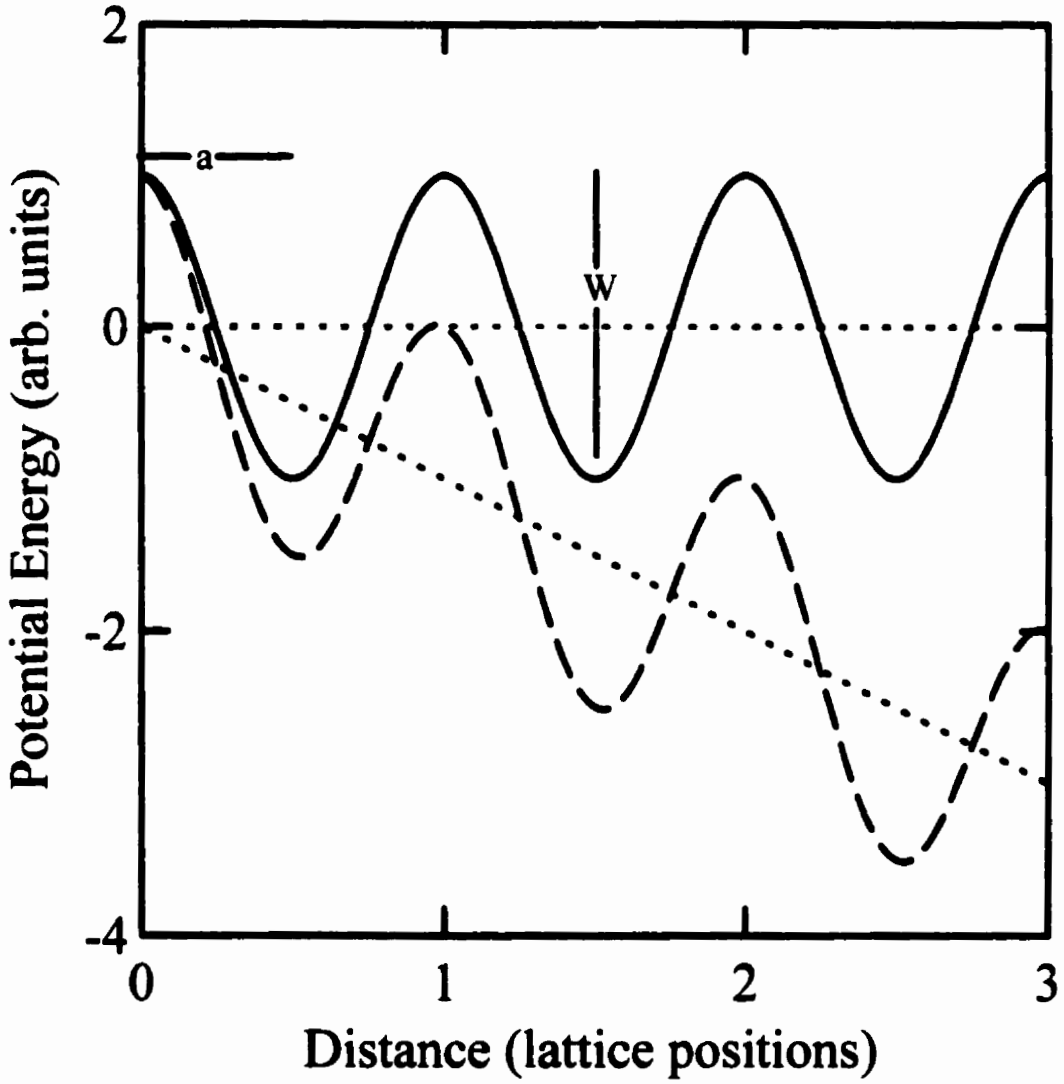

Figure 1.3.4-a The potential energy of a mobile ion in an ideal oxide crystal as a function of distance in the absence (solid curve) and presence (dashed curve) of an electrostatic field. The dotted lines indicate the electrostatic potential when the field is present (sloping line) and absent (horizontal line); a is the distance between adjacent potential energy minima and maxima, and W is the potential energy barrier height in the absence of an electrostatic field.

$$\vec{i} = 2anv\exp\left(-\frac{(W - qa\bar{E})}{k_B T}\right) \qquad \textbf{(1.3.4-a)}$$

and *against* the field,

$$\overleftarrow{i} = 2a\left(n + 2a\left(\frac{\partial n}{\partial x}\right)\right)v\exp\left(-\frac{(W + qa\bar{E})}{k_B T}\right) \qquad \textbf{(1.3.4-b)}$$

where x is the distance within the oxide[1] and $\frac{\partial n}{\partial x}$ represents the mobile ion concentration gradient. The net film growth current density is the difference between these two current densities. Usually, for thin anodic films and passive layers, the electric field is extremely high ($\bar{E} > 10^6$ V·cm^{-1}), which makes the exponential factor in equation 1.3.4-b so small that even the presence of a large concentration gradient is insufficient to yield a current flow against the field that is significant compared to the current flowing with the field. Thus the current due to film thickening is adequately represented by equation 1.3.4-a. This approach has been termed the "high field approximation" [120].

The rate of film thickening is then:

$$\frac{\partial d}{\partial t} = \frac{2anvM}{zF\rho}\exp\left(-\frac{(W - qa\bar{E})}{k_B T}\right) \qquad \textbf{(1.3.4-c)}$$

where d is the film thickness, t is the time, M is the molar mass of the oxide, z is the number of moles of electrons transferred per mole of oxide formed, and ρ is the oxide

[1] Only one dimension need be considered here since the barrier height increases rapidly with the angle away from the field direction [134].

density [128]. Integration of this expression yields the so-called inverse logarithmic growth law, a relation with the form [120, 128, 132]:

$$\frac{1}{d} = A - B\ln(t) \qquad \textbf{(1.3.4-d)}$$

At constant electrode potential, the thickening of the film causes a continuous decrease in the field strength, and therefore a decrease in ionic current. As indicated by equation 1.3.4-c, there is no mathematical limit to the film growth period, although for many practical purposes[1] the film growth rate eventually becomes negligible or equal to the film dissolution rate [120, 126]. For oxide films grown under constant current conditions, the potential drop across the film must increase as the film thickens in order to maintain the electric field required for continued film growth at a constant rate.

Measurements of the anodic film thickness on Ti as a function of applied potential using ellipsometry [85, 87, 104, 114, 118], EIS (capacitance measurements) [131, 135], RBS [105], XPS [84], coulometry [87, 104, 127], and optical interference [88] are surprisingly consistent in indicating an anodization ratio of about $2.5\pm0.5\ \text{nm}\cdot\text{V}^{-1}$ for formation potentials up to the breakdown crystallization potential. That is, the Ti oxide film thickness increases linearly with potential up to the point of breakdown crystallization according to the empirical relationship [130]:

$$\Delta d = \alpha_a \Delta E_f \qquad \textbf{(1.3.4-e)}$$

[1] It is very common in the literature to relate film thickness to applied potential by an "anodization ratio" in units of $\text{nm}\cdot\text{V}^{-1}$. According to the FAIT model this is strictly incorrect, because the oxide thickness at a given potential is forever dependent on time, but works in practice since anodic films rapidly achieve a miniscule growth rate, or one that matches the film dissolution rate [126].

where α_a is the anodization ratio and ΔE_f the change in oxide formation potential. After breakdown crystallization the anodization ratio has been observed to increase [84, 85, 87, 114]. The latter phenomenon will be discussed later in this Section.

Although FAIT theory was developed assuming metal cations to be the mobile species, it has been determined experimentally that for the growth of the oxide films on Ti, both the Ti cations and oxygen anions are transported through the oxide [111, 135]. The fraction of the total amount of ionic movement attributable to cation transport during oxide growth, termed the transport number for the metal, t_m, was determined to be 0.35-0.39 for Ti by radiolabelling experiments [135]. A value of $t_m = 0.33$ was inferred from X-ray scattering studies of epitaxial film growth [102], consistent with the former measurements. This relatively low value of t_m implies that most of the oxide formation occurs close to the metal-oxide interface. A value of t_m approaching unity should result in a large fraction of the oxide being formed at the oxide-solution interface, yielding the greatest possibility for inclusion of solution species in the film. Film growth at the metal-oxide interface should generate purer oxides. Thus, it is not surprising that Ti anodic films contain few impurities originating from the solution, including water (except in the vicinity of the oxide/solution interface) [93, 96].

The anionic and cationic transport properties of different metal oxides have been rationalized by classifying the oxides as network forming or network modifying oxides [132]. Network formers tend to have an open reticulated structure that contains channels through which the large anions are able to move. The small and highly charged cations are held more tightly by the network structure and are therefore less mobile. Network

modifiers, by contrast, have a more compact reticulation through which the motion of the large anions is difficult. In this case the small cations are loosely bound and more mobile [132]. Ti has been described as a network former [132], a classification that is consistent with the small reported values of t_m [111, 135].

Some anodization ratio values significantly different from the common 2.5 $nm \cdot V^{-1}$ have also been reported [84, 87, 93, 107, 108, 114, 116, 131]. Some variation in the anodization ratio reported by different researchers is expected, since this parameter depends on the film growth rate, temperature, and other conditions [84, 130]. As mentioned previously, the duration of film growth before the thickness measurement is made is probably important since FAIT theory predicts no limit to film growth. The solution composition could also affect the measured value of the anodization ratio, as it influences the rate of film dissolution during anodization.

The stability of the oxide film and the reproducibility of the relationship between the anodization potential and the amount of film growth have been demonstrated by cyclic voltammetry experiments in which the positive potential limit was increased on each potential cycle [114, 130]. Very little current flowed on either the forward or reverse sweeps at potentials previously experienced by the electrode, but once the potential exceeded the anodic limit of the previous sweep, significant anodic currents were generated as the existing film thickened in response to the increased potential drop.

The fact that metal cations are produced at the metal/oxide interface and oxygen anions at the oxide/solution interface results in the film being locally non-stoichiometric while growth is under way. That is, near the metal/oxide interface, the growing oxide will

contain an excess of metal cations and a deficiency of oxygen anions (*i.e.*, oxygen vacancies will be present). Similarly, near the oxide/solution interface, the film will contain an excess of oxygen anions (on their way to combine with the excess metal ions deeper within the film) and a deficiency of metal cations (represented as cation vacancies)[1]. It is possible that some of the controversy over the composition of anodic films on Ti, reported in Section 1.3.2 above, arises from observation of excess metal cations, including Ti(III) [97] and perhaps Ti(II) interstitial ions, within the film.

The differences in structure between slowly grown (crystalline) and rapidly grown (amorphous) films on Ti described in Section 1.3.3 may also be a consequence of this mode of film growth. Interstitial anions or cations and anionic or cationic vacancies are agents of disorder within the solid oxide. Given sufficient time, under conditions that allow these defects to be mobile, interstitial anions and cations should meet and fill anion and cation vacancies, respectively, thereby restoring order within the film. If, on the other hand, large numbers of such defects are created in a short period of time and their mobility is denied or at least restricted, then the film may remain in a highly disordered state. These two scenarios may reflect the situations occurring during slow and rapid oxide growth, respectively. The driving force for defect mobility, according to FAIT theory, is the high electrostatic field. This field would be expected to have an annealing effect on slowly grown oxides, allowing the small number of defects to annihilate each other and a crystalline oxide to form. A strong, rapidly applied field, by contrast, would

[1] This implies the existence of a polarized film in the absence of an electrochemically imposed potential gradient. This should not seem unreasonable if one considers that such polarization must develop spontaneously during oxide film growth by FAIT under air oxidation conditions.

generate many defects in a short time, but the thickening of the film, and perhaps the experimental procedure as well, may cause the field strength to drop, thereby "freezing" the defect structure in place and creating an amorphous oxide. This is analogous to the melt-spinning process whereby molten metal alloys are rapidly quenched ($>10^{6}$°C·s^{-1}) to yield glassy metals [136].

Evidence to support the idea of a field-driven annealing process was given by Leitner *et al.* [89] who showed that the sustained application of a potential slightly less (1 V less) than the oxide formation potential, resulted in a decrease in the number of defects[1] and the crystallization of the oxide. Field annealing had a much greater effect on films formed at lower potentials (6.8 and 17 V) than it did on oxides grown at higher potentials (55 V), probably reflecting the greater degree of crystallinity already present in the latter, as discussed in Section 1.3.3. This field annealing effect was not observed when the applied ageing potential was only 1.3 V; the authors suggested that at this potential the field was too weak to enable sufficient ionic mobility for crystallization to occur.

One can draw further analogy to the formation of glassy metals that relates the formation process, structure and composition of the oxide. Glassy metals cannot be formed from pure metals, but require the presence of alloying elements, preferably at a concentration corresponding to a deep eutectic point on the phase diagram, to help preserve the metastable amorphous structure [136]. Crystallization is slower in the presence of impurities [83]. Similarly for the passive film, the presence of "impurities", in the form

[1] As measured by photocurrent spectroscopy.

of reduced metal defects[1] (Ti(III) and perhaps Ti(II)), interstitial ions, and vacancies may help stabilize the oxide in an amorphous configuration by occupying awkward sites where unusual bond lengths are called for.

Although FAIT theory is clearly useful in describing anodic film formation on Ti, it has some shortcomings. The assumption of evenly spaced potential energy maxima and minima of identical shape cannot be totally correct in this case since the oxide is often amorphous [120]. FAIT theory also does not allow for the possibility that ionic movement might be blocked by other interstitial ions, nor does it deal with the possibility that the mobile species in the oxide environment may have an effective charge different from its formal oxidation number [120].

Other passive oxide film growth mechanisms have also been proposed (though not specifically for Ti). These include the place-exchange model [137, 138] and the point defect model [126]. In the place-exchange model, oxide film growth is envisaged to occur by a repeated sequence of simultaneous rotational steps. That is, oxygen would adsorb at exposed metal centres, then the metal-oxygen pairs would undergo a 180° rotation, thereby exchanging the anion and cation positions, creating new metal-oxygen pairs below the surface, and regenerating the surface-exposed metal centres for further oxygen adsorption. In subsequent growth steps, all underlying metal-oxygen pairs would exchange places simultaneously, thickening the oxide one atomic layer at a time. The mechanism is illustrated schematically in Figure 1.3.4-b.

[1] If the term defect is valid in a structure lacking long range order.

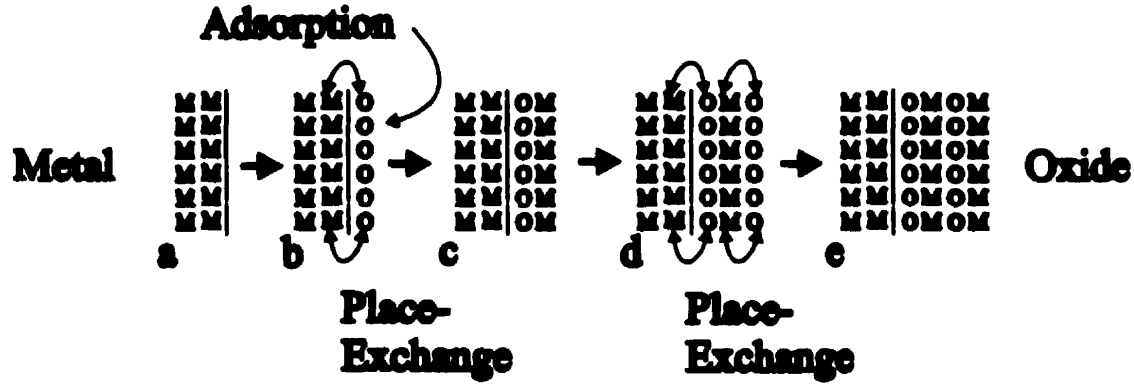

Figure 1.3.4-b Schematic representation of oxide film growth (progressing left to right) by the place-exchange mechanism [137]. The bare metal surface (stage a) adsorbs a layer of oxygen (stage b). The metal-oxygen pairs then trade places (step b-c), regenerating the layer of exposed metal centres on the exposed surface (stage c). Another oxygen layer can then adsorb at the re-exposed metal centres (stage d). The next step requires simultaneous place-exchange between two layers of metal-oxygen pairs (step d-e). Oxide thickening would then occur by repetition of these steps. Note that, for simplicity, an oxide of 1:1 stoichiometry is shown in this scheme and the third spatial dimension is ignored.

Unlike FAIT, this model does not rely on an electric field to overcome potential energy barriers and drive ions through the film for continued growth. Instead, because of the requirement for simultaneous place exchanges in underlying layers, the activation energy required would increase linearly with oxide film thickness, making further film thickening more difficult. Such a mechanism would lead to the following growth rate law (expressed as a current density):

$$i = k \exp\left(\beta E - \frac{Q}{B_2}\right) \qquad \textbf{(1.3.4-f)}$$

where E is the applied potential, Q the total charge passed during film growth ($Q = \int_0^t i dt$), and k, β, and B_2 are constants [137]. This integrates to yield a logarithmic growth law of the form:

$$d = A_3 \ln(B_3 t) \qquad \textbf{(1.3.4-g)}$$

The point defect model depicts the passive oxide as a bilayer composed of an inner "barrier layer", which acts as the primary passive film, and an outer porous precipitated layer. The transmission of ions through the barrier layer is accomplished entirely by the movement of anion and cation *vacancies*. This scheme is illustrated in Figure 1.3.4-c.

At the metal/barrier layer interface, metal cations ionize and become part of the oxide, either by filling cation vacancies arriving at the metal surface (Reaction 1) or by producing anion vacancies (Reaction 2). At the barrier layer/porous layer interface, metal cations may quit the barrier oxide by dissolving into solution, leaving behind cation vacancies (Reaction 3), or the oxide may dissolve stoichiometrically (Reaction 5). Some

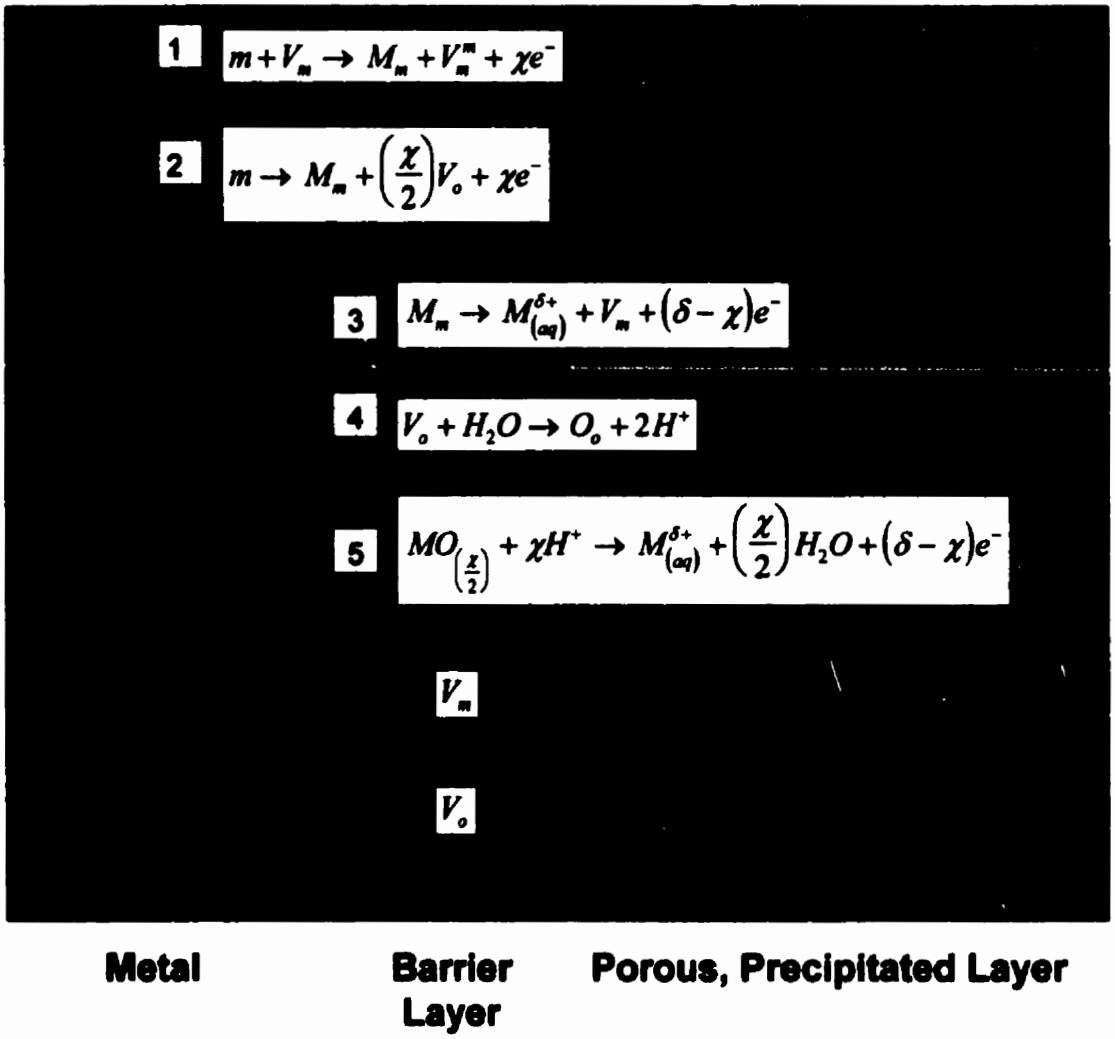

Figure 1.3.4-c Schematic representation of oxide growth by the point defect mechanism. m signifies a metal atom, M_m a metal cation in a cation site in the oxide, V_m^m a vacancy in the metal phase, χ the formal oxidation state of the metal in the oxide, e^- an electron, V_o an oxygen vacancy, $M_{(aq)}^{\delta+}$ a dissolved metal ion, δ the charge on a dissolved metal ion, V_m a metal vacancy in the oxide phase, and O_o an oxygen anion in an anion site in the oxide [126].

of this dissolved metal would precipitate as oxide to form the porous outer layer[1]. Also at the barrier layer/porous layer interface, oxygen may enter the lattice by filling anion vacancies (Reaction 4).

Overall, cation vacancies would be produced at the barrier layer/porous layer interface and consumed at the metal/barrier layer interface, anion vacancies would be produced at the metal/barrier layer interface and consumed at the barrier layer/porous layer interface, and the oxide would thicken by accumulation of precipitated oxide in the outer layer [126]. This model yields a growth law of the form

$$\exp(A_4 d) - A_4 d - 1 = B_4 t \qquad \textbf{(1.3.4-h)}$$

which, for large values of d (≥ 5 Å), can be reasonably approximated by:

$$\exp(A_4 d) = B_4 t \qquad \textbf{(1.3.4-i)}$$

This can be rearranged and expressed as another logarithmic growth law of the form

$$d = A_5 + \ln(t) \qquad \textbf{(1.3.4-j)}$$

which would manifest a current density of form:

$$i = A_6 t^{-1} \qquad \textbf{(1.3.4-k)}$$

Various diagnostic criteria aimed at distinguishing these mechanisms using experimentally measured parameters have been tabulated [126, 139]. Unfortunately, experiments seldom allow a clear distinction [139].

[1] This presumably occurs once the dissolved metal ions reach a point in the solution where they are no longer soluble (Footnotes continued next page.)

Breakdown crystallization is an important phenomenon in terms of the oxide growth rate, composition, structure, and, because it creates grain boundaries and cracks that can act as low-impedance pathways for ion transport [110, 119], reactivity of the underlying metal. This phenomenon has been observed on other valve metals such as Nb [120], Al [119] and Ta [119, 120]. As previously stated (Section 1.3.3), breakdown crystallization is observed for rapidly grown films on Ti at potentials in the 4-8 V range [84-87, 89, 110, 117, 119] or at temperatures above 333 K [84], although breakdown crystallization potentials as high as 12-80 V have been reported [90, 91, 118]. It has been suggested that neither current density nor formation potential directly determine the point at which breakdown crystallization is triggered, but rather that the process occurs once a critical oxide thickness is achieved (or, synonymously, once a certain amount of charge has passed) [119]. Breakdown crystallization is characterized by a drop in the coulombic (or current) efficiency for oxide growth (implying increased conductivity and electron transfer to or from water, or other available reducible or oxidizable species) [87, 110, 119], an increase in the apparent anodization ratio [84, 85, 87, 114], the appearance of a direct bandgap [89], changes in the refractive index [87, 118] and dielectric constant [84, 110, 118, 140], a decrease in the slope of the potential transient under galvanostatic conditions [83, 87, 119], gross morphological changes (*i.e.*, the appearance of ripples, "craters" and cracks on the surface) [84-86, 110, 119] and, of course, the development of crystalline oxide on the Ti surface [84, 86, 87, 90, 117-119].

---

due to changes in pH, etc.

As with many aspects of passive films on Ti, there remains much uncertainty about this phenomenon. In this case there is a "chicken-and-egg" type problem; that is, it is unclear whether ionic breakdown precedes and induces crystallization, or whether breakdown is a consequence of the crystallization process [119]. The activating process for crystallization from the metastable amorphous state is also in question. Some authors have concluded that film breakdown permits a large increase in the ionic current density [87], which, in turn, causes significant local heating, thereby promoting crystallization of the oxide [83, 119]. Evidence to support this view has been taken from experiments in which an electron beam, *in vacuo*, was shown to cause local heating and crystallization of TiO_2 films [83, 119].

Some authors [83-85, 119, 121, 122] also contend that crystallization occurs in response to high compressive stresses that develop within the oxide, and the grain boundaries and cracks generated by crystallization offer low-resistance current leakage sites and short diffusion paths for ion transport [110, 119]. The compressive stresses required for crystallization of metal oxides or hydroxides, though not reported specifically for Ti, have been shown to be in the range of 10-100 MPa [121]. Stress in anodic films can result from interfacial tension, electrostriction, volume expansion upon oxide formation, atmospheric pressure, hydration, dehydration, or impurity incorporation [121]. The first four sources of stress are discussed below, but no specific treatment of hydration, dehydration, or impurity incorporation could be found in the literature.

Electrostriction, that is, constriction of the film as a consequence of the intense potential gradient across it ($\sim 10^6$ V·cm^{-1}), and interfacial tension effects have been thoroughly

treated by Sato [121]. The governing equation for the film pressure at the oxide/solution interface, π_{os}, derived by Sato is

$$\pi_{os} = \frac{\varepsilon(\varepsilon - 1)\overline{E}^2}{8\pi} - \frac{\gamma}{d} + P_0 \qquad \textbf{(1.3.4-1)}$$

where P_0 is the atmospheric pressure, ε the dielectric constant of the film, $\overline{E}$ the electric field strength, γ the interfacial tension at the oxide/solution interface[1] and d the thickness. (This treatment ignores contributions to the film pressure from volume expansion upon oxide formation, hydration, dehydration, and impurity incorporation.) In equation 1.3.4-1, one can see that the first term corresponds to the electrostriction pressure and the second to the interfacial tension effects and, in the absence of these, that the film pressure would simply be equal to the atmospheric pressure. This dependence on interfacial tension is consistent with reports that the solution composition affects the potential at which breakdown crystallization occurs [121]. Shibata and Zhu [84] attempted to determine the value of π_{os} for the titanium oxide/solution interface using equation 1.3.4-1. Unfortunately they could not obtain an accurate value of γ for the titanium oxide/solution interface. However, using an estimated value of $\gamma = 0.2\ \text{N}\cdot\text{m}^{-1}$ (a middle value in the range $0.01\text{-}0.5\ \text{N}\cdot\text{m}^{-1}$ reported for metal oxides [121]), they determined values of π_{os} as a function of temperature[2] between 303 and 353 K. They

[1] The interfacial tension was only considered at the oxide/solution interface since it was assumed that the metal/oxide interface was restrained. This may not be entirely true –it is possible that some local deformation occurs at the metal-oxide interface [Roger Dutton, personal communication].

[2] Shibata and Zhu used the point defect model to determine the temperature dependence of the electric field strength in the oxide ($\overline{E}$ decreases with increasing T) and measured the relationship between film thickness and temperature (d increases with increasing T) [84] and between dielectric constant and temperature (ε increases with increasing T) [140].

found that at low temperatures (<323 K) the film pressure was small, perhaps even yielding tensile stress at 303 K, but at T ≥ 323 K jumped to very high values, generating compressive stresses > 150 MPa -enough to exceed the critical stress required for breakdown (10-100 MPa [121]). This radical increase in film pressure roughly coincides with the temperature at which Shibata and Zhu observed breakdown crystallization on a film maintained at a potential of 1 V (Ag/AgCl) [84].

Nelson and Oriani [122] presented a somewhat different treatment of electrostriction in anodic films of Ti, which they used to calculate the electrostrictive component of the film stress. They then subtracted the electrostrictive stress from the values of the total stress determined from measurements of the stress-induced deflection of a thin metal foil undergoing anodization. This procedure allowed them to determine the stress associated with other film phenomena. According to their experiments, the total stress, and therefore the stress associated with the other processes, was always *tensile* in nature at potentials up to 2 V. Unfortunately these measurements were not extended to the potential range where breakdown crystallization is observed (4-8 V) to establish whether high *compressive* stresses exist under the latter conditions.

Nelson and Oriani [122] also offered an interesting discussion of the volume expansion during oxide formation and the relationship between the ionic transport numbers and the development of stresses within the film. The ratio of the volume of an oxide containing a given number of metal ions to the volume occupied by the same number of metal atoms in their metallic state, called the Pilling-Bedworth ratio, is given in Table 1.3.4-a for each of

the TiO_2 polymorphs[1]. It seems reasonable to assume that most Ti oxide formation occurs at the surfaces of the oxide and not within its bulk, where no free space is available. This assumption has been verified explicitly for Ta_2O_5 by experiments employing implanted radioactive noble gas markers [141]. The fact that the Pilling-Bedworth ratio for all TiO_2 polymorphs is greater than unity means that if all oxide growth took place at the metal/oxide interface (*i.e.*, $t_m = 0$), the volume required to accommodate the oxide would be much greater than the free space created by oxidizing the Ti substrate; enormous compressive stresses would be generated [122] (greatly exceeding the elastic limit of the oxide [Roger Dutton, personal communication]). Conversely, if all of the film growth took place at the oxide/solution interface (*i.e.*, $t_m = 1$), then a large amount of free volume would be generated at the metal/oxide interface and tensile stress would arise [122]. Since the oxide/solution interface is unrestrained, there would be no stress generated there due to oxide formation. Thus, there should exist a critical transport number, t_m^c, for which the amount of oxide formed at the metal/oxide interface would exactly fill the free volume created by metal oxidation and no stresses due to volume considerations would arise. This critical value is given by

$$t_m^c = 1 - \frac{1}{\Re_{PB}} \qquad \textbf{(1.3.4-m)}$$

where $\Re_{PB}$ is the Pilling-Bedworth ratio. For $t_m < t_m^c$, more oxide would form at the metal/oxide interface than the free volume could accommodate and compressive stresses would develop. Conversely, for $t_m > t_m^c$, tensile stresses would prevail [122].

[1] The Pilling-Bedworth ratio is a *calculated* value based on the densities of the metal and corresponding oxides.

Table 1.3.4-a Pilling-Bedworth Ratios and Critical Metal Ion Transport Numbers for TiO_2

Form	Specific Gravity	Pilling-Bedworth Ratio	t_m^c
Rutile	4.26	1.77	0.44
Anatase	3.84	1.96	0.49
Brookite	4.17	1.80	0.44

The values of t_m^c calculated for the three crystalline polymorphs of TiO_2 are given in Table 1.3.4-a. These values of t_m^c are reasonably close to the values of $t_m = 0.35 - 0.39 \pm 10\%$ measured by Khalil and Leach [135] and, t_m^c being slightly larger than t_m, suggest compressive stress should be generated within the oxide film. However, tensile stresses were observed by Nelson and Oriani [122]. An explanation for this apparent contradiction might be that the values of t_m and t_m^c change with film growth conditions or thickness. Tensile stresses could be superseded by compressive stresses if t_m^c increased or t_m decreased. Indeed, t_m has been observed to depend on the electrolyte as well as the applied current density in constant current growth experiments. Both of these parameters have independently been observed to affect the potential at which breakdown crystallization occurs [121]. For TiO_2 films, t_m increased from 0.35 at an applied current density of 6 $mA \cdot cm^{-2}$ to 0.39 at 50 $mA \cdot cm^{-2}$ [135]; the value of t_m in Al_2O_3 films ranges from 0.35 at 0.1 $mA \cdot cm^{-2}$ to 0.72 at 10 $mA \cdot cm^{-2}$ in 3% aqueous ammonium citrate, but remains nearly constant at 0.6 over the same range of current density in tetraborate-glycol solution [141]. One might also expect t_m to be different depending on whether the oxide is crystalline or amorphous, since the solid-state

transport pathways may be radically different in the two cases. In addition, t_m might change as the oxide thickens and the transport path length increases.

It has been suggested [141] that t_m may be field-dependent. The equations describing the anionic and cationic motion derived from FAIT theory are

$$n_a = n_a^0 \exp\left(-\frac{\left(W_a - qa\bar{E}\right)}{k_B T}\right) \qquad \textbf{(1.3.4-n)}$$

$$n_c = n_c^0 \exp\left(-\frac{\left(W_c - qa\bar{E}\right)}{k_B T}\right) \qquad \textbf{(1.3.4-o)}$$

where n_a and n_c are the number densities of moving anions and cations, n_a^0 and n_c^0 the concentrations of anions and cations available to move from an interface, and W_a and W_c the barrier potentials for anion and cation movement in the absence of an electric field, respectively. The transport number for the metal would then be given by

$$t_m = \frac{n_c}{n_a + n_c} \qquad \textbf{(1.3.4-p)}$$

which will change with the electric field strength and surface conditions.

The value of t_m^c could also change with growth conditions through its dependence on the Pilling-Bedworth ratio. This should result in a small decrease in t_m^c with an increase in electrostriction, but would also yield higher values of t_m^c for amorphous oxide (*if* it is more dense than the crystalline oxides). As reported in Section 1.3.3, the oxide may be amorphous or crystalline depending on the growth conditions. The Pilling-Bedworth

ratio for amorphous TiO_2 may be as high as 2.4 [87], which would put t_m^c at 0.58 and make compressive stresses more likely in the amorphous film. Since it is the relative values of t_m and t_m^c that determine whether the stresses due to volume change on oxidation are compressive or tensile, it seems quite plausible that under different conditions the stress may change sign. This may explain why there is controversy in the literature [83] over whether the stress is compressive or tensile.

Other evidence that supports the theory of stress-induced crystallization is found in microscopy results that show ripples, cracks and "craters" in the oxide film after breakdown crystallization [84, 86, 110, 119]. Whether induced by resistive heating or by stresses, the ordering of material into crystals requires a high ionic mobility. An increase in ionic mobility associated with breakdown crystallization has been reported [87, 110].

1.3.5 Reactivity and dissolution

The passive film on Ti is a wide-bandgap semiconductor, known to have n-type semiconducting characteristics [92, 97, 101, 105, 110, 114, 125, 129-131, 142]. When the oxide is intact, the reactivity of Ti is determined by the ability of the oxide to transport electrons between the solution and the underlying metal. Therefore, the reactivity of Ti is controlled by the oxide film's semiconducting properties. The implications of this statement [125] are illustrated in Figure 1.3.5-a.

The movement of electrons in a semiconductor is dependent on potential in an extremely non-linear fashion. Frame c of Figure 1.3.5-a describes the electronic band structure of the n-type semiconductor under flatband conditions, that is, at a potential, called the

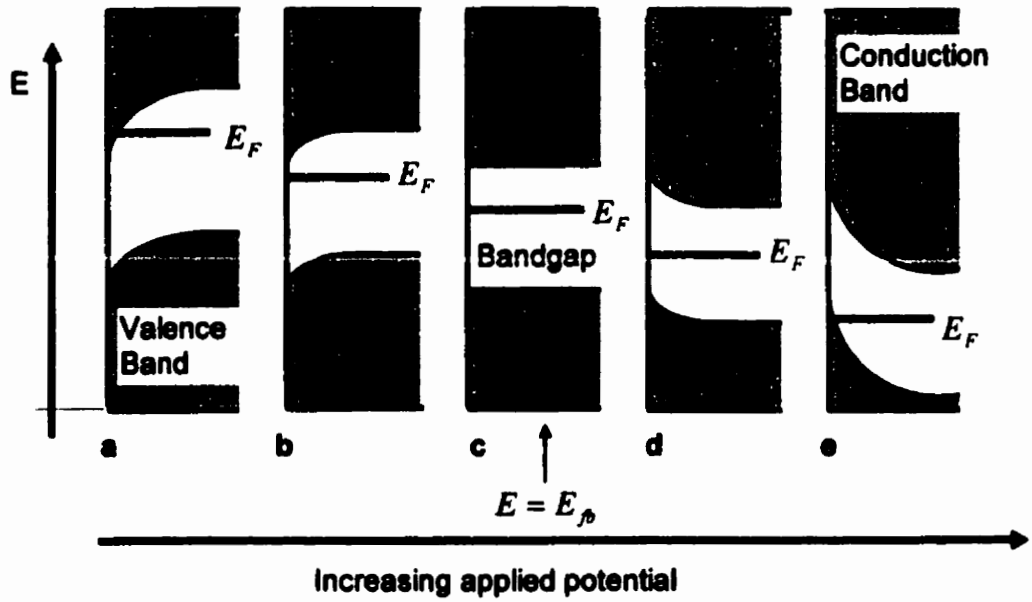

Figure 1.3.5-a The effect of applied potential on the band structure of TiO_2. The applied potential increases from a to e across the Figure. (Note that the potential energy scale in this diagram is inverted with respect to the usual electrochemical sign convention.) Frame c represents flatband conditions, frames b and d indicate some band-bending at moderate potentials, and frames a and e represent conduction band and valence band degeneracy at more extreme low and high potentials, respectively [125]. For n-type semiconductors, such as TiO_2, conduction band degeneracy (frame a) should require less polarization than valence band degeneracy (frame e) because the lower edge of the conduction band is closer to E_F at $E = E_{fb}$.

flatband potential, E_{fb}, at which no net electric field, and therefore no space-charge layer, exists within the film. At $E = E_{fb}$, the energies of the conduction band and the valence band are constant with distance within the film (*i.e.*, the bands are "flat"). The Fermi level, E_F is the energy at which the probability of finding an electronic level in the occupied state is 0.5 [143]. At E_{fb}, the Fermi level lies within the bandgap, that range of energies between the largely unoccupied conduction band and the fully-occupied valence band. Within the bandgap, the number of electronic levels (*i.e.*, the density of states) is low, and the levels that are available tend to be localized in nature (probably corresponding more closely to atomic orbitals than to the long-range, delocalized continuum of levels associated with a band). Since neither the fully occupied valence band nor the localized states at energies within the bandgap have a strong ability to carry electronic current, the oxide displays a highly resistive behaviour. When a potential bias is applied to the semiconductor, an electric field develops and E_F changes accordingly. Band-bending arises because the applied potential creates a space-charge layer in the surface of the semiconducting oxide and the valence and conduction band energies are "pinned" at the oxide/solution interface, but change with potential in the interior of the film[1]. If E_F remains fully within the bandgap, then the potential change occurs only within the oxide; the Helmholtz layer potential drop remains constant (*i.e.*, an ion in solution near the oxide surface experiences no change in potential, and the rates of

[1] If the semiconducting film is thin enough, the space-charge layer, and therefore the band bending, may extend across the entire width of the film.

electrochemical reactions are not affected). Figure 1.3.5-a shows the band bending that occurs when potentials $E < E_{fb}$ and $E > E_{fb}$ are applied.

An exception to the display of resistive behaviour at potentials for which E_F lies fully within the bandgap occurs when the semiconductor is exposed to light of sufficient energy to excite electrons from the valence band to the conduction band. Once in the conduction band, electrons formed within the space-charge region may travel to the oxide/solution interface (if $E < E_{fb}$) where they could participate in redox reactions with solution species, as could the corresponding holes created in the valence band (if $E > E_{fb}$) [115]. The key requirement of this process is that the exciting radiation be of energy equal to, or greater than, the bandgap energy[1], E_g, which, for TiO_2, corresponds to violet/ultraviolet (UV) light. The values of E_g for crystalline and amorphous[2] anodic films on Ti are ~3.2-3.3 eV and ~3.3-3.4 eV [89, 115], while those of single crystal rutile and single crystal anatase are 3.0 eV[3] [88, 89, 115, 142] and 3.2 eV [88, 115], respectively.

Arriving at the oxide/solution interface, photo-excited electrons or energetic holes are capable of effecting high-energy chemical reactions such as the decomposition of water

[1] The bandgap refers to the difference between the energy of an electron at the upper edge of the valence band and the energy of an electron at the lower edge of the conduction band.

[2] For amorphous or highly-defective semiconductors that lack well-defined band edges, and have a rather broad distribution of states that are not necessarily identical or completely delocalized, it is more correct to use the term "mobility gap" in lieu of the term bandgap. Mobility gap refers to the energy gap between the upper and lower energies beyond which enough orbital overlap exists that charge carriers are able to move through the material [143]. The upper and lower bounds of the mobility gap could, in a sense, be viewed as the transition points between molecular orbitals and bands. For simplicity, the term bandgap will be used in this Thesis.

[3] For reference, 3 eV light has a wavelength of ~413 nm and lies at the boundary between the visible and UV regions of the electromagnetic spectrum [146].

[88, 144]. This principle has been put to commercial use in Japan in the form of passive, self-cleaning items such as clothing or ceramic tiles that use TiO_2 and UV light to break down organic "dirt' or to kill micro-organisms. Tsujikawa [144] has even proposed this photoelectrochemical effect as a means to cathodically protect stainless steel or copper nuclear waste containers. In his model, X-rays emanating from the radioactive waste would be absorbed directly by a TiO_2 coating on the containers, or by glass scintillators that would convert their energy to UV light, which would then be absorbed by the TiO_2. In either case, the holes generated in the TiO_2 valence band could then be used to oxidize water, while the electrons would be supplied to the metal, lowering its potential and protecting it from corrosion.

In the absence of light, at potentials for which E_F remains fully within the bandgap, a limited amount of reactivity should still be observed on TiO_2 since the conduction band is partially occupied, due to the presence of defects in the oxide. The degree of reactivity will be controlled by the density of available charge carriers, a value determined by the number and types of defects and impurities in the semiconductor. For passive films on Ti, the major contributing surface defects have been shown by scanning tunneling microscopy and tunneling spectroscopy to be oxygen vacancies [109], which are electron donor states located ~0.7 eV below the conduction band [101, 109]. Oxygen vacancies have been proposed to consist of a missing bridging oxygen atom and a pair of adjacent Ti^{3+} ions [100, 101, 118]. Interstitial Ti^{3+} ions have also been suggested to be among the important defects in the films [97, 109, 115, 145]. Oxidation reactions under these conditions should proceed much more slowly than reduction reactions, since the holes required for oxidation are the minority charge carriers in the n-type film (*i.e.*, the

concentration of holes in the valence band is much less than that of electrons in the conduction band). The charge carrier density, N_D, for passive films on Ti has been determined from the slope of Mott-Schottky plots and usually found to be on the order of ~10^{19}-10^{20} cm^{-3} [89, 95-97, 110, 114, 117, 131, 142]. Torresi *et al.* [130] have tabulated values of N_D from 5×10^{17} cm^{-3} to 1.5×10^{20} cm^{-3}, showing the dependence of N_D on film growth rate and anodization potential.

Figure 1.3.5-a illustrates extreme conditions of polarization in which E_F is pushed into the conduction band ($E < E_{fb}$) or valence band ($E > E_{fb}$) at the electrode surface. Once this occurs the semiconductor is said to be *degenerate*; the conduction band will have a continuous supply of electrons ($E < E_{fb}$) or the valence band will have a continuous supply of holes ($E > E_{fb}$) at the semiconductor/solution interface, where they may participate in redox reactions with solution species [125, 130]. At this point, the oxide conductivity is nearly metallic, and further changes in E will begin to change the Helmholtz layer potential, providing an increasing driving force for electrochemical reactions [125]. For an n-type semiconductor, E_{fb} resides slightly below the conduction band, so achieving degeneracy requires less band bending at $E < E_{fb}$ than at $E > E_{fb}$.

Wholesale *electronic* breakdown of the semiconductor leading to very high conductivity may occur under extreme levels of polarization. Two mechanisms of electronic breakdown are known: Zener and avalanche breakdown. Zener breakdown occurs when the band bending in the semiconductor is so great that for two physically nearby points, electrons having the same energy will be located in different bands (*i.e.*, in the valence

band at one point and in the conduction band at the other point). If these points are close enough (3 nm or less), then the electrons can tunnel from the valence to the conduction band and provide high current densities. In avalanche breakdown, the very high electric field accelerates charge carriers to energies at which, upon collision within the semiconductor, they can excite an electron from the valence band to the conduction band. Either member of the newly-created electron-hole pair could also be accelerated, collide and create a new electron-hole pair in a cascading or "avalanche" fashion, again providing high current densities. For the avalanche to occur, the charge carrier acceleration must occur over a short distance (*i.e.*, before a collision robs the carrier of kinetic energy). For example, if an electron has a "mean free path" of 10 nm before collision, and $E_g = 3$ eV, then an electric field of at least 3×10^6 V·cm^{-1} would be required to initiate avalanche breakdown [143]. Electric fields of similar magnitude are generated during film growth on Ti (see Section 1.3.4), implying that the oxide is on the verge of breakdown as it grows, and possibly explaining why it is difficult to determine whether or not breakdown precedes crystallization (see Section 1.3.4).

Mott-Schottky plots and photocurrent onset potentials have been widely used to determine the value of E_{fb} for anodic films on Ti. A large number (187) of E_{fb} values for TiO_2 (including, but not limited to, anodic films) have been compiled (from 82 references) by Finklea [147]. The value of E_{fb} is dependent on both N_D and pH, yielding a -60 mV shift for each decade increase in N_D or unit change in pH. Considering the entire set of E_{fb} data collected by Finklea, the difference between the minimum and maximum reported values was ~ 1.5 V, with a variation in E_{fb} at each pH

of ~0.7 V. The latter distribution was roughly centred on the standard potential for proton reduction at each pH. The isoelectric pH (*i.e.*, the pH at the point of zero charge at open circuit) was reported to be ~5.8.

Mott-Schottky plots and potential-modulated reflectance spectroscopy specifically for anodic films on Ti have indicated E_{fb} values corresponding to[1] -0.6 V in 1 mol·dm^{-3} $HClO_4$ [95], -0.75 V in 3 mol·dm^{-3} H_2SO_4 [129], -0.54 V in 0.5 mol·dm^{-3} H_2SO_4 [130], -0.38 V (*sic*)[2] in 0.5 mol·dm^{-3} H_2SO_4 [97], -0.65 V (SHE) (*sic*)[3] in phosphate buffer (pH = 7) [96], -0.74 to -0.67 V in NaOH (pH = 12.8), and -0.81 to -0.58 V in 0.1 mol·dm^{-3} NaOH [148]. Oxide film degeneracy leading to high rates of proton reduction has been observed at potentials just negative of E_{fb} [130, 147]. Reduction reactions involving other solution species also occur once $E < E_{fb}$ [143]. Positive polarizations resulting in valence band degeneracy and oxygen evolution (from water oxidation) have been reported for potentials of ~2 V in 1 mol·dm^{-3} H_2SO_4 [105], 2.76 V in 0.2 mol·dm^{-3} HCl or 0.1 mol·dm^{-3} H_2SO_4 [85], and 2.46 V in HCl/NaOH mixtures (pH = 0-10.5) [127]. At this point the current efficiency for oxide growth decreases from 100 % due to competition from oxygen evolution [85]. The difference between the potentials of hydrogen and oxygen evolution roughly corresponds to the

[1] A variety of different reference electrodes were used in the original references. Except where noted otherwise, values reported here have been converted to the SCE scale to facilitate easy comparisons.

[2] This datum is out of line with the others and seems to indicate an error in the original paper [97], perhaps arising from a confusion of reference potential scales. If the result of a confusion between SCE and SHE scales, the correct value is probably -0.62 V (SCE), which would put it in line with the other values.

[3] This appears to be another error. The authors referred to the SCE scale for all other potentials reported in their paper [96], and discussed their E_{fb} value as being consistent with others in this list, so this value probably should be -0.65 V (SCE).

bandgap energy [85]. Similar behaviour has also been observed for oxide films on Ni and Fe [125]. It should be noted that degeneracy is also possible when E_F corresponds to the energy of a dense cluster of surface states within the bandgap [125]. Such degeneracy might be of a transient nature if the physical defects giving rise to the surface states are eliminated by reaction or dissolution once degeneracy is achieved.

Once degeneracy is achieved in the conduction band at the oxide surface, compositional changes begin to take place in the oxide film and hydrogen evolution becomes important. The film becomes loaded with hydrogen possibly in the form of TiOOH [131, 149, 150]. This would associate absorbed hydrogen with the existence of Ti(III) and hydrated oxide in the film ($TiOOH \equiv Ti_2O_3 \cdot H_2O$) [131, 149]. The same effect has been noted for sputter-deposited TiO_2 in 0.1 $mol \cdot dm^{-3}$ NaOH [148]. Ohtsuka *et al.* [150] determined that the absorbed hydrogen concentration in the film does not depend on oxide layer thickness but on the cathodic potential, attaining a maximum value of 1 H atom per Ti atom at E = -1.14 V (suggesting a complete conversion of the oxide film to TiOOH).

The introduction of hydrogen results in a peak in film capacitance at potentials near E_{fb} and a dramatic decrease in film impedance at lower potentials [148, 149]. It appears that hydrogen acts as a donor state, increasing film conductivity [149]. The value of the dielectric constant, ε, for the film increases with increasing hydrogen content [131, 148]. Only a small fraction ($\leq 0.01\% \approx 2 \times 10^{17}$ cm^{-3})[1] of the hydrogen species formed act as electron donor states, however, suggesting that the energy levels of the electrons

[1] Determined from the difference in slopes of Mott-Schottky plots taken in the presence and absence of a known amount of hydrogen in the film.

associated with the absorbed hydrogen are well below the conduction band edge [148]. Ohtsuka *et al.* [150] reported a new absorption band in the bandgap region of their anodic oxide films after hydrogen absorption. The peak in film capacitance was surmised to be due to a hydrogen absorption process or a bulk dielectric effect associated with dielectric saturation[1] in the film [148]. The increased doping caused by hydrogen absorption also results in the appearance of a blue/violet colour in the film [131, 147, 150].

Weber *et al.* [148] found that some of the hydrogen is reversibly absorbed, while some can only be removed by anodic photo-bleaching (*i.e.*, oxidizing in the presence of light), which presumably means that this last portion of the hydrogen must be ionized before it can be expelled from the film [148]. Ohtsuka *et al.* [150] also recognized reversibly absorbed hydrogen, but suggested a third "type" of hydrogen, which could be re-oxidized from the film only very slowly. This was thought to be hydrogen absorbed into the metal substrate that escaped slowly through the oxide overlayer. This interpretation is at odds with the neutron reflectometry observations of Wiesler and Majkrzak [108] who found that hydrogen, once absorbed through the oxide into the metal, did not escape back through the oxide, even after achieving significant concentrations. Dyer and Leach [149] determined a diffusion coefficient for reversibly absorbed hydrogen of 3×10^{-13} $cm^2 \cdot s^{-1}$, which, they concluded, could only be attributed to mobile protons.

One of the properties that make the oxide film on Ti so protective is its very low solubility over a broad range of conditions and solution compositions. Anodic dissolution

[1] Dielectric saturation is a process expected for thin films of high dielectric constant under high electric field conditions. Once the electric field is high enough, the space charge region extends across the entire thickness of the film and the capacitance levels off.

of the passivated metal must take place *through* the oxide film when the latter is still intact. As described in Section 1.3.3, with respect to film formation by FAIT, oxide film growth proceeds until the film thickness reaches a steady state condition at which the film formation rate is equivalent to the film dissolution rate. The metal dissolution rate, according to Sato [125] is equivalent to the oxide dissolution rate, which is controlled by the Helmholtz layer potential. According to the description of semiconductor electrochemistry offered earlier in this Section, the Helmholtz potential is unaffected by the applied bias as long as E_F remains fully within the semiconductor bandgap. It is well known that the current on *passive* Ti electrodes is very low and depends little on the applied potential with E_F in this range (see, for example, Figure 2 of [151]). The match between metal and oxide dissolution rates under constant anodic bias was elegantly confirmed by the neutron reflectometry experiments of Wiesler and Majkrzak [108]. The dissolution rate they measured in $0.2\ mol{\cdot}dm^{-3}\ H_2SO_4$ was $7 \times 10^{-2}\ nm{\cdot}h^{-1}$ at $1\ V \leq E \leq 5\ V$. In aqueous solutions, strong anodic polarization ($E > 7$ V at 90°C) may lead to pitting of Ti, but this occurs at potentials beyond the point of breakdown crystallization when the film is no longer intact. Pitting has been discussed in detail in a recent review by Shoesmith and Ikeda [52] and need not be discussed further here.

In acidic solution the oxide film on Ti may dissolve "reductively" [104, 116, 131, 150, 152] or "chemically" [104, 107, 108, 116, 125, 152]. In neutral solutions, cathodic reduction of the oxide to TiOOH occurs, but does not result in film dissolution [150], since neither Ti(IV) nor Ti(III) is soluble in neutral aqueous solutions. Reductive dissolution, as its name suggests, involves the reduction of Ti(IV) ions in the oxide to

Ti(III), perhaps in the form of TiOOH [116, 150]. The Ti(III) then dissolves in the acidic solution. It has been suggested that the soluble form is $Ti(OH)^{2+}$ [116]. Reductive dissolution competes with proton reduction for the cathodic charge [116, 131, 150].

Chemical dissolution takes place without the need for redox transformation; the Ti dissolves in the Ti(IV) state. The dissolution reaction

$$TiO_2 + H_2O + H^+ \rightarrow Ti(OH)_3^+ \qquad \textbf{(1.3.5-a)}$$

has been suggested [116]. The rate of chemical dissolution is much less than that of electrochemical dissolution and is strongly dependent on the pH of the solution; stronger acid (or strong base) increases the chemical dissolution rate over that of intermediate pH solutions. Blackwood *et al.* [116] reported chemical dissolution rates in a wide variety of solutions. Extremely low rates[1] (7×10^{-2} nm·h^{-1}) were found in near-neutral oxalate solution (1.0 mol·dm^{-3} $K_2C_2O_4$), even though oxalate is expected to complex Ti(IV). Higher dissolution rates (>2 nm·h^{-1}) were observed in strongly acidic (3.0 mol·dm^{-3} H_2SO_4) and strongly basic (1.0 mol·dm^{-3} KOH) solutions. By comparison, reductive dissolution in 3.0 mol·dm^{-3} H_2SO_4 yielded dissolution rates of 6.2 nm·h^{-1}.

The oxide structure also has a strong influence on the dissolution rate. Slowly grown films (*i.e.*, highly crystalline oxide, see Section 1.3.3) dissolve about ten times more slowly than the rapidly grown films [116]. Uniform dissolution has been observed for chemically and reductively dissolved films on Ti [104, 116]; however, localized attack of the oxide is sometimes observed [107, 108, 152]. It is not clear what conditions

[1] One might well argue that even 6.2 nm·h^{-1} is extremely slow, which is true, but the emphasis here is on the *relative* dissolution rates.

determine this behaviour; however, the results of recent anisotropy microellipsometry measurements on Ti at the single-grain level have shown that the electron donor densities (*i.e.*, the number of defects, which tend to be sites of easier attack during dissolution) of slowly grown oxide films are texture-dependent, while those of fast-grown oxide films are not [114, 153-155]. Films of the former type may be more prone to localized oxide dissolution, while the latter may tend toward uniform attack.

The relationship between film thickness and potential for reductive dissolution is linear with a slope equal to the anodization ratio for very thin films, but deviates substantially for films grown to $E > 1$ V ($Hg/HgSO_4$) [116]. According to ellipsometry experiments, the oxide film can be removed completely by reductive dissolution at $E \leq -0.9$ V [152]. An oxidative dissolution mechanism has also been proposed for TiO_2 [125]

$$TiO_2 \rightarrow Ti^{4+} + O_2 + 4e^- \qquad \textbf{(1.3.5-b)}$$

but does not seem likely to occur in aqueous solution, where water oxidation should take precedence.

The passive dissolution of Ti has become a concern in biomedical implant applications. Surprisingly high *in vivo* corrosion rates, not expected from initial *in vitro* testing, have led to investigations of potentially aggressive components of human bodily fluids, such as complexing biomolecules [106] and hydrogen peroxide (H_2O_2) [96, 156]. Solution ligands such as human serum molecules (proteins) and even EDTA (ethylenediaminetetraacetic acid) were found to enhance the dissolution of the oxide film by complexing, and therefore solublizing, the hydrated outer oxide [106].

Exposure of passive Ti to low concentrations of H_2O_2 (≤ 0.1 mol·dm^{-3}) appeared to make the film electronically defective and porous. The film thickness and roughness increased with time, and a porous, hydrous precipitated oxide layer accumulated, incorporating mineral ions from solution [96, 156]; a blue colour also developed. Eventually, as the film thickened, the pores became sealed, perhaps by precipitated deposits, and the high corrosion resistance of the metal was renewed.

The latter biomedical reports have been included at the end of this review because, although *in vivo* conditions are beyond the range of consideration of this Thesis according to the objectives as defined in Section 1.1.2, complexing organic molecules may be present in the buffer and backfill materials proposed for the nuclear fuel waste disposal vault, and H_2O_2 will be created in small quantities at the waste container surfaces by water radiolysis [1].

1.4 Hydrogen absorption by titanium

1.4.1 Introduction

In addition to metal wastage by corrosion processes, Ti structures are vulnerable to failure by cracking. The types of Ti alloys discussed in this Thesis (see Section 1.1.3) are immune to stress corrosion cracking in aqueous environments [40], but could be susceptible to hydrogen-induced cracking (HIC) [40, 157]. HIC is a phenomenon involving fast crack growth in a metal under tensile stress, and is a consequence of the build-up of absorbed hydrogen in the metal as particles of brittle metal hydride phases [157-160].

Previous work by Clarke *et al.* [158] has shown that there is a threshold hydrogen concentration (~500 $\mu g \cdot g^{-1}$ at room temperature) below which fast crack growth does not occur in Ti. At hydrogen concentrations below this critical value, only ductile tearing occurs, provided the tensile stress is high enough [157, 158]. However, once the appropriate combination of tensile stress and hydrogen concentration is achieved, the material will fail rapidly (relative to the long lifetimes required for nuclear waste disposal containers) by HIC [158].

The critical parameters that determine when HIC could occur are: the tensile stress intensity; the value of the critical hydrogen concentration ($[H]_c$); the rate of hydrogen absorption into the metal (R_{HA}), including the surface adsorption step; and the rate of hydrogen redistribution within the metal (J_H) [161]. The relationship between the latter three factors is illustrated pictorially in Figure 1.4.1-a. Of these parameters, this Thesis

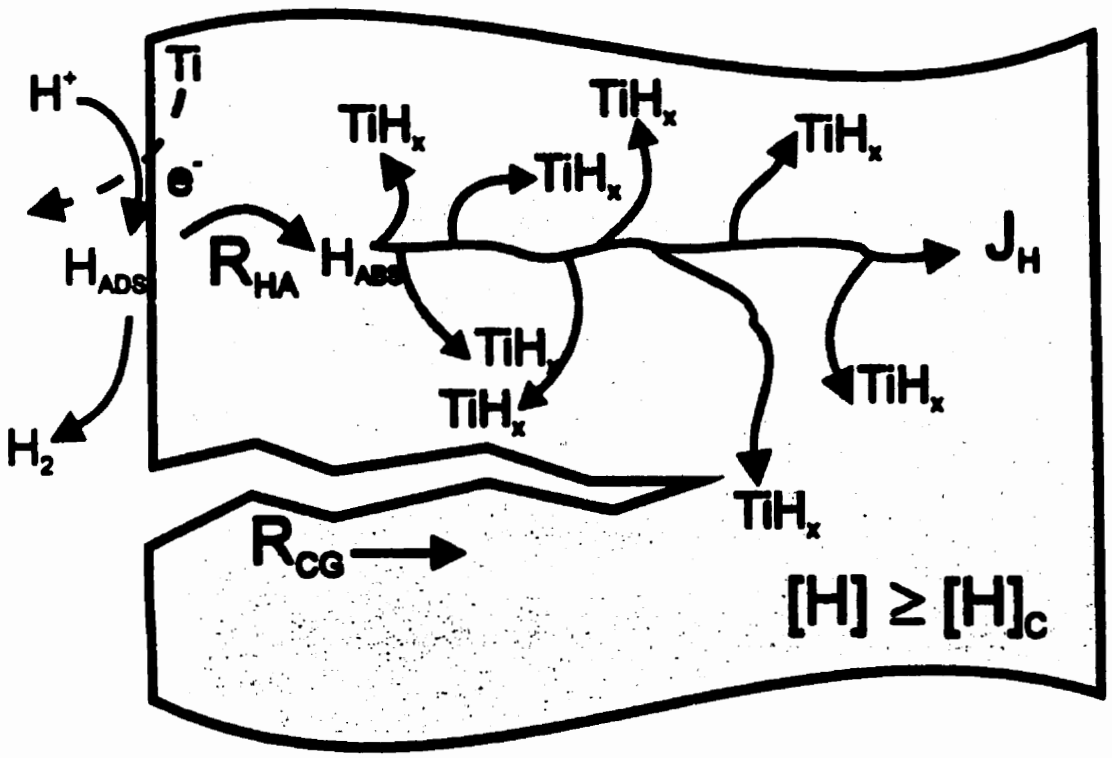

Figure 1.4.1-a The relationship between the critical parameters that determine when HIC could occur: the critical hydrogen concentration ($[H]_C$), the rate of hydrogen absorption into the metal (R_{HA}), and the rate of redistribution of hydrogen within the metal (J_H). Also shown is the rate of crack growth (R_{CG}), although cracking is expected to be relatively fast once $[H] \geq [H]_C$.

focuses mainly on hydrogen absorption, since this is a project on Ti electrochemistry; hydrogen absorption from aqueous solution involves the electrochemical reactivity of the surface and can be probed using electrochemical methods. Industrially, hydrogen absorption is expressed as the hydrogen uptake efficiency, also called the hydrogen absorption efficiency. This quantity can be defined as the fraction of the electrolytically produced hydrogen that is absorbed into the metal, expressed as a percentage.

Since the hydrogen that is absorbed during corrosion or cathodic polarization is of electrochemical origin, it would be useful to discuss the mechanism by which it is produced. Hydrogen evolution in acidic solutions is accomplished by the reduction of hydronium ions or protons following the reaction scheme

$$H_3O^+_{(aq)} + e^- \rightarrow H_{(ads)} \qquad \textbf{1.4.1-a}$$

$$H_{(ads)} + H_3O^+_{(aq)} + e^- \rightarrow H_{2(g)} \uparrow \qquad \textbf{1.4.1-b}$$

$$2H_{(ads)} \rightarrow H_{2(g)} \uparrow \qquad \textbf{1.4.1-c}$$

where $H_{(ads)}$ refers to a surface-adsorbed hydrogen atom. This is known as the hydrogen evolution reaction (HER), *the* most well-studied electrochemical reaction scheme [10] and the stuff of standard electrochemical textbooks [12, 99].

Hydrogen gas evolution consists of the "discharge" (Volmer) reaction (equation 1.4.1-a), followed by either the "electrodic-discharge" (Heyrovsky) reaction (equation 1.4.1-b), or the "recombination" (Tafel) reaction (equation 1.4.1-c) [12, 99]. According to Kelly [10], diagnosing the favoured reaction pathway and rate-determining step (RDS) of the HER on a particular type of metal surface is largely accomplished by determining the value of

the cathodic Tafel slope[1,2] and the reaction order with respect to proton activity at a constant potential[3], as well as other less-prominent diagnostic criteria. Bockris and Reddy [12] point out, however, that the reaction order, while often a good criterion for determining reaction mechanisms, is not generally very helpful in determining the mechanism of a HER, since many of the possible mechanistic paths and rate-determining steps predict the same dependence of the current density on the hydrogen ion concentration. A similar argument could be made in the case of the Tafel slope (see Table 1.4.1-a). The parameters in Table 1.4.1-a indicate how the favoured mechanism and RDS relate to the measured values of the Tafel slope [12]. The details of these diagnoses are well-presented elsewhere [12, 99], but have not proven as simply applicable to Ti [10] as they have to metals such as Pt, Ni, Hg and many others [12].

Concluding that the mechanism of the HER on Ti requires further investigation, Kelly [10] noted that the relative lack of information on the HER on Ti is not the result of disinterest by electrochemists, but stems from the fact that, in Kelly's words, "... this reaction has proven in the past to be singularly unyielding to the onslaughts of competent

---

[1] The Tafel slope is the slope of a plot of electrode potential (E) versus the logarithm of the current density (I) at a constant pH (*i.e.*, $\left(\frac{\partial E}{\partial(\log(I))}\right)_{pH}$).

[2] Alternatively, one could use the value of the transfer coefficient (α), which is related to the Tafel slope (b) by

$$b = \frac{-2.303RT}{\alpha nF}$$

where n is the number of electrons in the reaction, F Faraday's constant, R the gas constant, and T the absolute temperature.

[3] This is given by $\left(\frac{\partial(\log(I))}{\partial pH}\right)_E$

investigators." The apparent difficulty in verifying the mechanism and RDS of the HER on Ti results from uncertainty in the measured values of the cathodic Tafel slope and reaction order with respect to proton activity, which were found to vary between -0.060 V·decade^{-1} and -0.180 V·decade^{-1}, and between 0.6 and 1, respectively [10].

Table 1.4.1-a Diagnostic Criteria Used to Determine the Favoured Mechanism and RDS of the HER

Mechanism	Tafel Slope[a] (V·decade^{-1})
Volmer reaction RDS, followed by Tafel reaction	0.118
Volmer reaction, followed by Tafel reaction RDS	0.030
Coupled rate control by Volmer and Tafel reactions	0.118
Volmer reaction RDS, followed by Heyrovsky reaction	0.118
Volmer reaction, followed by Heyrovsky reaction RDS	0.039
Coupled rate control by Volmer and Heyrovsky reactions	0.118

[a] Assuming a symmetry factor $\beta = 0.5$.

A fourth reaction involving hydrogen on Ti is the hydrogen absorption reaction (HAR) [162, 163]:

$$H_{(ads)} \rightarrow H_{(abs)} \qquad \textbf{1.4.1-d}$$

The HAR occurs simultaneous with the HER, consuming adsorbed hydrogen atoms produced by the Volmer reaction (equation 1.4.1-a). In so doing, it must compete with the Heyrovsky (equation 1.4.1-b) and Tafel (equation 1.4.1-c) reactions for the supply of adsorbed hydrogen atoms, thereby possibly influencing the apparent kinetics of the HER, a possibility not noted by Kelly [10]. As more and more hydrogen is absorbed by the metal, another effect that could influence the HER kinetics is a change in the nature of the

substrate, that is, the test electrode evolves from metallic Ti to titanium hydride phases, TiH_x. The presence of an oxide film, as a phase oxide or adsorbed monolayer species, would also affect the HER kinetics [164].

1.4.2 Factors influencing hydrogen absorption

Hydrogen absorption by Ti may be influenced by a number of environmental and materials factors, including the pH, temperature, electrolyte solution composition, electrochemical potential, cathodic current density, polarization time, metal surface condition, and alloy composition. The effects of each are summarized briefly in the sections that follow; they have also been the subject of short reviews by Shimogori [159, 165]. Industrially, hydrogen absorption is expressed as the hydrogen uptake efficiency or hydrogen absorption efficiency. This quantity can be defined as the fraction of the hydrogen produced at the metal surface that is absorbed into the metal, expressed as a percentage.

1.4.2.1 pH

Passive Ti-2 has a poor hydrogen absorption efficiency [40, 166], largely due to the performance of the oxide film as a hydrogen barrier; in neutral solutions no measurable hydrogen absorption occurs except when very negative potentials are applied (*e.g.*, during excessive cathodic protection or as a result of galvanic coupling to an active metal such as carbon steel). Hydrogen absorption is prevented in industrial situations by avoiding cathodic protection potentials below about -1 V and by electrically isolating dissimilar metals [40, 159].

Active Ti, on the other hand, *does* absorb easily measurable amounts of hydrogen. For example, hydrogen precipitated as hydride needles can be seen by optical microscopy below the surface of crevice-corroded Ti coupons [161, 167]. Although hydrogen absorption occurs readily under the acidic conditions developed within crevices during crevice corrosion, Clarke *et al.* [161] have suggested that during rapid crevice corrosion attack the dissolution of metal and hydride from the crevice interior may occur faster than the accumulation of sufficient hydrogen for embrittlement of the material. However, they also concluded that hydrogen uptake during crevice corrosion might be important if the corrosion process was slow relative to the hydrogen absorption process.

Hydrogen absorption by Ti under acidic conditions has been quantified by many researchers [51, 160, 162, 168-170]. In these studies, hydrogen was generated electrolytically at a Ti electrode exposed to solutions at various pH values, and the amount of hydrogen absorbed by the metal was measured. From a knowledge of the total charge passed and the amount of absorbed hydrogen measured at the end of the tests, average hydrogen absorption efficiencies could be calculated. The hydrogen absorption efficiency decreased dramatically with increasing pH on pure Ti specimens[1] [159, 160, 162, 169]. For pH 1 solutions at room temperature, average hydrogen absorption efficiencies of 7-24% [51, 162, 169] were observed. These values declined rapidly to < 5% at pH 2 and above [162, 169].

A number of explanations for this pH dependence have been put forth. Shimogori [159] pointed out that the quantity of hydrogen produced per unit of charge passed is not

[1] Surface contamination and alloying effects are described separately in Section 1.4.2.6

thought to depend on pH in deaerated solution. Therefore, the change in efficiency must be limited to changes in the factors that determine whether or not the hydrogen produced is absorbed or evolved as gas. Shimogori offered that the mechanism of the hydrogen reactions changes with pH, but did not suggest in what ways. Okada [162] proposed that the absorption efficiency was related to the surface coverage by H_{ads} (θ_H), with absorption rates increasing with increasing θ_H. The value of θ_H would be strongly affected by any oxide layer present on the surface; the nature of the oxide present would also be highly dependent on pH. Other authors [171, 172] have proposed that two different forms of adsorbed hydrogen exist, one of which participates in the HER and the other of which favours the HAR.

Foroulis [160] also observed changes in the morphology of the Ti hydride phase with changing pH. In acidic solutions, the hydride formed in a continuous layer across the metal surface, whereas in mildly alkaline solutions only isolated patches of hydride were detectable, with most of the surface remaining free of hydride.

1.4.2.2 Temperature

Okada [162] found that temperature did not influence the hydrogen efficiency on pure Ti, while Phillips *et al.* [170] observed a clear increase in absorption efficiency with increasing temperatures. Okada [162] did see an increase in hydrogen absorption efficiency with temperature on Ni-modified Ti, however. Accelerated diffusion of hydrogen in the metal at higher temperatures was thought to play a role in the increased absorption efficiencies [159, 162, 170].

1.4.2.3 Electrolyte solution composition

Species that are known to influence the hydrogen absorption efficiencies of Ti can be divided into two classes: oxidants and "promoters". Oxidants (other than hydronium) present in solution tend to reduce the apparent hydrogen absorption efficiency by consuming electrons that might have gone toward hydrogen reduction [159, 165, 173] or by passivating the Ti surface, making hydrogen penetration more difficult [165].

A number of species, in particular certain compounds containing elements from Groups V and VI of the periodic table, have been found to increase the efficiency for hydrogen absorption by Ti [160]. Their activity in enhancing hydrogen absorption on Fe under cathodic polarization had previously been noted. Because of this action, they have been dubbed "promoters". The list of promoters for Ti includes SH^-, pyrophosphate ($P_2O_7^{4-}$), AsO_2^-, SbO_2^- [160], and $Fe(OH)_2$ [165]. The strongest of these appears to be $P_2O_7^{4-}$; hydrogen absorption by Ti cathodically polarized at 10 $mA \cdot cm^{-2}$ was increased by ~300% in 0.05 $mol \cdot dm^{-3}$ H_2SO_4 solution when 3.1×10^{-3} $mol \cdot dm^{-3}$ $Na_4P_2O_7$ was present [160].

The mechanism by which promoters function to enhance the hydrogen absorption efficiency is uncertain, as is the form of the surface-adsorbed species actually responsible for the phenomenon. Several ideas have been put forth [160]: that the promoter increases the Ti-H adsorption bond strength, thereby increasing θ_H and the hydrogen absorption efficiency; that the hydrogen entry step is facilitated by prior formation of a bond between the hydrogen atom and the promoter species; or that the promoter species inhibits the Tafel reaction (equation 1.4.1-c), resulting in a higher value of θ_H. $Fe(OH)_2$ was

hypothesized to promote hydrogen absorption by generating hydrogen at the metal surface via the Schikorr reaction,

$$3Fe(OH)_2 \rightarrow Fe_3O_4 + 2H_2O + H_2 \qquad \textbf{(1.4.2.3-a)}$$

or by lowering the value of E_{oc} [165, 167] (see Section 1.4.2.4).

Hydrogen absorption is also enhanced by the presence of dispersed sand or dissolved chlorine gas [173]. These two were thought to act by thinning the passive film -mechanically, in the case of the sand, and by lowering the pH via the disproportionation reaction,

$$Cl_2 + OH^- \rightarrow Cl^- + HClO \qquad \textbf{(1.4.2.3-b)}$$

in the case of chlorine.

1.4.2.4 Electrochemical potential

It has been widely recognized [40, 78, 148, 159, 165, 167, 173] from empirical observation that a threshold potential for hydrogen absorption by Ti seems to exist at around -0.6 to -0.9 V, even though the HER proceeds at much more noble potentials. Significant hydrogen damage generally occurs only when the metal experiences sustained exposure at potentials below about -1 V. Therefore, the range -0.6 to -1 V is considered the practical lower potential limit for cathodic protection of metals in contact with Ti in industrial applications [40, 159].

It has been suggested [173] that a surface oxide layer (that exists even in acidic solution at potentials in the range -0.6 to -0.9 V [10]) prevents hydrogen absorption by Ti at potentials above the threshold potential. At potentials below the threshold (which are

also below the flatband potential, $E_{fb} = -0.54$ V [130]), band bending within the semiconducting oxide leads to electronic degeneracy at the oxide surface. Degeneracy seems to be accompanied by chemical changes in the oxide, as hydrogen penetrates the oxide, eventually entering the metal [130, 131, 148-150] (see also Section 1.3.5).

1.4.2.5 Cathodic current density and polarization time

Papers by Okada [162] and Phillips *et al.* [169] both reported that the hydrogen absorption efficiency of Ti decreased with increasing cathodic current density, although the *rate* of hydrogen absorption increased. Okada [162, 168] offered an explanation based on the competition for H_{ads} between the HER and the HAR. Calculating the dependence of each on θ_H, Okada showed that the rate of the HER increases more rapidly with increasing θ_H than does that of the HAR. Therefore, at higher cathodic current densities, when θ_H is higher, the hydrogen absorption efficiency would be expected to decrease, even though the *rate* of hydrogen absorption would increase.

The hydrogen absorption efficiency appeared to be constant with time at a given applied current density initially (for > 6 h [169] or > 14 C [162]), but eventually decreased with time on pure Ti [169]. Such an initial period of constant absorption efficiency was not observed on Ni-modified Ti, which showed a very high, but decreasing efficiency for hydrogen absorption, even after short charging periods [162]. Phillips *et al.* [169] suggested that the initial stage corresponded to the formation of a uniform layer of hydride below the electrode surface and the development of an equilibrium hydrogen concentration gradient in the hydride layer. The second stage, in which the hydrogen absorption rate decreased parabolically with time, was attributed to rate-control of the

HAR by diffusion of hydrogen through the existing hydride layer, leading to thickening at its inner boundary. This proposal was supported by the observation that the surface hydride layer thickness was directly proportional to the square root of the polarization time. A diffusion coefficient, D, for hydrogen diffusion in the surface hydride was determined, including its temperature dependence in the range 25-100°C [170]:

$$D = 6 \times 10^{-2} \exp\left(\frac{-14400 \pm 800}{RT}\right) \qquad \textbf{(1.4.2.5-a)}$$

where D is in units of $cm^2 \cdot s^{-1}$, R = 1.987 $cal \cdot mol^{-1} \cdot K^{-1}$, and T is the absolute temperature in Kelvins. At 25°C this corresponds to D = 1.6×10^{-12} $cm^2 \cdot s^{-1}$, slightly lower than the value of 4×10^{-12} $cm^2 \cdot s^{-1}$ reported in an earlier paper by the same authors [169].

Phillips *et al.* [169] also suggested that, due to the establishment of an equilibrium concentration gradient, the average H:Ti ratio in the hydride layer (*i.e.*, the mean composition) should remain constant with time but increase with increasing cathodic current density. Their measurements, which show an increase in the average H:Ti ratio in the hydride from 1.21 at a current density of 0.1 $mA \cdot cm^{-2}$ to 1.48 at 3.0 $mA \cdot cm^{-2}$, support this idea.

1.4.2.6 Metal surface condition and alloy composition

The surface condition of the metal has a very strong influence on the absorption of hydrogen by Ti [159, 165, 170]. This influence appears to come from two sources, namely the quality of the surface oxide film and the contamination of the surface oxide film with foreign metals. The latter effect is closely related to the influence of alloying constituents.

The dependence of the hydrogen absorption efficiency on the quality of the oxide film present on Ti is in keeping with its roll as a barrier to hydrogen penetration. Freshly abraded Ti surfaces absorb hydrogen most readily while vacuum-annealed and pickled surfaces have much lower absorption efficiencies [165, 170]. These rankings are maintained across the entire pH range from 0.3 to 13 [170], an observation that supports the suggestion that Ti is always covered by an oxide layer [10]. While differences in surface roughness, and therefore true surface area, on electrodes prepared by different treatments could change the apparent hydrogen absorption efficiency, the magnitude of the observed changes could not be explained solely in terms of variations in the true surface area [170].

Ageing abraded surfaces in air at room temperature decreases the hydrogen absorption efficiency and the absorption efficiency decreases with increased ageing time [170]. This observation is consistent with the results of Andreeva [71], who showed that the air-formed oxide film on Ti thickens with time over an extended period of air-exposure at room temperature. In addition to film thickening, air exposure is also thought to repair defects in the passive oxide layer [170]. Anodic oxides and high-temperature air oxidation films also effectively inhibit hydrogen absorption by Ti [159]. Air oxidation films are more effective at preventing hydrogen absorption in acidic solutions than are anodic oxides, since the latter are less resistant than the former to dissolution in acid [159].

Empirical evidence has demonstrated that the presence of foreign metal contaminants on Ti surfaces tends to enhance the hydrogen absorption efficiency and rate [165, 168, 170],

although some metals also act as inhibitors of hydrogen absorption [73, 168]. The most common foreign metal surface contaminant appears to be Fe, which finds its way onto Ti surfaces when they are contacted by Fe or steel tools [159, 165]. Contaminant Fe greatly enhances hydrogen absorption by Ti as does Pt, while Cu has little or no effect [159, 165]. Anodization or pickling were found to restore the hydrogen absorption resistance of Fe-contaminated Ti surfaces by oxidizing and dissolving the contaminant [159, 165].

A different influence of surface "contaminant" metals was found in experiments involving Ti surfaces onto which had been deposited a complete layer of foreign metal atoms [162, 168]. In this case, Pb inhibited hydrogen absorption, while Au, Ni, Fe, and Cu increased the hydrogen absorption efficiency[1]. These observations were explained in terms of the ability of d-metals such as Au, Fe, Cu, and Ni to absorb hydrogen themselves, and transmit it to the underlying Ti, and the resistance of sp-metals (Pb in this case) to hydrogen uptake [168]. Au was also noted to have prevented the formation of an absorption-inhibiting oxide film.

Pt-modified Ti displayed very strange hydrogen absorption behaviour [162, 168]. At pH 0.3 its hydrogen absorption efficiency was less than that of unmodified Ti, but it became greater than the latter at pH > 1 [162]. Furthermore, the absorption efficiency of Pt-modified Ti peaked at > 40% at ~pH 2 before declining to < 5% above pH 3. In discussing this unusual behaviour, Okada [162] invoked an explanation involving a pathway for the HER that does not include the Volmer reaction (equation 1.4.1-a):

[1] For example, the hydrogen absorption efficiency at pH 1 for Ni-modified Ti was 60%, compared to ~10% for unmodified Ti [162].

$$2H^+ + e^- \rightarrow H_2^+ \qquad \textbf{(1.4.2.6-a)}$$

$$H_2^+ + e^- \rightarrow H_{2(g)} \uparrow \qquad \textbf{(1.4.2.6-b)}$$

It was proposed that this pathway, which does not produce the H_{ads} required for the HAR (equation 1.4.1-d), dominates at low pH, with the Volmer reaction (and therefore θ_H) increasing in importance at higher pH. At even higher pH values, the low availability of H^+ causes θ_H to decline again. This would produce a maximum in a plot of the hydrogen absorption efficiency as a function of pH.

Alloying Ti with Pd or Ni increases the hydrogen absorption efficiency [40, 159, 165], although using Ti-Pd or Ti-Ni alloys can reduce the incidence of hydrogen damage under free corrosion conditions (as opposed to polarized conditions) since the corrosion rate on these alloys, and therefore the absolute amount of hydrogen produced, is much lower than on unalloyed Ti [40, 159]. In strange contrast to its enhancement of hydrogen absorption when present as a surface contaminant, Fe was reported to have almost no effect when present as an alloy constituent [165]. No explanation was offered for this behaviour.

2. Experimental

2.1 Principles of selected techniques

As a prelude to the detailed experimental procedure, this first part of the Experimental Section is meant to provide a basic outline of the principles of several techniques that are important to the project, but perhaps not well known to the reader. The descriptions that follow are intended to enhance understanding of the results obtained and their interpretation, not to offer an exhaustive exploration of the techniques themselves, since these were not developed, only employed, during completion of this project. A number of other techniques were also used in this work, but further background and theoretical descriptions of these were deemed unnecessary.

2.1.1 Open circuit potential measurements

The open circuit potential, E_{oc}, is the measured potential difference between the working electrode and the reference electrode, with the counter electrode at open circuit, that is, without any net external current applied to the system. Also called the (free) corrosion potential of the working electrode, *the value of* E_{oc} *indicates the electrode potential at the balance point where the sum of the partial currents from all anodic and cathodic half-reactions occurring on the electrode surface is zero.* The establishment of E_{oc} is therefore a manifestation of the law of conservation of charge. This is NOT an equilibrium potential, except in very specific situations (*i.e.*, systems at equilibrium). Corroding systems are *not* at equilibrium (otherwise no corrosion would occur) and considerable net chemical conversion at (sometimes) very high rates can occur at

$E = E_{oc}$. The value of E_{oc} relative to the reversible potentials of the relevant anodic and cathodic half-reactions can sometimes give an indication of the balance in kinetics between these two.

The value of E_{oc} is a diagnostic indicator of limited use. It is determined by the types and concentrations of redox species available and the reactivity of the electrode surface toward these species, variables that are often not precisely known. In these experiments, E_{oc} is therefore most useful as a qualitative factor for comparisons between similar experiments, especially to indicate whether a reproducible set of conditions had been achieved prior to starting another type of experiment (EIS, XPS, *etc.*). Figure 2.1.1-a illustrates schematically, for three arbitrary concentrations of the oxidant species, how E_{oc} is established from the combination of all redox reactions occurring on the surface, determines the corrosion current, I_{corr} (which is directly proportional to the corrosion rate), and differs from the reversible potential, E_{rev}.

2.1.2 X-ray photoelectron spectroscopy

XPS measurements on different Ti alloys were undertaken to evaluate the composition of the passive film on each specimen after exposure to 0.27 mol·dm^{-3} NaCl solutions at a series of different temperatures. The principle behind XPS is described briefly here, but more extensive references are available [174, 175].

This technique involves bombarding the sample surface, in vacuum, with X-rays that ionize atoms, or further ionize ions, within the sample. The ionizations in question are normally those that remove an electron from a core energy level in the atom or ion (as

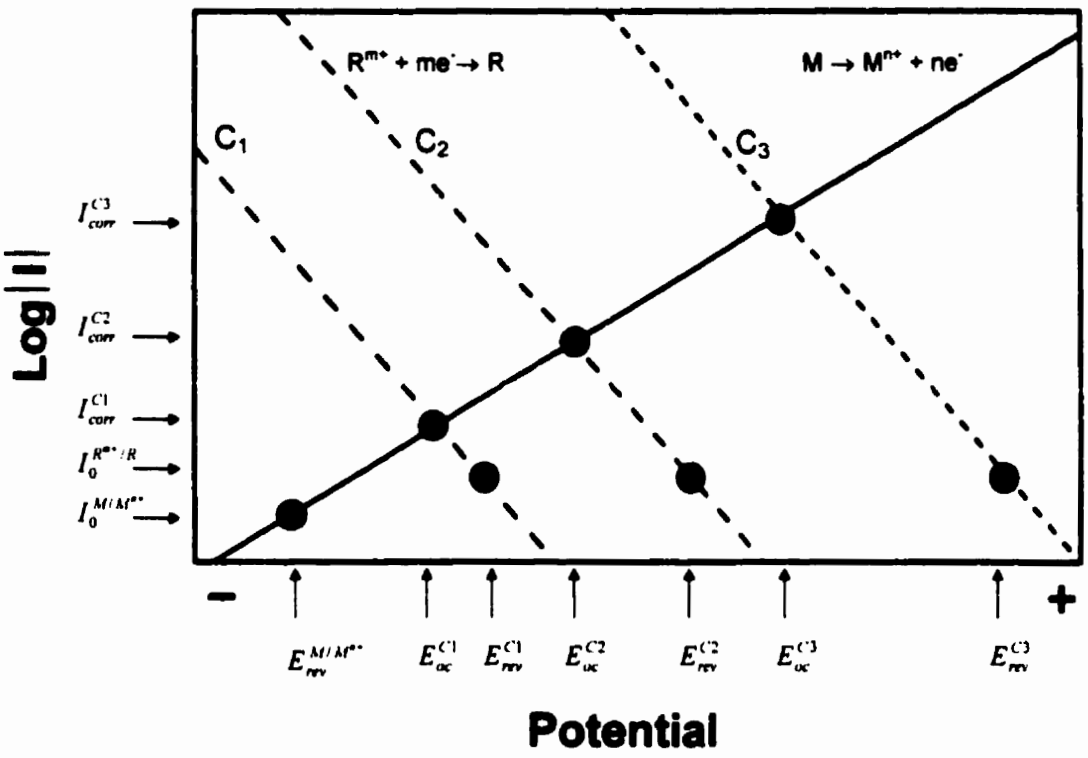

Figure 2.1.1-a Schematic illustration of how the value of E_{oc} is established by the combination of redox reactions occuring on the surface. The solid line represents the partial current due to metal oxidation and the dashed lines represent that due to reduction of an oxidant, R^{m+}. The three dashed lines represent three different concentrations of R^{m+}: $C1 < C2 < C3$. Assuming the exchange current density for the oxidant, $I_0^{R^{m+}/R}$, is constant, each concentration of R^{m+} generates a different value of E_{oc}, E_{rev}, and the corrosion current, I_{corr}.

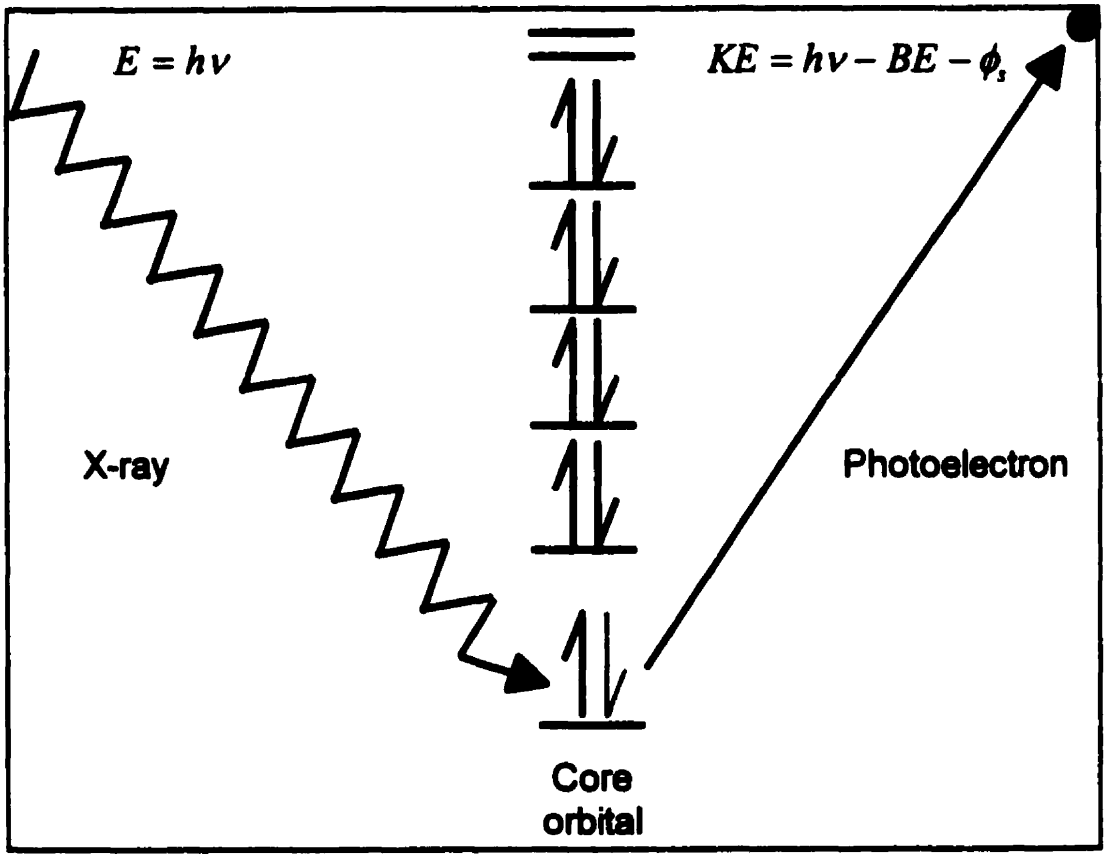

Figure 2.1.2-a Photoelectron generation process in XPS. The kinetic energy (KE) of the emitted photoelectron is the difference between the ionizing photon energy (hν) and the binding energy of the electron in the core orbital (BE), less the work function of the surface, ϕ_s.

opposed to a valence electron). The energy required to do this, called the binding energy (BE), is characteristic of the type (atomic number) of atom ionized *as well as its chemical environment*. Since the X-rays used to generate the photoelectrons are monochromatic (*i.e.*, of a single, known energy), the BE can be determined from the difference between the energy of the impinging X-rays ($h\nu$) and the resulting kinetic energy of the ejected photoelectrons (KE), less the surface work function (ϕ_s) (see Figure 2.1.2-a). Comparison of the measured BE values with standard spectra [175], in combination with curve-fitting procedures, reveals the sample's chemical composition.

Although X-rays penetrate the sample surface to a depth of 1-10 μm, XPS is a highly surface-sensitive technique, since the kinetic energy of the photoelectrons is low and therefore their maximum escape depth (without energy loss), determined by their "inelastic mean free path" in the sample, is very small (<60 Å [175]). The depth probed by XPS also depends on the angle between the sample surface and the electron energy analyzer, again because of the limited electron escape depth. Photoelectrons emitted from deeper within the sample have much less likelihood of escaping at shallow angles than at high angles because the path length through the sample is greater at shallow angles.

2.1.3 Electrochemical impedance spectroscopy

EIS treats electrochemical systems as electrical circuits (which they are) and represents them in terms of a network of passive circuit elements such as resistors, capacitors, and inductors. In this technique, a fluctuating voltage or current perturbation is applied to an electrochemical system, the corresponding current or potential response measured, and the transfer function relating the perturbation and response determined, as a function of

the perturbation frequency. In the special case when the system is linear, stable, causal and finite, the transfer function is the system impedance in the representation

$$E(\omega) = I(\omega)Z(\omega) \qquad \textbf{2.1.3-a}$$

where ω is the angular frequency, E the potential, I the current and Z the transfer function (*i.e.*, impedance) [176]. This is a more general, frequency-domain expression of the well-known Ohm's Law [8],

$$E = IR_a \qquad \textbf{2.1.3-b}$$

where R_a is the apparent d.c. resistance. Equation 2.1.3-a, however, takes into account the frequency dependence of the impedance. Thus, the perturbation and response signals may differ by both an amplitude change and a phase shift. Equally, one can treat the transfer function as a tensor having real (in phase) and imaginary (out-of-phase) components.

Current-potential relationships of interest in electrochemistry are not normally linear. In fact, they are usually exponential, according to the Butler-Volmer equation [177],

$$I = nFAk^0\left[C_O(0,t)\exp\left(-\frac{\alpha nF}{RT}\left(E - E^{0'}\right)\right) - C_R(0,t)\exp\left(\frac{(1-\alpha)nF}{RT}\left(E - E^{0'}\right)\right)\right] \qquad \textbf{2.1.3-c}$$

where n is the number of equivalents of electrons, F Faraday's constant, A the surface area, k^0 the standard rate constant, α the transfer coefficient, R the gas constant, $E^{0'}$ the formal potential, and $C_O(0,t)$ and $C_R(0,t)$ the concentrations of oxidant and reductant, respectively, at the electrode surface at any time, t. However, for small

changes in potential, ΔE, the change in the current, ΔI, is nearly proportional to ΔE. Thus, an electrochemical system can be made to appear approximately linear for the purpose of EIS by using a small-amplitude perturbation signal. Although small perturbations often result in small response signals, the precision of impedance measurements can be improved by signal averaging over long[1] time periods.

EIS has also been called "a.c. impedance", however this is somewhat of a misnomer because, in addition to sinusoidally varying alternating currents, many other types of stimuli (such as single step functions and white noise) have been used to determine electrochemical impedances [178]. EIS measurements, like the diagnostic impedance measurements made on electrical circuits, allow one to build a representation of the electronic pathways present in the electrochemical system in terms of individual passive circuit elements, such as resistors, capacitors, inductors, *etc.* In EIS, one attempts not only to define an adequate network of circuit elements to represent the current-potential transfer function, but also to assign physical significance to these elements. For example, an apparent resistance to current flow in an electrochemical system may arise due to the presence of a poorly-conductive passive film on an electrode, and an apparent capacitance may be the symptom of a chargeable interface, such as the electrochemical double layer.

EIS measurements can be used to determine interfacial parameters (such as reaction rates and rate constants, interfacial capacitances, diffusion coefficients, and reaction mechanisms) and materials properties (such as conductivity, dielectric constants, film thicknesses, charge-carrier mobilities, and charge-carrier generation or recombination

[1] Long relative to the period of the perturbation.

rates) [176]. Many of these properties can be evaluated using other "conventional" electrochemical techniques (such as cyclic voltammetry, potential or current step experiments, or steady-state polarization methods), but these generally require that the system be driven far from the natural corrosion conditions, to extreme conditions that may irreversibly change the system under study. By contrast, EIS is (often) a non-destructive technique that is easy to automate[1]. It can be used effectively in low-conductivity electrolytes since the electrolyte resistance simply adds an easily measurable resistive component in series with the rest of the system response. This feature alone gives EIS a major advantage over other electrochemical techniques, in which the electrolyte resistance is not so easily deconvoluted from the desired signal.

Interpretation of EIS data must be done with caution, since it involves fitting a model with a changeable number of adjustable parameters to the data. With this type of procedure, there exist an infinite number of solutions that would fit the data equally well. Therefore the model must be limited to the bare minimum number of adjustable parameters. All of these must make reasonable chemical and physical sense, and independent complementary information should be used to supplement EIS data.

2.1.4 Neutron reflectometry

Neutron reflectometry is a small-angle neutron scattering technique based on specularly reflected neutrons[2]. It benefits from the relative ease with which neutrons can pass

[1] Unfortunately, this also makes it easy to collect meaningless data, especially if the conditions of linearity, causality, and stability, are not satisfied.

[2] This implies elastically scattered neutrons, reflected from the sample surface at an angle θ_r equal to the angle of incidence, θ_i.

through many types of solid matter. Reflection of a highly collimated thermal neutron beam from a flat sample occurs at the sample surface and at other interfaces within the sample, since, in the absence of total external reflection, part of the beam is reflected and part transmitted at each interface present within the sample. Specular reflection is virtually limited to atoms close to the interfaces, making neutron reflectometry a surface-sensitive, rather than a bulk, technique, but one that is different from most other surface-sensitive techniques in that it probes *each surface within the sample, not just the outermost one.*

The reflectometry experiment involves measuring the reflected intensity of the neutron beam as a function of the scattering vector, Q. The scattering vector is the difference between the incident neutron wavevector and the reflected neutron wavevector, and is related to the scattering angle ($\theta = \theta_i = \theta_f$) by [108]

$$Q = \frac{4\pi \sin(\theta)}{\lambda} \qquad \textbf{2.1.4-a}$$

where λ is the de Broglie wavelength of the neutrons. For each medium, there exists a critically small value of Q, denoted Q_c, below which total external reflection occurs; that is, all neutrons are reflected from the surface of the medium and none pass through. The value of Q_c is dependent on the scattering length density (SLD) of the medium, which is related to the medium's neutron refractive index. The SLD is determined by the product ρb (which may be a function of depth, z, into the sample, hence $\rho b(z)$), where ρ is the

number density of atomic nuclei[1] (per unit volume) and b is the coherent neutron scattering length, an empirically measured property of each isotope [179]. For media other than isotopically pure elements, the effective $\rho b(z)$ is the sum of ρb for all constituent nuclei at that particular depth. The value of Q_c is given by [107]:

$$Q_c^2 = 16\pi\rho b \qquad \textbf{2.1.4-b}$$

Since b may have either a positive or a negative value, Q_c may be either real or imaginary. If Q_c is real, then an angle θ_c exists at which total external reflection is observable. For media with imaginary Q_c, total external reflection is not observable; however Q_c may still be estimated from the reflected intensities[2]. Knowing Q_c and either ρ or b, one can determine the third parameter from Equation 2.1.4-b, thereby gleaning information about the sample composition or structure.

In the case where multiple interfaces are present within a sample, constructive and destructive interference between neutrons reflected from each interface generates an interference pattern[3] in the reflected beam (for $Q > Q_c$). Thus, as the angles[4] are changed during a neutron reflectometry scan, a series of interference minima is observed in the reflected intensity values. The layer thickness, d, within the sample (*i.e.*, the distance

---

[1] Neutron scattering results from neutron-nucleus interactions. X-ray scattering, which may be used in an analogous way for X-ray reflectometry [111], involves X-ray-electron interactions.

[2] Ti, TiH_x, and H_2O are among these materials.

[3] A manifestation of quantum mechanical effects.

[4] As the sample is rotated to change the incidence angle by an amount $\Delta\theta$, the detector must be moved by an angle $2\Delta\theta$ to capture the specularly reflected beam.

between adjacent reflective interfaces) can be determined from the interference pattern using the Bragg condition [146],

$$d = \frac{n_r \lambda}{2\sin(\theta)} \qquad \textbf{2.1.4-c}$$

where n_r is an integer that refers to the order of the interference minimum.

Since only specular reflectivity is measured, and the neutron beam footprint on the sample is large, the technique is unable to distinguish features distributed laterally across the sample surface. Instead, the sample must be flat and homogeneous in the lateral direction (x-y plane). The de Broglie wavelengths of thermal neutrons (a few Å) and their ability to pass through many bulk materials make them ideal for probing thin film and atomic-length structures (5 - 2000 Å) [107], with high resolution in the direction normal to the sample surface (z-direction). A few elements (such as boron) cannot be studied in this way by neutron reflectometry because of their high neutron absorption cross-sections.

2.2 Electrode materials

A number of different Ti materials were used for working electrode fabrication: high-purity Ti (AESAR, 99.99%), Grade-2 (TIMET, c.p. Ti), Grade-12 (TI Titanium, Ti-0.8Ni-0.3Mo[1]), Grade-16 (RMI Titanium, Ti-0.05Pd), and Ti-0.1Ru (RMI Titanium, special experimental ingot). For brevity, these will be referred to as high purity Ti, Ti-2, Ti-12, Ti-16, and Ti-0.1Ru, respectively. The composition of each material is given in

[1] In this style of notation, the number immediately preceding the symbol for each element indicates the nominal amount of that element specified for the alloy, expressed as a weight percent. Of course, with the exception of minor impurities, Ti makes up the balance of material.

Table 2.2-a. Figure 2.2-a displays photomicrographs showing the microstructure of each alloy. Sample surfaces were prepared for photomicrography by careful polishing and etching, following standard metallographic procedures [180]. All of these materials are categorized as α-alloys of Ti, with the exception of Ti-12, which is designated a near-α alloy because it contains small amounts of β-phase [40].

One can see from these photomicrographs that the grain size is rather large (> 100 μm) in the high purity Ti sample by comparison with the others. The grains in the Ti-2 sample are generally in the range of 20-50 μm, while those in the Ti-12 are smaller still. It is much more difficult to make out individual grains in the Ti-16 specimen, but they seem to be of similar size to those of the Ti-2. Many of the grain boundaries in this specimen are decorated with tiny black spots; these appear to be areas that were more aggressively attacked during metallographic etching than the rest of the surface. A possible explanation for their appearance is that they resulted from localized anodic attack during etching adjacent to the cathodes provided by even smaller noble metal precipitates present along the grain boundaries. The number density of such spots on the photomicrograph of the Ti-0.1Ru surface is much higher than on Ti-16. In this case they appear to run in oriented strings, but no underlying grain structure is apparent in the photo. This may indicate a much smaller grain size in this piece of Ti-0.1Ru. It is not a consequence of looking at the microstructure from a different orientation with respect to the rolling direction of the plate from which the sample was cut, since all of these surfaces show the rolling plane (except that of the high purity Ti, which came from rod rather than plate stock).

a)

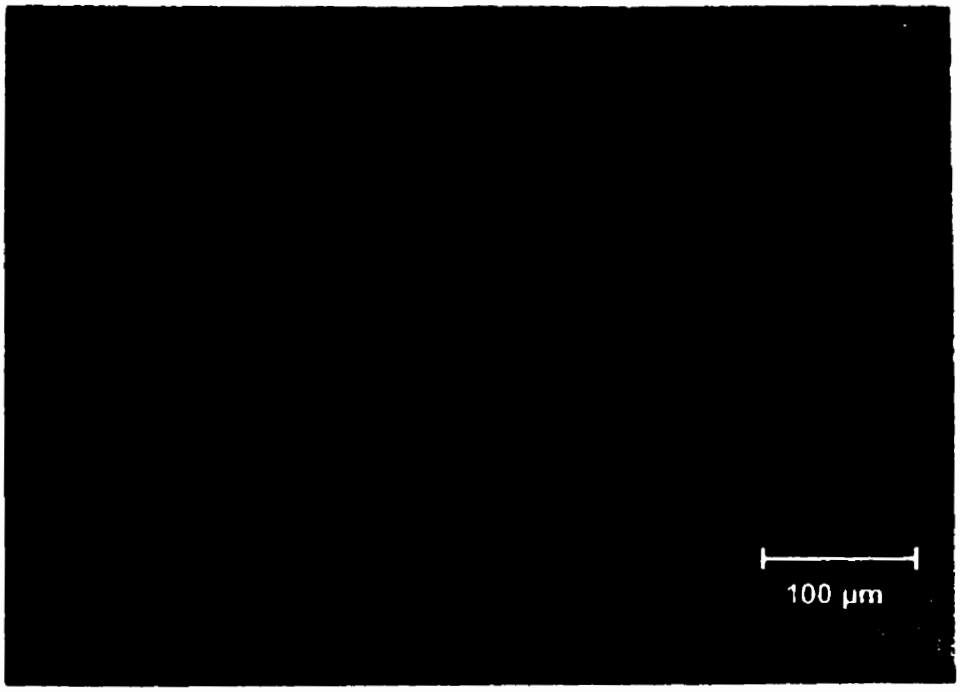

b)

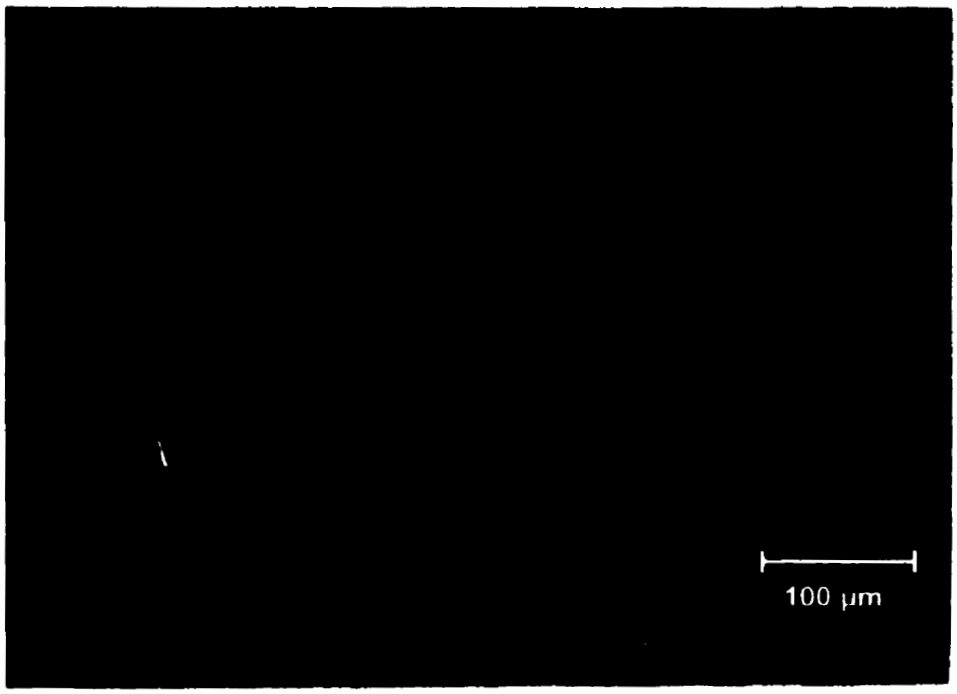

Figure 2.2-a Photomicrographs of polished surfaces of: a) high purity Ti, b) Ti-2,

c)

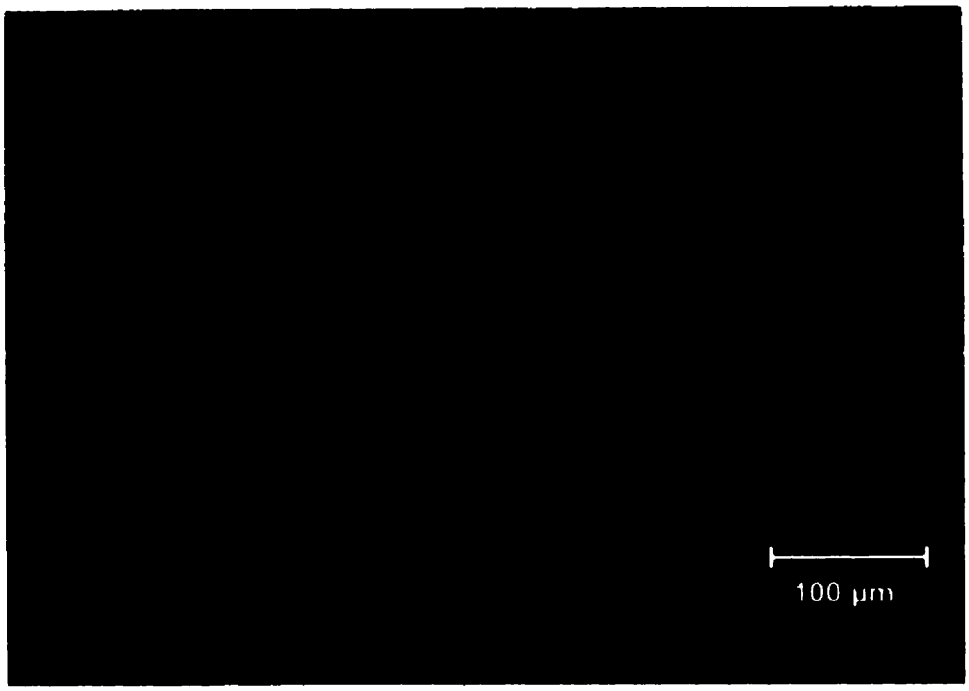

d)

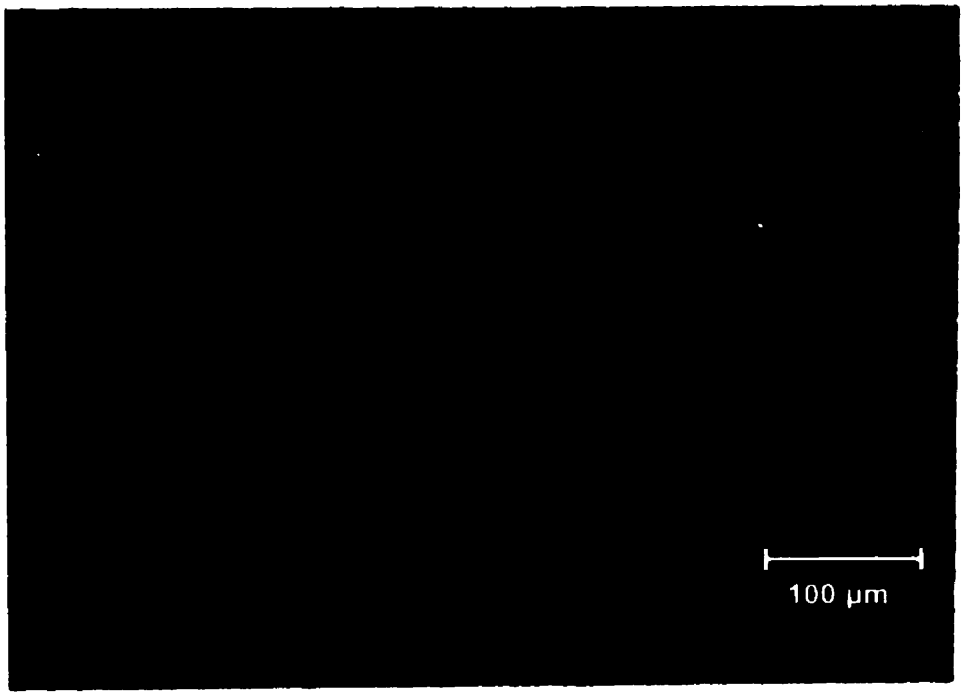

c) Ti-12, d) Ti-16,

e)

e) Ti-0.1Ru.

Table 2.2-a Compositions of Ti Alloys Used as Electrode Materials

Element	High purity Ti (%)	Ti-2 (μg/g)	Ti-12 (μg/g)	Ti-16 (μg/g)	Ti-0.1Ru (μg/g)
Al		ND[c]		<47[c]	1000[a]
C		220[a]	180[a]	100[a]	100[a]
Ca		85±8[c]			
Cr		ND[c]		50±30[c]	
Fe		1052±16[c]	1145±60[c]	925±40[c]	600[a]
H		50±2.6[c]	60[a]	25[a]	
Mn		68±8[c]			
Mo		ND[c]	2890[a]	<60[c]	
N		180[b]	125[b]	120[a]	150[a]
Ni		ND[c]	7330±370[c]	<60[c]	
O		1321[b]	1548[b]	1040[a]	700[a]
Pd				420[a]	
Ru		ND[c]			1000[a]
S		<20[c]			
Si		4925±60[c]			100[a]
Ti	99.99[d]	Balance	Balance	Balance	Balance

Sources of chemical analyses:
[a] Manufacturer's mill report.
[b] IBM Analytical Services, East Fishkill, NY.
[c] AECL Analytical Sciences Branch, Whiteshell Laboratories, Pinawa, MB.
[d] Alfa AESAR, Ward Hill, MA (metals basis analysis).

ND = element looked for but not detected in analysis.

2.3 Working electrodes

Four different forms of Ti electrodes were used in the different types of experiments reported in this Thesis: disk electrodes, crevice coupons, thin film electrodes, and hydrogen absorption coupons. Disk electrodes, 6 mm thick and 10 mm in diameter were cut from ¼-inch thick[1] plates of Ti-2, Ti-12, Ti-16, and Ti-0.1 Ru. High purity Ti disks of the above dimensions were machined from a 12.7 mm diameter rod. Each disk had a centred hole, 3 mm deep, on one circular face, tapped to accept a 3/48-threaded Ti

[1] Ti plate material is fabricated in the USA to dimensions reported in imperial units.

welding rod for suspension in the electrochemical cell and for electrical contact (see Figure 2.3.1-a). The welding rods were made of Grade-1 Ti. They were not analysed for composition, but the specifications for Grade-1 Ti welding rod [181] are given in Table 2.3-a. The welding rods did not generally contact the electrolyte solutions during experiments employing disk electrodes, except for experiments after which XPS analysis was performed (see Section 2.6.3).

Table 2.3-a Compositional Specifications for Grade-1 Ti Welding Rod [181].

Element	C	O	H	N	Fe	Ti
Amount (μg/g)	<300	<1000	<50	<150	<1000	Bal.

Crevice coupons were cut from ¼-inch thick plates of Ti-2 and Ti-12 and had nominal dimensions of 50 mm × 22 mm × 6 mm, with two 5 mm unthreaded bolt holes drilled completely through the 50 mm × 22 mm faces, one near either end, to enable assembly of artificially creviced electrodes (see Figure 2.3.1-b). Ti bolts and nuts were fabricated from the same plate materials as the crevice coupons to avoid any galvanic coupling due to dissimilar metal contact or surface cross-contamination due to different alloying constituents. The bolts were 35 mm long, threaded 10/24, and the nuts were 10 mm square, 6 mm thick, and tapped to fit the bolts (see Figure 2.3.1-c). Each bolt had a 5 mm deep, 3/48-tapped hole in one end to accept the Ti welding rod used to suspend the crevice assemblies in the electrochemical cell and to make electrical contact, as was done with the disk electrodes.

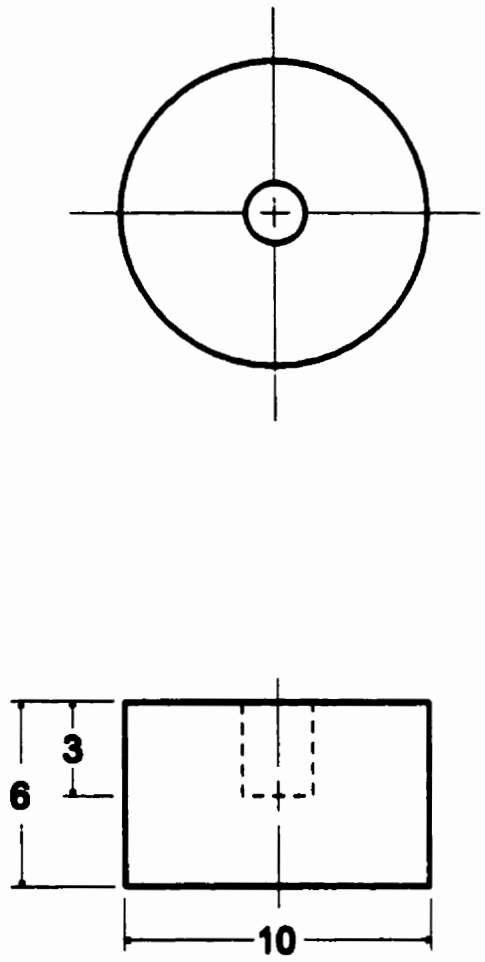

Figure 2.3.1-a Scale diagram of a disk electrode. Dimensions given in millimetres.

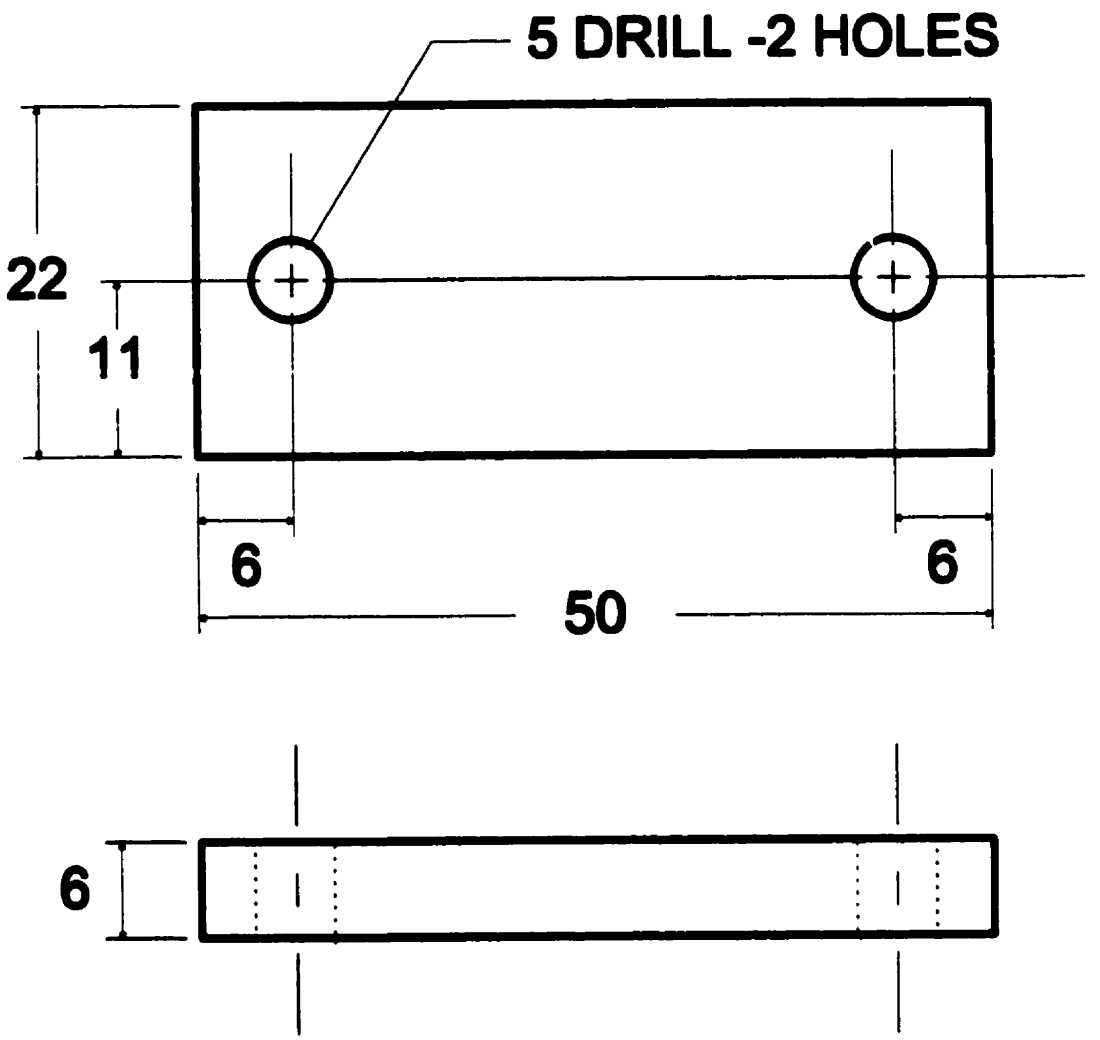

Figure 2.3.1-b Scale diagram of a crevice coupon. Dimensions in millimetres.

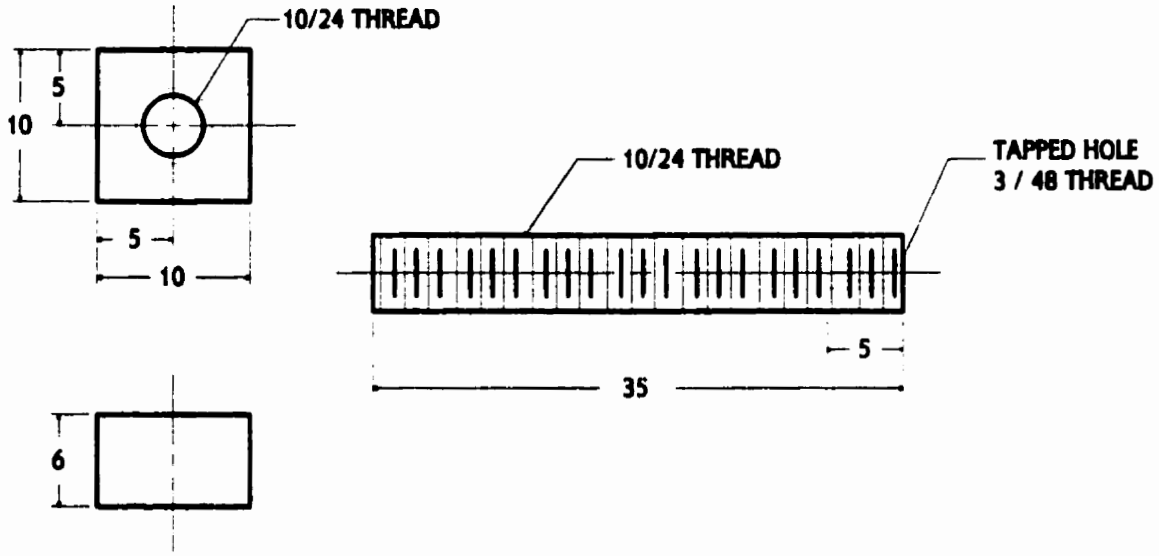

Figure 2.3.1-c Scale diagram of nut and bolt used in assembling artificial crevices. Dimensions in millimetres.

Thin film electrodes (prepared by Zaven Altounian, McGill University, Montreal) consisted of a Ti film (nominally 150 or 300 Å thick) sputter-deposited onto the polished (111) face of a ¼ inch[1] (6.35 mm) thick, 4 inch (100 mm) diameter, phosphorous-doped, single crystal Si slab (Semiconductor Processing Co.). Film deposition was carried out by sputtering Ti in a low-pressure Ar atmosphere (base pressure = 5×10^{-7} Torr) at a rate of 0.56 $Å \cdot s^{-1}$. No attempt was made to prevent air oxidation of the Ti film surface upon removal from the sputtering chamber.

The thin film electrodes were designed specifically to meet the requirements for neutron reflectometry experiments. Single crystal Si slabs provided an ideal substrate for this purpose for several reasons. Si is highly transparent to neutrons, and the single crystal has no internal grain boundaries (*i.e.*, unwanted interfaces that may scatter neutrons). Thus, a loss of only ~13% of the neutron flux was realized after the neutron beam passed through the entire 100 mm of Si. Since reflectometry only yields an averaged scattering length density in the plane of the reflecting interface, and is intended to measure nanometer-scale features perpendicular to that plane, it is crucial that the samples be as flat as possible. Fortuitously, large, flat, highly polished Si slabs from the electronics industry are readily available.

Highly doped slabs were used in order to minimize the electrical resistivity of the substrate, since electrical contact was not made on the metallic film surface but through the Si backing of the electrode. The d.c. resistivity of the electrodes was ~10 Ω·cm.

[1] The U.S. semiconductor industry uses imperial units in dimensioning Si.

Phosphorous doping was chosen over boron doping because boron has a high neutron absorption cross-section.

Hydrogen absorption coupons were cut from ¼-inch thick Ti-2 and Ti-12 plates. Their nominal dimensions were 6 mm × 6 mm × 1.5 mm. Each electrode had a 1 mm diameter hole through the 6 mm × 6 mm faces for suspending it in the cell from a 0.6 mm diameter Ti-2 wire (Metron Incorporated), which was simply pinched onto the coupon to give a good electrical contact (see Figure 2.3.1-d). Such relatively small, thin specimens were required for the hydrogen absorption experiments due to limitations of the hydrogen extraction device used to measure the amount of absorbed hydrogen after charging.

2.4 Electrochemical cells

2.4.1 General-purpose cell

For identification in this Thesis, the electrochemical cell designed for general-purpose electrochemical tests and used in this project for most of the open circuit potential (E_{oc}) measurements and polarization curves, and all of the EIS experiments, will be called the general-purpose cell. A schematic diagram of the cell is shown in Figure 2.4.1-a. This cell was a double-walled, cylindrical Pyrex® vessel with an open top. The gap between the inner and outer walls served as a jacket through which water could be circulated to provide temperature control during experiments. The open top was sealed with a 13 mm thick poly(tetrafluoroethylene) (PTFE) lid, which had circular entry holes for the working and counter electrodes, the reference electrode compartment, and the purge gas inlet and outlet. The cell volume was ~750 cm^3. The counter electrode was a piece of Pt gauze

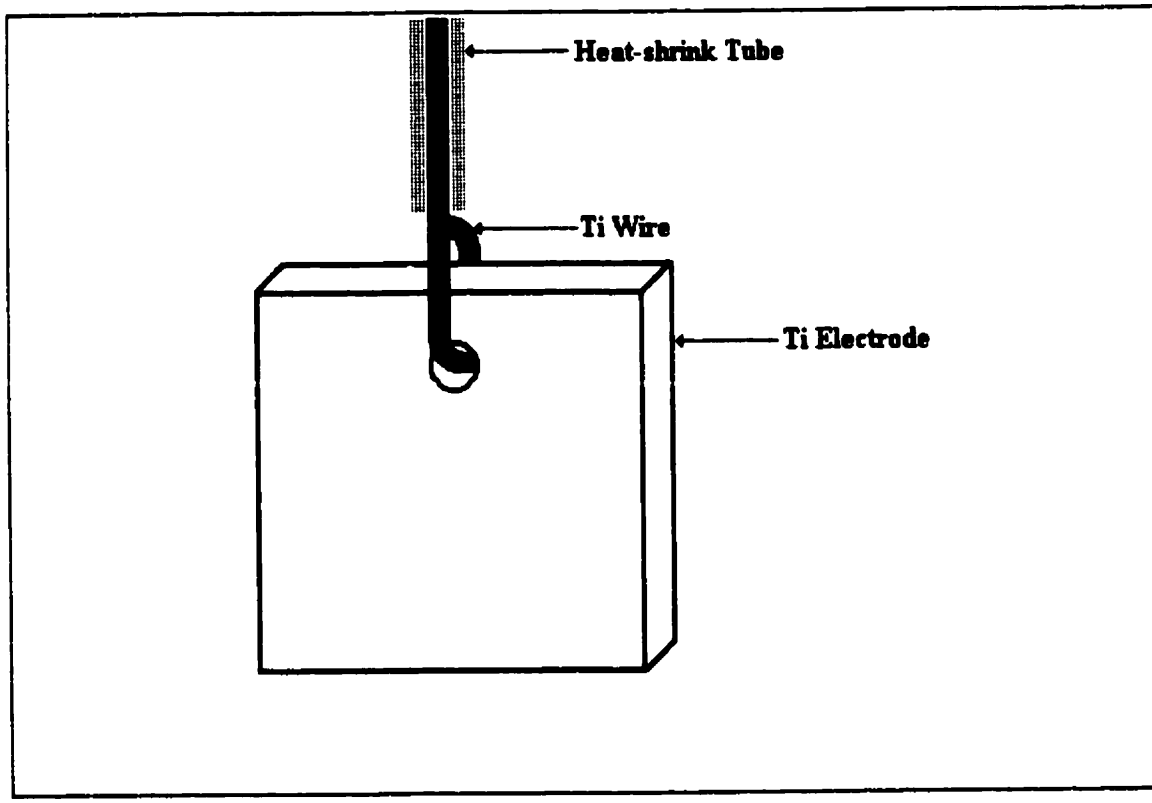

Figure 2.3.1-d Hydrogen absorption coupon shown suspended from a sheathed wire.

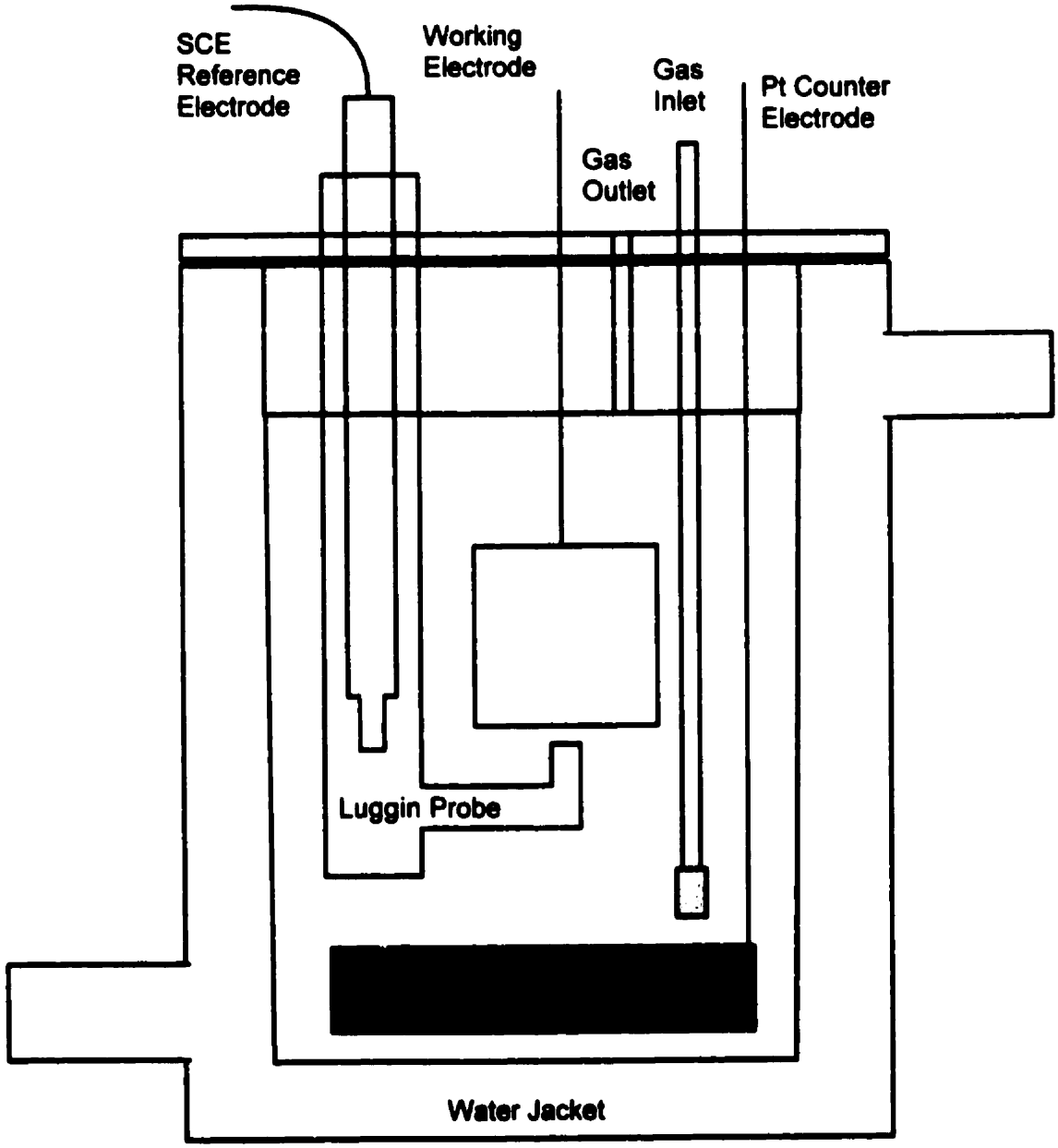

Figure 2.4.1-a Schematic diagram of the general-purpose electrochemical cell.

(45 mm × 120 mm) attached to a bare, 1.5 mm diameter Pt wire for the electrical lead. The gauze was positioned ~10 mm from the cell bottom, oriented parallel to the working electrode in order to provide the most uniform distribution of current pathways possible. The reference electrode was a commercially produced saturated calomel electrode (SCE) (Fisher) housed in a separate glass compartment within the main cell. This ensured that the SCE was maintained at the same temperature as the other electrodes and the electrolyte, thereby avoiding development of thermal liquid junction potentials (see Section 2.4.4). The reference electrode compartment was filled with the same electrolyte solution as the main cell. A Luggin capillary provided the electrical connection between the solutions in the main cell and reference electrode compartment. The Luggin tip (orifice diameter ≈ 0.5 mm) was positioned ~5 mm from the working electrode surface to minimize the uncompensated solution resistance during the experiments. A 3.5 mm inner diameter glass tube served as an inlet connection for purge gas. The inlet tube terminated in a glass frit that dispersed the purge gas into small bubbles, giving the gas increased contact with the solution. The gas outlet was a simple 5 mm hole in the cell lid, over which was placed a piece of Ti-2 as a cover.

All glass components of the cell were cleaned by soaking overnight in a 1:1 mixture of concentrated H_2SO_4 and HNO_3, followed by several rinses with Millipore water (18 MΩ·cm). The SCE was rinsed well with Millipore water before each use. The Pt counter electrode was cleaned by rinsing in Millipore water, flaming to red heat in a propane-air Bunsen burner, then rinsing again in Millipore water. The PTFE cell lid was soaked in methanol (Anachemia, HPLC grade) for 1 h then rinsed with Millipore water to

clean it. Electrolyte solutions were prepared in 1 dm^3 Pyrex volumetric flasks that had previously been acid-cleaned and rinsed with Millipore water as described above for the cell. All cell components and glassware were handled with PTFE-coated steel tongs or latex surgical gloves that had been rinsed well with Millipore water, to avoid contamination by fingers.

Cell temperatures during experiments were controlled to ± 2°C by pumping water from a circulating bath (Lauda, K-2/R) through the cell jacket. Before each experiment the potential of the reference electrode was checked against that of a master SCE that was maintained as a standard. The potential difference was always found to be less than 1 mV.

2.4.2 Reflectometry cell

The electrochemical cell designed specifically for neutron reflectometry experiments -the "reflectometry cell"- was, like the general purpose cell, a double-walled Pyrex vessel with the gap between the two walls serving as a jacket through which water could be circulated to provide temperature control during experiments (although this has not been done in any experiments to date). The cell volume was approximately 800 cm^3. A schematic diagram of the cell is shown in Figure 2.4.2-a.

The inner cell wall was shaped like "a football[1] with the ends cut off". The openings at either end were ~90 mm in diameter. The two open ends were closed off by the working and counter electrodes; a neoprene gasket made the seal between the cell and each

[1] What is known as a football in North America, *i.e.*, not a soccer ball.

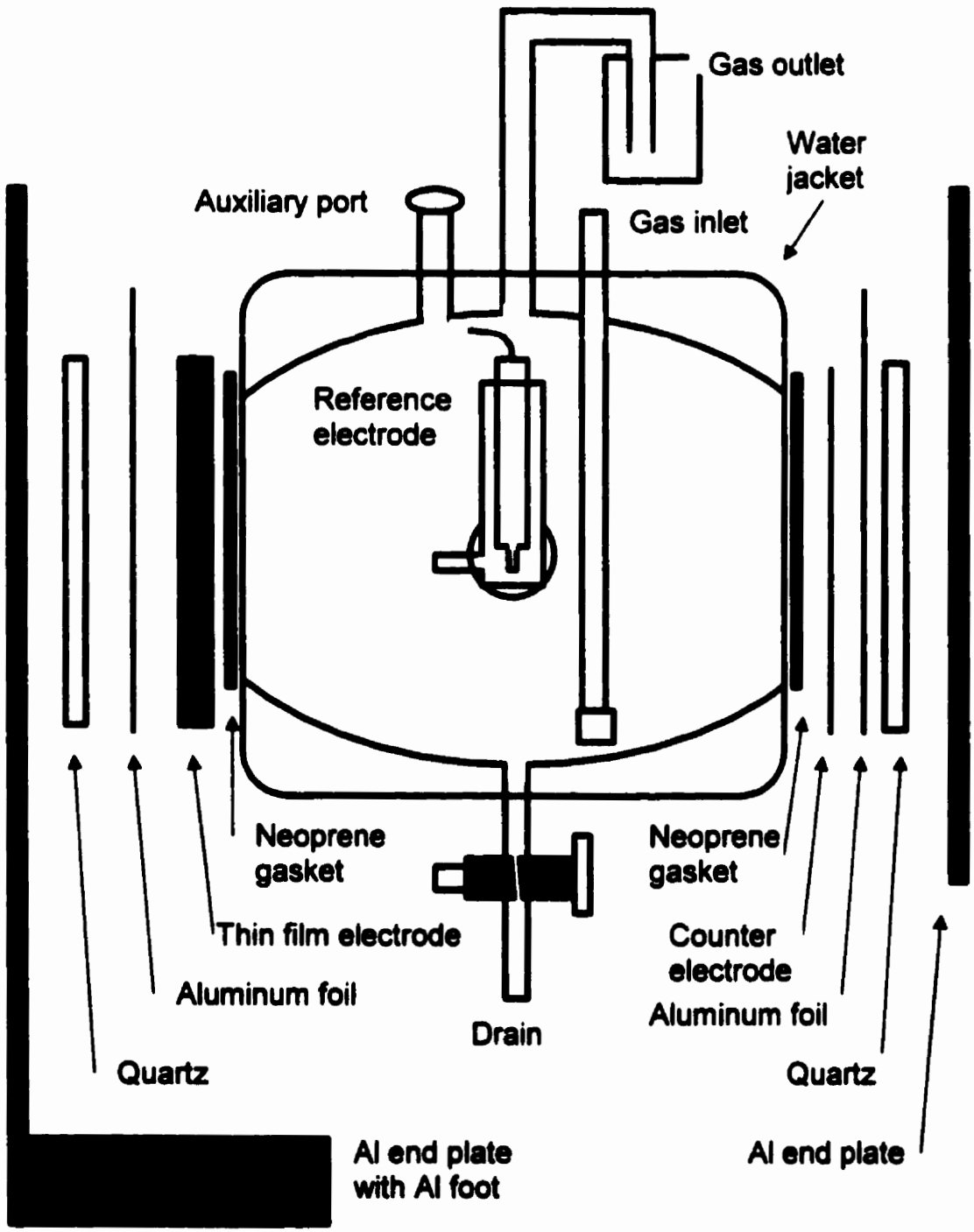

Figure 2.4.2-a Schematic diagram of the neutron reflectometry cell. The electrode assemblies at either end are shown in an exploded arrangement for clarity. The four long bolts that run between the aluminum end plates to hold the assembly together are not shown.

electrode. The cell and electrodes were configured this way because of the need to maintain the working electrode in the vertical plane to align it with the neutron beam, which was a thin "ribbon beam", orientated vertically.

The inner cell wall was designed in a "football" shape so that at every point there existed a smooth continuous slope toward the cell equator. This shape ensured that gas bubbles formed at the electrode surfaces (*e.g.*, by electrolysis) would be transported away from the electrodes, and that they and the purge gas bubbles would be channelled to the gas outlet positioned at the highest point on the inner wall. This design also helped keep the electrodes totally submerged, even if the cell was not completely full of electrolyte solution. The cell was easy to drain while in place (*i.e.*, without having to move it and lose the carefully-established alignment with the neutron beam) through an outlet positioned at the lowest point on the inner wall.

In addition to the gas outlet, which was a glass tube ending in a ground glass joint, and the drain (a glass tube with a PTFE stopcock), three other penetrations ending in ground glass joints were built into the cell. One of these penetrations allowed entry of a gas inlet tube, and another the Luggin capillary from the reference electrode compartment. The third was an auxiliary port that was not used in the experiments reported here.

The counter electrode was a 25 μm thick Pt foil (AESAR, 99.99%), 100 mm square. Electrical insulation and mechanical support were provided by a 4 mm thick quartz disk, 100 mm in diameter, backing the foil. Because of the delicate nature of such a thin foil, electrical contact was made by placing a piece of aluminum foil (Reynolds) between the

Pt and quartz backing, leaving a tab of Al foil sticking out for easy attachment of electrical leads.

The working electrode was always a thin film electrode (see Section 2.3) positioned at the end of the reflectometry cell opposite the counter electrode, with the sputtered Ti side facing the cell interior (of course). Electrical contact was made, as described above for the counter electrode, by placing Al foil between the Si slab and another quartz disk. The entire assembly was held together with a clamping system comprising two parallel aluminum plates and four long bolts running between them. The bolts were tightened to sandwich the cell and electrodes firmly between the plates. The bottom edge of the plate closest to the working electrode had an aluminum foot that was used to secure the clamp and the entire assembly to the neutron spectrometer table, holding the cell at the proper height and preventing any movement that would destroy the alignment between the working electrode and the neutron beam.

The reference electrode was a SCE electrode, as used in the general-purpose cell, housed in a separate glass compartment outside of the main cell. The reference electrode compartment was filled with the same electrolyte solution as the main cell and connected to it by a glass frit and a Luggin capillary with a ground glass joint. The Luggin tip (orifice diameter $\approx$ 0.5 mm) was located ~50 mm from the working electrode surface.

A 3.5 mm inner diameter glass tube with a ground glass joint served as the inlet connection for purge gas. The inlet tube terminated in a glass frit that dispersed the gas into small bubbles. The gas outlet port from the cell was fitted with a small, glass, water-

filled bubbler that acted as a one-way airlock to keep air out of the cell. The unused auxiliary port was closed with a ground glass stopper.

Since the seal between the inner and outer cell walls was made with transparent silicone caulking (General Electric), the acid washing procedure used for the general-purpose cell was not performed on this cell. Instead, the cell, other glass components, neoprene gaskets, and stopcock were washed in a solution of detergent (Alconox Inc.) and carefully rinsed with Millipore water. The reference and counter electrodes were simply rinsed with Millipore water. Electrolyte solutions were prepared in 1 dm^3 volumetric flasks as described in Section 2.5.

2.4.3 Crevice corrosion cell

The cell used for crevice corrosion experiments was made from a Ti pressure vessel (Parr Instrument Co., 236HC10), and is similar to the crevice corrosion cells already in use at Whiteshell Laboratories [16]. The vessel and the lid, or head, (Parr Instrument Co., 942HC75) were made of ASTM Grade-4 Ti. A PTFE gasket provided the seal between the body and the head, which were held together with a split-ring clamp and drop band. The lid was modified to accept four sealing glands (Conax Buffalo Corp., type MCH-040-A2-T) for electrode feedthroughs, a gauge block (Parr Instrument Co., 4317), and a thermocouple well (Parr Instrument Co., A256HC2) as shown in Figure 2.4.3-a. The gauge block assembly consisted of a stainless steel coned pressure fitting, a needle valve and inlet fitting for pressurizing the vessel and relieving pressure, a pressure gauge (Ashcroft, Duraguage), and a safety rupture disk (Fike, 526HCPD) rated to burst at 1027 PSIG @ 72°F. The thermocouple well was made of ASTM Grade-4 Ti and made a

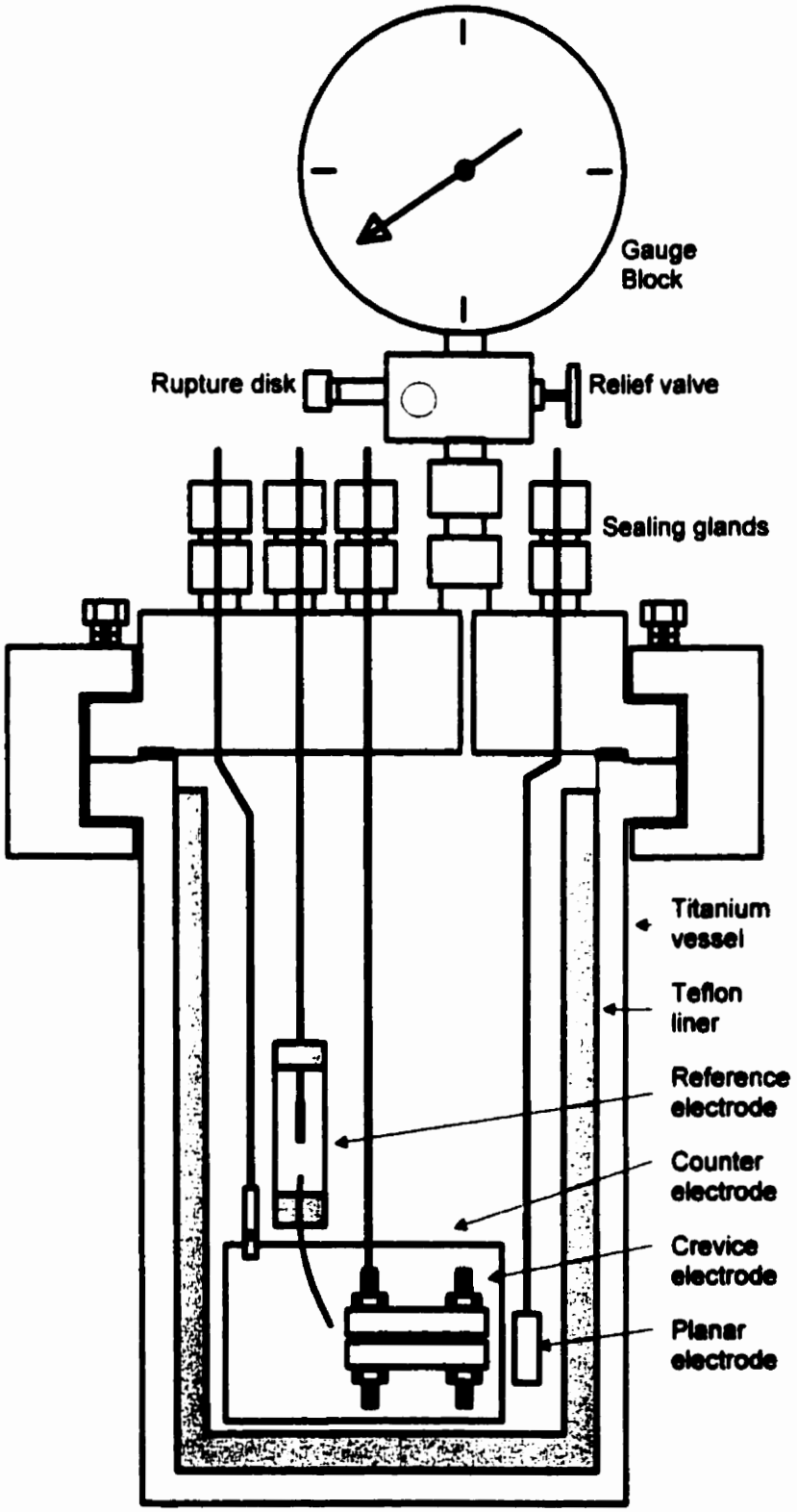

Figure 2.4.3-a Schematic diagram of the crevice corrosion cell with electrodes in place. (Thermocouple well omitted for clarity).

pressure-tight seal with the lid via a gold gasket. The sealing glands, made of 316 stainless steel, contained modified inner seals for the feedthroughs. The original inner seals were replaced with a PTFE sealant with a single 3 mm centred hole in it (to accept the Ti welding rod used to support the electrodes, or the Ag wire from the reference electrode) and two 316 stainless steel followers, each with a single 3 mm hole. The pressure vessel was cylindrical in shape with a 100 mm inner diameter and a volume of 1000 cm^3. It was lined with a 3 mm thick, cylindrical PTFE liner with a 93 mm inner diameter, 130 mm high.

The working electrode -called the "crevice electrode" in this cell- was suspended near the centre of the cell from a Ti welding rod that was sheathed in 4 mm diameter heat-shrink PTFE tubing that had been shrunk tightly around the rod[1]. The sheathed welding rod was held in place and sealed by a sealing gland.

The counter electrode, also suspended from a PTFE-sheathed Ti welding rod held by a sealing gland, was a piece of Ti foil, 0.3 mm thick, spot-welded to form a cylinder 50 mm high and 67 mm in diameter. The foil was affixed to the rod with a small Ti screw clamp. This electrode was centred in the cell, encircling the crevice electrode to try to provide the most uniform distribution of current pathways possible between the counter and crevice electrodes. To avoid the establishment of classic galvanic coupling (*i.e.*, an electrochemical driving force between dissimilar metals in contact with each other), a

[1] Fortunately, and perhaps a little surprisingly, crevice corrosion did not occur between the sheath and welding rod in any of the experiments performed in this type of cell.

counter electrode and screw clamp made of Ti-2 were used with Ti-2 crevice electrodes and ones made of Ti-12 were used with Ti-12 crevice electrodes.

The reference electrode was a rugged, high temperature Ag/AgCl electrode made according to a procedure developed in our laboratories [182]. This reference electrode was composed of a 2.4 mm diameter Ag wire (Alfa AESAR, 99.9%, spring hard grade) onto which a layer of AgCl was anodically electrodeposited. The Ag wire was sheathed in heat-shrink PTFE tubing and sealed in a sealing gland. A small PTFE vial containing about 5 cm^3 of 0.1 $mol \cdot dm^{-3}$ KCl surrounded the AgCl-coated tip of the Ag wire. A Luggin capillary made from a KCl-saturated asbestos string sheathed in heat-shrink PTFE tubing provided an ionic link between the reference compartment and the electrolyte in the main cell. The Luggin tip was positioned within 5 mm of the crevice electrode. Before each experiment the potential of the Ag/AgCl reference electrode was checked against the potential of the master SCE described above (Section 2.4.1) and always found to be -40 ± 3 mV[1].

A fourth electrode was used in the crevice corrosion cell. It was a Ti coupon, 20 mm × 6 mm × 6 mm, referred to as the "planar electrode" because it had flat-polished surfaces with no crevices. In each experiment, a planar electrode having the same composition as the crevice electrode (Ti-2 or Ti-12) was used. The purpose of the planar electrode was to provide another electrode of the same composition as the crevice electrode, immersed in the same solution, but not undergoing crevice corrosion nor coupled to a crevice-corroding electrode, for comparison of potentials with those of the

[1] The expected value for the Ag/AgCl, KCl (saturated) reference system is -45 mV [177].

crevice electrode/counter electrode couple. One square face of the planar electrode had a 3/48-tapped hole that was used to suspend it from a PTFE-sheathed Ti welding rod.

The interior of the pressure vessel body was cleaned by abrading lightly with wet 600 grit silicon carbide paper (Buehler), to remove any stains, then rinsing with Millipore water. The pressure vessel head, with reference electrode and sheathed welding rods in place was just rinsed with Millipore water. The PTFE liner was washed with detergent (Alconox Inc.), then rinsed well with Millipore water. The counter electrode was rubbed with 600 grit silicon carbide paper until any brown stains were removed, then rinsed with Millipore water. The planar electrode was polished with wet silicon carbide paper (120, 240, 400, then 600 grit the first time it was used, then with 600 grit thereafter). After polishing, it was rinsed well with Millipore water. Solutions were prepared in acid-washed volumetric flasks. All cell components, glassware, and electrodes were handled only with forceps or Millipore-rinsed latex gloves.

2.4.4 Hydrogen absorption cell

The hydrogen absorption cell, as one might guess, refers to that which was used for hydrogen absorption experiments. This was another double-walled Pyrex cell with the inter-wall gap serving as a jacket for temperature control by circulating water. Temperatures were controlled to ± 2°C by water from a circulating bath (Haake, model DC3). This was a large one-piece (*i.e.*, no separate lid), cylindrical cell of about 2.5 dm^3 capacity. The cell body had penetrations, with ground glass joints, for the Luggin capillary, working electrode, counter electrode, and purge gas inlet and outlet, along with one unused auxiliary port. The cell is shown schematically in Figure 2.4.4-a. The ports

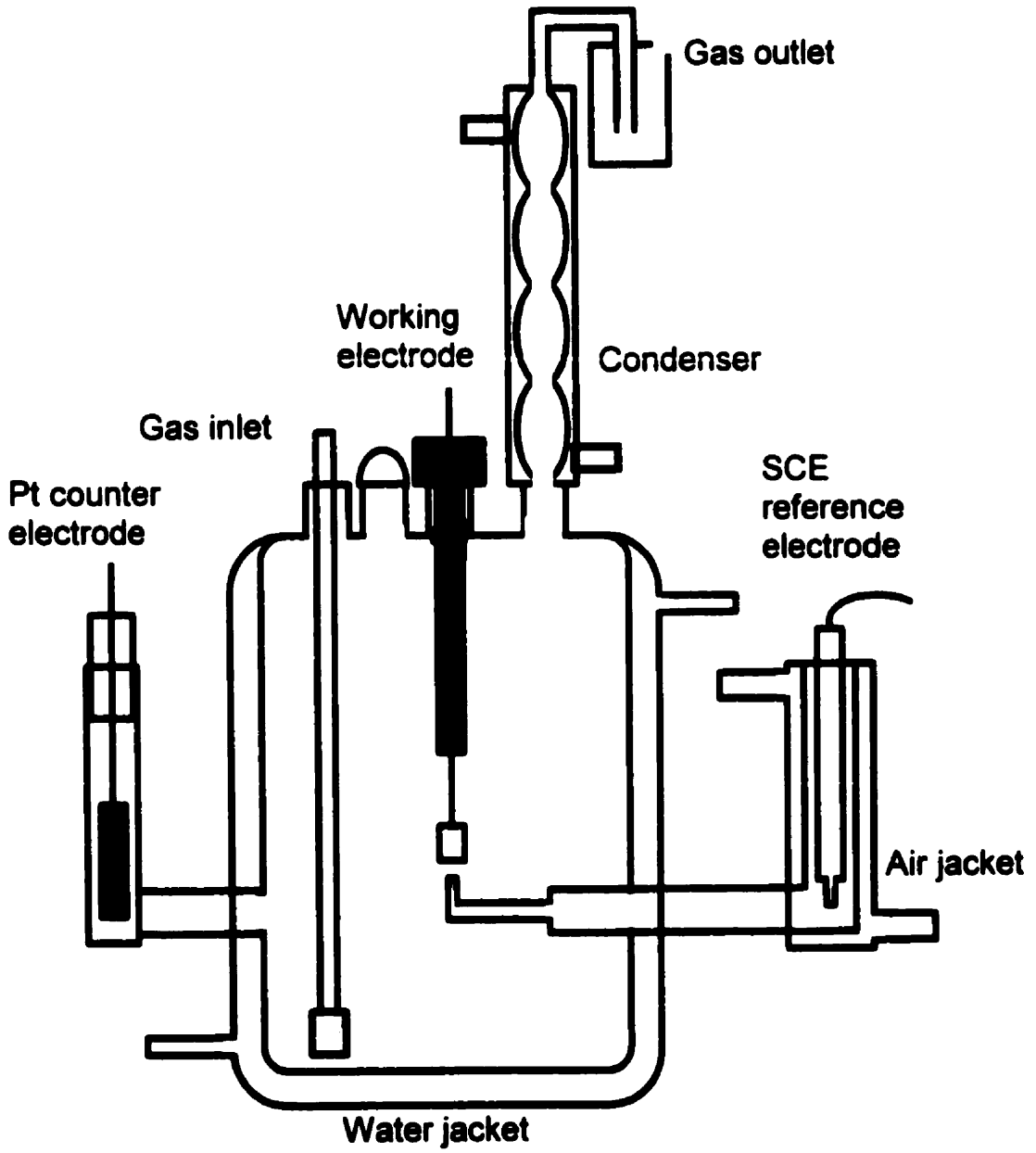

Figure 2.4.4-a Schematic diagram of the hydrogen absorption cell.

for the Luggin capillary and counter electrode were located on opposite sides of the cell, while the others were positioned on the flat cell top. The reference electrode was a commercial SCE (Fisher) that was checked against the master SCE before each use, as described in Section 2.4.1. When in use, the reference electrode was located in a separate jacketed compartment connected to the main cell by a glass frit and a Luggin capillary. The reference compartment was filled with solution from the main cell. The reference compartment and electrode were maintained at room temperature during all experiments by flowing compressed air through the jacket. This was done to prolong the life and increase the stability of the SCE, both of which deteriorate at temperatures >80°C. The Luggin tip (orifice diameter ≈ 0.5 mm) was positioned ~5 mm from the working electrode to minimize the uncompensated solution resistance. No corrections were made to the measured potential values to account for the temperature difference between the cool electrolyte in the reference compartment and the warmer electrolyte in the main cell body however, they are of minor significance to the results and conclusions derived from them.

The error in reported potentials due to the temperature difference between the working and reference electrodes can be broken into three components: the thermocouple potential, the temperature dependence of the reference electrode, and the thermal liquid junction potential [182]. The thermocouple potential, arising from metal junctions at different temperatures in the circuit, is on the order of a few millivolts or less [8], and so can be ignored. The temperature dependence of the SCE is known [177] and amounts to -55 mV for the largest temperature difference used in these experiments (~70 Celsius degrees). The thermal liquid junction potential is a result of the Soret effect, that is the tendency to form a concentration gradient as a result of thermal diffusion in a temperature

gradient [182, 183]. The concentration gradient established is different for ions of different mobility, and therefore a potential difference arises at the thermal junction. The severe thermodynamic calculations required to determine the thermal liquid junction potential are beyond the scope of this Thesis, and the necessary experimental data does not exist for the electrolyte solutions employed. However, MacDonald [184] has estimated the temperature dependence of the thermal liquid junction potential for a number of solutions. For acidic solutions reasonably similar to those used in the hydrogen absorption experiments, the thermal liquid junction potential varies with temperature at a rate of roughly -400 $\mu V \cdot K^{-1}$. This would yield an error of about -28 mV for experiments at 95°C. Therefore, the total temperature based correction to the measured potential should be in the neighbourhood of -80 to -90 mV.

The counter electrode was a piece of Pt gauze, 57 mm × 124 mm, which was rolled up to form a cylinder. It was placed in a separate compartment that was connected to the main cell by a glass frit, in this case to minimize the contamination of the cell with chlorine (Cl_2), the product of the anodic half-reaction during electrolytic hydrogen charging experiments in chloride-containing solutions. This compartment was also filled with electrolyte from the main cell. The counter electrode compartment was not actively cooled during experiments, as was the reference compartment, but it would be expected to be somewhat cooler than the main cell because it was outside the water jacket and not actively heated either. The temperature of the counter electrode compartment did not affect the experimental results.

The purge gas inlet tube was a glass tube with a frit on the bottom to disperse the purge gas into small bubbles. The purge gas outlet was a vertically positioned Pyrex condenser tube, cooled with cold tap water circulating through the jacket to reduce solution loss from the cell by evaporation. The condenser terminated in a water-filled airlock to prevent oxygen entry. The working electrode was suspended from a 0.6 mm diameter Ti wire (Metron Incorporated, Ti-2) threaded through a PTFE plug that sealed the cell entry port. The Ti wire was sheathed with 1.5 mm heat shrink Kynar® tubing (Paisley Products of Canada Inc.) that had been tightly shrunk around the wire to help ensure that most of the current passed during experiments flowed through the working electrode and not the support wire. The auxiliary port was closed with a glass stopper.

The main cell and glass components were cleaned by soaking overnight in chromic acid[1], followed by several rinses in Millipore water. Other components were cleaned by rinsing with methanol (Anachemia, HPLC grade), followed by Millipore water. Electrolyte solutions were made in chromic acid-washed volumetric flasks, using acid-washed glass pipets.

2.5 Solutions

Most of the solutions used in the experiments described in the following sections were made with various concentrations of HCl and NaCl, since one would expect these to be present in the anolyte within the occluded region of an actively corroding crevice on Ti (in the saline groundwaters of the Canadian Shield). A few experiments employed

[1] Saturated CrO_3 (Fisher) in concentrated H_2SO_4 (BDH)

sulphuric or perchloric acids to help distinguish potential anion effects and, in the case of the former, to provide a direct comparison with published studies from other laboratories, many of which were done using sulphate solutions. Most of these solutions were deaerated before use, also to simulate the conditions expected within an actively corroding crevice[1], or within a waste disposal vault. Anoxic conditions are expected to prevail over the long term in a waste disposal vault after the oxygen, introduced by human intrusion into the rock and entrained in the buffer and backfill upon vault closure, is consumed by container corrosion and reactions with oxidizable minerals and organic material within the backfill and buffer [1]. Although dissolved Na^+ concentrations from 2×10^{-3} to 0.18 mol·dm^{-3} and Cl^- concentrations from 1×10^{-3} to 0.72 mol·dm^{-3} have been found in the groundwaters of the Canadian Shield, and many other soluble ions such as Ca^{2+}, SO_4^{2-}, Mg^{2+}, HCO_3^-, *etc.* have also been reported [185], when NaCl was used in the present experiments, solutions containing 0.27 mol·dm^{-3} NaCl were chosen for simplicity (concentration and composition were eliminated as variables) and to make the results more easily comparable with the bulk of related work already performed in these laboratories [2, 16, 19-21, 29, 32-34, 186].

Hydrochloric (BDH, AnalaR grade), sulphuric (BDH, AnalaR grade), and perchloric (BDH, AnalaR grade, 70%) acid solutions were prepared by pipetting appropriate volumes of the concentrated acids, using acid-washed volumetric and graduated pipets, into acid-washed volumetric flasks and diluting to the mark with Millipore water. The pH of each electrolyte solution was measured before use with a pH meter (Fisher

[1]The actual composition of crevice anolytes is unknown, and probably varies with location within a single crevice; however, they are expected to be acidic and depleted of dissolved oxygen.

Scientific, Accumet 910) that had undergone a temperature-corrected two-point standardization with standard buffer solutions (BDH, pH 2 and 6) immediately prior to the measurement, although this measurement was of limited value due to the difficulties in accurately measuring very low pH values.

Sodium chloride-containing solutions were prepared using NaCl crystals (Fisher, Certified A.C.S. grade). Solutions prepared for XPS, neutron reflectometry, EIS, and crevice corrosion experiments contained only NaCl and water and were neither pH-buffered nor pH-adjusted. This preparation resulted in solutions with pH = 6-6.5. For experiments in deaerated solutions, deaeration was accomplished in the electrochemical cell by bubbling Ar gas (Canadian Liquid Air Ltd., U.H.P. grade) through the electrolyte and excluding air from the cell. Dissolved oxygen concentrations in these solutions after 20 minutes or more of Ar bubbling were lower than detectable using visual colourmetric test vials (Chemetrics Inc., CHEMets model 0-40) designed to be sensitive in the 1-5 ppb range.

2.6 Experiments

2.6.1 Activation experiments

The term "activation experiments" will refer to tests in which the evolution of E_{oc} with time was measured on Ti electrodes in acidic solutions. The term "activation" was chosen since it represents the expected behaviour of the Ti during the experiment, *i.e.*, dissolution of the native passive oxide film, followed by active uniform corrosion of the underlying Ti.

Activation experiments were performed using Ti-2 and Ti-12 disk electrodes and hydrogen absorption coupons. The procedure used for the disk electrodes will be described first. The disk electrodes were degreased by immersing them in a mixture of 90% methanol (Anachemia, HPCL grade) and 10% water in an operating ultrasonic cleaning bath for about 15 minutes, then rinsing well with Millipore water. After drying, each disk was centred in a cup-shaped PTFE holder with a 6 mm hole in the bottom, through which a support rod was inserted and screwed into the back of the disk. A diagram of the holder is shown in Figure 2.6.1-a. The disk was then sealed into the holder with epoxy (10 parts Hysol EE4183 resin and 1 part HD3615 hardener). This was a silica-filled resin specifically selected for these experiments because of its high hardness (87 Shore D), low water absorption (0.14% after 24 h), long pot life (8 h), high electrical resistivity (4×10^{14} Ω·cm), high heat resistance (180°C), and low shrinkage (0.9%) [134], which made it easy to work with, relatively inert in the solutions used, and resistant to separation from the disk walls, even after temperature changes.

The epoxy was cured for 2 h at 80°C followed by 2 h at 150°C in a Blue M oven. Next, the electrode was polished in the holder with wet 120 grit silicon carbide paper until any epoxy covering the face of the metal disk was removed. Polishing continued on wet silicon carbide paper in the sequence 120, 240, 400, 600 grit. After the final polishing stage, the disk and holder were rinsed well with Millipore water. This preparation procedure was only required on the first use of each disk. The electrodes were handled with Millipore water-rinsed gloves only.

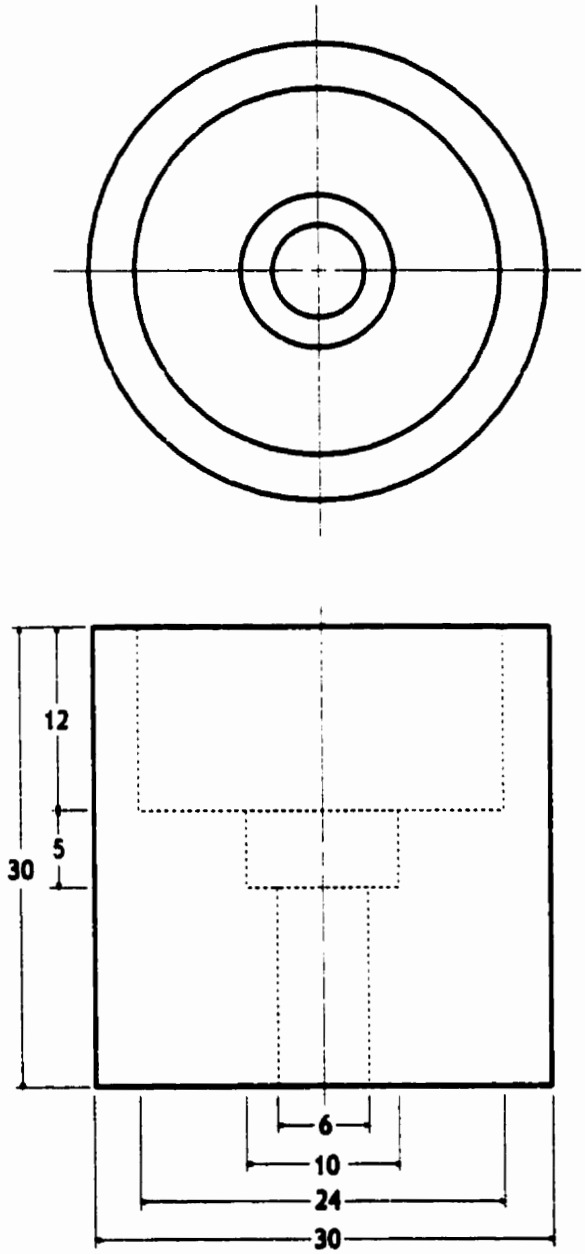

Figure 2.6.1-a Scale diagram of disk electrode holder. Dimensions in millimetres.

The general-purpose electrochemical cell was assembled, with all components in place except the working electrode and its support rod, and filled with ~600 cm^3 of electrolyte solution. The electrolyte was deaerated in the cell with a 20-minute Ar purge. Solutions with acid concentrations ranging from 1.0×10^{-4} $mol \cdot dm^{-3}$ to 2.0 $mol \cdot dm^{-3}$ were used in these activation experiments. For HCl solutions containing 1.0 $mol \cdot dm^{-3}$ acid or less, the chloride concentration was maintained at 1.0 $mol \cdot dm^{-3}$ by preparing the electrolyte solutions from appropriate mixtures of previously prepared 1.0 $mol \cdot dm^{-3}$ HCl and 1.0 $mol \cdot dm^{-3}$ NaCl.

When the cell and electrode were ready, the working electrode was threaded onto the support rod, given a final polish on wet, 600 grit silicon carbide paper, rinsed again with Millipore water, and immediately (within one minute) immersed in the electrolyte solution in the cell. Deaeration was continued for the duration of the experiment. As quickly as possible after working electrode immersion, the electrodes were connected to the appropriate leads from the potentiostat (Solartron 1286) and data acquisition begun. E_{oc} measurements were made with the potentiostat's internal digital volt meter (DVM)[1] and logged on a dedicated personal computer (PC) (Gateway 2000, 486DX2/66) running in-house software and communicating with the potentiostat through an IEEE-488 bus controlled by a plug-in GPIB card (National Instruments, AT-GPIB) in the PC. Data were acquired at a frequency of ~1 Hz for a period of up to 30 hours.

[1] The DVM had an accuracy of ±5 μV for potential measurements and 0.1% ± 0.0025% of full scale, with a maximum resolution of 100 pA, for current measurements.

For activation experiments employing hydrogen absorption coupons, the procedure was as follows. Each coupon was polished with 400, then 600 grit wet silicon carbide paper, measured dimensionally with digital callipers (Mitutoyo, Model 293-701, 0 to 25 mm in thousandths) rinsed with denatured ethanol (J.T. Baker, Photrex grade) for five minutes then with Millipore water, and dried in a dessicator overnight. The exposure to air (in the dessicator) allowed an oxide film to grow on the freshly polished surfaces, thereby establishing a more reproducible starting condition than could be achieved by use immediately after polishing. The dried coupon was weighed on an analytical balance (Sartorius, model R180D-**V40) before use.

The hydrogen absorption cell was filled with ~1500 cm^3 of electrolyte solution, either 0.1 $mol \cdot dm^{-3}$ HCl + 0.27 $mol \cdot dm^{-3}$ NaCl or 1.0 $mol \cdot dm^{-3}$ HCl + 0.27 $mol \cdot dm^{-3}$ NaCl, which was then deaerated with Ar overnight. When the cell and electrode were ready, the hydrogen absorption coupon was suspended in the cell such that it was totally submerged in the electrolyte solution. Deaeration was continued for the duration of the experiment. Data acquisition was begun as quickly as possible after electrode immersion and was carried out using the same data acquisition system used for the activation experiments employing disk electrodes. Data were acquired every 20 s in these experiments.

2.6.2 Potentiostatic polarization experiments

These tests were also carried out using Ti-2 and Ti-12 disk electrodes and hydrogen absorption coupons. Polarization experiments were normally carried out upon completion of an activation experiment, without removing the electrode from the cell. After E_{oc} measurements were halted, the PC software was set up to run a polarization

experiment, controlling the potentiostat and recording the data returned from it. The software commanded the potentiostat to apply a fixed potential to the working electrode while the corresponding current, measured by the potentiostat's internal DVM, was recorded, along with a time stamp produced by the potentiostat's internal clock. The applied potential was held constant until the software determined that the current had reached a reasonably steady state or until a time-out period had elapsed, whichever occurred first. The time-out period was normally set to 1000 s.

The software used the standard deviation in the current values to establish whether the current had achieved a reasonably steady state. If the standard deviation exceeded a critical value, then more measurements were taken and the standard deviation recalculated, based on the new data. Otherwise, the current was deemed to have achieved a steady state. The number of measurements included in the standard deviation calculation, and the value of the critical standard deviation, were user-selectable; in these experiments a critical standard deviation of ≤ 1 μA over the last 50 points was specified.

A computer-calculable definition of the steady state current was used so that polarization experiments could run (largely) unattended, like E_{oc} and EIS measurements. This allowed some experiments of very long duration (*i.e.*, several days) to be performed without interruption. A definition of the steady state current based on the standard deviation was selected over other definitions based on the slope of the current-time relationship or the range of current values over the specified interval because the slope is too insensitive to noise or other symmetrical fluctuations, and the range can be overly noise-sensitive. Some of the possibilities are illustrated in Figure 2.6.2-a. The transient

a)

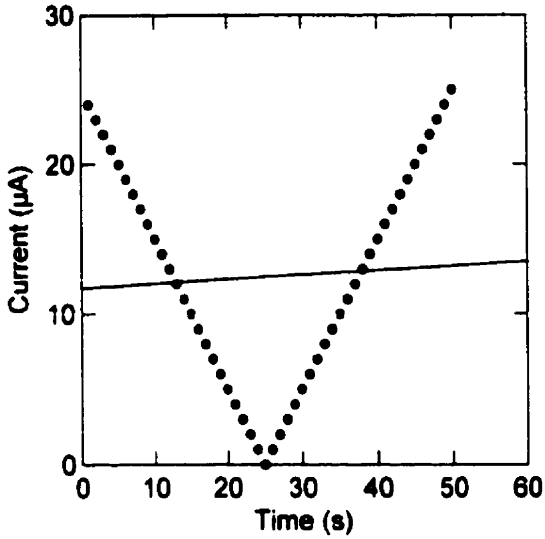

b)

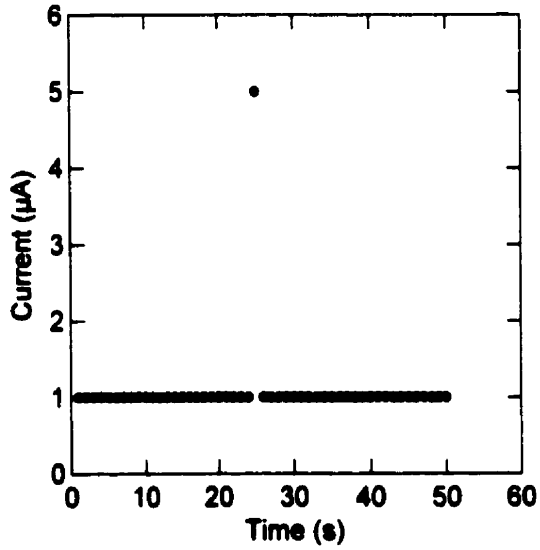

Figure 2.6.2-a Examples illustrating the advantages of defining the steady-state current based on the standard deviation rather than the slope or range of current data. (a) These non-steady state data have a low regression slope of 0.03 μA·s^{-1} (the linear regression is indicated by the solid line), but their standard deviation is high at 7.3 μA. (b) These data represent a steady state with some noise. The range of the data is high at 4 μA, but the standard deviation is only 0.6 μA.

current data were all saved to verify, after the experiment, whether the conclusion regarding the establishment of a steady state current was reasonable. In all cases for which a steady state current was identified by the program, it was.

Once the program determined that the current had reached a steady state, or the timeout period had elapsed, the applied potential was changed, in a single step, to a new value and the process repeated. In this way a potential staircase function was applied, with steps of (possibly) variable duration and user-defined height, beginning at the user-entered starting potential and ending at the user-entered final potential.

It was also possible to string together several different applied potential staircase functions in order to change the step size or direction (ascending or descending). Data were acquired at a frequency of ~1 Hz in the experiments employing disk electrodes and at ~0.05 Hz when hydrogen absorption coupons were used.

2.6.3 Electrochemistry/XPS experiments

These experiments were performed on disk electrodes of high purity Ti, Ti-2, Ti-12, Ti-16, and Ti-0.1Ru. The same procedures and set of test conditions were used with samples of each Ti material. Disk electrodes were first degreased by soaking in a mixture of 10% Millipore water and 90% methanol (Anachemia, HPLC grade) in an ultrasonic cleaning bath for about 15 minutes, then rinsed well with Millipore water. Next, on each disk, the circular face without the tapped hole was polished on wet silicon carbide paper in the sequence 120, 240, 400, 600 grit. The disk was then rinsed with Millipore water. This procedure was only required on the first use of each disk. Disks were handled only with stainless steel forceps and Millipore-rinsed latex gloves.

The general-purpose electrochemical cell was assembled with all components in place, except the working electrode and its support rod, and filled with ~600 cm^3 of 0.27 $mol \cdot dm^{-3}$ NaCl solution (not pH-adjusted). The circulating bath was brought to temperature and water circulated through the cell jacket to heat the electrolyte solution to the desired temperature. While the electrolyte was being heated, it was also deaerated by vigorously bubbling Ar gas through it. It normally required 1-2 h to heat the electrolyte to the desired temperature.

When the cell was ready, the working electrode was threaded onto the support rod, given a final polish on wet, 600 grit silicon carbide paper, rinsed again with Millipore water, and immediately (within one minute) immersed in the electrolyte solution in the cell. The electrode was suspended with the polished face pointing downwards and the electrode walls only partially submerged to minimize the area of unpolished electrode surface exposed to solution and to avoid immersing the Ti welding rod. Splashing from the gas bubbling, and condensation running down from the cell lid, kept these surfaces wet, however. Deaeration was continued for the duration of the experiment.

Readings of E_{oc} were taken every 20 s for a period lasting overnight (16-18 hours). When E_{oc} measurement was halted, the working electrode was immediately emersed, rinsed well with Millipore water, removed from the support rod, mounted on the XPS sample stub using the tapped hole on the reverse side of the disk, and entered into the vacuum system as quickly as possible to minimize the air exposure of the sample surface. The transfer time did not exceed 10 minutes and the disk was handled only with clean

stainless steel forceps. These contacted only the side walls of the disk. The polished disk face did not contact any solid surfaces during transfer.

The disk was held in the antechamber of the XPS vacuum system or in a special vacuum transfer flask in an auxiliary pumping system for 2-4 hours to allow for outgassing and water evaporation from the sample. Both the XPS antechamber and the transfer flask were pumped with turbomolecular pumps (Baltzers, TMU 065). After evacuation in the antechamber, the sample stub with the disk electrode was entered into the XPS ultra high vacuum (UHV) chamber. The elapsed time between entry into the UHV chamber and recording of the XPS spectrum varied from ~1 to 17 h. The effect of prolonged exposure to UHV conditions was tested and found to be negligible in an experiment in which the same sample was re-analyzed by XPS at intervals over a seven-day exposure period.

XPS spectra were recorded on a PHI ESCA 5300 spectrometer using MgK_{α} radiation filtered through an Al window. Specimens were analyzed as generated by the preparation treatment described above, without sputtering. The binding energies were corrected for surface charging effects with respect to C_{1s} = 284.8 eV [175]. XPS survey spectra covering BE values from 0 to 1100 eV were recorded first, followed by high resolution spectra that examined the Ti_{2p} region (BE = 450-470 eV), O_{1s} region (BE = 525-545 eV), and C_{1s} region (BE = 280-300 eV). XPS spectra were recorded for disks of all five Ti materials, as polished (without exposure to the electrolyte solution), and after E_{oc} measurements in electrolytes held at 20, 40, 60, and 80°C.

2.6.4 Electrochemical impedance spectroscopy

These experiments were performed to complement the electrochemistry/XPS experiments, and therefore used the same exposure conditions (see Section 2.6.3). In the present experiments, however, the disk electrodes were mounted differently and, instead of emersion after completion of the E_{oc} measurements, electrochemical impedance spectroscopy (EIS) was performed.

Disk electrodes of high purity Ti, Ti-2, Ti-12, Ti-16, and Ti-0.1Ru were mounted in holders with epoxy as described in Section 2.6.1. The general-purpose electrochemical cell was set up and E_{oc} measurements were made as described in Section 2.6.3. At the end of the period of E_{oc} monitoring, EIS measurements were made using the same potentiostat, now coupled to a frequency response analyzer[1] (FRA) (Solartron, 1250). The instruments were controlled, and the EIS data acquired, by the PC, this time running Z-plot software (Scribner Associates, version 1.2b). EIS spectra were recorded with the base potential set to the last recorded value of E_{oc}, the applied potential stimulus varying sinusoidally at a (logarithmically spaced) series of single frequencies over a frequency range of 0.01 to 2×10^4 Hz, with the FRA autointegration function set to "short". A.C. voltage amplitudes of 10, 20, and 30 mV were used in these initial spectra to determine whether potential stimuli as large as ± 30 mV would still provoke a linear current response from the test system. With passivated electrodes, such as Ti in neutral solution, a small-amplitude potential stimulus results in a very small current response, so it is

[1] Also known as a transfer function analyzer.

advantageous to use as large an a.c. voltage amplitude as possible to increase the signal-to-noise ratio of the current response. However, the choice of an overly large a.c. voltage amplitude may result in a non-linear current response and therefore an invalid EIS measurement. A.C. voltage amplitudes of 10, 20, and 30 mV were found to yield the same impedance spectrum for a given electrode at a given temperature over the range of materials and conditions used. After this was confirmed for each experiment, an EIS spectrum of much longer duration was recorded over an a.c. frequency range of 10^{-3} to 2×10^{4} Hz with the FRA autointegration function set to "long" and with the potentiostat's low-pass filter turned on at frequencies below 5 Hz.

2.6.5 *In situ* electrochemistry/neutron reflectometry

In situ neutron reflectometry experiments were based on the work of Wiesler and Majkrzak [107, 108] at the National Institute for Standards and Technology (NIST) in Gaithersburg, MD. The current experiments were carried out using the C5 DUALSPEC triple-axis neutron spectrometer facility at the NRU reactor, Chalk River, ON. A schematic diagram showing the neutron beam path is given in Figure 2.6.5-a. Thermal neutrons generated within the reactor were collimated, then reflected by a pyrolytic graphite monochromator (using the (002) Bragg reflection), before passing through a graphite low-pass filter. This produced a collimated, monochromatic, incident neutron beam with de Broglie wavelength $\lambda = 2.37$ Å. The neutron beam was further collimated and reduced to a narrow ribbon beam of cross-section 0.2 mm × 50 mm using two slits in series. The first slit consisted of a pair of Be jaws that could be accurately positioned via computer-controlled stepper motors, yielding a variable-width slit. The second was a

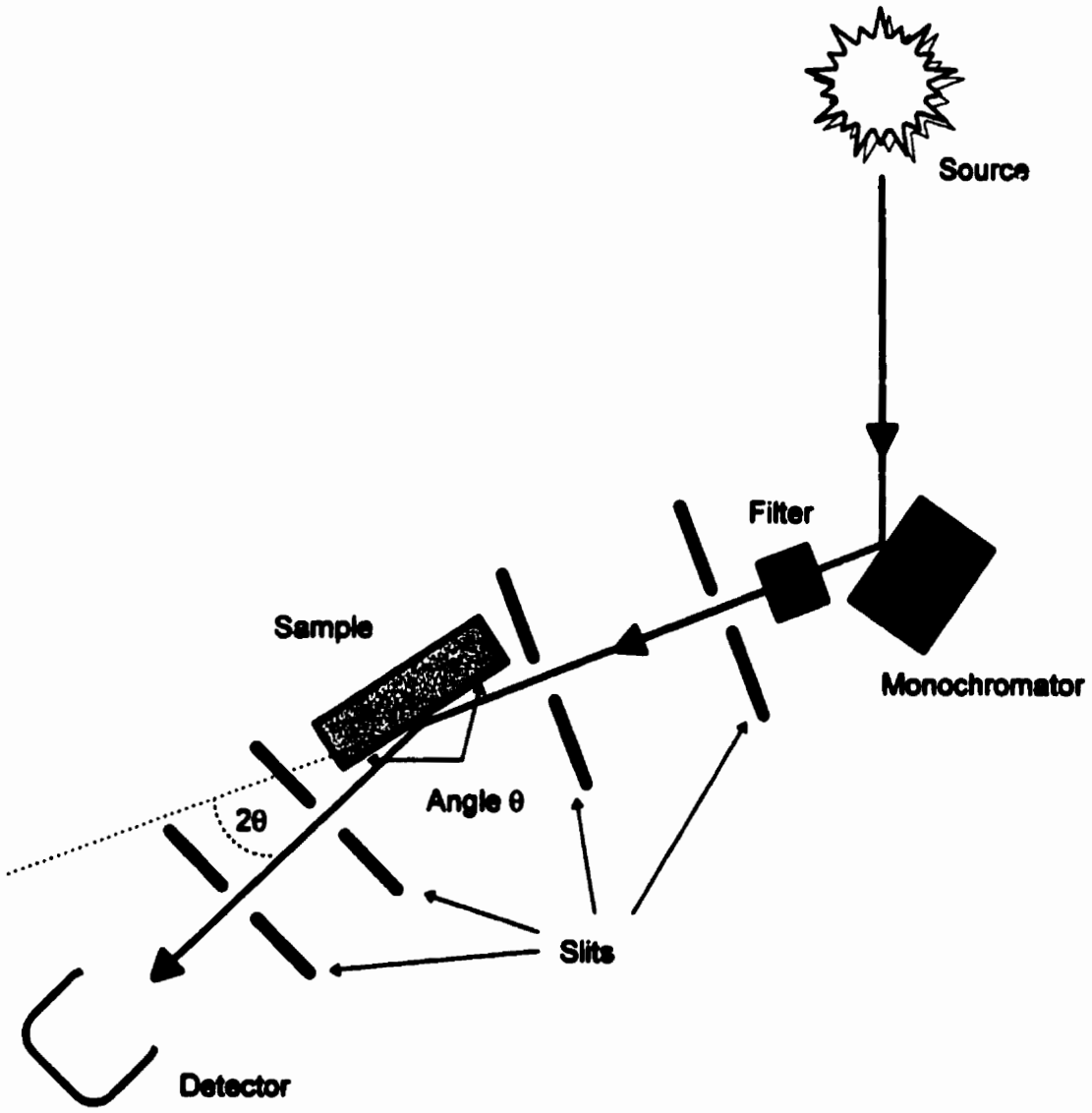

Figure 2.6.5-a Schematic diagram of a neutron reflectometer indicating the neutron beam path and the incidence (θ), reflection (θ) and detector (2θ) angles.

fixed-width slit cut in a piece of Be foil positioned on a computer-controlled slide that allowed lateral translation of the slit position. Two more slits defined by the gaps between another two pairs of computer-controlled Be jaws, positioned on the opposite side of the sample table, collimated the neutrons scattered from the sample before they were counted by the neutron detector. The slits and detector were aligned using the neutron beam, fixing the zero position of the detector (*i.e.*, $2\theta = 0$).

The neutron reflectometry experiments began with a characterization of the as-prepared thin film electrode without the neutron reflectometry cell in place. A holder was mounted on the sample table and the electrode clamped in it, in one of two orientations: first, such that the neutrons were incident on the Ti thin film from the air side; and, second, such that the impinging neutrons passed through the Si slab before striking the Ti film (see Figure 2.6.5-b). This second orientation is also the configuration used for thin film electrodes mounted on the electrochemical cell for *in situ* neutron reflectometry experiments. Once in place, the sample was carefully adjusted to be at the same elevation as the neutron beam and aligned such that the film was parallel to the incident ribbon beam and bisecting it. This fixed the zero position of the rotating sample table (*i.e.*, $\theta = 0$). The alignment was performed using the neutron beam and verified by checking that, with the sample (and sample table) rotated an apparent angle θ with respect to the incident beam, the maximum intensity of specularly-reflected neutrons was found with the detector positioned at an angle 2θ from the incident beam (see Figure 2.6.5-a). This alignment procedure, followed with painstaking care, required roughly a day to complete and yielded an error of less than 0.001 degrees in the value of θ (corresponding to an error in Q of $\pm 9 \times 10^{-5}$ Å^{-1}). With the sample in position and

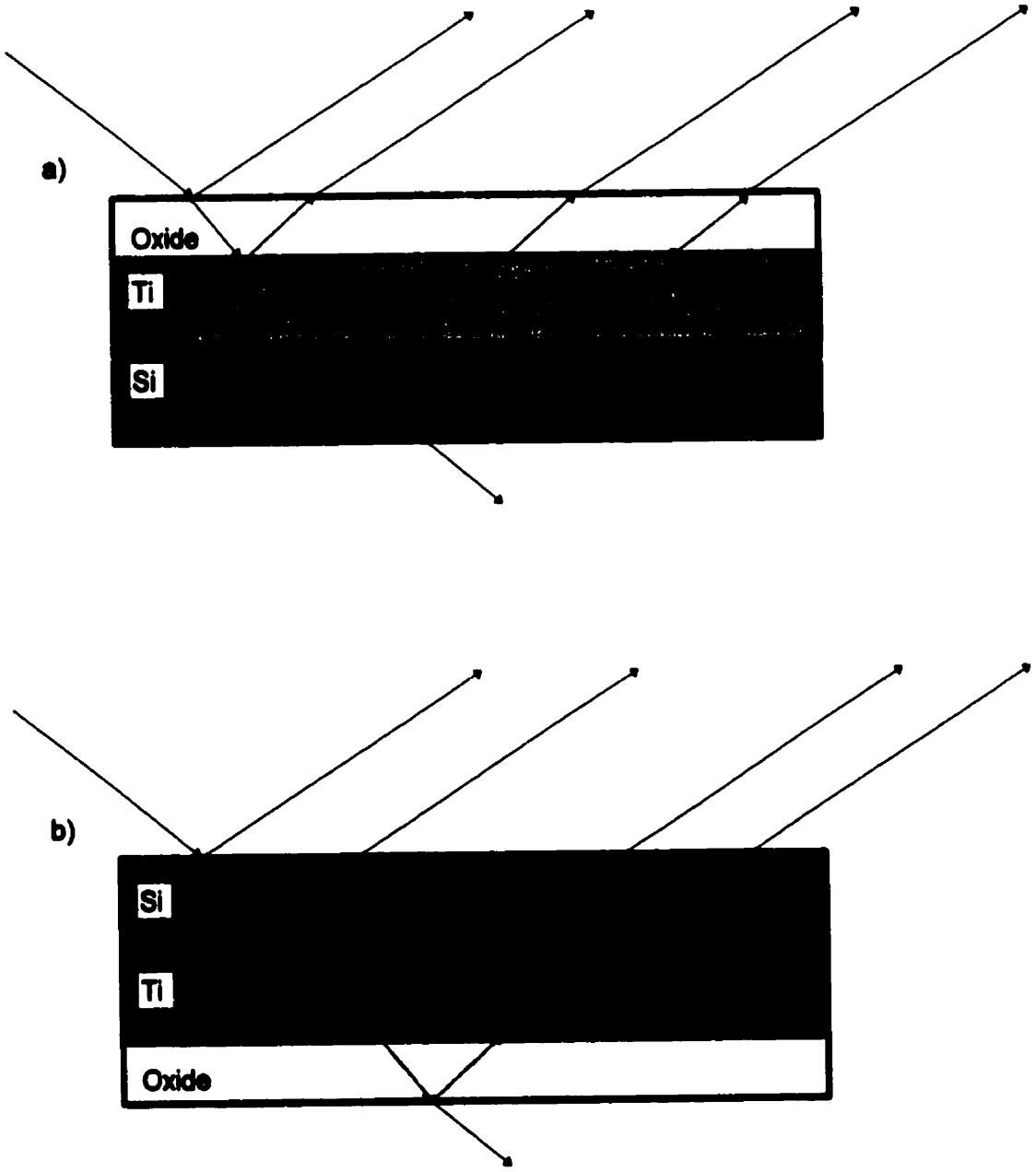

Figure 2.6.5-b Representation of the two sample orientations used for neutron reflectometry experiments, indicating the paths of incident and reflected neutrons (angles greatly exaggerated for illustrative purposes and dimensions not to scale). (a) Neutrons incident on the film from the air side. (b) Neutrons incident on the thin film from the Si side. The latter configuration was always used for electrodes mounted on the electrochemical cell.

aligned, its specular reflectivity was measured by scanning the angles θ and 2θ in a stepwise fashion[1], in increments corresponding to evenly-spaced steps in the magnitude of Q, and counting the number of neutrons that were specularly reflected at each angle. The counting period at each angle was of variable duration, based on the neutron flux, and corresponded to the time required for a certain number of neutrons (the base count) to be emitted from the reactor. This normalization of the neutron count to a known base count of emitted neutrons compensated for variations in the reactor power and allowed direct comparisons between scans acquired at different rates simply by scaling the neutron counts in each scan by the ratio of base counts. The scans were relatively slow, requiring several hours or even overnight to complete, depending on the parameters selected and the reactor power. The neutron spectrometer was fully automated, running under the control of a dedicated DEC μVAX computer.

After reflectometry scans had been recorded on the as-received thin film electrode in the clamp holder, in both orientations, the electrode was mounted on the neutron reflectometry cell, assembled as described in Section 2.3.2. After the sample was realigned in the spectrometer, another reflectometry scan was recorded to ensure that neither the thin film nor its reflectometry profile had been changed in any way by mounting on the cell. Once this scan was completed, the cell was filled with electrolyte (deaerated, 0.27 mol·dm^{-3} NaCl) and E_{oc} recorded every 20 s as described for the electrochemistry/XPS experiments in Section 2.6.3. The Ar purge gas was kept bubbling through the cell for the entire sequence of reflectometry experiments. While E_{oc} was

[1] Done by rotating the sample table through an angle $\Delta\theta$ and moving the detector through an angle of $2(\Delta\theta)$.

being measured, series of *in situ* neutron reflectometry scans were recorded (over the next two days) to monitor any changes in the thin film with exposure time.

Next, the electrode was anodized at +2.0 V, applied in a single step using a Solartron 1286 potentiostat under computer control. While the constant potential was maintained, the current flow was measured by the potentiostat and recorded by the computer (Compaq, 386/16s) every 20 s, and repeated neutron reflectometry scans were acquired. These scans were relatively rapid (requiring ~4 h each) because they had a limited scan range ($Q \leq 0.08$ Å^{-1}). Comparisons of the sequence of rapid scans allowed one to determine when the rate of change in the film reflectivity had become negligible. Once a pair of sequential scans looked identical (usually the second and third scans) an extended scan ($Q \leq 0.16$ Å^{-1}) was recorded, requiring a period of ~15 h.

This procedure of applying a constant potential, recording the current, and acquiring neutron reflectometry scans *in situ* was repeated for a series of lower potentials from 0 to -1.8 V, stepped down at intervals of 0.2 V. A little over one day was spent performing neutron reflectometry scans at each fixed potential. The cell was kept topped up with additions of deaerated 0.27 mol·dm^{-3} NaCl solution to replace electrolyte solution lost by evaporation or through a slow leak around the gasket sealing the working electrode to the cell.

Analysis of the reflectometry scans to determine the thickness and ρb value (see Section 2.1.4) of each layer was performed by least squares fitting of model layer profiles using the MLAYER computer program [187] developed at NIST. The technique of analyzing reflectometry data to determine ρb(z) has been described previously [188]. The

program requires that an estimated trial layer profile be input as a starting point, along with the observed reflectivity data, $R_x(Q)$. This approach treats the sample as a series of layers of constant ρb and d. Rough interfaces between layers are modelled with a sigmoidal[1] variation of ρb between the two media over an interfacial distance, d_i. The user may include as many layers as required to fit the data, and the values of ρb, d, d_i, and other factors may be set as fixed or variable during the least squares fitting procedure. Therefore, care must be taken in the interpretation of reflectometry data, since good agreement of the model with the experimental data can be achieved with models that do not accurately depict the true state of the sample surfaces. Caution was exercised in analyzing the data from these experiments by starting the fitting procedure using the simplest possible model of the sample and adding no features to this model unless they led to significant improvements in the fit, by supporting the model profile with independent evidence (*e.g.*, from XPS or AES) when possible, and by considering whether the fitted model was chemically and physically reasonable.

The thin film electrode was subsequently inspected (*ex situ, in vacuo*) by Auger electron spectroscopy (AES). AES was performed using a Physical Electronics model 590 A SAM spectrometer. The electron beam energy was 3 keV; a low current (3 nA) and beam rastering were used to reduce electron-stimulated desorption of oxygen. Auger spectra were recorded at intervals, alternated with 30 s periods of Ar^+ ion bombardment at 4.5 keV with an average current density of 15.1 $\mu A \cdot cm^{-2}$, to generate a depth profile

[1] A hyperbolic tangent function was used.

through the deposited metal film. The electron beam diameter was 0.5 μm and the analyzed area ~3.6×10^{-3} mm^2.

2.6.6 Crevice corrosion experiments

The apparatus and procedures for these experiments were adapted from those used by McKay and Mitton [19] and Ikeda *et al.* [16]. Crevice coupons of either Ti-2 or Ti-12 were used in these experiments. Separate electrochemical cells were maintained for experiments with each of the two materials to avoid cross-contamination. Each crevice coupon was stamped with steel[1] dies (Imperial Marking Stamps) to impress a unique three-character identification code on one of its 6 mm × 50 mm faces.

Crevice coupons, nuts, and bolts were degreased by sonication in wet methanol (containing ~10% Millipore water). The bolts were then rinsed well with Millipore water and dried in a desiccator containing ~500 cm^3 of anhydrous calcium sulphate (W.A. Hammond Drierite Company, Indicating Drierite). The coupons and nuts were polished with wet silicon carbide paper in the sequence 120, 240, 400, 600 grit on all flat surfaces before being given a final rinse in Millipore water. They were then dried in the desiccator. A small block of PTFE, 12.5 mm × 25 mm, to be sandwiched between the crevice coupons as a "crevice former", was cut with scissors from a 0.8 mm thick PTFE sheet. The crevice former was sonicated in wet methanol, rinsed with Millipore water and dried in the desiccator.

[1] No special corrosion problems (see Section 1.2.5) were observed in the stamped areas, in spite of the use of steel dies.

After the coupons, nuts, bolts, and crevice former had dried in the desiccator for a period of between several days and several months, they were carefully weighed to 0.01 mg on a digital analytical balance (Sartorius, model R180D-**V40). Each of the two crevice coupons required for an artificial crevice assembly was weighed individually, while the two bolts, four nuts, and crevice former were weighed together as a group. All parts were handled only with stainless steel forceps. Three separate weighings of each part or group of parts, taken four hours or more apart, were recorded to ensure the mass was constant and precisely measured. The usual variation in mass was ≤ 0.15 mg.

After weighing, the coupons, nuts, bolts and crevice former were assembled into an artificial crevice by sandwiching the crevice former between 25 mm × 50 mm faces of the two crevice coupons and bolting the assembly together using the nuts, bolts and the bolt holes on the crevice coupons. The crevice former was centred between the bolt holes on the coupons such that it was kept away from the coupon edges as well. This helped avoid "edge effects" during crevice corrosion. The nuts were tightened carefully and evenly using open-faced wrenches while trying to keep the coupons parallel to each other. The tightness was adjusted with the help of a PTFE "feeler" strip cut from the same sheet as the crevice former. The nuts were tightened such that the gap between the coupons was even around its periphery and just small enough that the PTFE feeler strip could not be inserted. This assembly produced two artificial crevices -one between the crevice former and each coupon. In order to ensure wetting of the crevice interior, thereby aiding the initiation of crevice corrosion, the entire artificial crevice assembly procedure was performed with all components submerged in a separate quantity of the same electrolyte solution to be used in the cell.

Before the cell was filled, about 400 cm^3 of electrolyte solution was measured out in an acid-washed, 1000 cm^3 Pyrex graduated cylinder, then poured back and forth between the PTFE pressure vessel liner and the graduated cylinder about ten times with liberal splashing to help aerate the solution. Next, the reference electrode potential was checked against the master SCE potential, and the artificial crevice was mounted on the pressure vessel head by threading the welding rod support (already mounted in the sealing gland in the head) into the tapped hole in one of the bolts holding the crevice together. The planar electrode was threaded onto its support rod and the counter electrode clamped in its holder. The liner was placed inside the pressure vessel body and filled with electrolyte solution, then the head, with all electrodes in position, was lowered onto the body. The three Ti electrodes and the Luggin tip were completely submerged in the electrolyte when the head was in place. The assembled cell is depicted in Figure 2.3.3-a.

Finally, the head was firmly sealed onto the body with the clamping system provided by the manufacturer, and the vessel pressurized with 60 psig of Ar gas. The latter procedure prevented boiling of the electrolyte solution upon heating. The Ar was added without flushing out the air that occupied the vessel headspace when it was closed. This air (~450 cm^3 at room temperature and atmospheric pressure), along with the air-saturated electrolyte solution, provided the supply of oxygen necessary to drive crevice corrosion within the cell.

The sealed and pressurized cell was then placed in an autoclave heater (Parr Instrument Co., model 4913) and fibreglass insulation was added around exposed parts of the pressure vessel head to try to maintain a uniform temperature within the cell. A chrome-

alumel thermocouple, covered with heat-shrink polyolefin tubing to prevent electrical contact with the metallic vessel, was inserted into the cell's thermocouple well and the well opening stuffed with Al foil to reduce heat loss. The thermocouple was connected to a Type K "thermocouple-to-mV" converting panel meter (Omega Engineering Inc., model DP116-KC-GR) with a digital display in Celsius degrees and an analogue output. The working and counter electrodes were coupled together through an electrometer (Keithley, model 617) operating in current-measurement mode. The electrometer's input voltage burden in this mode was < 1 mV. This configuration allowed the measurement of the current flowing between the crevice electrode and the counter electrode, called the "coupled current" by Ikeda *et al.* [16]. This coupled current results from the physical separation of anodic and cathodic sites within the cell, *i.e.*, from electrons produced within the crevice by metal oxidation flowing to the counter electrode to be consumed by oxygen reduction. The electrometer was controlled by a computer (Gateway 2000, 486DX2/50) through an IEEE-488 bus (National Instruments, AT-GPIB). The in-house software adjusted the electrometer's current measurement range such that the measured current was always in the range 5 to 95% of full scale.

Potential measurements were made with a high input impedance ($>10^8\ \Omega$) analogue-to-digital converter (ADC) (Iotech, ADC488/16A). This device offered optical isolation between the analogue inputs and the amplifiers, which eliminated common mode signals and protected the instrument up to 250 V. The ADC had 16-bit resolution over a user-selectable input range of $\pm 1, \pm 2, \pm 5$ or ± 10 V. An internal 1 MByte sample storage buffer and a timer on board the ADC allowed data acquisition to proceed at a precise, regular rate, asynchronous with data transfer to the computer. This freed the computer to

perform other tasks, alternated with reading data from the ADC buffer. All data in these experiments were acquired at a rate of 1 Hz, with a channel-to-channel offset of <10 μs (per channel) since this device was not equipped with simultaneous sample-and-hold circuitry.

The ADC was operated in differential input mode, meaning each input channel required a "high" and a "low" input lead. The output datum was the potential difference between the high and low inputs. Thus, the planar electrode potential measurement required a lead from the planar electrode for the "high" signal and one from the reference electrode for the "low". Similarly, leads from the crevice electrode/counter electrode couple and the reference electrode yielded a potential measurement termed the "crevice potential[1]". The current measurements and temperature values were also digitized by the same ADC, via leads from the analogue outputs on the electrometer and thermocouple converter, respectively. The input voltage range on the ADC was fixed at ± 1 V for the planar electrode potential, crevice potential and temperature measurements, yielding a digitization error of ± 33 μV in the potential and ± 0.03 Celsius degrees in the temperature. The ± 2 V input range was selected for the conversion of current measurements to match the ± 2 V full-scale analogue output of the electrometer. The absolute digitization error in the current measurements depended on the electrometer's current measurement range setting, and varied from 6.6 μA at the highest current range (2 to 20 mA) to 6.6×10^{-17} A at the most sensitive (< 2 pA). All analogue inputs to the

[1] In fact, this is a mixed potential determined by both electrodes in the couple, not just the crevice electrode and is measured from outside the corroding crevice. Consequently it is not, and cannot be used to determine, the potential at active, acidic sites within the creviced area.

ADC were filtered through low-pass RC filters with a 2 s time constant to prevent aliasing of noise and other high-frequency signals beyond the Nyquist sampling frequency.

When the electrical leads were all connected and data acquisition started, the autoclave heater was turned on to heat the cell to the desired temperature. The heater was controlled by a programmable PID temperature controller (Parr Instrument Co., model 4824), which maintained the heater temperature constant to ± 3°C once the desired temperature was reached. The temperature controller received temperature feedback signals via a Type J (Iron-Constantan) thermocouple projecting into the centre of the heater and positioned just below the bottom of the pressure vessel. A second, identical thermocouple, located just below the first, provided temperature signals to a high-temperature safety cut-off circuit in the temperature controller.

Two different methods of heating the cell were used in these tests. In one, the "slow-heat-up" method, the temperature controller was adjusted manually, as required, to induce incremental changes in the cell temperature over a period of days to weeks. In the other heating method, the "rapid-heat-up" method, the cell was heated to the desired temperature as quickly as possible. Rapid-heat-up was desirable in some experiments to ensure maximum temporal separation between changes in the electrochemical signals related to the increasing temperature and those related to the initiation of crevice corrosion. Rapid-heat-up was able to achieve this, since the latter signals were preceded by an "induction period". For the ~100°C temperatures used in the experiments reported in this Thesis, it was determined by trial-and-error that the most rapid cell heat-up,

without temperature overshoot, could be obtained by setting the temperature controller to heat the cell at 250°C (heater temperature) until the interior cell temperature, as indicated by the thermocouple in the cell's thermocouple well, read 80°C. At this point, the temperature controller setting was reduced to ~130°C, which, when combined with the latent heat of the heater at 250°C, resulted in the cell temperature levelling off at 100±3°C. The temperature response of the crevice corrosion cell was very sluggish, due to its large mass and the poor heat transfer properties of the PTFE liner, PTFE thermocouple well sheath, and polyolefin thermocouple sheath. In fact, the actual temperature of the crevice electrode inside the cell *during heat-up* was not accurately known because of this slow response. Even the steady-state temperature of the crevice electrode was somewhat uncertain because neither the temperature controller feedback thermocouple (which indicated ~130°C) nor the measurement thermocouple in the thermocouple well (which indicated ~100°C) was in direct contact with the electrode. However, for the purposes of this experiment, the temperature measured inside the thermocouple well was assumed to be equal to the crevice electrode temperature under steady-state conditions. This is a reasonable assumption since the thermocouple well extended deep within the cell, adjacent to the crevice electrode, the thermocouple was positioned at the bottom of the thermocouple well, and the entire system was well insulated to minimize any steady-state temperature gradients within the cell.

When a crevice corrosion experiment was completed[1], acquisition was halted, the crevice and counter electrodes were immediately decoupled, the other measurement leads and thermocouple removed, the pressure vessel lifted out of the heater (by hand, using thick leather gloves), the gauge block valve opened to relieve the pressure, and the cell opened. The electrolyte solution and PTFE cell liner were briefly examined for milky, white Ti corrosion products or rust-coloured deposits, the latter being a telltale sign of Fe contamination from corrosion of the steel feedthroughs or unseen pieces of tools broken off inside the holes in machined Ti parts. Only one case of Fe contamination was noted and the results rejected. The electrolyte solution was reserved for pH measurement once it had cooled.

The pressure vessel head was removed from the body and all interior components rinsed well with Millipore water. The crevice electrode was unscrewed from its support rod (handling only with latex gloves and stainless steel forceps) and visually examined for outward signs of corrosion or mechanical damage before rinsing again for several minutes with Millipore water and, finally, with methanol. It was then dried in the desiccator for several days before being weighed several times, as was done before the experiment, in this case without disassembling the crevice. When three consecutive weighings gave masses within $\pm$ 0.2 mg of each other, the artificial crevice was opened and the interior surfaces examined visually and with an optical microscope (Olympus, BX60M). Corroded coupons were photographed with a camera (Polaroid, MP-4 Land Camera). Used crevice coupons, nuts, bolts, and the crevice former from each

[1] Completion in this context refers to the achievement of the experimental goals, and did not always correspond to cessation of crevice corrosion.

experiment were preserved in tin-plated canisters for later reference or metallographic image analysis.

2.6.7 Hydrogen absorption experiments

These experiments were performed using hydrogen absorption coupons made of Ti-2 or Ti-12 as the working electrodes. The coupons, hydrogen absorption cell and electrolyte were prepared as described in Section 2.6.1 for the activation experiments with hydrogen absorption coupons. The cell temperature for these tests was held at either 25 or 95°C. Electrochemical measurements were made with a Solartron 1286 potentiostat/galvanostat working in the three-electrode configuration. The potentiostat/galvanostat was controlled by a Compaq 386/16s computer through a National Instruments AT-GPIB IEEE-488.2 interface running in-house software.

Each hydrogen absorption experiment began with an activation experiment, in which E_{oc} was monitored for about six hours. This procedure allowed the electrode to come to a reasonably steady condition before hydrogen charging was begun. Any hydrogen generated by corrosion reactions while the electrode was at E_{oc} was not separately quantified, as it generated no measurable external current. Consequently, any hydrogen absorbed by the metal during this period would contribute to an overestimation of the hydrogen absorption efficiency. The results of galvanostatic (*i.e.*, constant current) hydrogen absorption experiments at 95°C demonstrated that hydrogen was not absorbed under the usual open circuit conditions at 95°C (see Section 3.4.3). It has not yet been determined how significant this absorption may have been in 25°C experiments.

Subsequent to completion of the E_{oc} measurements, electrochemical control was established and the hydrogen absorption part of the experiments performed. This was done galvanostatically (*i.e.*, by applying a constant current) while the resulting electrode potentials were recorded, at approximately 20 s intervals. In each experiment a single fixed current was applied to the working electrode for a known period of time in order to pass a known amount of charge. Argon gas continually purged the cell throughout these experiments. Upon expiration of the charging period, the application of external current was immediately stopped and the hydrogen absorption coupon emersed from solution, rinsed with Millipore water, cut from the Ti support wire along with the small amount of bare wire that had been exposed to solution, dried, weighed and submitted for absorbed hydrogen analysis.

Absorbed hydrogen analysis was performed by a hot vacuum gas extraction technique. In this analysis a Ti coupon was inserted into a vacuum chamber, which was subsequently evacuated, and inductively heated to ~900°C. At this high temperature, the Ti-H phase equilibrium strongly favours hydrogen in the gaseous phase over dissolved hydrogen in metal [189], and the hydrogen rapidly exits the metal. After the hydrogen had been extracted from the coupon, the pressure of the gas released by heating was measured in a known-volume vessel in the vacuum system. The concentration of hydrogen in the metal was calculated from the amount of gas released and the mass of the coupon. The accuracy of this technique was ± 10% and the precision was ± 5%. The detection limit was about 1 $\mu g \cdot g^{-1}$ absorbed hydrogen in metal. Coupons that had not undergone any electrochemical treatment were also submitted for analysis to determine the hydrogen concentration of the as-received material. These values are reported in Table 2.1-a.

3. Results and Discussion

3.1 General electrochemistry of titanium in aqueous chloride solutions

3.1.1 Activation experiments

Figure 3.1.1-a shows a series of activation transients recorded on Ti-2 specimens in deaerated 1.0 mol·dm^{-3} HCl at 25°C. Before immersion in the acid, each sample was polished then exposed to air for a period of between 0 and 20 h. In each case, the measured value of E_{oc} was observed to decrease from its starting point of -0.2 to -0.3 V to a value of -0.6 to -0.7 V. This can be explained as an activation event [11], since E_{oc} decreases from a value associated with the passive region on Ti in acid (E > -0.3 V) to one associated with the active dissolution region ($E \leq$ -0.5 V, see Section 1.2)[1]. For activation to occur, the passive oxide film that forms spontaneously on the fresh Ti surface when it is exposed to the air must be penetrated or thinned to a degree that renders it non-protective. In the current experiments it is reasonable to think that the highly acidic solution dissolves the oxide film, exposing the underlying metal, which then undergoes active corrosion [11]. These results are consistent with those of experiments performed by Kelly [11], Thomas and Nobe [151], and Brauer and Nann [190].

As Figure 3.1.1-a shows, the time required for activation to occur depends on the length of time that the surface was exposed to air. This is an expected result, since it should take longer to dissolve the thicker, less defective oxide films that should be produced by

[1] See also the potentiostatic polarization curves for Ti in aqueous chloride solutions at various pH values recorded by Kelly [11].

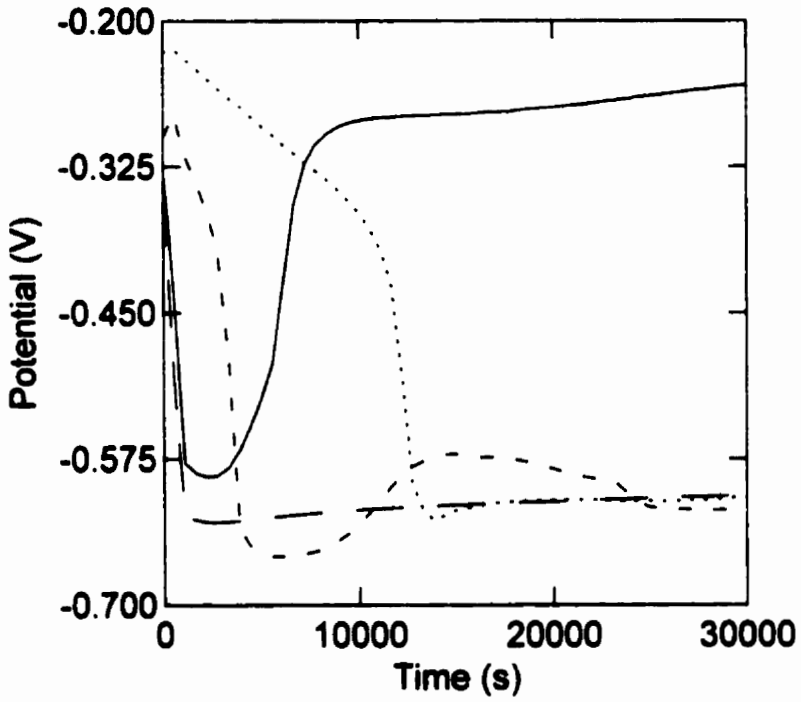

Figure 3.1.1-a Activation transients for Ti-2 in deaerated 1.0 mol·dm^{-3} HCl at 25°C recorded after the electrode surfaces had been exposed to air for <1 min (———), 5 min (—— —— ——), 4 h (– – – –), or 20 h (· · · · · ·).

longer periods of air exposure [71]. A similar series of pre-treatment-dependent activation transients was acquired by Brauer and Nann [190] in 3 mol·dm^{-3} H_2SO_4 after they exposed their electrodes to a variety of different environments with different oxidizing characteristics. Another similarity between the two series is that the starting values of E_{oc} were higher in those tests for which activation was slower. This observation is also consistent with the suggestion that the longer treatments generate oxide films of increasing thickness and decreasing defectiveness.

The results of E_{oc} measurements do not provide sufficient information to determine whether oxide penetration occurs generally or locally. For example, similar activation transients were observed on magnetite-covered carbon steel or iron electrodes exposed to an acidic magnetite-dissolving reagent [191-193]. When these specimens were examined under an electron microscope it was observed that the magnetite layer had been stripped from only a small fraction of the underlying metal surface during activation. While it has been reported by some authors [104, 116] that chemical dissolution of oxide from Ti occurs uniformly (see Section 1.3), localized attack has been observed by others [107, 108, 152]. It is highly likely that the oxide layer formed on the current specimens is not uniform since their surfaces have a relatively rough (600 grit) finish. Therefore, it seems even less likely that activation would occur uniformly across these sample surfaces.

In all but one of the activation experiments reported in Figure 3.1.1-a, once the activation event occurred, E_{oc} remained in the active region, suggesting that the electrode was undergoing active corrosion. The exception occurred on the electrode that had been immersed in the acid immediately after polishing. In this case, E_{oc} remained in the active

region for only a short period (~4000 s) before rebounding to a value in the passive region (E > -0.3 V). This sort of "activation-rebound" phenomenon was observed many times on freshly polished Ti-2 electrodes in HCl in the concentration range 0.1 to 1.0 mol·dm^{-3}, but never, in spite of over 15 trials in 1.0 mol·dm^{-3} HCl, on specimens that had been exposed to air overnight before immersion at 25°C. This potential rebound effect has also been observed on Ti-12 in 1.0 mol·dm^{-3} HCl. Figure 3.1.1-b shows activation transients for freshly polished Ti-2 and Ti-12 in 1.0 mol·dm^{-3} HCl at 25°C for comparison. It is noteworthy that the time required for the rebound to occur on Ti-12 (~100 s) was roughly 40 times shorter than that on Ti-2.

The genesis of this potential rebound effect remains uncertain, however the comparison between Ti-2 and Ti-12 lends credibility to the following speculation. As discussed in Section 1.2.5, built-in anodic protection is afforded Ti alloys incorporating dilute distributions of elements or compounds that catalyze proton reduction, most notably Ni or noble metals. Exposure of these catalytic species to strong acid at the metal surface drives E_{oc} in the positive direction, into the passive region, to a value at which the cathodic half-reaction is as slow as the anodic one [13]. Thus, E_{oc} would drop initially, signifying activation, and rise again soon after as the catalytic sites were exposed.

This explanation seems quite reasonable in the case of Ti-12, which contains small amounts of Ni, largely in the form of Ti_2Ni intermetallic precipitates at grain boundaries [43, 44]. These intermetallic compounds are known to be catalytic for proton reduction [43, 68]. Activation of the Ti-12 surface would expose these catalytic sites at the metal surface, causing E_{oc} to be driven rapidly into the passive region (see Section 1.2.5). On

a)

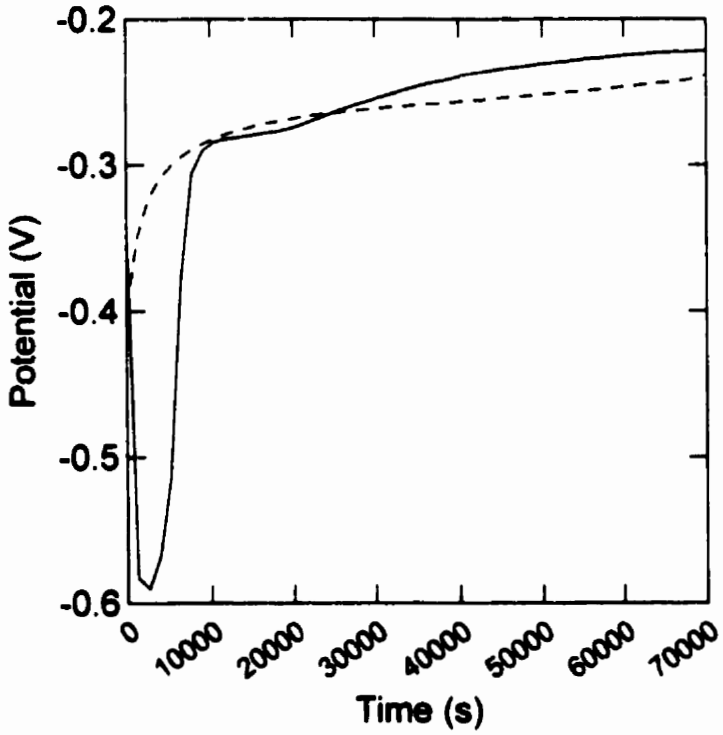

Figure 3.1.1-b a) Activation transients for freshly polished Ti-2 (———) and Ti-12 (- - - -) in deaerated 1.0 mol·dm^{-3} HCl at 25°C.

b)

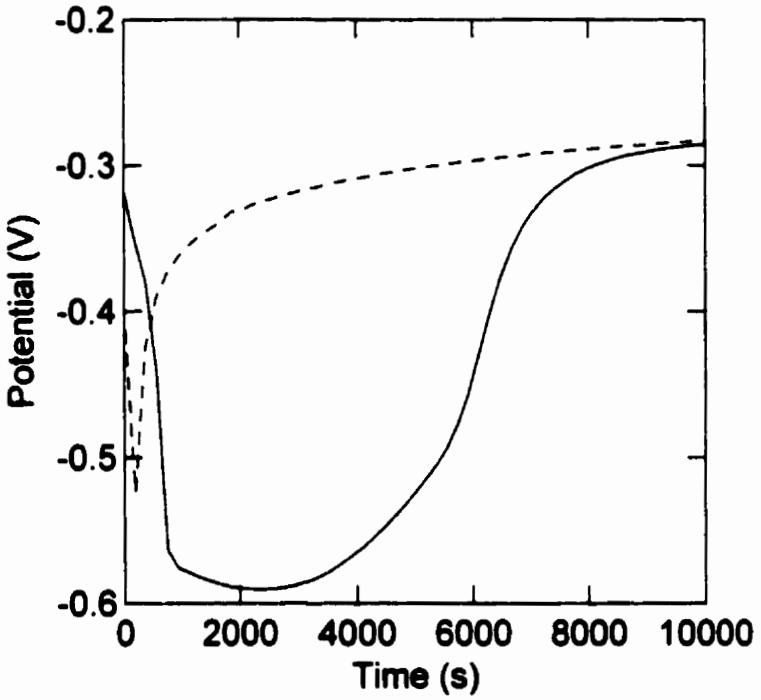

b) Expansion of part a) above showing the initial activation behaviour.

the other hand, the Ti-2 used in these experiments contained no detectable Ni or noble metals (see Table 2.2-a); its main impurities are Si and Fe. The effect of these two elements is uncertain, but intuition suggests that Si would be unlikely to offer the catalytic response necessary to passivate Ti under these conditions. The literature contains contradictory opinions as to the beneficial or detrimental effects of Fe on the corrosion properties of Ti [16, 33, 44, 80-82]. The exchange current density for hydrogen on iron is about 3×10^{-6} A·cm^{-2} [194], roughly two orders of magnitude higher than that on Ti. There are suggestions that sufficient concentrations of Fe may help to passivate Ti [81, 82] but other data show that Fe contamination accelerates Ti corrosion [80], especially if the Fe is present in the form of embedded particles [80, 81].

Bailey *et al.* [27] and Ikeda *et al.* [34, 35] performed and reported on a number of crevice corrosion experiments on a high-iron (~1200 ppm Fe) Ti-2 material whose crevice corrosion performance mimicked that of Ti-12. Further investigations of the effect of Fe concentration on Ti corrosion revealed that Fe can provide anodic (corrosion) sites and adds a degree of unpredictability when it is present incorporated into β-phase or martensitic phases [44]. However, Ni impurities often accompany Fe impurities [43, 44], and it is the former that enhance the corrosion resistance of Ti, by the cathodic modification mechanism described above (see Section 1.2.5). Even in the presence of Fe, Ni, in sufficient concentrations, can provide Ti alloys with enhanced corrosion resistance [43]. The Ti-2 material containing 1200 ppm Fe, mentioned above, was found to contain ~120 ppm of Ni, which was credited for generating the Ti-12-like behaviour towards crevice corrosion [44]. The Ni concentration of the Fe-containing corrosion-resistant materials used by other researchers [81, 82] was not reported.

Since the Ti-2 used in the experiments presented here contained about 1050 ppm Fe and *no* detectable Ni or noble metals, yet behaved as if rendered passive by cathodic modification, an alternative explanation must be found. One hypothesis is that active corrosion of the Ti, driven by proton reduction, results in hydrogen absorption or adsorption by the Ti to form a surface "hydride"[1], which can then catalyze proton reduction sufficiently well to passivate the Ti-2. Titanium hydride is a known hydrogen catalyst, with exchange current densities on the order of $2.5\text{-}5.0 \times 10^{-7}$ A·cm^{-2} [195], or about an order of magnitude greater than Ti, but much less than the exchange current densities of cathodically modifying alloying elements (see Section 1.2.5). Furthermore, Fe present in the surface in particulate form is known to aid in the uptake of hydrogen by Ti [80, 81] by providing a pathway through (around, really) the oxide film that normally protects the Ti metal from hydrogen absorption. Perhaps the Fe-containing intermetallic precipitates present in this material can behave in a similar fashion under certain circumstances.

The longer period of active dissolution seen for Ti-2 compared with Ti-12 is consistent with the requirement that a certain amount of corrosion, and therefore proton reduction, take place in order to generate sufficient amounts of surface "hydride" to effect repassivation. Furthermore, the lower exchange current density on Ti hydrides compared to that of noble metals would mean larger surface coverages by hydride would be necessary to yield an equivalent level of anodic protection. In that sense, Fe-rich precipitates in the Ti-2 may have a dual role in promoting surface "hydriding" in this

[1] It is unclear whether a phase hydride (TiH_x), or simply adsorbed H on Ti would be required at the electrode surface to generate this response.

case, acting as both corrosion accelerators and entry points for hydrogen. This dual effect of Fe, along with the participation of Ni co-contaminants, may also account for some of the contradictory evidence concerning the beneficial or detrimental effects of Fe in Ti alloys.

The effect of pH on the shape of the activation transients is shown in Figure 3.1.1-c for freshly polished Ti-2 disk electrodes at 25°C in acidic chloride solutions with HCl concentrations[1] ranging from 10^{-4} to 2.5 mol·dm^{-3} (pH ≈ 4 to -0.4). Three distinct types of behaviour have been observed. At acid concentrations stronger than about 1.0 mol·dm^{-3}, freshly polished Ti-2 activates and remains active. At pH values in the range 0 to 1, the specimens appear to activate, then E_{oc} rebounds to the passive region as discussed above. Finally, in less acidic solutions (pH > 1), spontaneous activation does not seem to occur, and E_{oc} even increases with time. The latter observation is consistent with the reports of Kelly [11] and Thomas and Nobe [151] that the *maximum* pH for which a stable active state could be achieved, even after cathodic polarization or activation in HF, is about 2-2.5 in chloride-containing solutions at 30°C. The observation that E_{oc} increases with time in the higher pH solutions was also reported by Thomas and Nobe [151] and may indicate an ongoing repair of defects in the passive film present on the electrode surface.

An interesting "dual" or "bifurcated" response appears to be possible in 0.1 mol·dm^{-3} HCl (pH ≈ 1). Repeated experiments in these solutions have shown significant variability. Figure 3.1.1-d shows three activation experiment trials on freshly polished Ti-2 in pH 1

[1] For solutions with pH ≥ 0, the total chloride concentration was fixed at 1.0 mol·dm^{-3} by adding NaCl.

a)

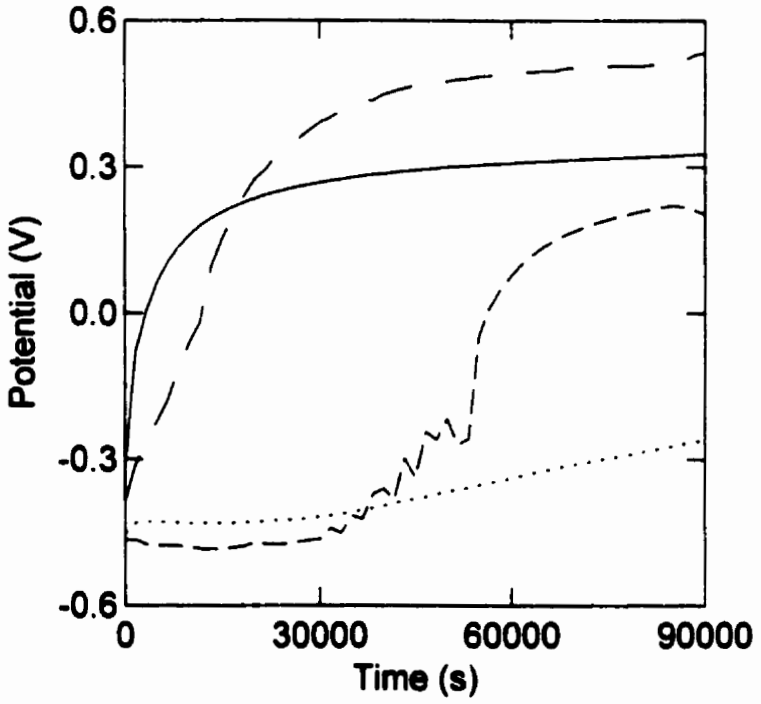

Figure 3.1.1-c Activation transients for freshly polished Ti-2 disk electrodes in chloride solutions at various pH values. a) High pH range; pH = 1.5 (· ·· ··· ····), pH = 2 (— — — —), pH = 3 (— — —), pH = 4 (— — — — —).

b)

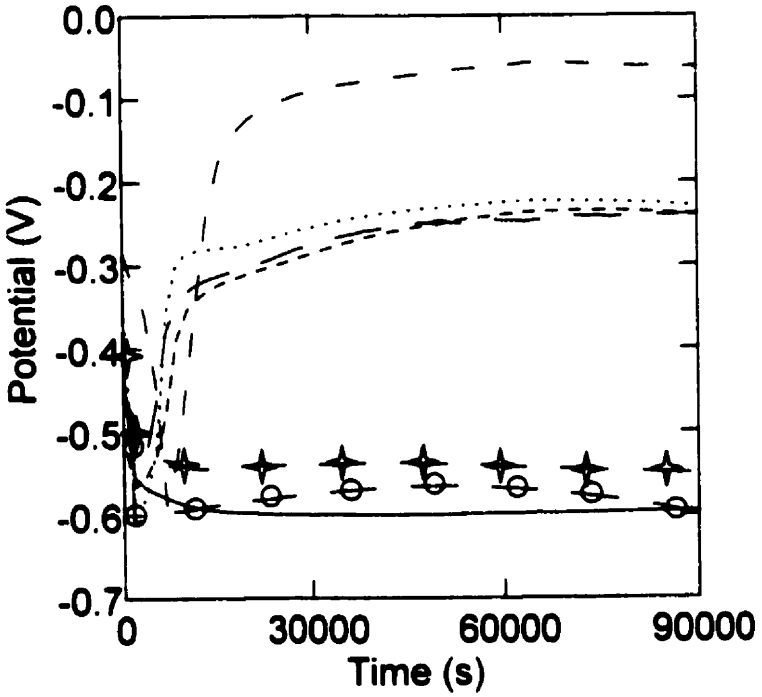

b) Low pH range; pH = -0.4 (—O— —O— —O—), pH = -0.2 (—✦— —✦— —✦—), pH = 0 (· · · · · ·), pH = 0.2 (- - - - -), pH = 0.5 (— — — — —), pH = 0.6 (—— —— ——), pH = 1 (———).

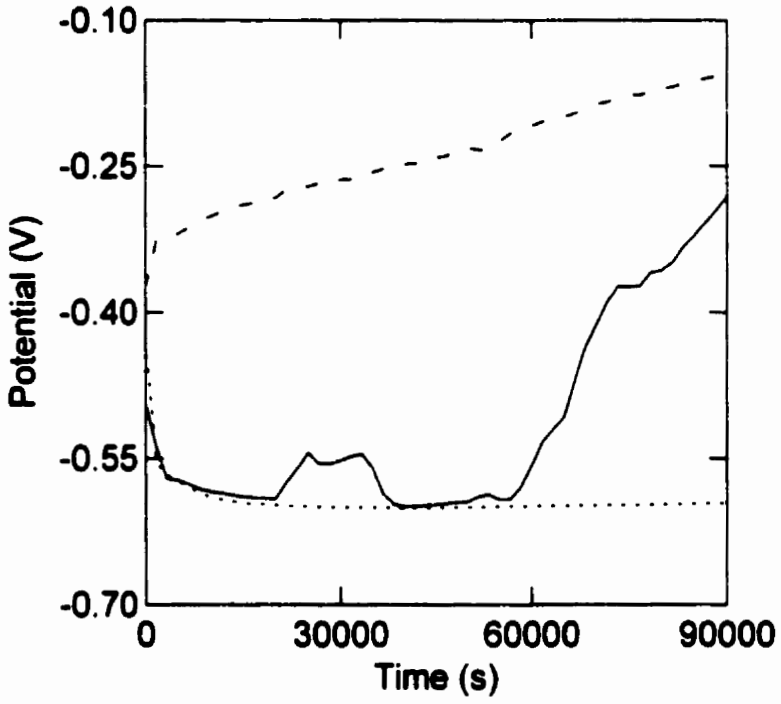

Figure 3.1.1-d Activation transients recorded on freshly polished Ti-2 in 1.0 mol·dm^{-3} chloride solution at pH = 1, three trials.

chloride solution at 25°C. In one experiment, activation was not observed and E_{oc} drifted in the positive direction, similar to the behaviour exhibited in higher-pH solutions. In another, E_{oc} dropped to values within the active region and remained there for the duration of the experiment. Finally, in the third test, a combination of behaviours was observed. Initially, the electrode appeared to activate and E_{oc} remained within the active region for about 20 000 s. Next, a rapid rise in E_{oc} was observed, followed later by a return to the previous active region values, as if the electrode was about to passivate but, for some reason, was unable to do so and re-activated instead. After another period of about 20 000 s at active region values, E_{oc} climbed, in a somewhat noisy way, to values within the passive region. Again, E_{oc} measurements provide insufficient information to draw any solid conclusions from these observations, but hint that pH 1 is probably a condition near the balance point of kinetics between reactions that lead to active corrosion and those that lead to repassivation of Ti in 1.0 mol·dm^{-3} chloride solution at 25°C.

In contrast to tests performed on freshly polished samples, numerous activation experiments (a total of 37) performed in 0.1 mol·dm^{-3} HCl + 0.27 mol·dm^{-3} NaCl at 25°C on Ti-2 hydrogen absorption coupons that had been exposed to air overnight showed little variability (as intended by the air exposure treatment), and none of the specimens exhibited active E_{oc} values at any point during the acid exposure period. In a sense, then, it was impossible to observe any potential rebound behaviour in these experiments because the electrodes did not undergo any (apparent) activation.

It is difficult to rationalize these observations with those for freshly polished specimens other than to say that, because of the longer period of air-exposure, the passive oxide was

probably more uniform and complete on the aged specimens at the time of immersion [71]. One can only speculate on how this would generate the effects observed. Two possible explanations are that once the alloy is well-passivated, activation is too difficult to proceed under these conditions, or that the activation is slowed enough and limited to so few sites that it largely overlaps the "rebound" process that repassivates the surface, and therefore no large potential change is measurable.

In Figure 3.1.1-e, the E_{oc} values at the end of the activation experiments were plotted against the solution pH for freshly polished Ti-2 disk electrodes in 25°C solutions. These data should be viewed with caution, however, since they do not necessarily represent steady-state conditions, nor are they wholly comparable with each other, because some were acquired after relatively short periods of electrode immersion, and others after much longer periods. The relatively wide scatter in the data reflects the consequences of these experimental inconsistencies. In spite of this, one can see that there is a general trend to higher E_{oc} values with increasing pH. Furthermore, there appears to be a plateau in E_{oc} values over the pH = 0 to 1 range, coinciding with the series of transients that displayed the activation-rebound behaviour illustrated in Figures 3.1.1-a and -b and discussed above.

E_{oc} values taken at the end of the activation experiments performed with the air-exposed hydrogen absorption coupons are also plotted in Figure 3.1.1-e. These data are much more reliable, in the sense that the E_{oc} values at the end of these tests were generally close to a steady state, and the duration of the immersion period was nearly the same in each experiment. As a result, much less scatter was observed in the final E_{oc} values. As

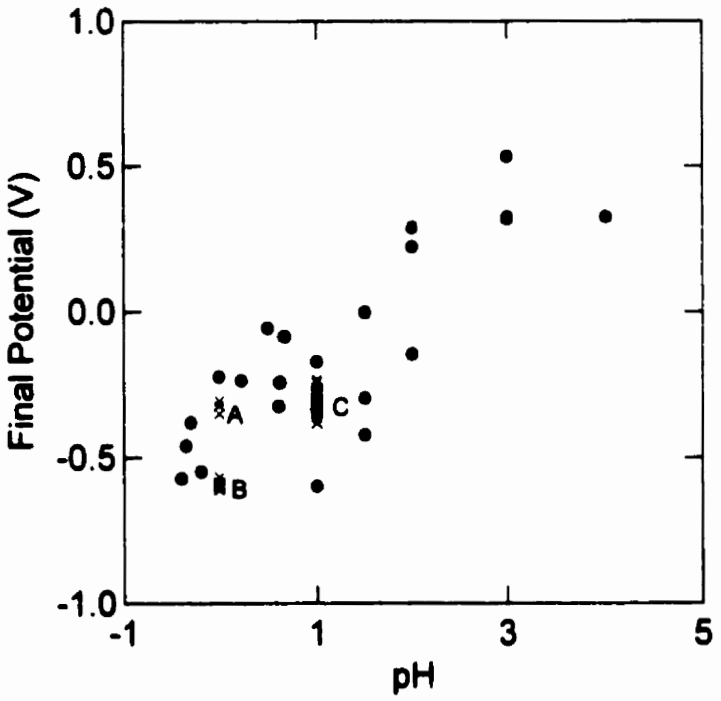

Figure 3.1.1-e E_{oc} *values at the end of activation experiments on Ti-2 in chloride solutions at 25°C;* (•) *freshly polished disk electrode,* (×) *hydrogen absorption coupon exposed to air for 20 h before immersion. The letters indicate the number of replicate experiments in each cluster of points with symbol "×"; (A) three trials, (B) ten trials, (C) 37 trials.*

described above, no activation-rebound phenomena were observed in 13 experiments performed on air-exposed samples at 25°C in 1.0 mol·dm^{-3} HCl solutions (pH ~ 0). Under these conditions, the electrodes either activated and remained at active-state E_{oc} values (10 trials), or did not activate at all within the measurement period and remained at passive-state E_{oc} values (three trials). In 0.1 mol·dm^{-3} HCl + 0.27 mol·dm^{-3} NaCl solutions (pH ~ 1) at 25°C (37 trials), the air-aged electrodes did not activate within the measurement period and only passive-state E_{oc} values were observed.

A collection of E_{oc} transients recorded on Ti-2 hydrogen absorption coupons that had been exposed to air for 20 h before immersion in 0.1 mol·dm^{-3} HCl + 0.27 mol·dm^{-3} NaCl solutions at a series of temperatures from 25 to 95°C is given in Figure 3.1.1-f. Unfortunately, it is difficult to extract any clear pattern of temperature-related behaviour from this jumble of E_{oc} transients. Active region E_{oc} values were only observed during the acid exposure period at two temperatures: 50 and 95°C. The electrode immersed in 50°C solution appears to have experienced a long slow activation, followed by an equally slow rebound to higher E_{oc} values. At 95°C, the initial E_{oc} values on immersion were within the active region, but E_{oc} usually climbed quickly into the passive region. On several occasions however (four cases out of 34 experiments), E_{oc} remained in the active region for the duration of the experiment at 95°C (see Figure 3.1.1-g). This apparent dual nature of the E_{oc} behaviour was noted earlier in this Section for freshly polished Ti-2 disk electrodes in pH 1 chloride solutions at 25°C.

The values of E_{oc} at the end of the activation experiments on air-exposed Ti-2 hydrogen absorption coupons in 0.1 mol·dm^{-3} HCl + 0.27 mol·dm^{-3} NaCl are plotted as a function

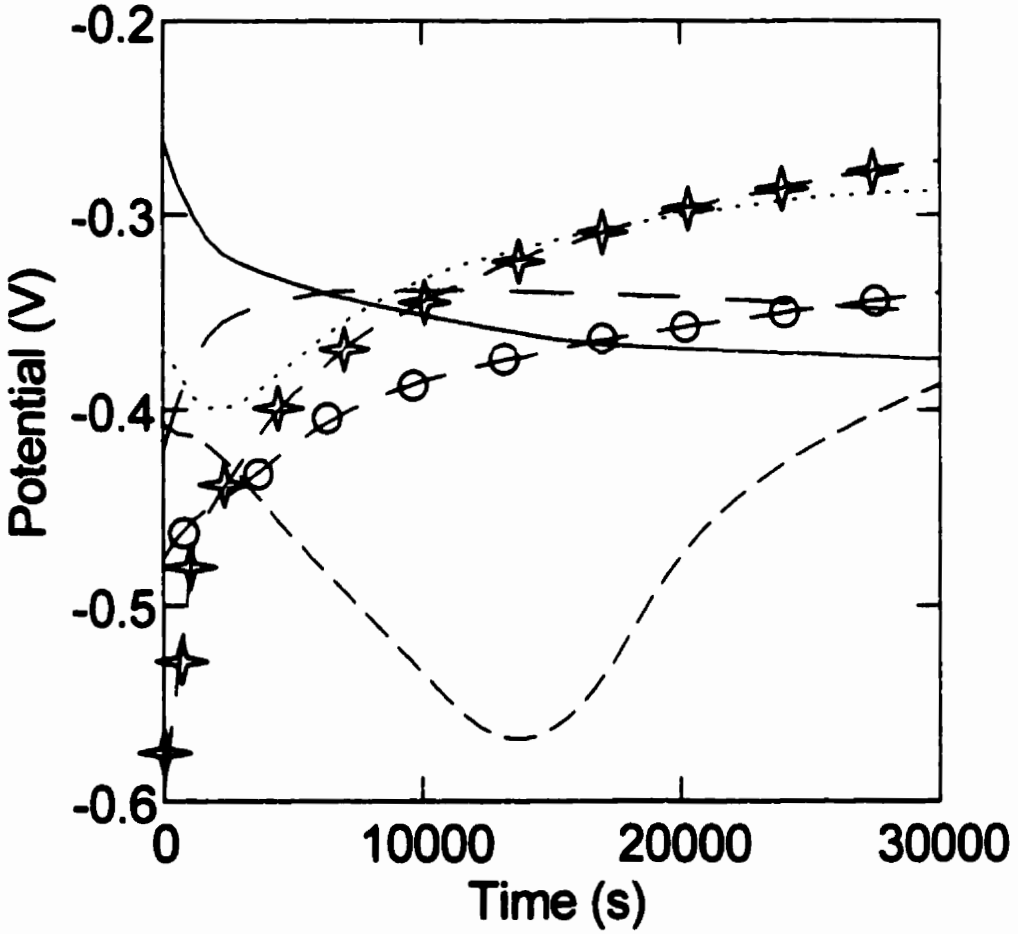

Figure 3.1.1-f Activation transients for Ti-2 hydrogen absorption coupons that had been exposed to air for 20 h before immersion in 0.1 mol·dm^{-3} HCl + 0.27 mol·dm^{-3} NaCl at temperatures of 25°C (———), 35°C (— — —), 50°C (— — — —), 65°C (· · · · · ·), 85°C (—o— —o— —o—), and 95°C (—✦— —✦— —✦—).

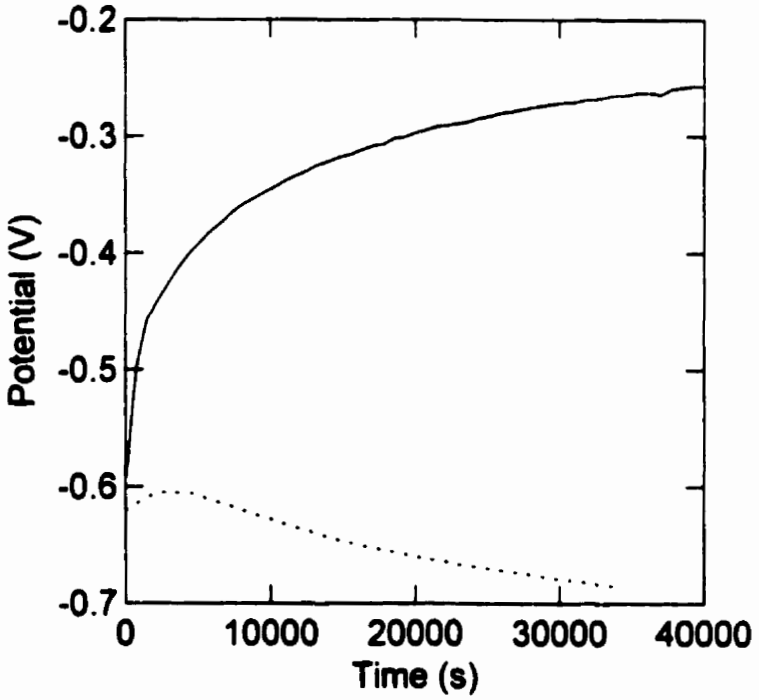

Figure 3.1.1-g Open circuit potential transients recorded in 0.1 mol·dm^{-3} HCl + 0.27 mol·dm^{-3} NaCl at 95°C. Normally, E_{oc} rebounded to a value greater than -0.3 V under these conditions (————), however, it occasionally remained at active region values (· · ·····).

of temperature in Figure 3.1.1-h. This plot indicates that the final E_{oc} values were not directly related to the temperature, but the range of possible values was wider at 95°C. Insufficient data exist at temperatures between 25 and 95°C to determine the temperature dependence of the range of final E_{oc} values; however, one might expect that it is not the *range* of E_{oc} values that is influenced by temperature but rather their *probability distribution*. The range of E_{oc} values possible should be determined by the boundaries of the active and passive regions under the given set of conditions. According to Kelly [11], increasing the temperature causes an increase in the current due to metal oxidation, but not the potential. Thus, it seems more reasonable to consider the temperature dependence of the final E_{oc} values in terms of the likelihood of achieving active or passive conditions[1].

In keeping with this approach, the E_{oc} data recorded on Ti-2 hydrogen absorption coupons at 25 and 95°C from Figure 3.1.1-h are re-plotted in the form of histograms in Figure 3.1.1-i. The histogram for experiments done at 25°C shows a distribution of values centred near -0.3 V. Consistent with the above hypothesis, the E_{oc} values from 95°C experiments are most densely distributed near -0.3 V, but show signs of a bimodal distribution, with the second peak density at active region potentials. Unfortunately, the number of data is too small to clearly define the second mode and distinguish it as being separate, rather than just part of a long tail on the primary distribution mode.

[1] Potentials in the range corresponding to the active-to-passive transition should not be stable, however they may be observed from time to time in non-steady-state experiments such as these.

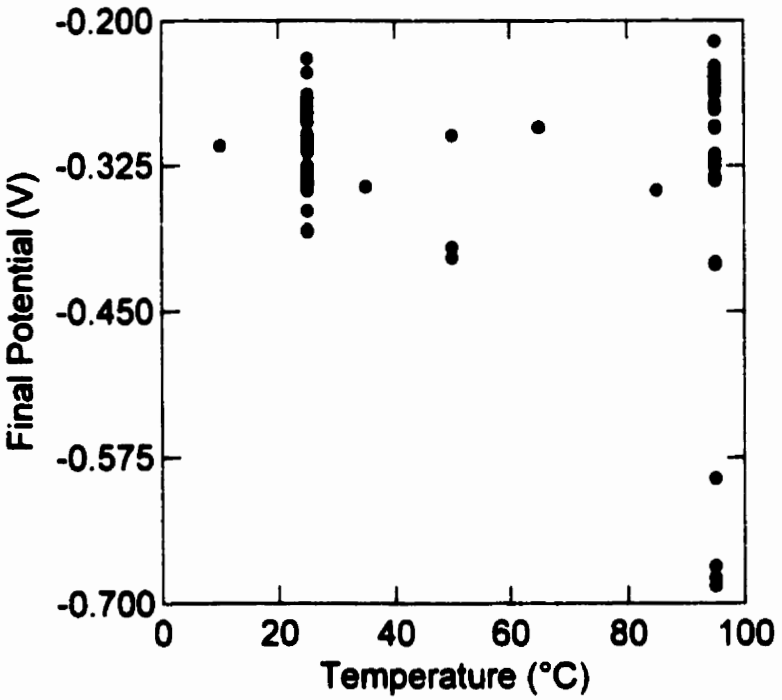

Figure 3.1.1-h E_{oc} *values at the end of activation experiments on Ti-2 hydrogen absorption coupons that had been exposed to air for 20 h before immersion in 0.1 mol·dm^{-3} HCl + 0.27 mol·dm^{-3} NaCl at various temperatures.*

a)

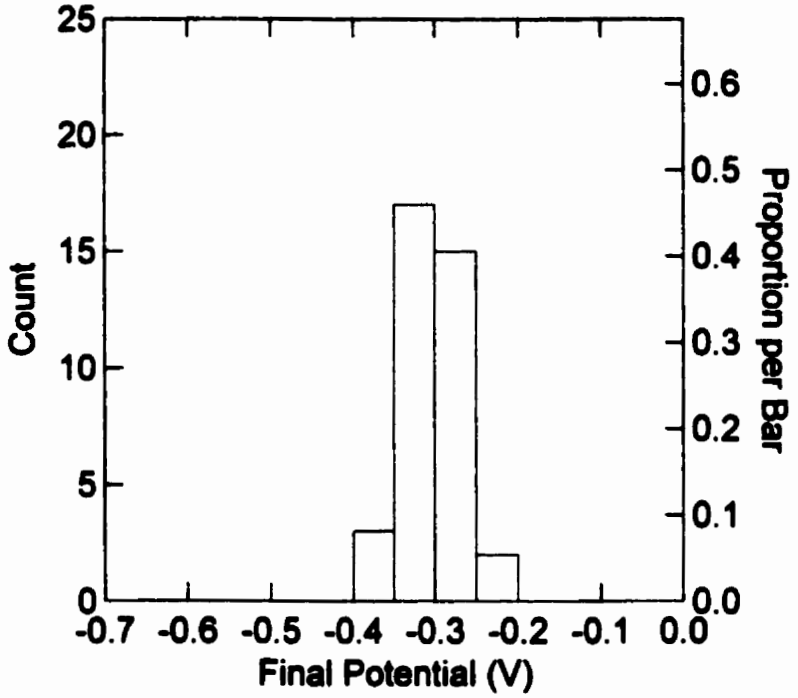

Figure 3.1.1-i Distribution of E_{oc} values at the end of activation experiments on Ti-2 hydrogen absorption coupons that had been exposed to air for 20 h before immersion in 0.1 mol·dm^{-3} HCl + 0.27 mol·dm^{-3} NaCl: a) 25°C,

b)

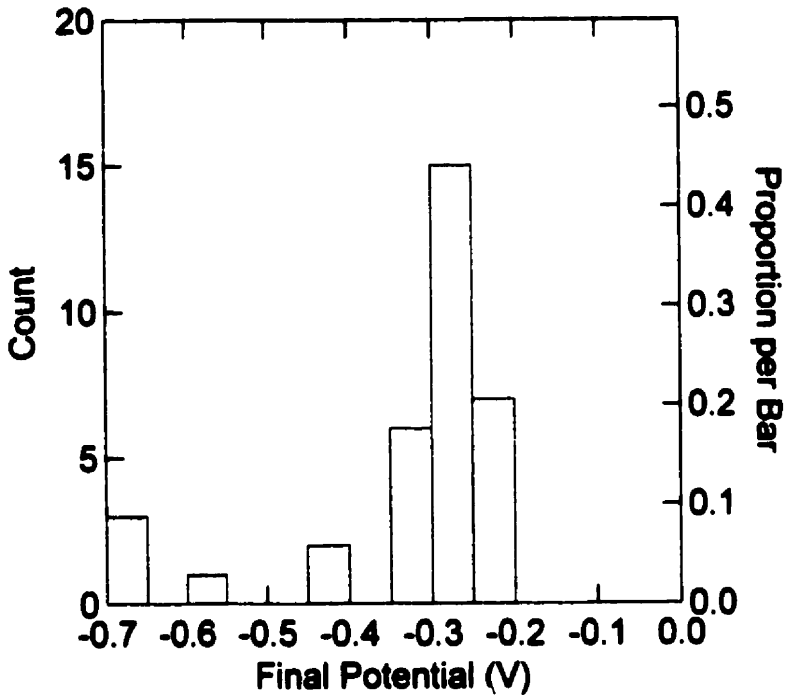
20
15
10
5
0
Count
0.5
0.4
0.3
0.2
0.1
0.0
Proportion per Bar
-0.7 -0.6 -0.5 -0.4 -0.3 -0.2 -0.1 0.0
Final Potential (V)

b) 95°C.

So far, this discussion has focused on describing the phenomenon of occasional activation at 95°C in an observational sense. Much less is revealed by these experiments about the mechanism by which this activation takes place, but evidence gathered from other experiments can provide the basis for conjecture. Clearly, the mechanism of activation on Ti-2 surfaces previously exposed to air for 20 h is not the same in 0.1 mol·dm^{-3} HCl + 0.27 mol·dm^{-3} NaCl at 95°C as it is in 1.0 mol·dm^{-3} HCl at 25°C. As was shown in Figure 3.1.1-a, activation under the latter conditions requires oxide film dissolution to the point of penetration. This could not be the case for the few specimens that activated in 0.1 mol·dm^{-3} HCl + 0.27 mol·dm^{-3} NaCl at 95°C because they activated very rapidly (almost immediately upon immersion). If passive film dissolution was so rapid under these conditions, one would expect most or all of the other air-exposed coupons exposed to these conditions to show a similar activation, much like they did in pH 0 solution at 25°C (see Figure 3.1.1-e); instead, they remained passive for the duration of the tests. In fact, this majority of coupons that achieved passive region E_{oc} values at 95°C all initially showed active or active-to-passive region E_{oc} values for a very short time after immersion, before passive-state E_{oc} values dominated (see Figure 3.1.1-g, for example).

That the surfaces of the four samples that remained active were radically different than those of the other specimens is possible, but rather unlikely given the remarkable reproducibility observed in over 60 experiments with samples exposed overnight to air. A more likely explanation, and one that accounts for the fact that activation was not observed at 25°C under the same conditions, is that activation occurs at weak points and

cracks in the oxide afforded by thermally induced breakdown crystallization. Breakdown crystallization (see Sections 1.3.3 and 1.3.4) can occur at temperatures above 60-70°C [140]. Why only a small number of these electrodes should have activated on breakdown crystallization is uncertain, but it may be that the conditions employed were sufficiently mild that repassivation at the bases of the cracks formed by crystallization was more rapid than acid attack of the oxide or substrate metal in most cases, perhaps due, in part, to the presence of catalytic sites for the cathodic reactions on the metal surface. Thus, while all air-exposed samples immersed in 0.1 mol·dm^{-3} HCl + 0.27 mol·dm^{-3} NaCl at 95°C would have undergone breakdown crystallization to expose the underlying metal at the bases of cracks, and all displayed active or active-to-passive region E_{oc} values at first, most repassivated. This explanation also implies that activation should not be observed on air-exposed Ti-2 in 0.1 mol·dm^{-3} HCl + 0.27 mol·dm^{-3} NaCl at temperatures below 60-70°C and that the probability of activation at temperatures above the crystallization temperature should increase with a decrease in pH. This is also consistent with the observation that temperatures in excess of ~70°C are required for the initiation of crevice corrosion on Ti [40] (see also Section 3.3).

A similar set of activation experiments was performed on Ti-12 hydrogen absorption coupons that had been exposed to air for 20 h before immersion in 0.1 mol·dm^{-3} HCl+ 0.27 mol·dm^{-3} NaCl solutions at 95°C. In each of the 19 trials, E_{oc} measured -0.38 to -0.42 V initially, but increased quickly to more passive potentials. The distribution of E_{oc} values at the end of the activation experiments is shown in Figure 3.1.1-j. In this case, the range of final E_{oc} values was much narrower than that

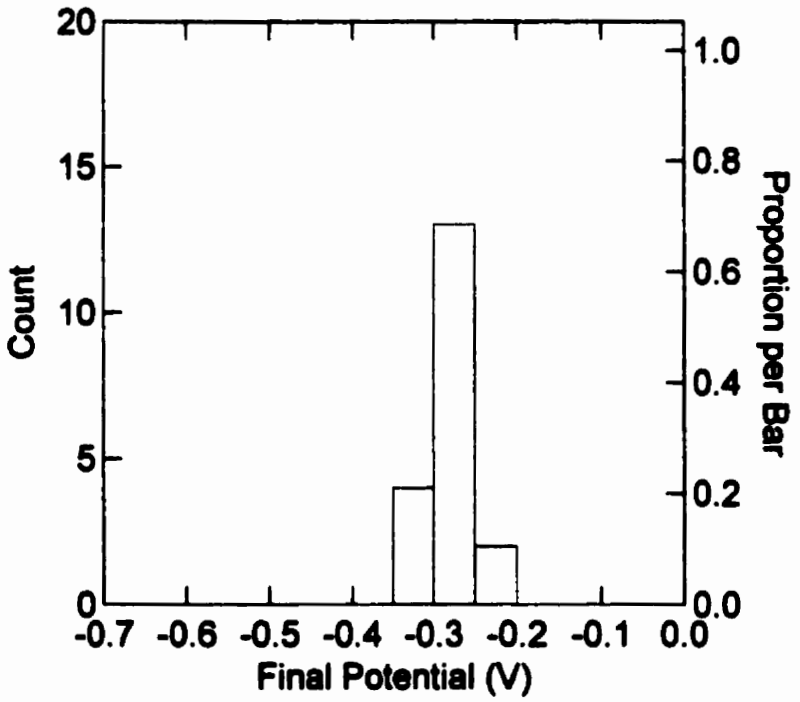

Figure 3.1.1-j Distribution of E_{oc} values at the end of activation experiments on Ti-12 hydrogen absorption coupons that had been exposed to air for 20 h before immersion in 0.1 mol·dm^{-3} HCl + 0.27 mol·dm^{-3} NaCl at 95°C.

observed for Ti-2 coupons (see Figure 3.1.1-i), and none of the Ti-12 coupons activated. The observed passive E_{oc} is expected behaviour, since Ti-12 was designed with Ni and Mo alloying additions specifically to resist activation and crevice corrosion [40] (see also Section 1.2.5). The narrower range of E_{oc} values and the remarkable reproducibility of activation transients on Ti-12 is probably another consequence of having alloying additions present on the metal surface to control the electrochemical behaviour. That is, E_{oc} would be established faster and more reproducibly by the fast kinetics at the catalytically active sites generated by cathodic modification than it would by the slower kinetics on a generally passive surface, or in the case where there is a competition between the kinetics of activation and passivation.

The difference in the activation transients for freshly polished Ti-2 at 25°C in different inorganic acids is shown in Figure 3.1.1-k. As previously noted, in 1.0 mol·dm^{-3} HCl at 25°C, Ti-2 activated then E_{oc} rebounded into the passive potential region. In 1.0 mol·dm^{-3} $HClO_4$, freshly polished Ti-2 did not show any signs of activation, and E_{oc} remained in the passive region for the entire period of electrode immersion. This experiment was repeated twice with the same result -freshly polished Ti-2 did not activate in 1.0 mol·dm^{-3} $HClO_4$ at 25°C. Finally, in 1.0 mol·dm^{-3} H_2SO_4 (pH $\approx$ 0), the freshly polished Ti-2 electrode immediately displayed active E_{oc} values, and showed no sign of repassivating over the duration of the experiment, which, however, was unfortunately very short compared to the length of the other activation experiments. This information is too limited to be used to draw any major conclusions, but suggests that, in addition to the solution pH, the anion plays an important role in the activation process on Ti-2 at 25°C.

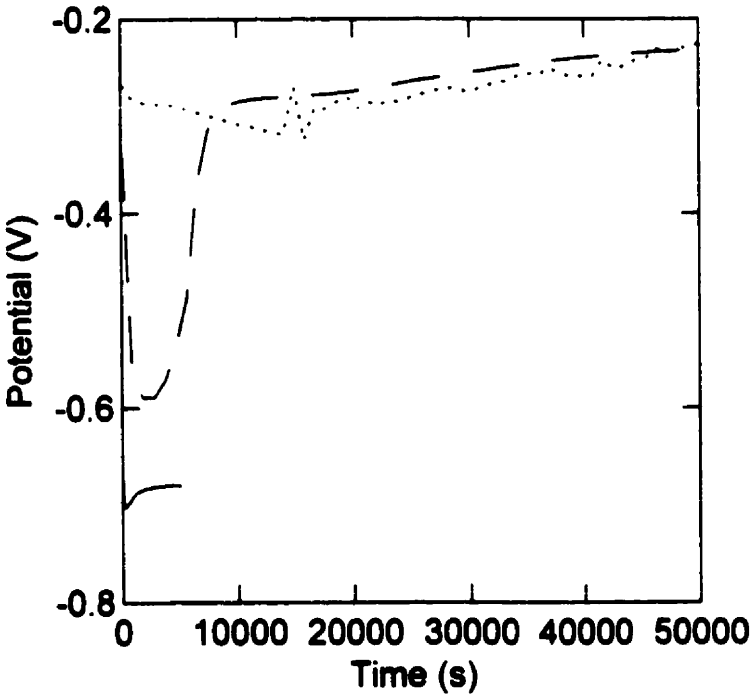

Figure 3.1.1-k Activation transients for freshly polished Ti-2 in 1.0 mol·dm^{-3} concentrations of various inorganic acids at 25°C: HCl (—— —— ——), $HClO_4$ (· ··· · · ·), and H_2SO_4 (————).

Activation experiments were also performed on air-exposed Ti-2 hydrogen absorption coupons in acidic sulphate solutions and acidic mixtures containing both sulphate and chloride at 95°C. The various solution compositions and measured initial pH values are listed in Table 3.1.1-a. In each of these ten experiments the Ti-2 activated and, with the exception of one trial in which E_{oc} rebounded to the passive region, remained active for the duration of the tests. The distribution of final E_{oc} values is shown in Figure 3.1.1-l.

Table 3.1.1-a Composition and Measured Initial pH Values for Sulphate-Containing Electrolyte Solutions.

Solution Composition	Measured Initial pH
0.14 mol·dm^{-3} Na_2SO_4 + 0.05 mol·dm^{-3} H_2SO_4	1.45
0.14 mol·dm^{-3} Na_2SO_4 + 0.05 mol·dm^{-3} H_2SO_4	1.52
0.14 mol·dm^{-3} Na_2SO_4 + 0.05 mol·dm^{-3} H_2SO_4	1.52
0.14 mol·dm^{-3} Na_2SO_4 + 0.05 mol·dm^{-3} H_2SO_4	1.50
0.14 mol·dm^{-3} Na_2SO_4 + 0.1 mol·dm^{-3} HCl	1.40
0.14 mol·dm^{-3} Na_2SO_4 + 0.1 mol·dm^{-3} HCl	1.36
0.14 mol·dm^{-3} Na_2SO_4 + 0.1 mol·dm^{-3} HCl	1.31
0.14 mol·dm^{-3} Na_2SO_4 + 0.1 mol·dm^{-3} HCl	1.35
0.27 mol·dm^{-3} NaCl + 0.05 mol·dm^{-3} H_2SO_4	1.03
0.27 mol·dm^{-3} NaCl + 0.05 mol·dm^{-3} H_2SO_4	1.10

This apparent ability to activate and remain in an active state in solutions containing as little as 0.05 mol·dm^{-3} of sulphate and at pH values as high as 1.5 is in strong contrast with the behaviour observed in sulphate-free 0.1 mol·dm^{-3} HCl + 0.27 mol·dm^{-3} NaCl solutions at the same 95°C temperature. Within the range of conditions tested, neither the pH nor the concentrations of chloride or sulphate appeared to influence the activation behaviour. The rate of non-localized corrosion of Ti in acidic sulphate solutions is known to be greater than that in acidic chloride solutions [11], perhaps due to the greater

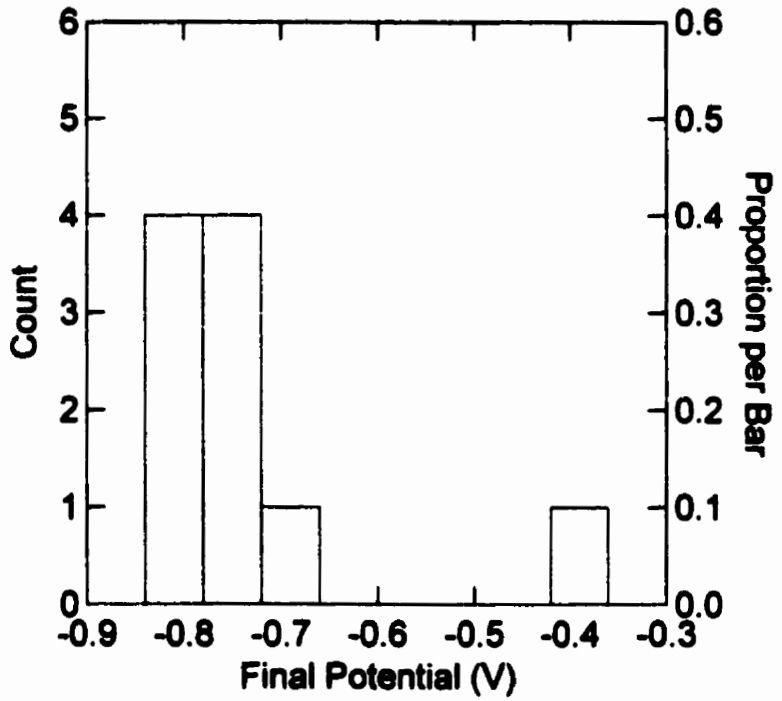

Figure 3.1.1-l Distribution of E_{oc} values at the end of activation experiments on Ti-2 hydrogen absorption coupons that had been exposed to air for 20 h before immersion in solutions containing sulphate or mixtures of chloride and sulphate, with various pH values, at a temperature of 95°C. The solution compositions and pH values are outlined in Table 3.1.1-a.

ability of sulphate to complex Ti cations (see Section 1.2.3). It appears that this aggressiveness also translates into a more facile activation process on Ti-2 at 95°C in acidic sulphate-containing solutions.

One may recall, however (see Section 1.2.4.3), that sulphate was found to *suppress* crevice corrosion propagation, and that this effect was attributed mainly to its ability to complex Ti cations or decrease the critical concentration of Ti(IV) ions required for autopassivation [2]. The activation-enhancing effects of sulphate observed in the former experiments and propagation-suppressing effects in the later need not be as contradictory as they may seem at first. The mechanism (complexation of Ti cations by sulphate) may be the same in both cases, but the contrasting outcome could be a consequence of the differing solution volumes and mass transport rates in the two situations, as well as the difference in the *initial* pH. In the small, restricted space of the crevice, the sulphate may become sufficiently concentrated to be able to control the local pH by preventing hydrolysis or lower the critical concentration of Ti(IV) required for autopassivation, but in the above activation experiments, the large, open volume of the general purpose electrochemical cell would have diluted any complexed Ti cations. Additionally, the pH inside a crevice must develop from near neutral into very acidic on its own by metal cation hydrolysis, while the pH in the activation experiments was acidic by manufacture (*i.e.*, the evolution of an acidic pH could not be prevented because it already existed from the start).

A graph of the distribution of E_{oc} values at the end of activation experiments is presented in Figure 3.1.1-m to help summarize the results of the activation experiments performed.

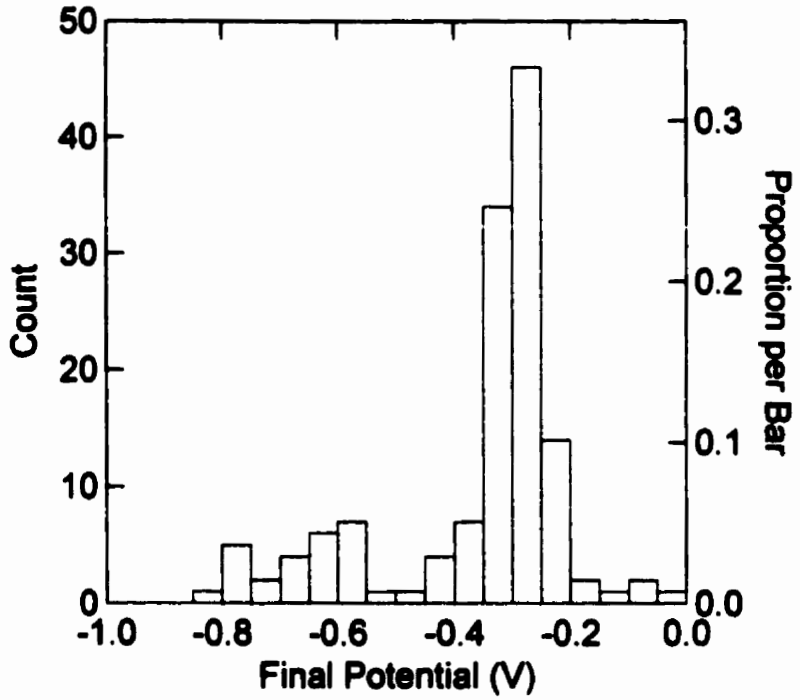

Figure 3.1.1-m Distribution of $E_{\alpha c}$ values at the end of activation experiments for all activation experiments performed in acidic aqueous solutions, irrespective of temperature, pH, and electrode material and type.

The data presented in the Figure consist of final E_{oc} values from all of the activation experiments performed in acidic aqueous solutions, irrespective of the temperature, pH, and electrode material and type. In spite of the variety of conditions under which the experiments were performed, Figure 3.1.1-m helps to emphasize the assertion that only two final steady "states" (active or passive) are possible for Ti surfaces in acidic aqueous solutions. The few indications of E_{oc} values outside these two behavioural regions seen on the graph can be explained as cases in which a steady-state E_{oc} value was not established during the course of the experiment.

One should also be careful not to over-interpret this Figure. The distribution shown must not be interpreted in terms of a probability distribution in this case. Because it contains data from experiments performed under several different conditions, the relative intensity of each peak is related to the number of experiments of each type performed. For example, the magnitude of the peak in the active region could have been made larger by performing more experiments in deaerated 2.0 $mol \cdot dm^{-3}$ HCl, a solution found to yield active-region potentials almost exclusively.

It has been suggested that the state displaying the lower final potential values is characterized by the active dissolution of Ti metal, probably through a residual monolayer of oxygen-containing species on the metal surface (as opposed to bare metal) [10]. Two mechanisms are proposed for the generation of passive-state final potential values. At $pH \geq 2$, the surface is probably passivated by a thin, perhaps somewhat hydrous, phase oxide that spontaneously forms when the rate of oxide accumulation exceeds the rate of oxide dissolution, or by a pre-existing oxide film that could not be stripped by the

relatively high-pH solution. For passivation in solutions with pH < 2, spontaneous passivation via the mechanism described for cathodically modified alloys, wherein the cathodic kinetics are enhanced, seems reasonable for Ti-12 electrodes. It is also suggested here that a similar mechanism of passivation may operate on the Ti-2 material used. In the latter case, however, cathodic modification would be generated not by catalytic or noble metal alloying additions, but by a surface hydride formed on the Ti during the initial corrosion process. Two remaining questions are the nature of the initial breakdown of the native oxide and how it is related to the final state achieved by the surface.

3.1.2 Polarization Curves

A number of potentiostatic polarization curves have been recorded on Ti electrodes in acidic aqueous electrolyte solutions. To clarify the discussion of the polarization behaviour, these can be divided into two types - anodic and cathodic polarization curves. The division point between the two types is usually E_{oc}; *i.e.*, cathodic polarization curves are characterized by a cathodic current response to the applied potential (normally a potential less than E_{oc}) and anodic polarization curves are characterized by an anodic current response (normally generated by applying potentials greater than E_{oc} to the electrode). As a consequence of this definition, anodic polarization curves yield information regarding the kinetics of oxidation reactions (specifically metal oxidation in this case), while cathodic polarization curves convey details of reduction reaction kinetics (specifically proton or water reduction in this case). In acknowledgement of these

differences, discussions of these two types of polarization curve continue separately, below.

3.1.2.1 Anodic polarization curves

The anodic polarization behaviour of Ti and Ti alloys has been well investigated by others [10]. The general shape of the polarization curve for Ti in acidic solution and the processes occurring at each stage have been described in Section 1.2 (see Figures 1.2.2-a and 1.2.3-a). The anodic polarization curves recorded during the course of this project add nothing to the current knowledge of the anodic behaviour of Ti and its alloys. However, they help to support the hypothesis, first presented in Section 3.1.1, that the "activation-rebound" phenomenon observed on Ti-2 in acidic solutions is the result of cathodic modification of the Ti-2 surface by a spontaneously formed surface "hydride".

Figure 3.1.2.1-a shows the anodic polarization curves, including segments of the cathodic polarization curves, recorded in deaerated 1.0 $mol \cdot dm^{-3}$ HCl solution at 25°C on Ti-2 after activation but before the potential rebound, on Ti-2 after the potential rebound had taken place, and on Ti-12 (for comparison). The anodic polarization curve for Ti-2, recorded after activation, but before the potential rebound, displayed the expected active, active-to-passive, and passive regions commonly reported in the literature [10]. In contrast, the anodic polarization curve for Ti-2 recorded after the activation-rebound event had taken place showed only a passive region at potentials greater than E_{oc} and cathodic current at lower potentials; there were no active regions apparent from the current measurements. Furthermore, because E_{oc} was about 0.3 V greater in this case (-0.3 V, as opposed to -0.6 V normally), the hydrogen region appeared at potentials

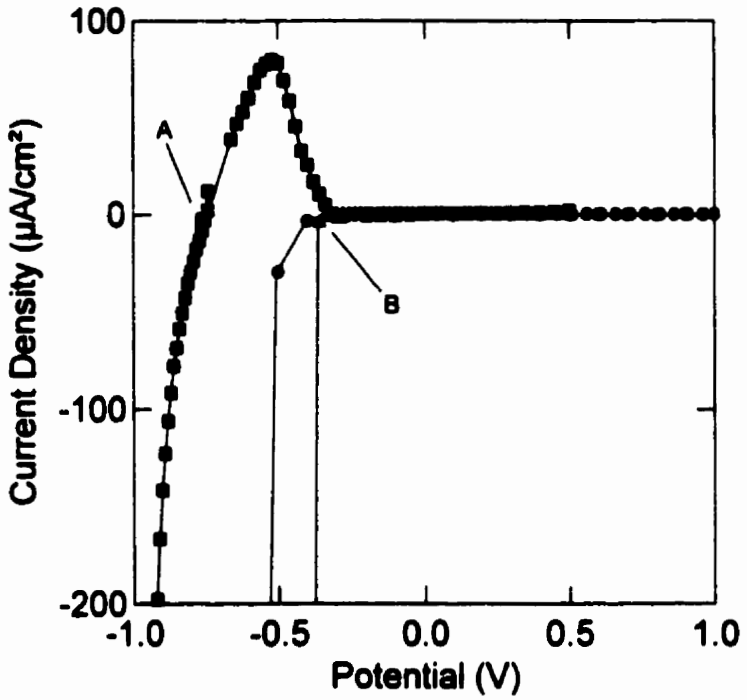

Figure 3.1.2.1-a Anodic polarization curves for Ti in deaerated 1.0 mol·dm^{-3} HCl at 25°C (showing a portion of the cathodic polarization); (■) Ti-2 polarized immediately after activation, (▲) Ti-2 polarized after activation-rebound, (●) Ti-12 polarized after activation-rebound. Points A and B indicate the values of E_{oc} immediately after activation and after activation-rebound, respectively.

~ 0.3 V higher. This behaviour was quite comparable to that exhibited by Ti-12 under the same conditions. The spontaneous passivation and high resistance to metal dissolution of Ti-12 are generally accepted to result from cathodic modification, as described in Section 1.2.5. It seems reasonable, therefore, to suspect a similar mechanism in the case of Ti-2 electrodes that exhibit the same polarization behaviour as the Ti-12. However, since Ti-2 does not contain significant amounts of Ni or noble metals, its cathodic modification must have been generated by something other than components of the original alloy, possibly a surface hydride as proposed in Section 3.1.1.

3.1.2.2 Cathodic polarization curves

To complete the discussion of spontaneous cathodic modification on Ti-2, one should look at evidence from the cathodic polarization curves, which represent the kinetics of the proton reduction reaction on Ti under these conditions. One of the underlying reasons for the effectiveness of cathodic modification in passivating Ti was noted to be a decrease in the Tafel slope for the HER (see Section 1.2.5), resulting in higher cathodic current densities and a shift of E_{oc} in the positive direction. A dramatic decrease in the cathodic Tafel slope has been noticed on Ti-2 after activation-rebound.

The cathodic polarization curves corresponding to the experiments that yielded the anodic curves shown in Figure 3.1.2.1-a are plotted in Figure 3.1.2.2-a, and re-plotted in Figure 3.1.2.2-b in semi-log format with fitted regression lines through the linear regions. For the Ti-2 electrode polarized before the potential rebound could occur, the cathodic Tafel slope was ~ -0.140 V·decade^{-1}. A value of -0.118 V·decade^{-1} is indicative of a reaction in which the first electron transfer is rate determining (see Table 1.4.1-a). In this

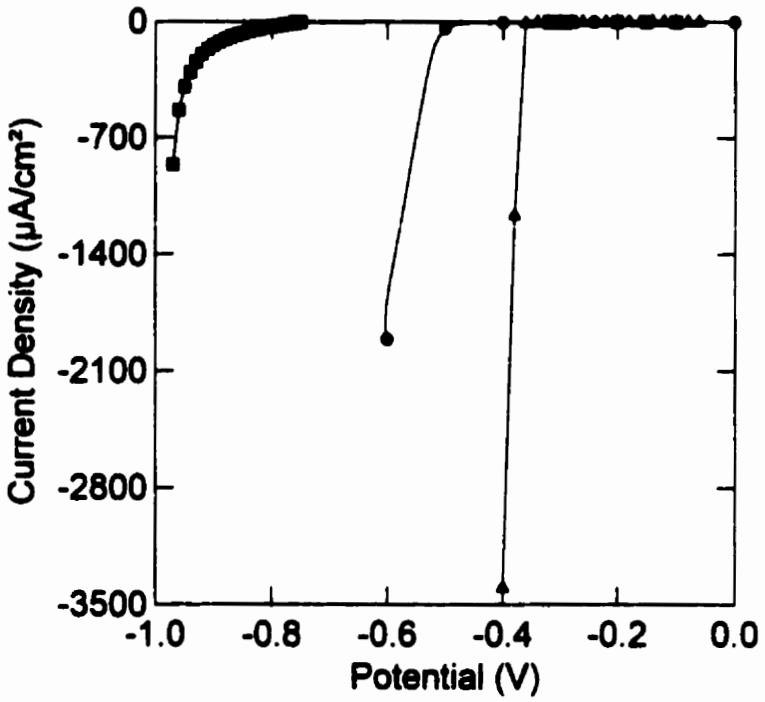

Figure 3.1.2.2-a Cathodic polarization curves corresponding to the anodic curves displayed in Figure 3.1.2.1-a; (■) Ti-2 polarized immediately after activation, (▲) Ti-2 polarized after activation-rebound, (●) Ti-12 polarized after activation-rebound.

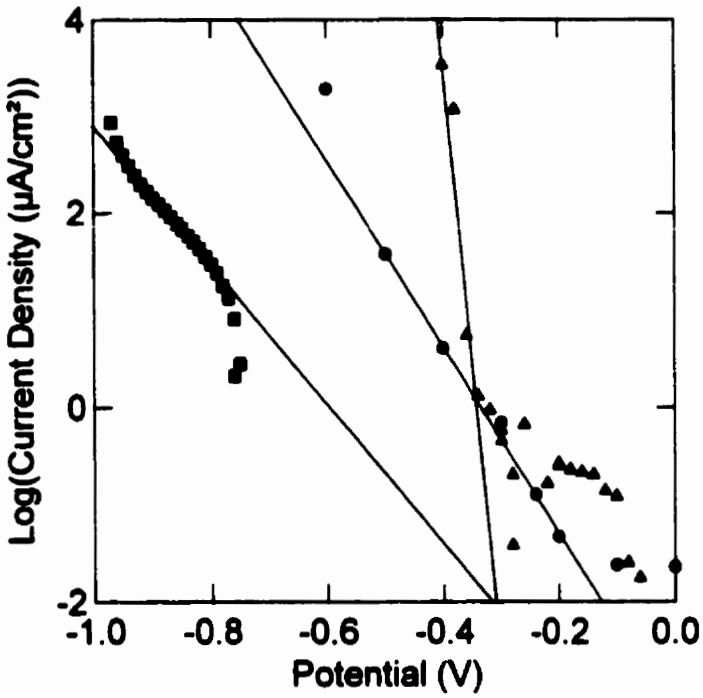

Figure 3.1.2.2-b Cathodic Tafel plots corresponding to the cathodic polarization curves shown in Figure 3.1.2.2-a with fitted regression lines through the linear portions; (■) Ti-2 polarized immediately after activation, (▲) Ti-2 polarized after activation-rebound, (●) Ti-12 polarized after activation-rebound.

case the higher Tafel slope suggests that this first electron transfer was probably rate determining, but also inhibited somewhat. The latter conclusion is consistent with the proposal [10] that the Ti surface under these conditions is covered by a monolayer of oxygen species.

For the Ti-12 electrode, the apparent cathodic Tafel slope was ~ -0.090 V·decade^{-1} and, at first inspection, seemed to be constant over several orders of magnitude in the current. This lower Tafel slope (by comparison with the Ti-2 described above) is consistent with the suggestion that the alloy surface is catalytic for the hydrogen reaction (*i.e.*, cathodically modified).

Finally, the Ti-2 polarized only after experiencing the activation-rebound phenomenon yielded an *apparent* Tafel slope of ~ -0.010 V·decade^{-1}. Such a low Tafel slope is not mechanistically significant in the direct way that Tafel slopes are commonly used. Instead, it implies that these measurements are not valid for use in determining the reaction mechanism from the Tafel plot because secondary, non-steady-state phenomena were occurring during the polarizations. This seemingly intense dependence of current on potential could have been generated by localized reactivity on a generally low-reactive surface, accompanied by an increasing surface coverage by the reactive areas.

Figure 3.1.2.2-c shows that the currents were indeed non-steady state, both on Ti-2 after activation-rebound and on Ti-12. The current transients plotted in the Figure were recorded at a constant potential E = -0.400 V on the Ti-2 electrode that had undergone activation-rebound and E = -0.600 V on the Ti-12 electrode. The transients clearly indicate that the reactivity of the electrode surface toward hydrogen reduction was

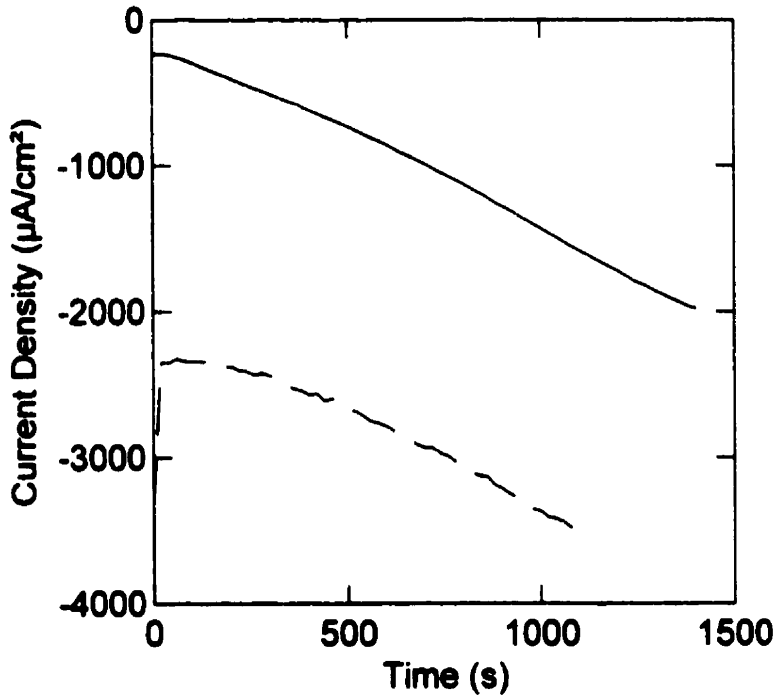

Figure 3.1.2.2-c Current transients showing long-term non-steady state behaviour during cathodic polarization of disk electrodes in 1.0 mol·dm^{-3} HCl; (— — —) Ti-2 at -0.4 V, and (———) Ti-12 at -0.6 V

increasing significantly with time for a period in excess of 1000 seconds, and therefore the apparent "Tafel" slope is not a mechanistically significant parameter in either case (*i.e.*, the slopes of the Log I vs. E plots for these two electrodes (Figure 3.1.2.2-b) are not valid Tafel slopes).

Another indication that the measurements in these two cases do not represent valid Tafel plots can be noted on Figure 3.1.2.2-b; the slope of the tangent to these two curves becomes shallower as one approaches the corrosion potential. Normally this tangent slope is steeper near the corrosion potential where the current-potential relationship is approximately linear.

This picture is consistent with the hypothesis that activation-rebound on Ti-2 is driven by the development of catalytic sites (potentially surface hydrides) that generate cathodic "self-modification" under free corrosion conditions. The surface coverage by such catalytic sites may be quite low under freely corroding conditions, since the current density for the matching anodic half-reaction would be relatively low. Such is the case for noble metal intermetallic particles in cathodically modified Ti alloys (see Section 1.2.5). Under conditions of cathodic polarization on Ti-2, the areas of catalytic sites may grow and new sites may form as more hydrogen is reduced at a higher rate at the polarized electrode surface. This increase in surface coverage by catalytic sites might involve the replacement of surface oxide with hydride, perhaps by a nucleation and growth mechanism. The shape of the current transients is not inconsistent with this possibility [136, 196].

The non-steady state behaviour of the Ti-12 electrode suggests the possibility of extending this hypothesis of cathodic self-modification to include other Ti alloys, notably Ti-12 and the noble metal alloys. The implication here is that hydrogen production by cathodic reactions at catalytic intermetallic particles could lead to the conversion of the surface adjacent to these particles into catalytic surface hydride, which could then enhance and reinforce the passivating effect of the cathodic modification. In effect, noble metal intermetallic particles could stimulate additional cathodic self-modification. Local hydride formation in the vicinity of intermetallic precipitates has been observed after acid etching of cathodically modified alloys [197].

Potentiostatic polarization curves for Ti-2 hydrogen absorption coupons in 0.1 mol·dm^{-3} HCl + 0.27 mol·dm^{-3} NaCl at 25°C, 50°C and 95°C are shown in Figures 3.1.2.2-d, 3.1.2.2-e, and 3.1.2.2-f, respectively. It should be noted that the currents reported in these Figures are the values measured after 600 s and do not necessarily represent steady-state currents (see Figures 3.1.2.2-g, 3.1.2.2-h, and 3.1.2.2-i), since the computer controlling the experiment was set to hold each potential for a fixed time period. For the potentiostatic polarizations performed at 25°C and 50°C the currents did achieve a steady-state value at each applied potential. The polarization curves recorded at 25°C are highly reproducible and remarkably similar to those recorded at 50°C. Each of these curves displays a long, linear Tafel region extending over about 6 decades of current and having a slope of -0.154 ± 0.004 V·decade^{-1}. This is comparable to the 0.140 V·decade^{-1} slope measured on a freshly polished disk electrode in 1.0 mol·dm^{-3} HCl immediately after activation but before potential rebound (see Figure 3.1.2.2-b). This slightly shallower Tafel slope may reflect a greater inhibition of the proton reduction

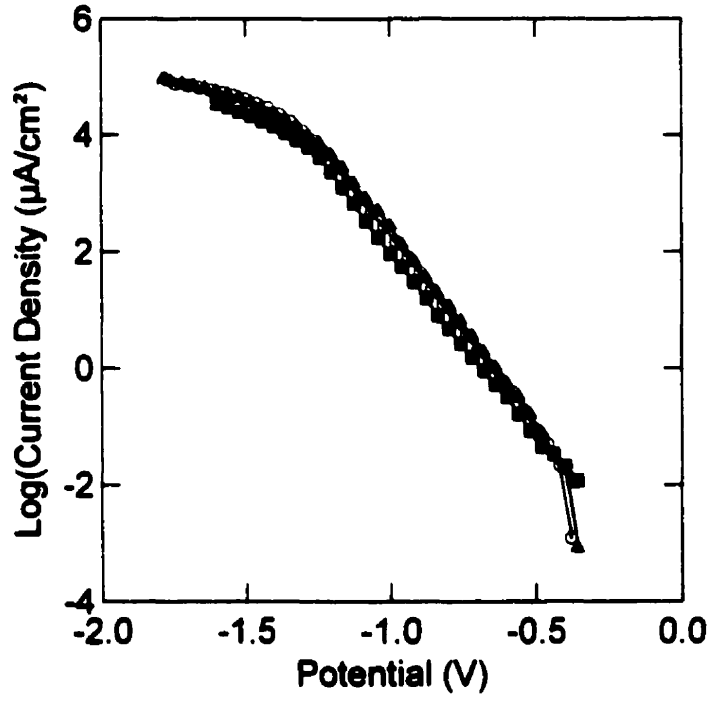

Figure 3.1.2.2-d Cathodic potentiostatic polarization curves for Ti-2 hydrogen absorption coupons in 0.1 mol·dm^{-3} HCl + 0.27 mol·dm^{-3} NaCl at 25°C. The results of three experiments demonstrate the reproducibility.

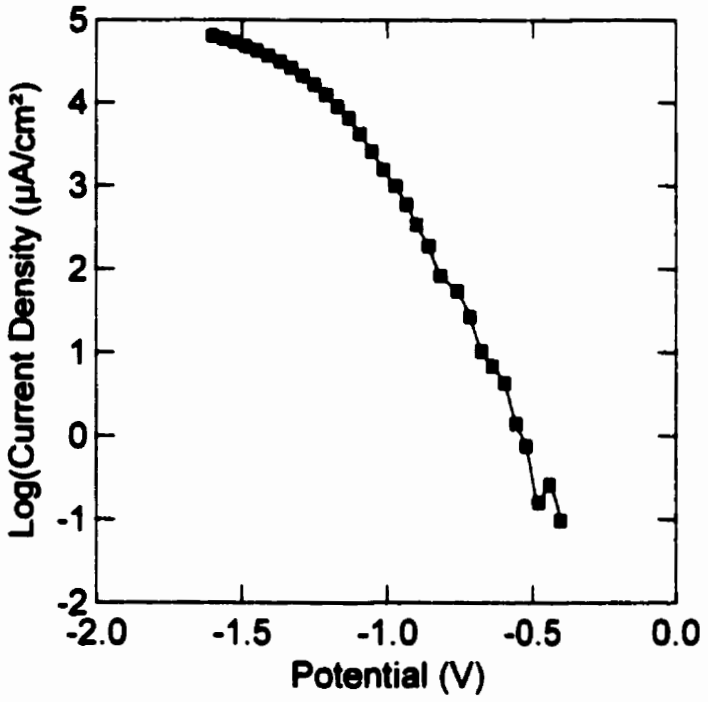

Figure 3.1.2.2-e Cathodic potentiostatic polarization curve for Ti-2 hydrogen absorption coupon in 0.1 mol·dm^{-3} HCl + 0.27 mol·dm^{-3} NaCl at 50°C.

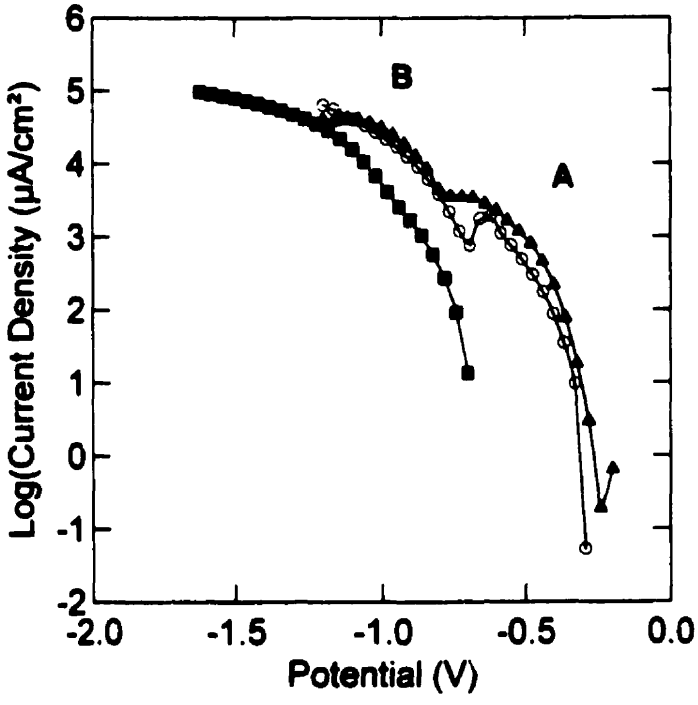

Figure 3.1.2.2-f Cathodic potentiostatic polarization curves for Ti-2 hydrogen absorption coupons in 0.1 mol·dm^{-3} HCl + 0.27 mol·dm^{-3} NaCl at 95°C. Two of these curves were measured after the electrodes displayed E_{oc} transients in which an initially active E_{oc} climbed into the passive region (○ and ▲), and the third after the electrode displayed an E_{oc} transient in which an initially active E_{oc} remained in the active region and did not undergo potential rebound for the duration of the experiment (■). A and B indicate the two curving segments of the polarization curves discussed in the text.

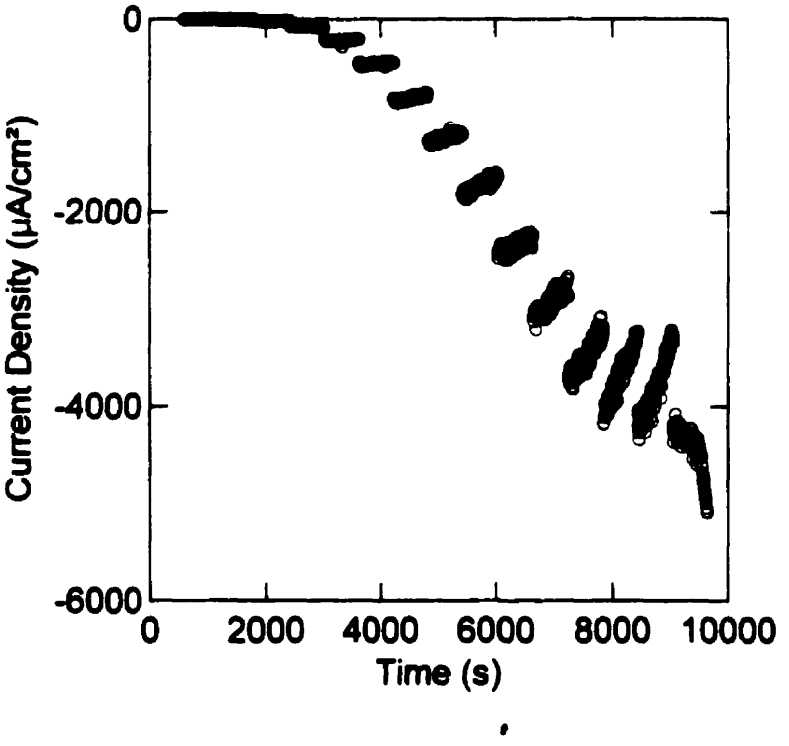

Figure 3.1.2.2-g Current transients recorded on a Ti-2 hydrogen absorption coupon in 0.1 mol·dm^{-3} HCl + 0.27 mol·dm^{-3} NaCl at 95°C during a potentiostatic polarization experiment (shown in Figure 3.1.2.2-f) measured after the electrode displayed an E_{oc} transient in which an initially active E_{oc} climbed into the passive region (curve marked by ▲ in Figure 3.1.2.2-f). Each cluster of points represents a set of measurements taken at a different fixed potential. Transients correspond to region A in Figure 3.1.2.2-f. Note the change from decaying cathodic current transients to a growing cathodic current in the last transient. This coincides with the cusp point between the two curving segments of the polarization curve in Figure 3.1.2.2-f.

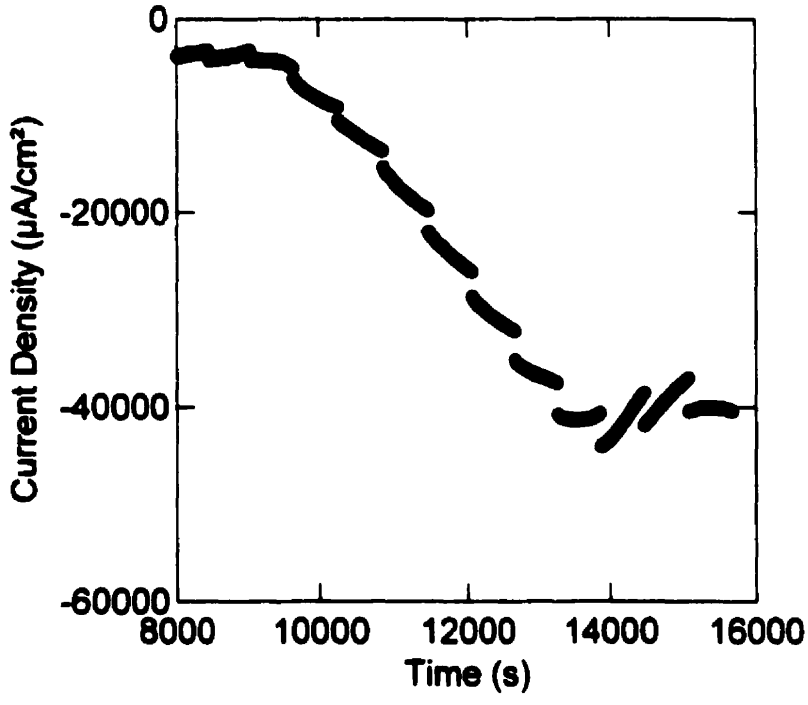

Figure 3.1.2.2-h Continuation of current transients shown in Figure 3.1.2.2-g corresponding to applied potentials from the cusp point to the negative potential limit (region **B** *in Figure 3.1.2.2-f). Each cluster of points represents a set of measurements taken at a different fixed potential. Note the factor of ten compression in the current density scale compared to Figure 3.1.2.2-g and the overlap with Figure 3.1.2.2-g (2.5 transients) along the time axis.*

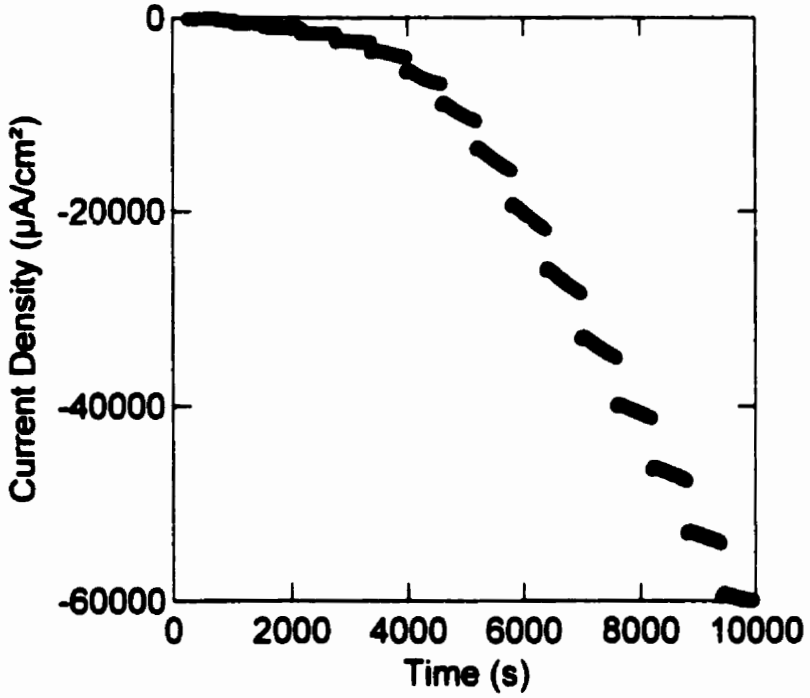

Figure 3.1.2.2-i Current transients recorded on Ti-2 hydrogen absorption coupons in 0.1 mol·dm^{-3} HCl + 0.27 mol·dm^{-3} NaCl at 95°C during a potentiostatic polarization experiment (shown in Figure 3.1.2.2-f) measured after the electrode displayed an E_{oc} transient in which an initially active E_{oc} remained in the active region and did not undergo potential rebound for the duration of the experiment (curve marked by ■ in Figure 3.1.2.2-f).

reaction by the oxide film, which would be expected to be thicker due to the long period of air exposure prior to the immersion of the coupon and may not have been fully stripped by the acidic solution.

At 95°C the polarization curves (Figure 3.1.2.2-f) usually appeared to be composed of two curving segments (A and B in the Figure), neither of which displayed a very long linear region, if any at all. In the infrequent instance when the electrode activated and E_{oc} remained in the active region for the duration of the open circuit experiment (see Figure 3.1.1-g), the subsequently recorded polarization curve seemed to include only a single curving segment, again bearing only a short linear region, if any. It is noteworthy that the cusp point between the two lobes in the "usual" 95°C polarization curves occurred at about the same potential as the E_{oc} value adopted by active Ti electrodes in this medium (about -0.6 to -0.7 V). Discussion of the significance of this effect to the absorption of hydrogen by the metal is given later in Section 3.4.

As observed on freshly polished Ti-2 after activation rebound and on freshly polished Ti-12, the cathodic currents in these polarization experiments at 95°C on air-exposed Ti-2 hydrogen absorption coupons did not reach a steady state after 600 s of potentiostatic polarization. Figures 3.1.2.2-g, 3.1.2.2-h, and 3.1.2.2-i show the current transients observed while recording the polarization curves at 95°C. While the potential was in region A (Figure 3.1.2.2-f), decaying current transients were observed (Figure 3.1.2.2-g), but beyond the cusp point when the potential entered region B, increasing current transients were observed (Figures 3.1.2.2-g and 3.1.2.2-h). For the rare case when the electrode activated and remained active, cathodic currents were only generated at

potentials typical of region B, and only rising current transients were observed (Figure 3.1.2.2-i). These transients suggest that, under true steady-state conditions, region A would be less, and region B more, prominent. That is, at steady state the currents observed in region A may be significantly smaller or perhaps even anodic and the cathodic currents observed in region B could be significantly higher. Arsov [152], working on Ti in sulphuric acid, observed the evolution of currents from cathodic to anodic under potentiostatic conditions in the potential range -0.3 to -0.5 V versus SCE (in region A). This transition took about 15 minutes. At potentials of -0.8 to -0.9 V (in region B) Arsov observed cathodic currents that continued to increase with time and did not achieve a steady state during the period of the experiment, similar to the results presented here.

From the polarization curves, one can conclude that the overpotential for proton reduction on Ti-2 in strongly acidic solution is smaller and the reduction rate higher on surfaces that underwent activation-rebound than those that did not. The cathodic currents on such surfaces increase with time over long periods. The rate of proton reduction also increases with increasing temperature for a given potential.

3.2 Passive film properties in neutral solution

Passive oxide films spontaneously formed under open-circuit conditions on freshly polished specimens of high purity Ti, Ti-2, Ti-12, Ti-16, and Ti-0.1Ru exposed to unbuffered, deaerated 0.27 mol·dm^{-3} NaCl solutions were studied as a function of solution temperature using E_{oc} measurements, EIS, and XPS. The goals of these experiments were to determine whether observable changes in the properties of the oxide could account for the onset of susceptibility to crevice corrosion at temperatures around 70°C on Ti-2 and Ti-12, but not on Ti-16, and to explore the effects of alloying additions on the protectiveness of the passive film. Several experiments were also performed on Ti-2 in 0.27 mol·dm^{-3} Na_2SO_4 to investigate the importance of the electrolyte anion to the passive film behaviour.

3.2.1 Open circuit potential measurements

E_{oc} measurements[1] were made in salt solutions to which no acid was added. Solutions of 0.27 mol·dm^{-3} NaCl having pH values of 6-6.5 (and in a few cases, 0.27 mol·dm^{-3} Na_2SO_4 solutions with pH = 8-8.5) were used without pH adjustment. These experiments, performed at a series of temperatures from 20 to 80°C, employed freshly polished disk electrodes of high purity Ti, Ti-2, Ti-12, Ti-16, and Ti-0.1Ru. As these E_{oc} measurements preceded either EIS or XPS measurements, the disks were either sealed or

[1] It doesn't seem appropriate to call these activation experiments when no active corrosion region exists at such high pH values [198][151].

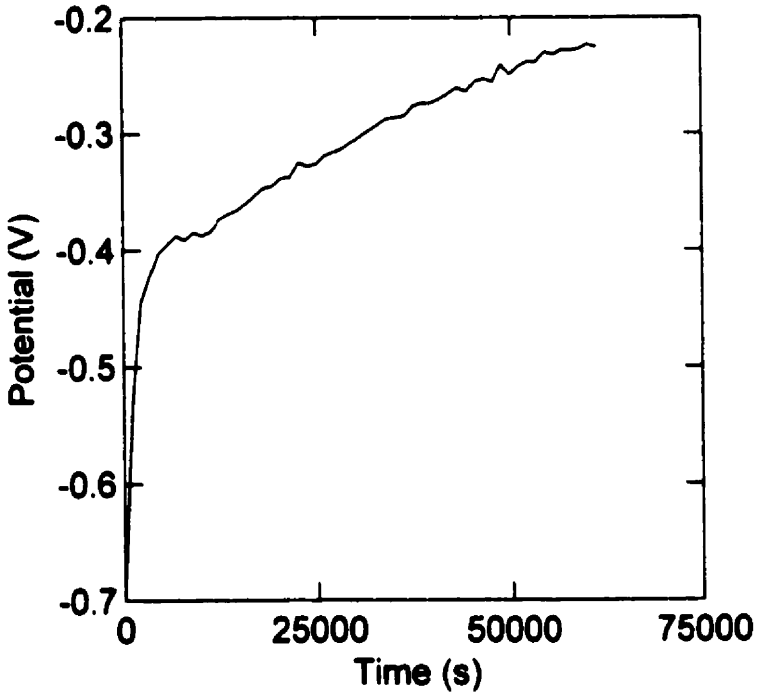

Figure 3.2.1-a E_{oc} transient recorded on Ti-2 in deaerated 0.27 mol·dm^{-3} NaCl at 80°C.

unsealed in epoxy, respectively, as described in Sections 2.6.1, 2.6.3, and 2.6.4. The value of E_{oc} was recorded throughout the immersion period (usually 16-30 hours).

A typical E_{oc} transient is shown in Figure 3.2.1-a. In this transient, as in most, a very low initial E_{oc} value rapidly increased to a position corresponding to what would be the passive potential range in acidic solution, whereupon it slowly drifted higher for an extended period. In some experiments a steady state was eventually achieved; in other cases, including the example shown in Figure 3.2.1-a, it was not.

The diagnostic worth of such transients is low because they did not always reach a steady state, the E_{oc} values were irreproducible, and they contained varying levels of noisy fluctuations. Some of the E_{oc} values were also surprisingly low. However, one must consider that these results come from freshly polished electrodes, which do not seem to yield as reproducible a starting condition as those treated with a long air exposure (see Section 3.1), and that, in these near-neutral-pH conditions, the polarization curve for Ti displays no active region -only passive and hydrogen evolution regions (see, for example, [70]). The broad passive region in neutral solution extends well beyond the potential range corresponding to the active and active-to-passive regions observed in acidic solutions. Therefore, whereas E_{oc} was found to be stabilized by the high corrosion current regions at the limits of the active and passive regions in acidic solutions, in higher-pH solutions E_{oc} may be subject to influences from reactions occurring at tiny localized sites that do not represent the state of the vast majority of the surface, or from minor redox couples present in the solution as contaminants (*e.g.*, Fe^{2+}/Fe^{3+} or dissolved

O_2). The value of E_{oc} may then settle at an appropriate potential anywhere within the broad, low-current passive region.

A plot of the final E_{oc} value in each test as a function of temperature is given for each material, in Figure 3.2.1-b. It can be seen that many of the final E_{oc} values fell within the range corresponding to what would be the passive potential region in acidic solutions (E > -0.3 V), while several were in the potential ranges associated with the active-to-passive transition (-0.5 V < E < -0.3 V) or active regions (-0.7 V < E < -0.5 V) in acidic solutions. A transient yielding a final E_{oc} value in the latter range is shown in Figure 3.2.1-c. Given the variability of these results it does not seem appropriate to generalize about trends in final E_{oc} values with increasing temperatures. No differences in the electrode surfaces before and after exposure were visible to the naked eye.

3.2.2 Electrochemical impedance spectroscopy

Immediately following some of the E_{oc} measurements described in Section 3.2.1, EIS was performed on the electrodes, without emersing them from solution. The EIS results are plotted in the form of Nyquist (complex plane) plots in Figures 3.2.2-a, 3.2.2-b, 3.2.2-c, 3.2.2-d, 3.2.2-e, and 3.2.2-f for high purity Ti, Ti-2, Ti-12, Ti-16, and Ti-0.1Ru in NaCl solutions and Ti-2 in Na_2SO_4 solutions at the various temperatures indicated on the figures, respectively. The corresponding Bode plots are given in Figures 3.2.2-g, 3.2.2-h, 3.2.2-i, 3.2.2-j, 3.2.2-k, and 3.2.2-l. Although based on the *same* experimental data, each type of plot emphasizes different aspects of the impedance response.

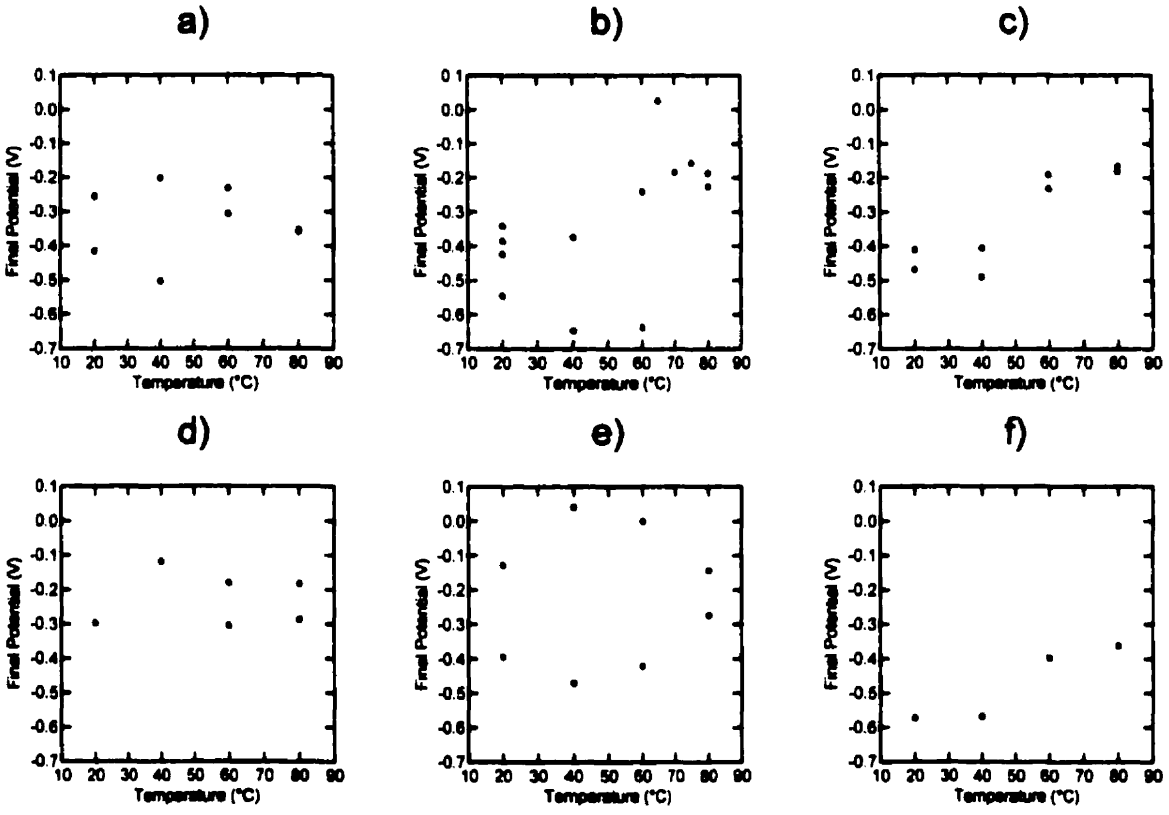

Figure 3.2.1-b Values of E_{oc} at the end of the measurement period on freshly polished disk electrodes in 0.27 mol·dm^{-3} NaCl (a-e) and 0.27 mol·dm^{-3} Na_2SO_4 (f) solutions at temperatures from 20 to 80°C: a) high purity Ti, b) Ti-2, c) Ti-12, d) Ti-16, e) Ti-0.1Ru, f) Ti-2.

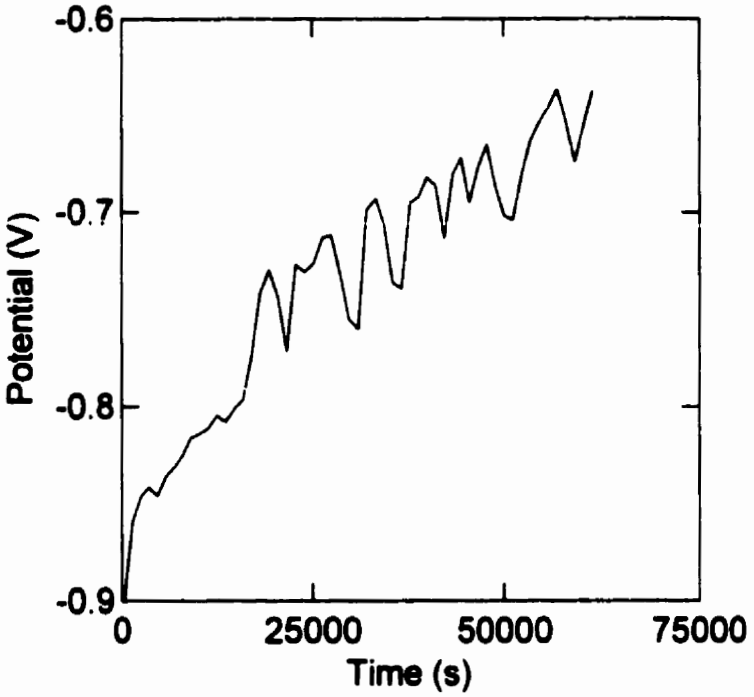

Figure 3.2.1-c E_{oc} transient recorded on Ti-2 in deaerated 0.27 mol·dm^{-3} NaCl at 60°C.

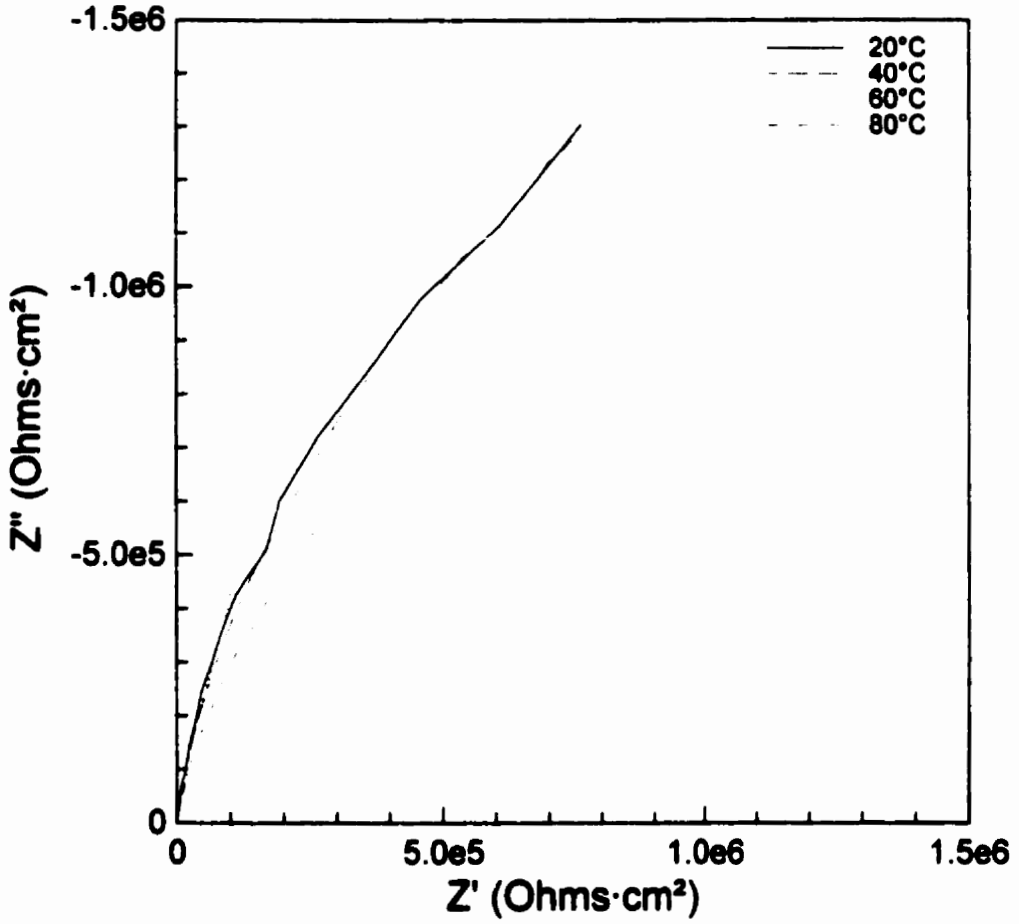

Figure 3.2.2-a Nyquist plot of electrochemical impedance spectra recorded on high purity Ti at E_{oc} in 0.27 mol·dm^{-3} NaCl at various temperatures as indicated in the legend on the graph.

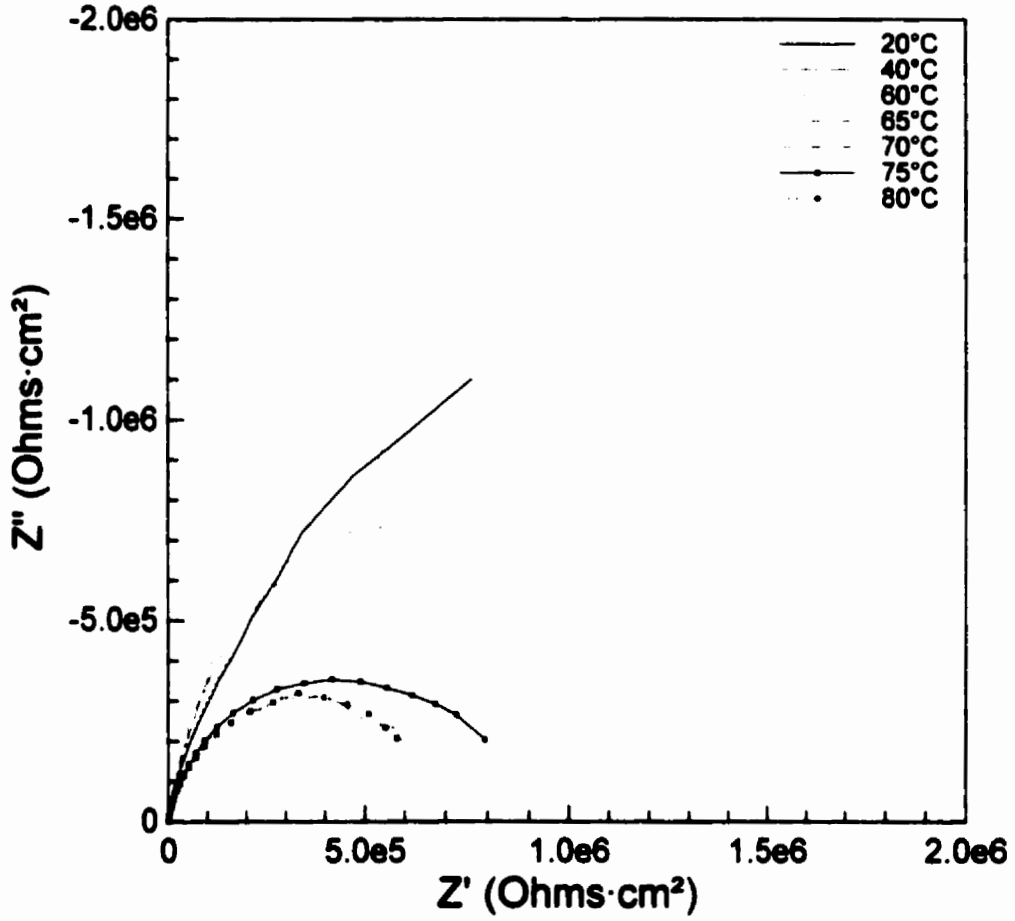

Figure 3.2.2-b Nyquist plot of electrochemical impedance spectra recorded on Ti-2 at E_{oc} in 0.27 mol·dm^{-3} NaCl at various temperatures as indicated in the legend on the graph.

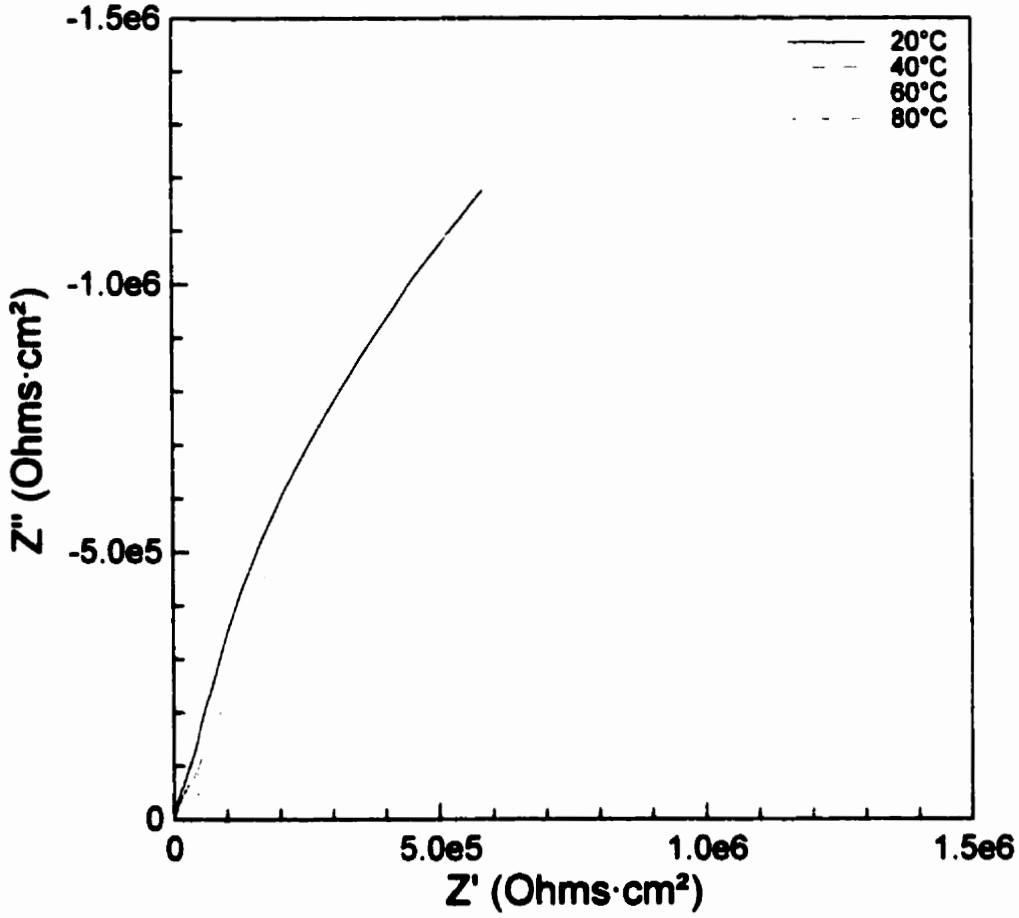

Figure 3.2.2-c Nyquist plot of electrochemical impedance spectra recorded on Ti-12 at E_{oc} in 0.27 mol·dm^{-3} NaCl at various temperatures as indicated in the legend on the graph.

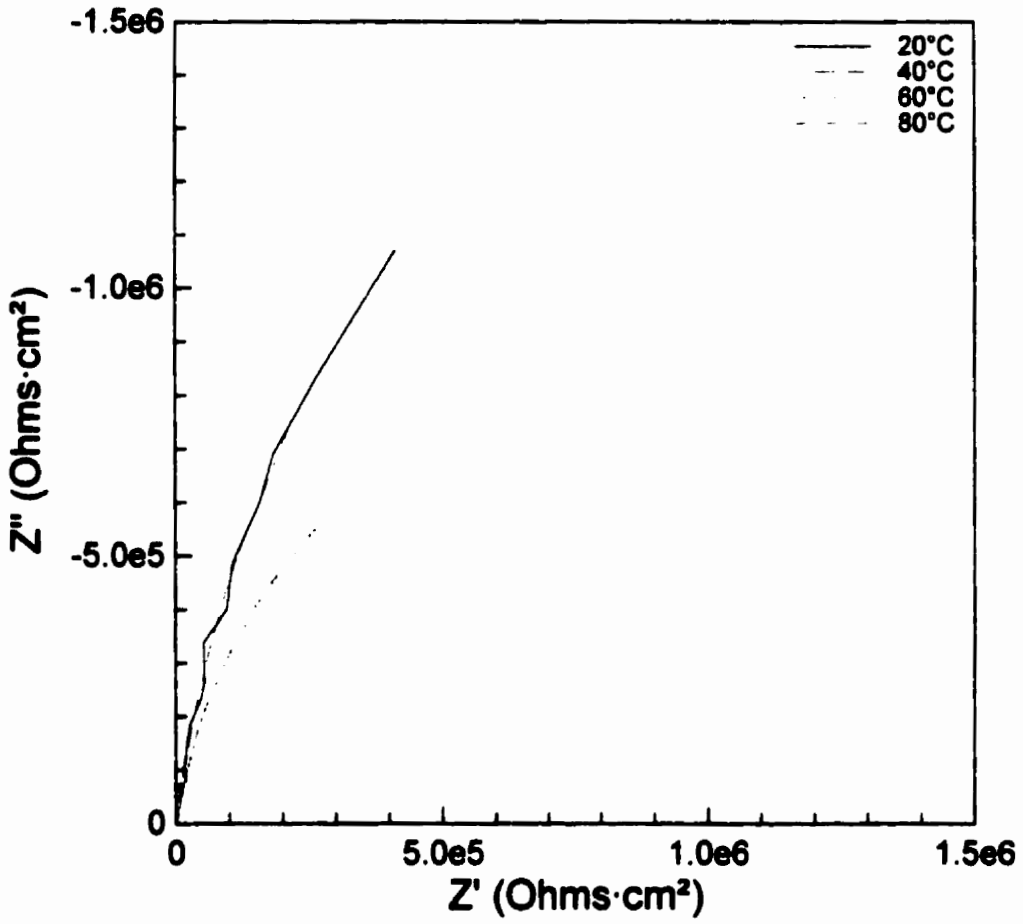

Figure 3.2.2-d Nyquist plot of electrochemical impedance spectra recorded on Ti-16 at E_{oc} in 0.27 mol·dm^{-3} NaCl at various temperatures as indicated in the legend on the graph.

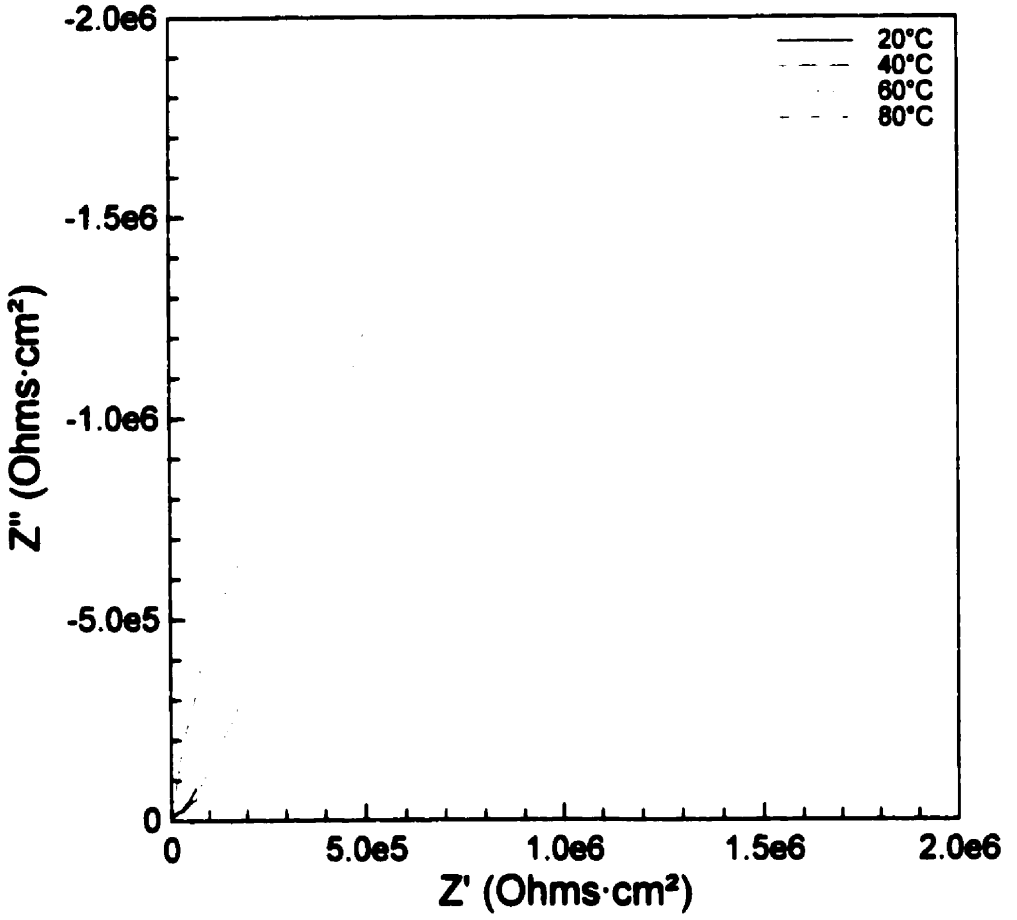

Figure 3.2.2-e Nyquist plot of electrochemical impedance spectra recorded on Ti-0.1Ru at E_{oc} in 0.27 mol·dm^{-3} NaCl at various temperatures as indicated in the legend on the graph.

a)

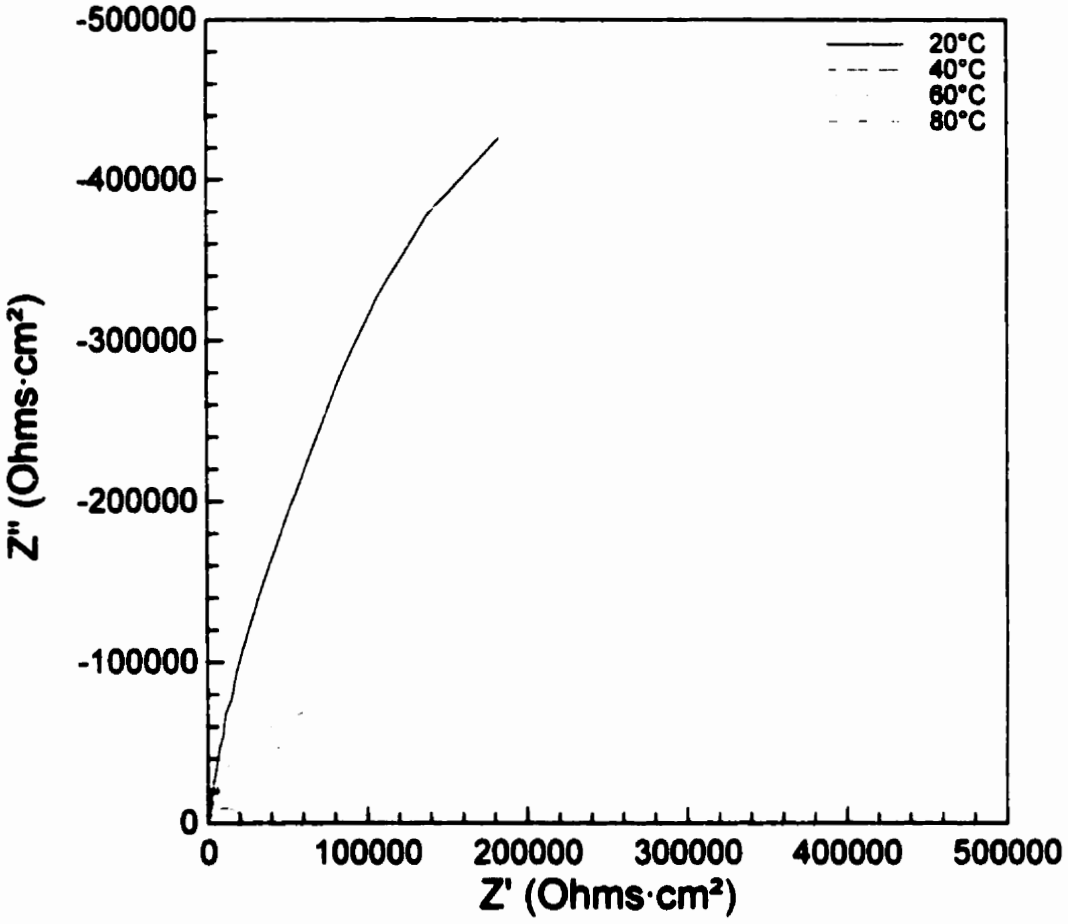

Figure 3.2.2-f a) Nyquist plot of electrochemical impedance spectra recorded on Ti-2 at E_{oc} in 0.27 mol·dm^{-3} Na_2SO_4 at various temperatures as indicated in the legend on the graph. (See expanded plot next page.)

b)

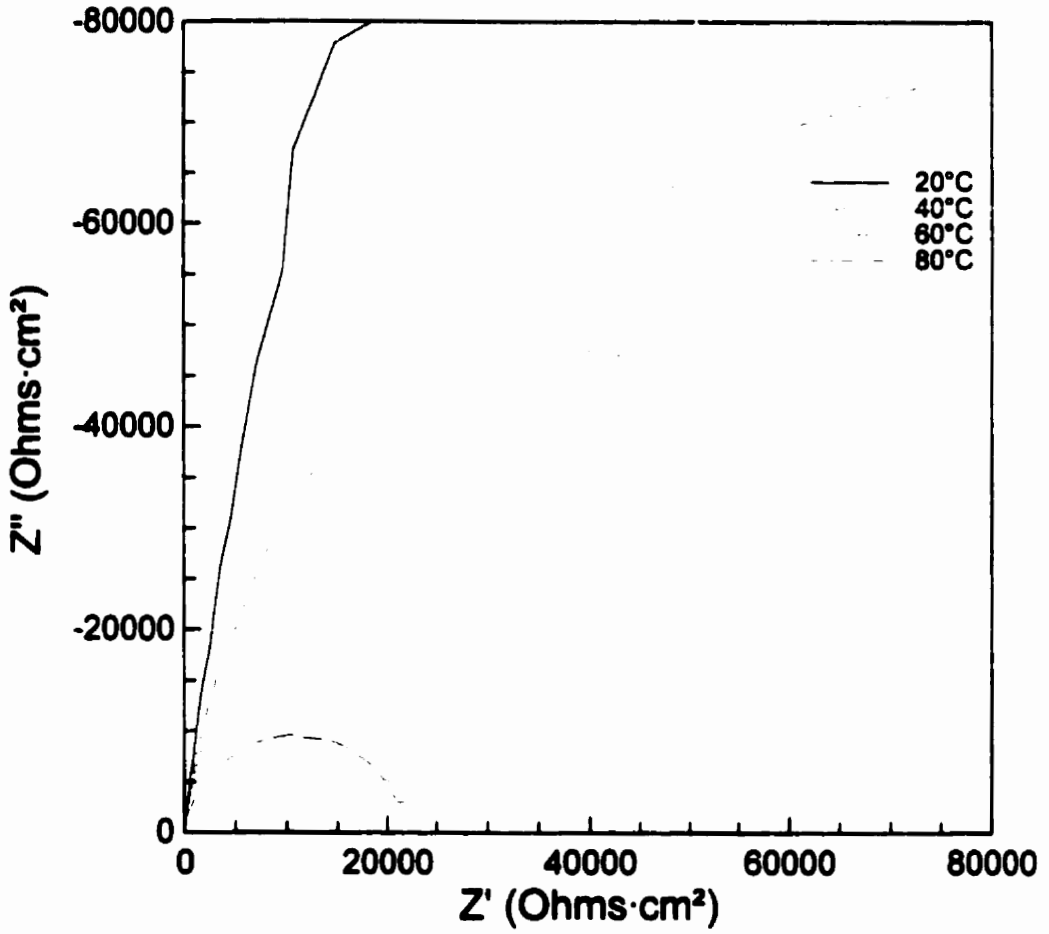

b) Expansion of the low impedance region of a).

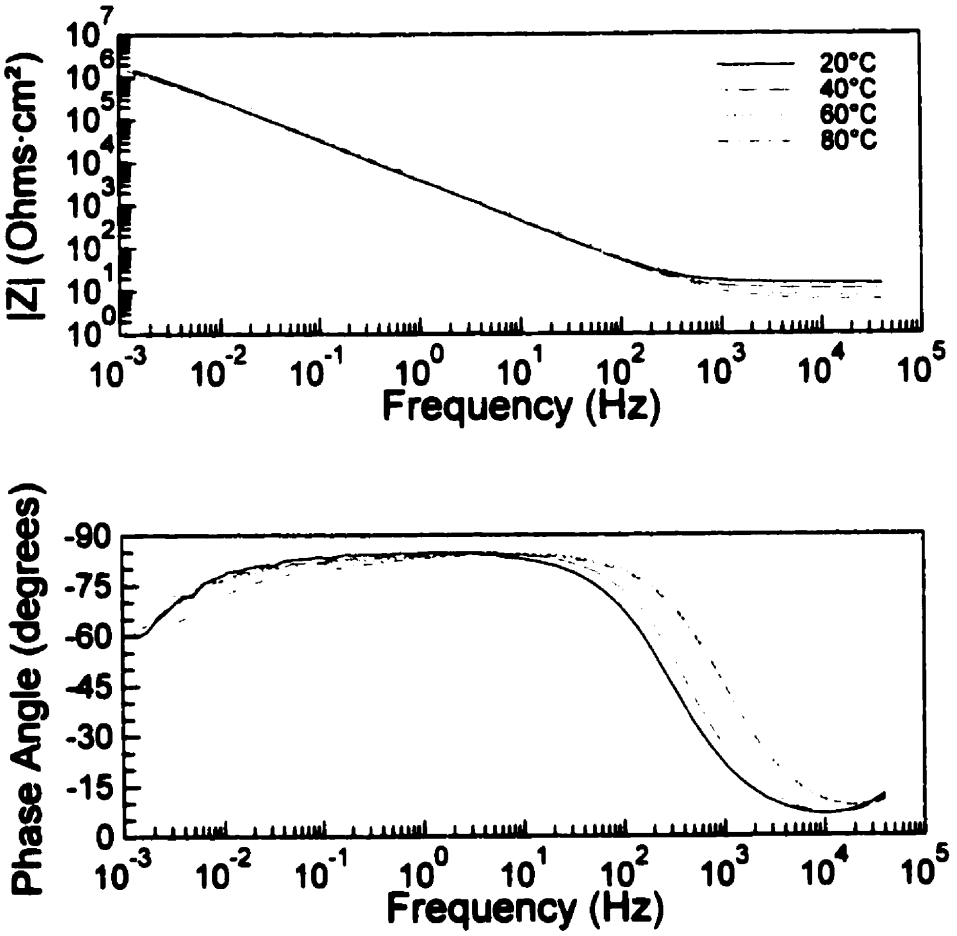

Figure 3.2.2-g Bode plots of electrochemical impedance spectra recorded on high purity Ti at E_{oc} in 0.27 mol·dm^{-3} NaCl at various temperatures as indicated in the legend on the upper graph.

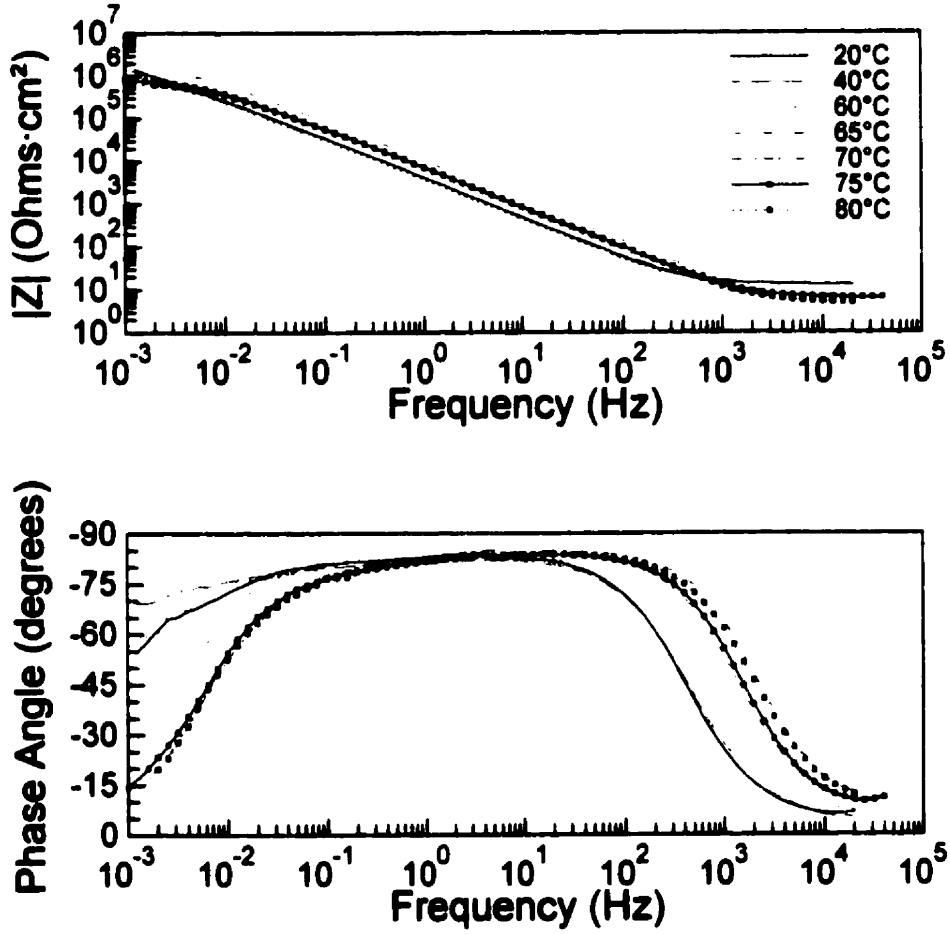

Figure 3.2.2-h Bode plots of electrochemical impedance spectra recorded on Ti-2 at E_{oc} in 0.27 mol·dm^{-3} NaCl at various temperatures as indicated in the legend on the upper graph.

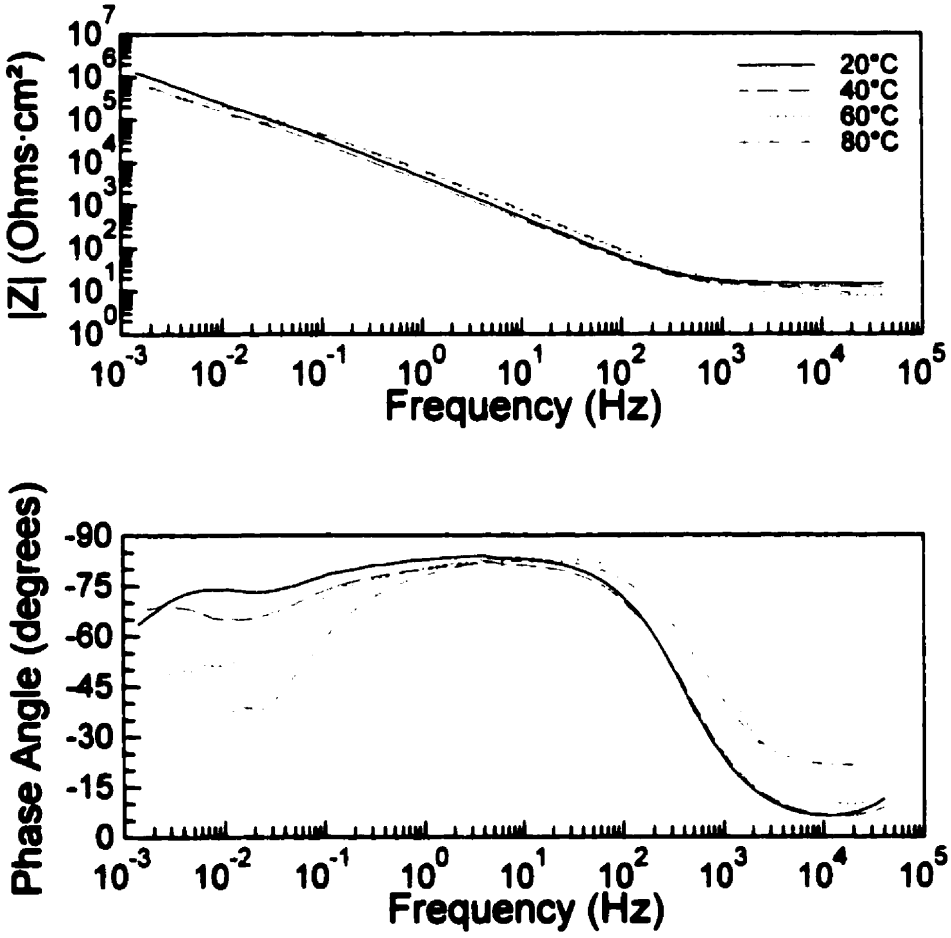

Figure 3.2.2-i Bode plots of electrochemical impedance spectra recorded on Ti-12 at E_{oc} in 0.27 mol·dm^{-3} NaCl at various temperatures as indicated in the legend on the upper graph.

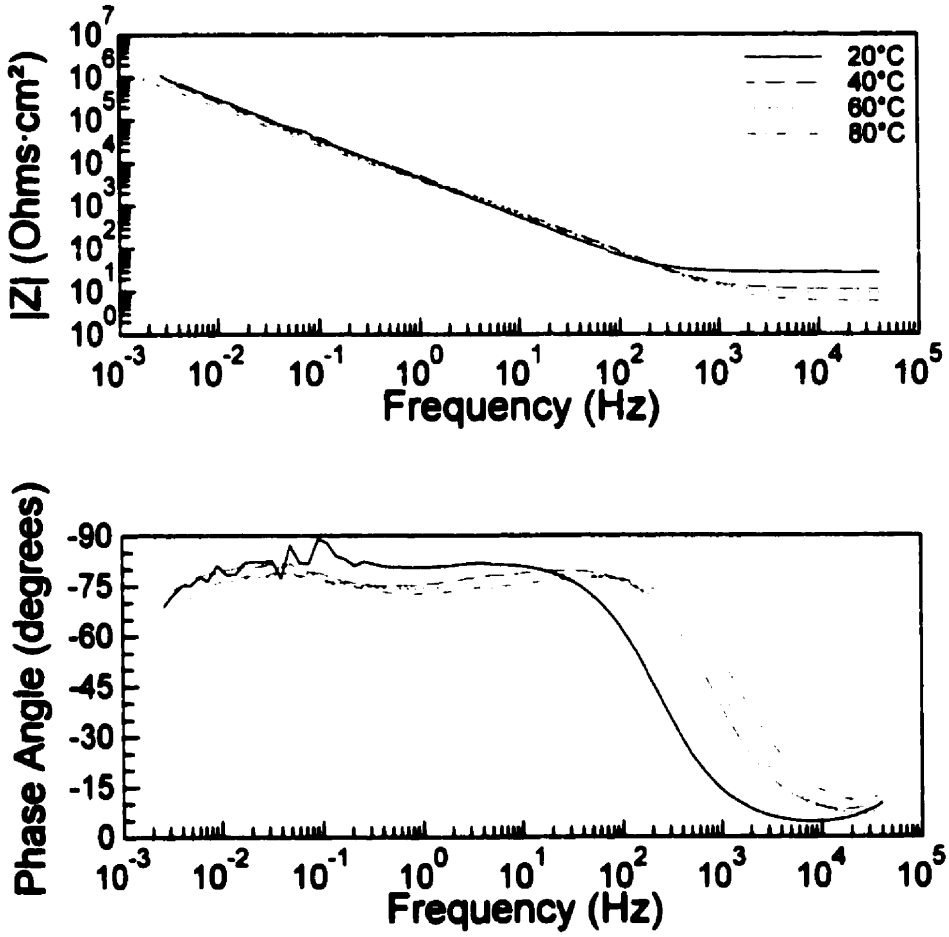

Figure 3.2.2-j Bode plots of electrochemical impedance spectra recorded on Ti-16 at E_{oc} in 0.27 mol·dm^{-3} NaCl at various temperatures as indicated in the legend on the upper graph.

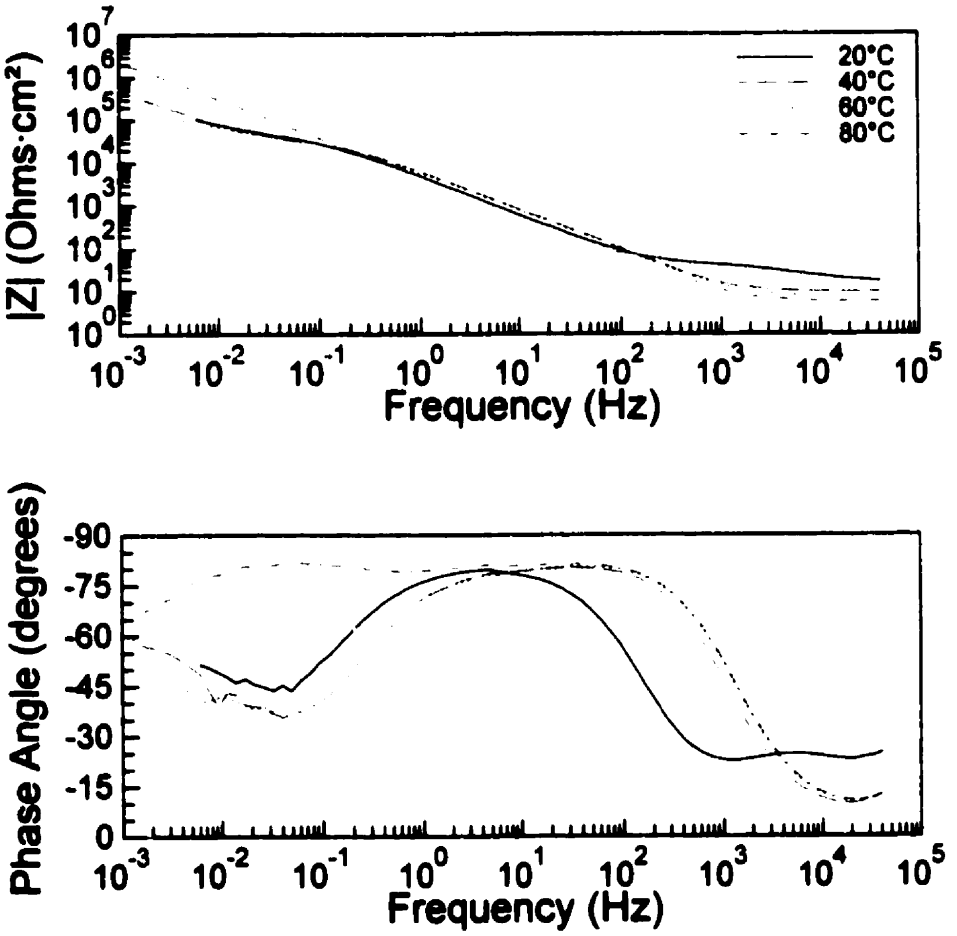

Figure 3.2.2-k Bode plots of electrochemical impedance spectra recorded on Ti-0.1Ru at E_{oc} in 0.27 mol·dm^{-3} NaCl at various temperatures as indicated in the legend on the upper graph.

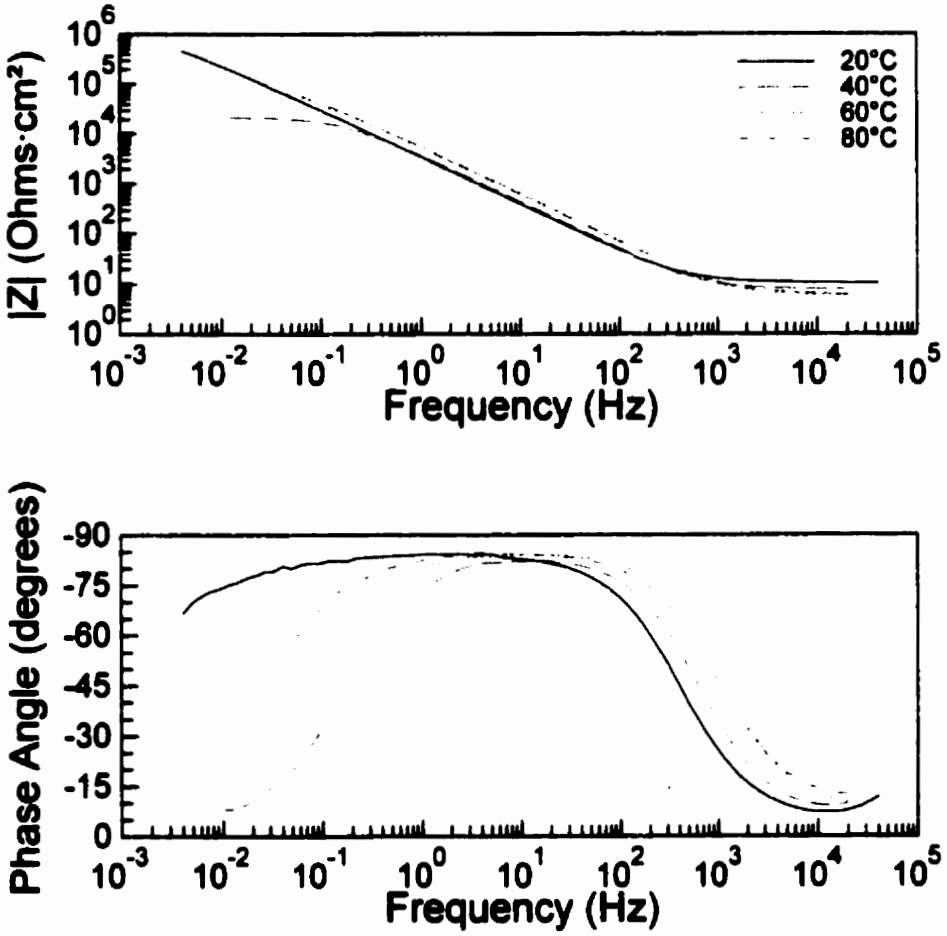

Figure 3.2.2-l Bode plots of electrochemical impedance spectra recorded on Ti-2 at E_{oc} in 0.27 mol·dm^{-3} Na_2SO_4 at various temperatures as indicated in the legend on the upper graph.

The interpretation of these impedance data was assisted by modeling the experimental spectra in terms of circuits of electrical elements (resistors, capacitors, *etc.*) that would yield an equivalent response to the applied stimulus. Equivalent circuits were least-squares fitted to experimental data using ZView for Windows software (Version 1.2b, Scribner Associates Inc.), which is based on the LEVM 6.0 program written by Dr. J. Ross Macdonald.

Unfortunately, there is no unique solution to the question of which equivalent circuit best fits the experimental data. Any number of electrical circuits that would yield the same impedance response could be contrived. Furthermore, as with any least-squares approach, the fit can be improved by adding more adjustable parameters (*i.e.*, more circuit elements) to the model. Therefore, the reader is cautioned that a good agreement between the experimental data and the impedance calculated for an equivalent circuit model does not necessarily mean that the model is correct, and the onus falls on the scientist who is fitting the model to select a sensible one. The philosophy employed in this project to reduce the modeling to a small number of reasonable models was to begin with the simplest possible model and to not add more circuit elements unless they led to a significantly better fit, made physical and chemical sense, and yielded models with credible numerical values for the fitted parameters.

The EIS data can be modeled well using the two equivalent circuits sketched in Figure 3.2.2-m. The individual circuit elements in the equivalent circuits correspond to specific physical features of the electrode or the charge transfer processes taking place. The first circuit is composed of: a resistor, R_s, intended to represent the solution

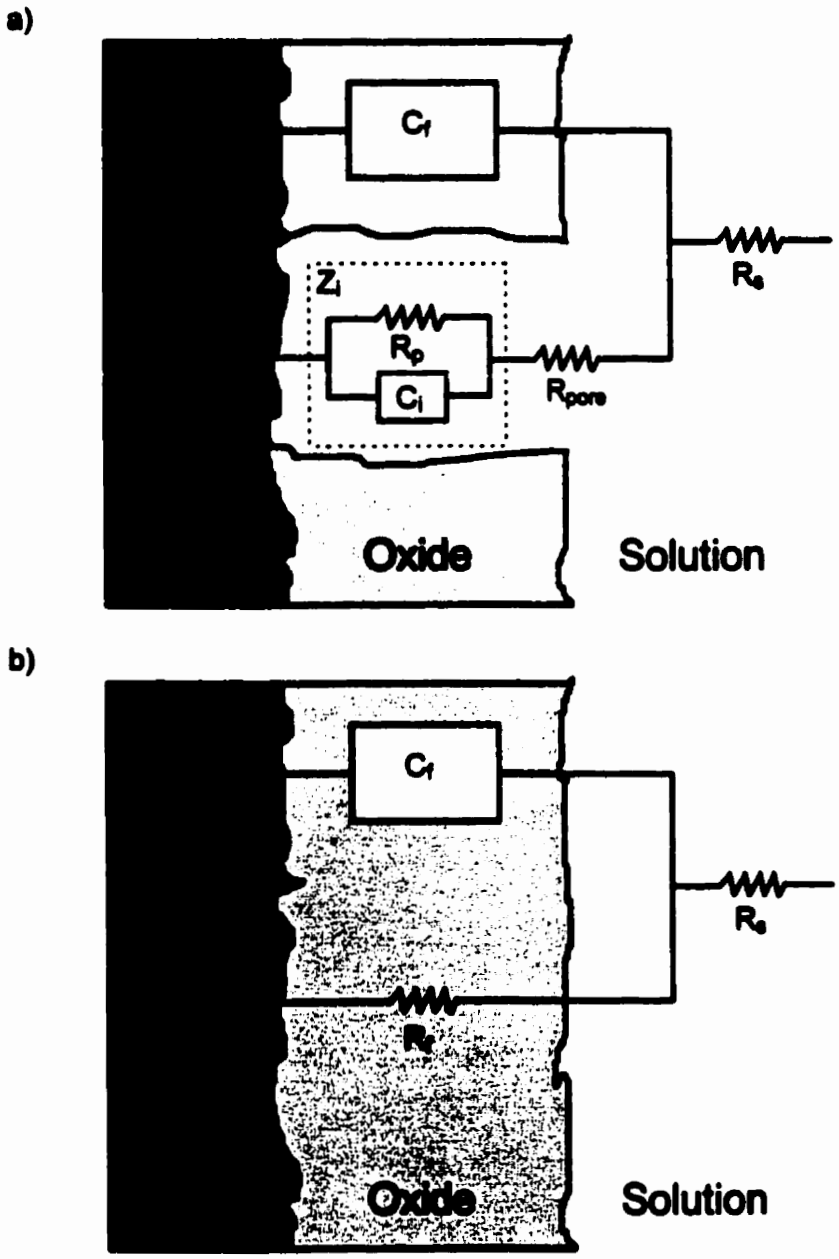

Figure 3.2.2-m Equivalent circuits used for modeling the impedance response of Ti alloy electrodes: a) Full (double time constant) circuit, including solution resistance (R_s), oxide film capacitance (C_f), resistance down pores, cracks or defects in the oxide (R_{pore}), and interfacial impedance (Z_i) at the bases of the pores. Z_i may be separated into a polarization resistance (R_p) and an interfacial capacitance (C_i); b) Reduced (single time constant) circuit representing the limiting case in which the pores are extremely small or nonexistent. The features representing the pores (R_{pore}, Z_i, R_p, and C_i) are replaced by a single film resistance (R_f).

resistance; a constant phase element (CPE), C_f, representing the non-uniform capacitance of the passive oxide film; another resistor, R_{pore}, representing the resistance of pores, cracks, or defects in the oxide; and an interfacial impedance, Z_i, representing processes taking place at the bases of the pores, cracks, or defects in the oxide. This interfacial impedance lies in series with R_{pore} and can be further separated into a parallel combination of a resistor, R_p, and a CPE, C_i, representing an interfacial polarization resistance and a non-uniform interfacial capacitance, respectively. The response of this circuit to electrical perturbations displays two time constants (*i.e.*, two resonant frequencies), and therefore will be referred to as the double time constant equivalent circuit.

The second equivalent circuit shown in Figure 3.2.2-m is not an independent circuit, but rather a special case of the first, representing the limiting case in which the pores are exceedingly fine or non-existent (an unbroken film). In this case, a film resistance, R_f, representing the bulk resistance to charge transfer across an intact, non-porous oxide film, replaces the elements associated with the pores (R_{pore}, Z_i, R_p, and C_i). The response of this circuit to electrical perturbations displays one time constant (*i.e.*, only one resonant frequency), and therefore will be referred to as the single time constant equivalent circuit.

The selection of these particular equivalent circuits was made by fitting the impedance response, beginning with the simplest models possible and considering the physical implications associated with each model circuit. The single time constant equivalent circuit differs from the simplest circuit possible for an electrode in solution that can sustain a Faradaic reaction (corrosion in this case) only by the replacement of a capacitor

by a constant phase element. This exchange greatly improved the fit between model and data and represents the combined effects of non-uniformity in the oxide film thickness, electrode surface roughness, and non-uniform current pathways due to geometrical effects in the electrochemical cell. This same substitution was used by Kolman and Scully [70] in their EIS analysis of a different Ti alloy. As can be seen from the Bode phase angle plots Figures 3.2.2-g, 3.2.2-h, 3.2.2-i, 3.2.2-j, 3.2.2-k, and 3.2.2-l, the nonidealities compensated by the use of a CPE rather than a pure capacitance were relatively minor. An ideal uniform capacitance would give a phase shift of -90° (potential lagging current by 90°). The peak phase angle for all these Bode plots is -75 to -85°.

The double time constant equivalent circuit was required to produce a good fit to the impedance data from some of the materials tested. The physical picture associated with this model circuit is that of an insulating film with cracks or pores. A similar circuit was employed by Pan *et al.* [156] for corrosion of Ti in phosphate-buffered saline solution, although their physical model of the oxide film was slightly different than the one proposed here[1].

It seems superfluous to include figures demonstrating the least-squares fit of the proposed equivalent circuits to the data acquired in *every* EIS experiment in this Thesis; a few representative examples should suffice. The calculated impedance spectra for the appropriate least-squares fitted equivalent circuit models are plotted with the experimental data acquired at 60°C on an electrode of each Ti alloy in Figures 3.2.2-n (high purity Ti), 3.2.2-o (Ti-2), 3.2.2-p (Ti-12), 3.2.2-q (Ti-16), and 3.2.2-r (Ti-0.1Ru).

[1] Pan *et al.* proposed a two-layer oxide film with pores penetrating only the outer layer.

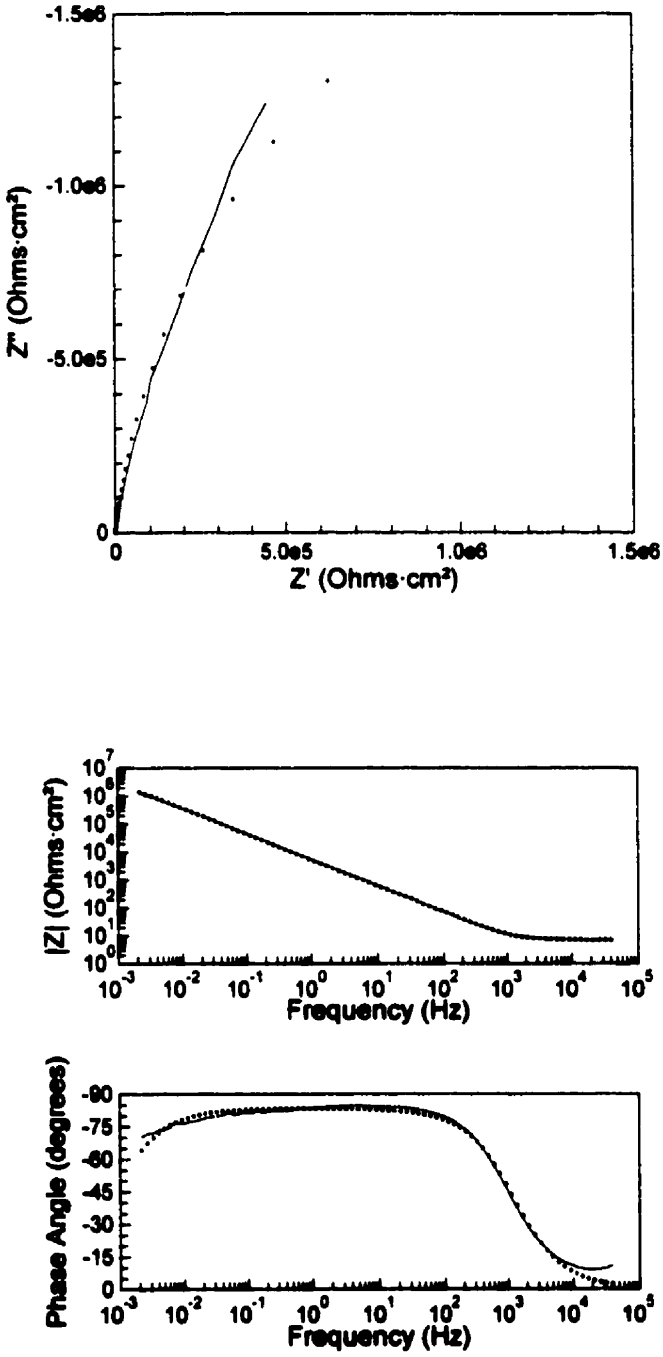

Figure 3.2.2-n Experimental impedance spectrum for a high purity Ti electrode in 0.27 mol·dm^{-3} NaCl at 60°C (————) and calculated impedance response for the least squares fitted single time constant equivalent circuit (· - - - - ·).

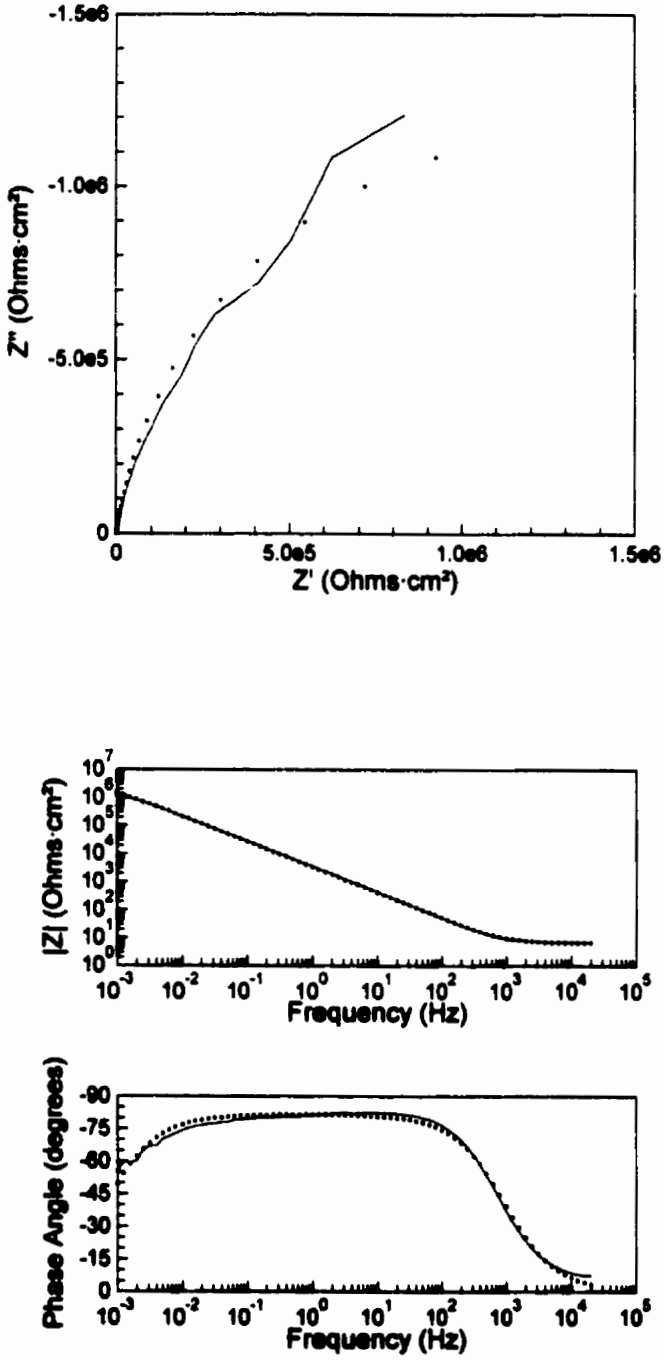

Figure 3.2.2-o Experimental impedance spectrum for a Ti-2 electrode in 0.27 mol·dm^{-3} NaCl at 60°C (————) and calculated impedance response for the least squares fitted single time constant equivalent circuit (· ·· ·· ·).

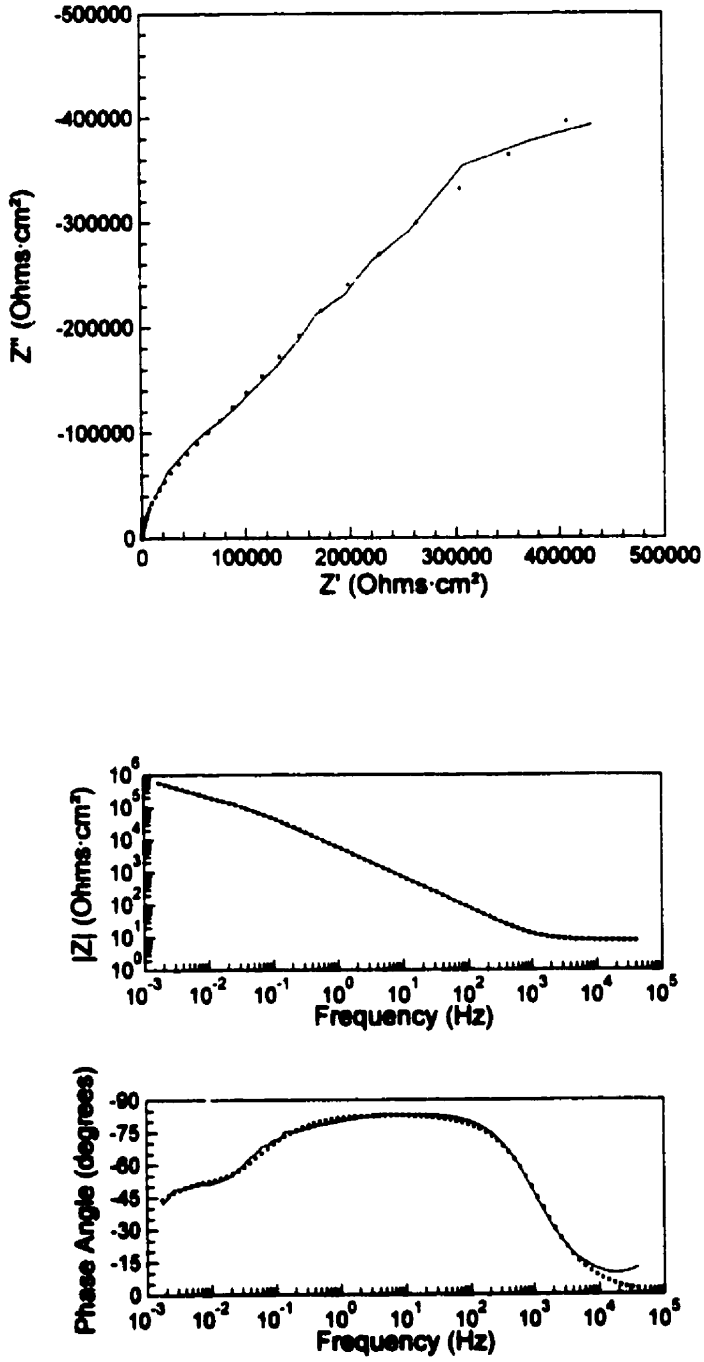

Figure 3.2.2-p Experimental impedance spectrum for a Ti-12 electrode in 0.27 mol·dm^{-3} NaCl at 60°C (————) and calculated impedance response for the least squares fitted double time constant equivalent circuit (· · · · ·).

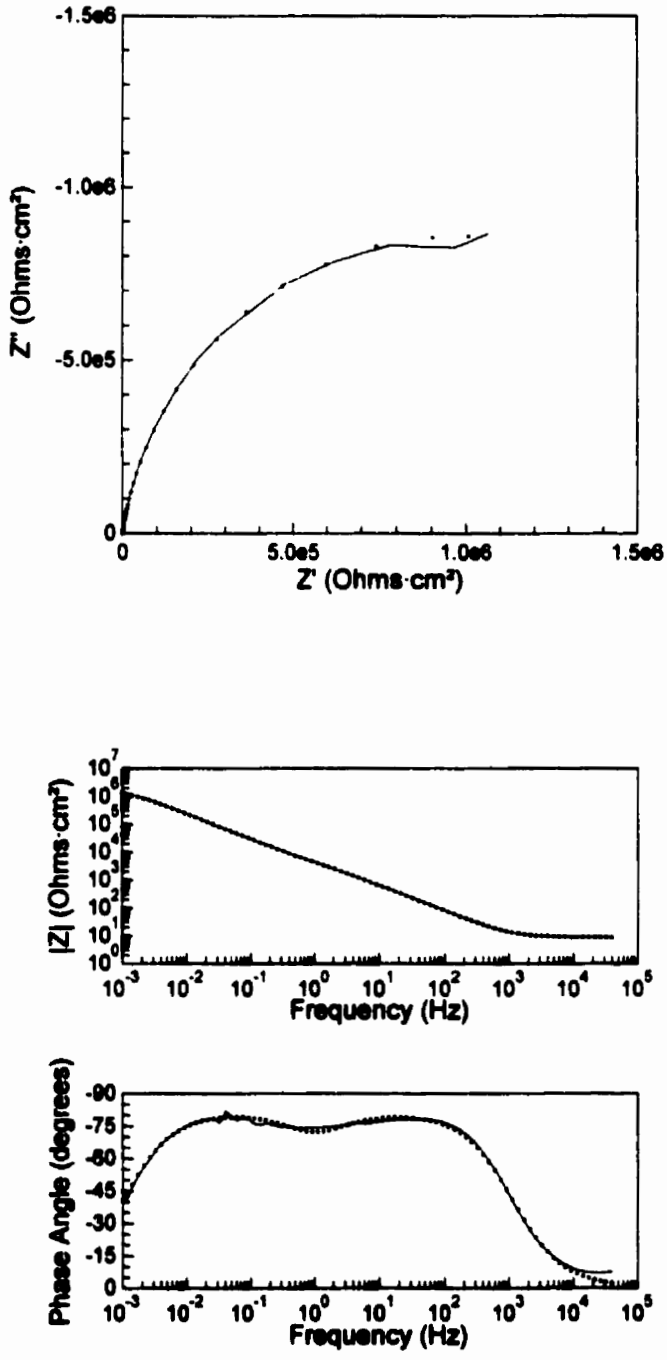

Figure 3.2.2-q Experimental impedance spectrum for a Ti-16 electrode in 0.27 mol·dm^{-3} NaCl at 60°C (———) and calculated impedance response for the least squares fitted double time constant equivalent circuit (· ·····).

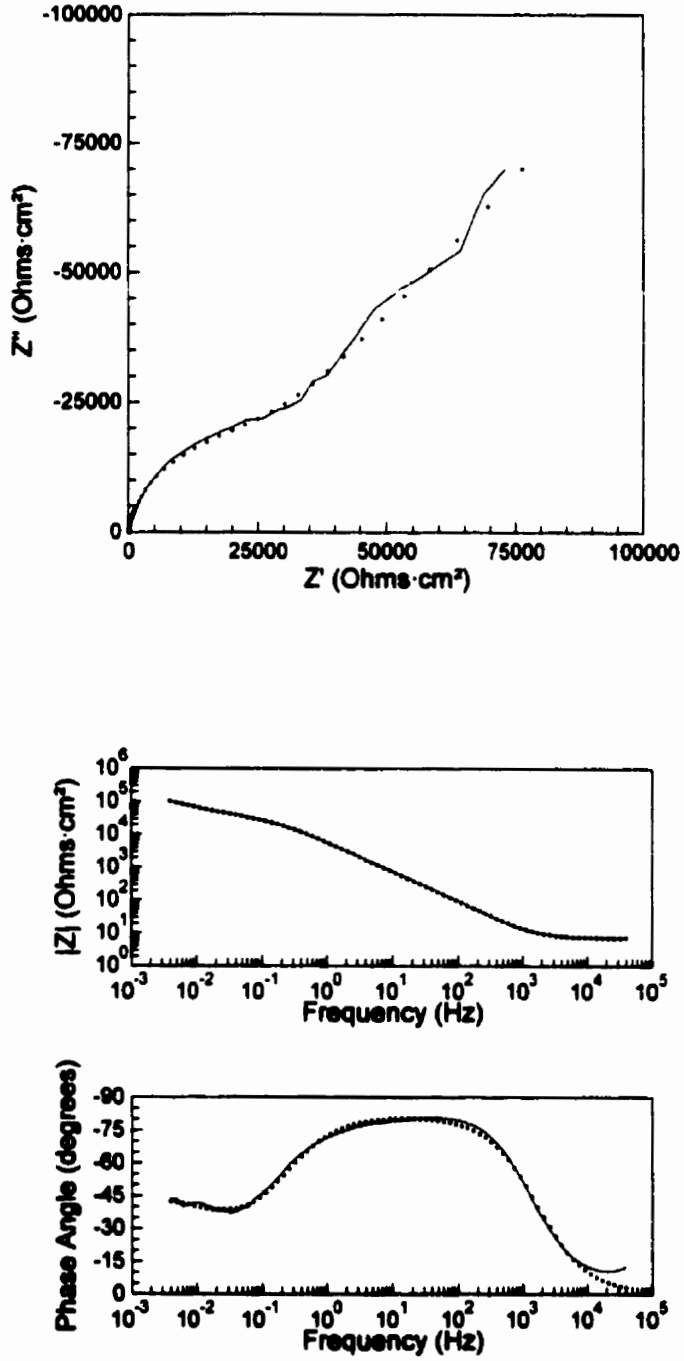

Figure 3.2.2-r Experimental impedance spectrum for a Ti-0.1Ru electrode in 0.27 mol·dm^{-3} NaCl at 60°C (————) and calculated impedance response for the least squares fitted double time constant equivalent circuit (· · ·∴·).

The model spectra fit the experimental data very well in all cases. Small discrepancies between model and data can be noted in some spectra at the high and low frequency limits. These discrepancies can be attributed largely to noise in the experimental spectra at the low frequency limit, due to the long times required to acquire each datum, and to the non-ideality of the electrochemical cell at the high frequencies, probably mainly due to the use of the high-impedance commercial SCE reference electrode.

The fitted parameter values for all of the impedance spectra acquired for each material are plotted against temperature in Figures 3.2.2-s (R_s), 3.2.2-t (C_f), 3.2.2-u (R_{pore}), 3.2.2-v (R_p), 3.2.2-w (Ci), and 3.2.2-x (R_f). The curves connecting the symbols in these Figures do not represent a model of predicted behaviour. They are simply spline fits through like symbols to help guide the reader's eye. A detailed interpretation of the results is given below.

Figure 3.2.2-s shows R_s values mostly in the 5-15 $\Omega \cdot cm^2$ range, similar for all electrodes, and decreasing with increasing temperature. One should expect R_s to be nearly identical in each of the experiments since it is determined not by the electrode materials themselves, but by the instrumentation used, the properties of the electrolyte solution, and the geometry of the electrochemical cell. The trend to lower R_s values at higher temperatures probably reflects the expected decrease in specific resistivity of the electrolyte solution as the ionic mobilities increase with increasing temperature. There appears to be only a small (perhaps insignificant) difference between R_s values determined for experiments performed in 0.27 $mol \cdot dm^{-3}$ NaCl and those performed in 0.27 $mol \cdot dm^{-3}$ Na_2SO_4, the latter being slightly lower. Two off-trend values appear at

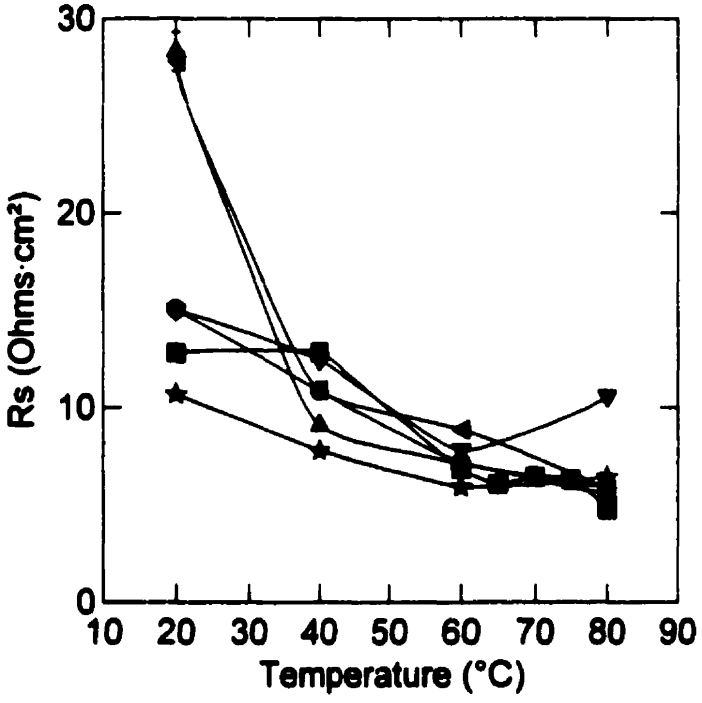

Figure 3.2.2-s R_s values determined by least squares fitting model equivalent circuits to experimental electrochemical impedance spectra recorded in 0.27 mol·dm^{-3} NaCl on high purity Ti (●), Ti-2 (■), Ti-12 (▼), Ti-16 (◁), Ti-0.1Ru (▲) and in 0.27 mol·dm^{-3} Na_2SO_4 on Ti-2 (★). Error bars indicate the rms error in the least squares fitting; however, the errors associated with most of the points are small enough that they are obscured by the graphing symbols.

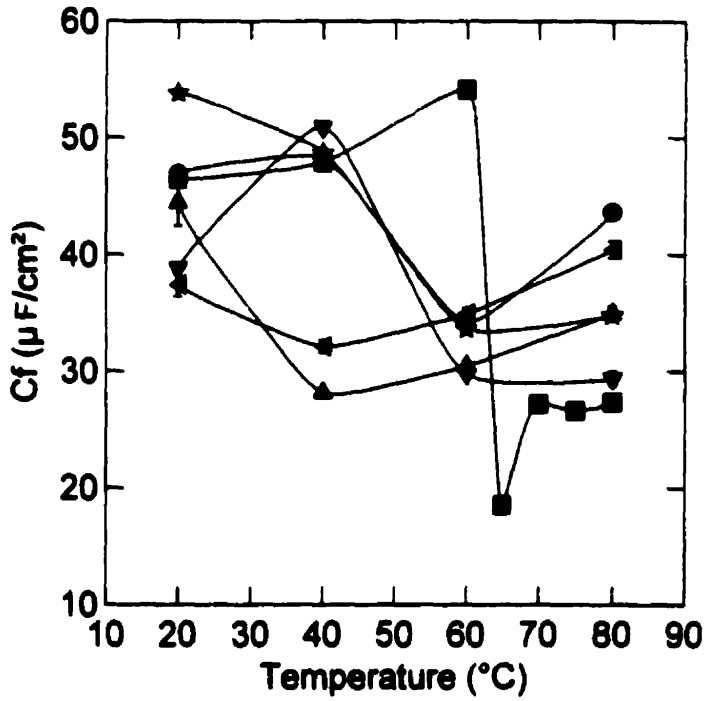

Figure 3.2.2-t C_f *values determined by least squares fitting model equivalent circuits to experimental electrochemical impedance spectra recorded in 0.27 mol·dm*$^{-3}$ *NaCl on high purity Ti* (●), Ti-2 (■), Ti-12 (▼), Ti-16 (◁), Ti-0.1Ru (▲) and in *0.27 mol·dm*$^{-3}$ Na_2SO_4 *on Ti-2* (★). *Error bars indicate the rms error in the least squares fitting; however, the errors associated with most of the points are small enough that they are obscured by the graphing symbols.*

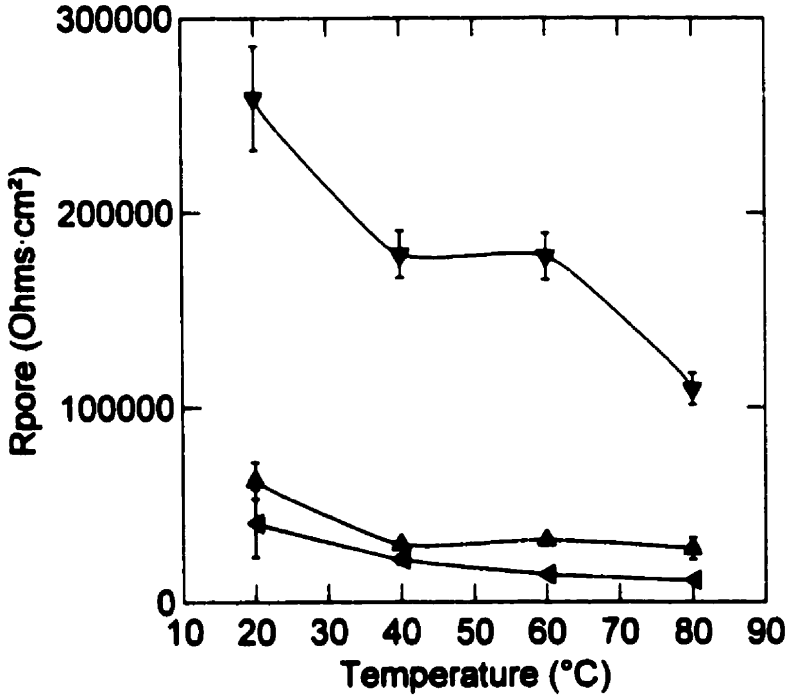

Figure 3.2.2-u R_{pore} *values determined by least squares fitting model equivalent circuits to experimental electrochemical impedance spectra recorded in 0.27 mol·dm*$^{-3}$ *NaCl on* Ti-12 (▼), Ti-16 (◁), and Ti-0.1Ru (▲). *Error bars indicate the rms error in the least squares fitting; however, the errors associated with many of the points are small enough that they are obscured by the graphing symbols.*

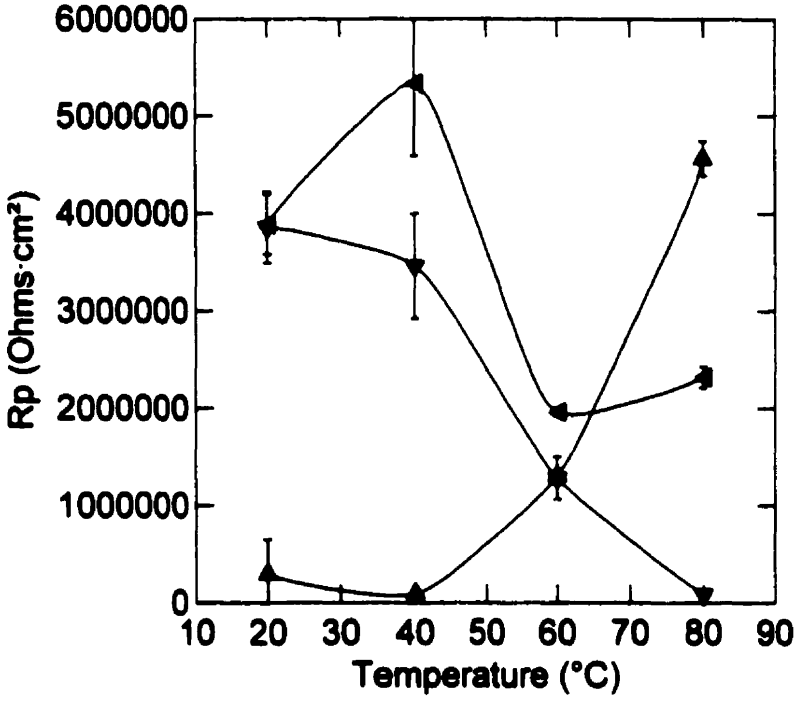

Figure 3.2.2-v R_p *values determined by least squares fitting model equivalent circuits to experimental electrochemical impedance spectra recorded in 0.27 mol·dm*$^{-3}$ *NaCl on* Ti-12 (▼), Ti-16 (◁), and Ti-0.1Ru (▲). *Error bars indicate the rms error in the least squares fitting; however, the errors associated with some of the points are small enough that they are obscured by the graphing symbols.*

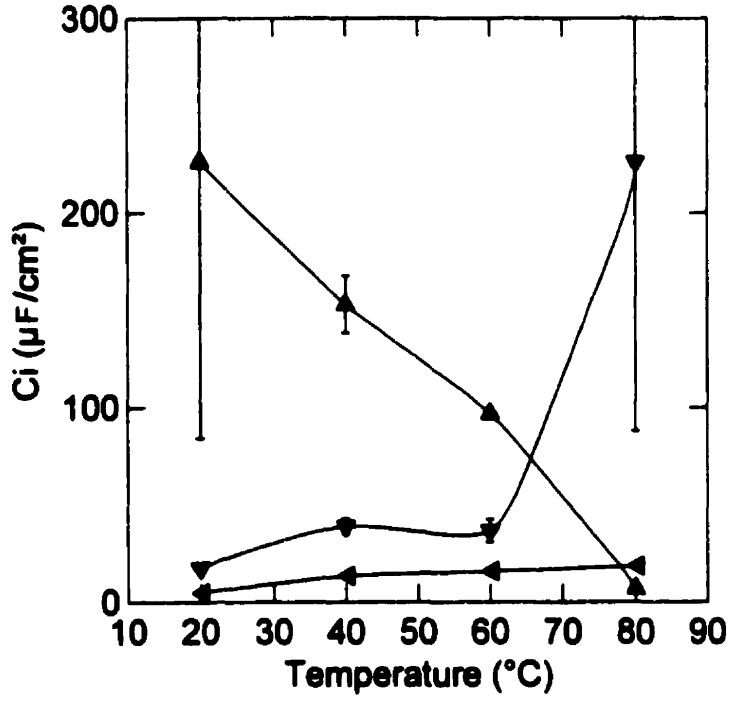

Figure 3.2.2-w C_l *values determined by least squares fitting model equivalent circuits to experimental electrochemical impedance spectra recorded in 0.27 mol·dm*$^{-3}$ *NaCl on* Ti-12 (▼), Ti-16 (◁), and Ti-0.1Ru (▲). *Error bars indicate the rms error in the least squares fitting; however, the errors associated with many of the points are small enough that they are obscured by the graphing symbols.*

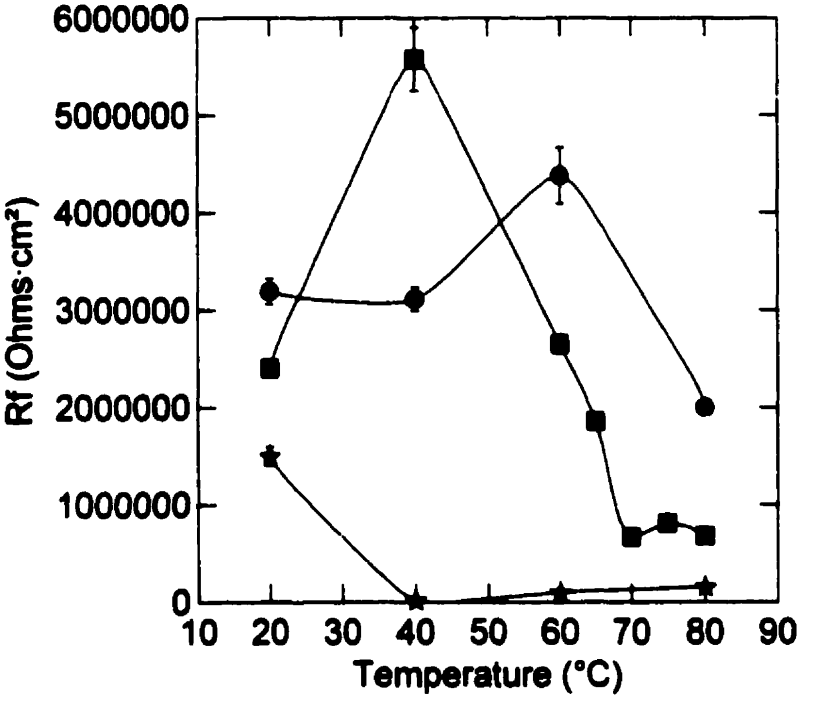

Figure 3.2.2-x R_f *values determined by least squares fitting model equivalent circuits to experimental electrochemical impedance spectra recorded in 0.27 mol·dm*$^{-3}$ *NaCl on high purity Ti (●) and Ti-2 (■), and in 0.27 mol·dm*$^{-3}$ Na_2SO_4 *on Ti-2 (★). Error bars indicate the rms error in the least squares fitting; however, the errors associated with most of the points are small enough that they are obscured by the graphing symbols.*

~28 $\Omega \cdot cm^2$ and correspond to Ti-16 and Ti-0.1Ru at 20°C. It is difficult to comment further on their significance without repeated experiments under the same conditions to verify their reproducibility.

The values of C_f, plotted in Figure 3.2.2-t, show some interesting trends. The high purity Ti, Ti-2, and Ti-12 all displayed a large drop in C_f at elevated temperatures. They all exhibited C_f values in the range 45-55 $\mu F \cdot cm^{-2}$ at 20 and 40°C (except Ti-12 at 20°C, which had a somewhat lower value), but at 60°C (65°C for Ti-2 in NaCl solution) and above, C_f dropped to 25-35 $\mu F \cdot cm^{-2}$ and remained nearly constant (except on high purity Ti, where it increased again at 80°C). If one ignores for a moment the few points that do not match this trend, one can develop an idea that there is a drop in the film capacitance (the data seem to trace roughly a *Z*-shaped curve) at temperatures in the range 40-60°C on these three materials. This is just below the temperature at which breakdown crystallization is expected to occur and in the range where water absorption by the oxide layer has been seen to increase significantly [84]. For the Ti-16 and Ti-0.1Ru electrodes, C_f dropped between 20 and 40°C and increased from 40 to 80°C. It is uncertain what this trend indicates about the changing state of the materials' surfaces with increasing temperature.

Figure 3.2.2-u shows how R_{pore} decreases with increasing temperature for the three materials whose impedance spectra required the double time constant equivalent circuit for fitting. The R_{pore} values for Ti-12 were all much larger than those determined for either Ti-16 or Ti-0.1Ru, and showed the greatest absolute decrease over the temperature range investigated (from about 260 $k\Omega \cdot cm^2$ at 20°C to about 110 $k\Omega \cdot cm^2$ at 80°C),

although R_{pore} for the latter two materials also decreased by more than 50%. The R_{pore} values for Ti-16 and Ti-0.1Ru were similar over the entire temperature range, those on Ti-0.1Ru being slightly higher than those on Ti-16. These observations imply that ionic access through (around) the oxide is more restricted on Ti-0.1Ru than on Ti-16, and much more restricted on Ti-12. The ease of ionic access follows the same order as the crevice corrosion resistance for these materials (expected positions in parentheses): (high purity Ti), ~Ti-2 < Ti-12 <Ti-16, ~(Ti-0.1Ru).

This idea of a "pore resistance" and the observation that it was only necessary to invoke it to explain the impedance spectra of Ti-12, Ti-16 and Ti-0.1Ru, and not those of high purity Ti nor Ti-2, is consistent with the model of corrosion protection by noble cathodic sites on the material surface. In order for such sites to act as cathodic modifiers, they must be open to solution, with reasonable access to the oxidants present. This would be the case if it was difficult to form a continuous oxide over the catalytic sites, possibly because of their noble (oxidation-resistant) nature. For the materials without intentional additions of cathodically modifying phases and on which cathodic modification is not observed[1] (high purity Ti and Ti-2), only a single time constant was observed in the impedance spectra, implying that no significant lower-resistance ionic pathways through the oxide were present.

The Ti-12, Ti-16 and Ti-0.1Ru alloys demonstrated different trends in R_p, as shown in Figure 3.2.2-v. R_p was quite high (3.8 $M\Omega \cdot cm^2$) on both Ti-12 and Ti-16 at 20°C, but

[1] Except spontaneous cathodic self-modification, which was only observed on Ti-2 in HCl solution over a limited pH range, and only after a period of oxide dissolution leading to penetration of the passive film.

decreased with increasing temperature on Ti-12. On Ti-16, R_p increased to ~5.4 $M\Omega \cdot cm^2$ at 40°C before dropping at higher temperatures. The R_p values on Ti-0.1Ru, by contrast, were much lower (< 1 $M\Omega \cdot cm^2$) at 20 and 40°C, then increased at the higher temperatures, reaching about 4.6 $M\Omega \cdot cm^2$ at 80°C. In general, these results imply that Ti-12 and Ti-16 become more reactive at higher temperatures, but the reactivity of Ti-0.1Ru decreases with increasing temperature. It is difficult to speculate on the reason for this strange behaviour of the Ti-0.1Ru.

The values of C_i in Figure 3.2.2-w highlight another difference between Ti-16 and Ti-0.1Ru. While Ti-0.1Ru had a very high C_i value at 20°C that decreased linearly with increasing temperature, C_i was very low on Ti-16, and remained so at all temperatures tested. The two materials had similar C_i values only at 80°C. The C_i values of Ti-12 were somewhat higher than those of Ti-16, but much lower than those of Ti-0.1Ru, and didn't change much over the temperature range 20-60°C. At 80°C C_i for Ti-12 jumped to a value as high as that seen on Ti-0.1Ru at 20°C.

The final equivalent circuit element values to be discussed are those of R_f, seen in Figure 3.2.2-x for high purity Ti and Ti-2. In chloride solution, the film resistances initially increased with increasing temperature before dropping significantly at temperatures above 40°C for Ti-2 and 60°C for high purity Ti. The Ti-2 electrodes exposed to sulphate solution showed much lower film resistance values at all temperatures above 20°C, R_f increasing slightly with temperature up to 80°C. The drop in film resistance at elevated temperatures in chloride solution is reminiscent of the drop in film capacitance values on these same materials (see Figure 3.2.2-t), although the

transition temperatures do not coincide exactly. These transition temperatures are just below the temperature at which breakdown crystallization is expected to occur and in the range where water absorption by the oxide layer has been seen to increase significantly [84].

Breakdown crystallization may account for the drop in film resistance on these electrodes by providing lower-resistance pathways for ion transport through the film, possibly along grain boundaries in the oxide. It is interesting to note, however, that breakdown crystallization does not result in the formation of open, active cracks and pores in this solution, since a second time constant in the impedance did not appear. Therefore, any cracks in the oxide formed by crystallization must have been relatively small or quickly filled with more oxide (not an unreasonable outcome in neutral pH solution). The high magnitude of R_f, even at its lowest values, support this conclusion. An acidic solution may be better suited to probing oxide cracking during breakdown crystallization if oxide self-repair is a concern, since repair should be hindered by a low pH. The comparatively low R_f values on Ti-2 in sulphate solution were a surprise and may relate to the greater ability of sulphate to complex Ti ions, perhaps resulting in a thinner or more defective oxide film because of interference with the film growth process.

Kolman and Scully [70] proposed a different double time constant equivalent circuit than the one used here in their studies of a Ti-15Mo-3Nb-3Al alloy in 0.6 $mol \cdot dm^{-3}$ NaCl solution at pH 1. Their equivalent circuit is illustrated in Figure 3.2.2-y. By appropriate choices of circuit element values, such a circuit can be made to generate the same response given by the double time constant circuit used in these experiments, however the

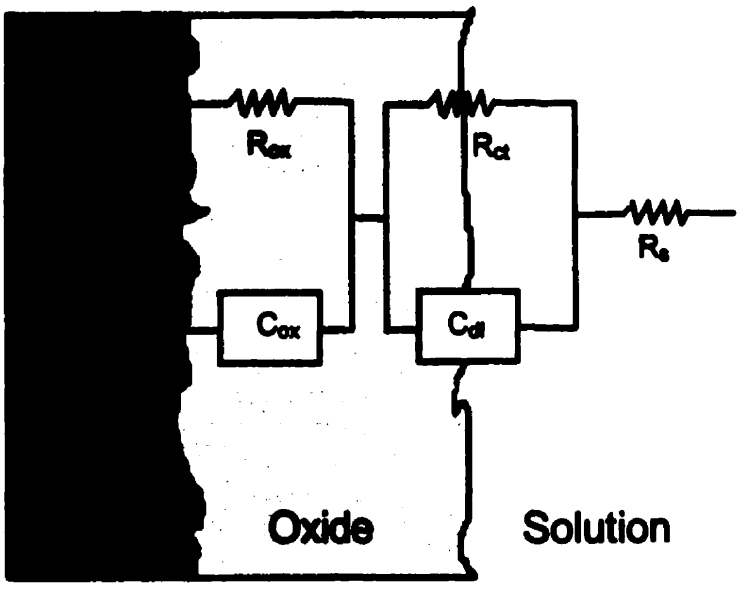

Figure 3.2.2-y Double time constant equivalent circuit used by Kolman and Scully [70] for modeling the impedance response of Ti-15Mo-3Nb-3Al alloy electrodes in 0.6 mol·dm^{-3} NaCl at pH 1. The circuit includes solution resistance (R_s), oxide film capacitance (C_{ox}), oxide film resistance (R_{ox}), charge transfer resistance (R_{ct}) and a double layer capacitance (C_{dl}).

physical circumstances implied by the two models are different. In Kolman and Scully's model, all charge transfer takes place through an unbroken passive oxide film, with charge transfer taking place on its surface. This is plausible for an oxide film into which are incorporated various alloying constituents that may contribute to its conductivity, and is consistent with the film's ability to evolve oxygen, as reported by the authors [70]. Another contributing factor may be the low pH (= 1) used by Kolman and Scully, which may have resulted in the growth of a more defective oxide film on their electrodes. The model invoked for the current studies uses the second time constant as a bypass around the passive oxide film. This approach is more consistent with the ideas previously presented regarding the functioning of the corrosion resistant cathodically modified alloys: for the alloys to offer corrosion resistance by catalysis of proton reduction at noble metal-containing intermetallic sites, these sites must be easily accessible to the electrolyte solution. This would be the case if the catalytic sites were located at the bottoms of pores in the oxide, such pores resulting from an inability of the material to grow a complete passive film over these locations due to the different local composition of the substrate material. The concentrations of alloying elements in these materials is very low, and it is unlikely that the composition of the oxide on these materials is much different from that on the high purity Ti or Ti-2 electrodes, yet when these noble metal-containing intermetallic particles are absent (*i.e.*, on high purity Ti and Ti-2) only a single time constant is needed to model the data (there is no shortcut around the passive film).

3.2.3 X-ray photoelectron spectroscopy

As quickly as possible following some of the E_{oc} measurements described in Section 3.2.1, XPS was performed on the electrodes. Unfortunately, this *ex situ* analysis required that the electrodes be emersed from solution, rinsed to remove traces of the electrolyte, mounted on a holder, and entered into the XPS vacuum system. Such a procedure exposed the electrodes to air and rendered the XPS results subject to the possibility that the state of their surfaces could have been influenced by oxygen, carbonaceous species and other undesirable atmospheric components, as discussed in Section 1.3.2. However, in spite of these caveats, the meaningfulness of the XPS analyses was not entirely defeated; the results are presented below.

The XPS analysis for each electrode consisted of an initial survey scan of electron binding energies from 0-1100 eV and three high-resolution scans that focused on the binding energy ranges corresponding to photoelectrons ejected from C_{1s}, $Ti_{2p3/2}$, and O_{1s} orbitals. The purpose of the survey scan was to verify that the measured signal originated from the sample (as opposed to the holder or other components of the apparatus), and to determine the presence of observable levels of alloying elements or foreign contaminants. Two of the high-resolution spectra were recorded to determine, quantitatively, the distribution of electron binding energies of Ti and O and therefore the oxidation states and chemical environments of these elements; the C_{1s} band was recorded at high resolution to determine a reference point for the other binding energies in the spectrum. The binding energy for the C_{1s} electrons of the adventitious carbonaceous material commonly found on sample surfaces was taken to be 284.8 eV [175] and the difference

between the latter and the measured value (usually a few electron volts or less) was used to correct the binding energy values for all measured peaks in the spectrum. Such a correction was required to compensate for the accumulation of a net charge on the sample during analysis, the presence of which changes the energy of the emitted photoelectrons via electrostatic interactions.

A typical XPS survey scan is shown in Figure 3.2.3-a, with peak assignments as indicated in Table 3.2.3-a. The particular spectrum shown in the Figure was acquired from a Ti-2 electrode that had been exposed to 0.27 $mol \cdot dm^{-3}$ NaCl solution at 20°C for ~17 h. The spectrum shows the expected Ti and O peaks from the ubiquitous surface oxide film, along with contributions from C, Cl, Ca, K, N, and Na impurities. The experimental procedure employed rendered adventitious carbon unavoidable and NaCl very difficult to eliminate, since electrolyte species could be adsorbed at the electrode surface, or included or entrained in the oxide itself. The traces of K may have originated from the SCE reference electrode or from impurities in the electrolyte[1]. The latter may also have been the source of the small amount of Ca that was detected. The N probably originated from the ambient atmosphere, to which the electrode was exposed during transfer to the XPS system.

The survey spectra for all alloys and exposure temperatures were qualitatively similar; quantitative differences in the Ti and O signals are presented and discussed below. No alloying components (other than Ti, of course) were found in any of the spectra, indicating that they were not present in the sample surfaces in detectable (>~1 at.%)

[1] The analytical report on the NaCl container label indicated that it contained 10 ppm K and up to 10 ppm Ca.

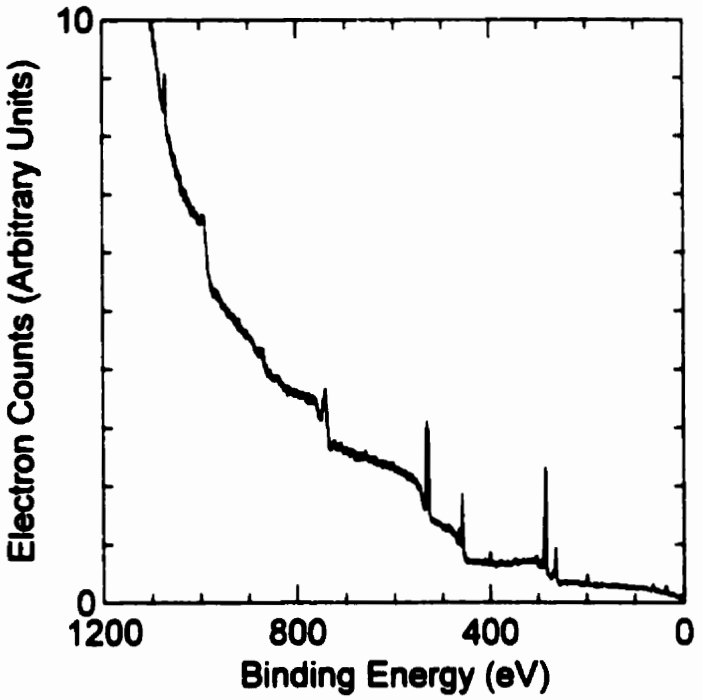

Figure 3.2.3-a X-ray photoelectron spectrum of Ti-2 after exposure to 0.27 mol·dm^{-3} NaCl at 20°C for ~17 h. The binding energies have been corrected (by 1.5 eV) for sample charging, X-ray satellite peaks have been subtracted, and a five-point smoothing procedure has been applied. Peak assignments [175] are indicated in Table 3.2.3-a.

quantities. This is not surprising since these dilute alloys contain <1 at.% of any single component (except Ti) in the alloy bulk. It also indicates that these alloying constituents did not become enriched to detectable levels at the electrode surfaces (that is, to the maximum depth observable by XPS) under the exposure conditions investigated.

Table 3.2.3-a Peak Assignments [175] for the XPS Spectrum Shown in Figure 3.2.3-a

Binding Energy (eV)	Assignment	Binding Energy (eV)	Assignment
1071	Na_{1s}[a], Cl_{LMM}[b]	302	Na_{KLL}
993	C_{KLL}	296	$K_{2p1/2}$
875	N_{KLL}	293	$K_{2p3/2}$
869	Ti_{LMM}	284.8	C_{1s}
741	O_{KLL}	268	Cl_{2s}
660	Unknown	264	Na_{KLL}
532	O_{1s}	198	$Cl_{2p3/2}$
530	O_{1s}	63	Na_{2s}, Ti_{3s}
464	$Ti_{2p1/2}$	36	Ti_{3p}
458	$Ti_{2p3/2}$	22	O_{2s}
400	N_{1s}	18	Cl_{3s}, K_{3p}
378	K_{2s}	5	O_{2p}
347	$Ca_{2p3/2}$		

[a] Subscripts 1s, 2s, 3s,2p, 2p1/2, 2p3/2, and 3p refer to the atomic orbitals from which the photoelectrons were emitted.

[b] Subscripts LMM and KLL indicate the three energy levels involved in Auger electron emissions.

The high resolution XPS scans of the $Ti_{2p3/2}$ and O_{1s} bands were deconvoluted to determine the chemical states in which Ti and O were present in the electrode surfaces, and the relative abundance of species in each state. Deconvolution was done using the data massaging routines on the spectrometer. Model parameter estimates and ranges of variability were selected based on binding energies and FWHM values from published spectra [93, 96-98, 100, 156].

Peak profiles comprising a mixture of Gaussian and Lorentzian character (almost entirely Gaussian) were developed in combination with the data extracted from literature spectra and fine-tuned[1] by comparison with one of the experimental spectra. After this, the form of the model was frozen and the deconvolution of other experimental spectra proceeded, with the peak shapes and positions fixed within the ranges allowed by the model. The fitting software used the established model to determine the peak heights, widths, and locations required to build a peak structure simulating that of the experimentally determined band. All bands underwent background subtraction and X-ray satellite peak removal prior to deconvolution.

An example of the deconvolution of the O_{1s} band on freshly polished Ti-0.1Ru is shown in Figure 3.2.3-b. The O_{1s} band was found to be composed of three components that can be attributed to oxygen atoms in H_2O (**A**, 532.1 eV), Ti-OH (**B**, 530.9 eV), and Ti=O (**C**, 529.6 eV) species [84, 96]. The deconvoluted curves corresponding to each oxygen-containing species present in the sample surface were integrated and the relative amount of O in each chemical state was calculated as the ratio of the area under the relevant deconvoluted curve to the total area enclosed by the O_{1s} band in each spectrum. The breakdown of the O_{1s} band into H_2O, Ti-OH, and Ti=O components after electrode exposure to NaCl solution at each temperature is given in Figures 3.2.3-c (high purity Ti), 3.2.3-d (Ti-2), 3.2.3-e (Ti-12), 3.2.3-f (Ti-16), and 3.2.3-g (Ti-0.1Ru).

[1] Admittedly, this procedure was somewhat subjective and relied on operator experience and judgements: however, the consistency of the results derived from the other independent experimental spectra supports the validity of the adjustments made.

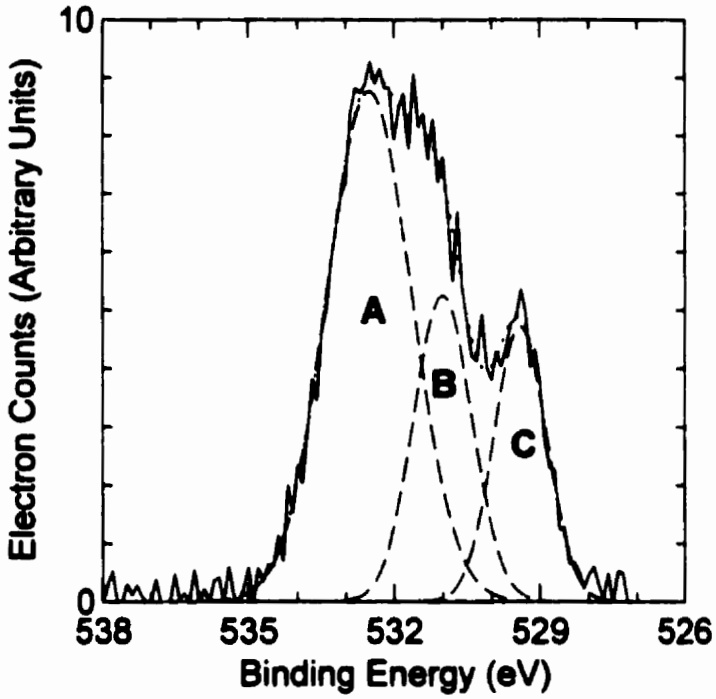

Figure 3.2.3-b O_{1s} *band from high-resolution XPS scan of a Ti-0.1Ru electrode immediately following wet polishing and its deconvolution into components attributable to water (A), Ti-OH (B), and Ti=O (C); experimental data (———), deconvoluted component peaks (— — —), and sum of fitted component peaks (· · ·· ·· ·).*

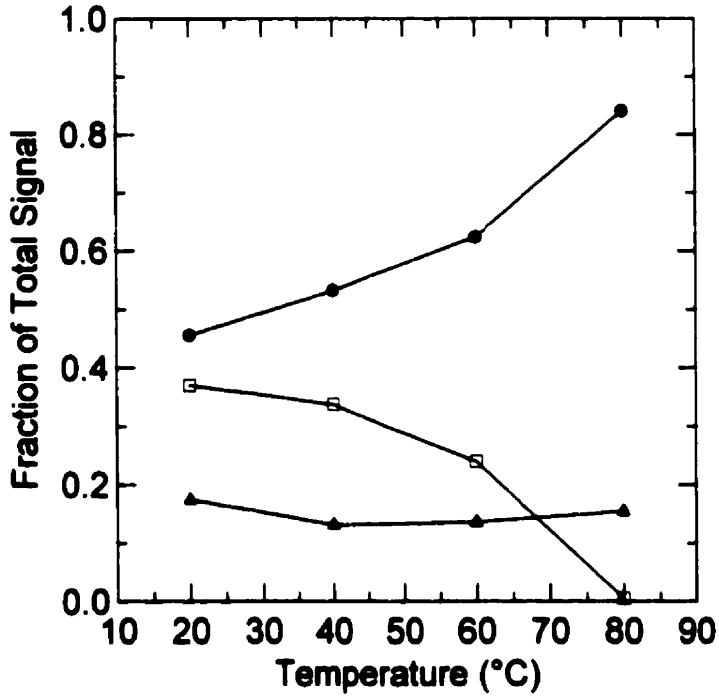

Figure 3.2.3-c Relative amounts of each oxygen species apparent in the surface of a high purity Ti electrode after exposure to deaerated 0.27 mol·dm^{-3} NaCl at various temperatures, as determined by deconvolution of the O_{1s} XPS band; water (□), Ti-OH (▲), and Ti=O (●).

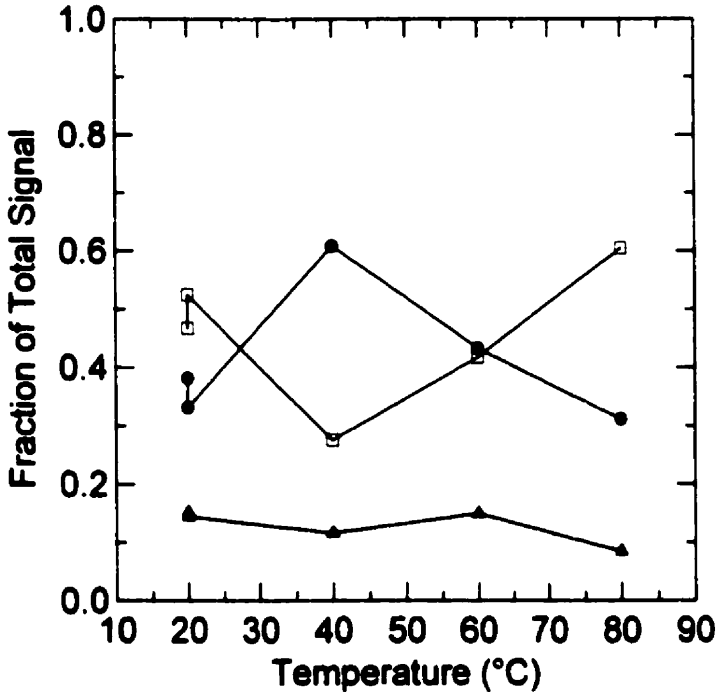

Figure 3.2.3-d Relative amounts of each oxygen species apparent in the surface of a Ti-2 electrode after exposure to deaerated 0.27 mol·dm^{-3} NaCl at various temperatures, as determined by deconvolution of the O_{1s} XPS band; water (□), Ti-OH (▲), and Ti=O (●).

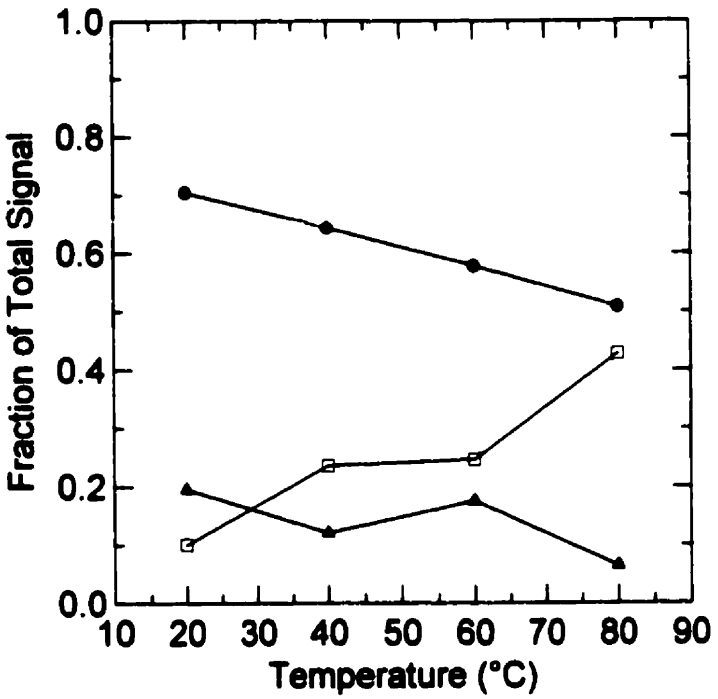

Figure 3.2.3-e Relative amounts of each oxygen species apparent in the surface of a Ti-12 electrode after exposure to deaerated 0.27 mol·dm^{-3} NaCl at various temperatures, as determined by deconvolution of the O_{1s} XPS band; water (□), Ti-OH (▲), and Ti=O (●).

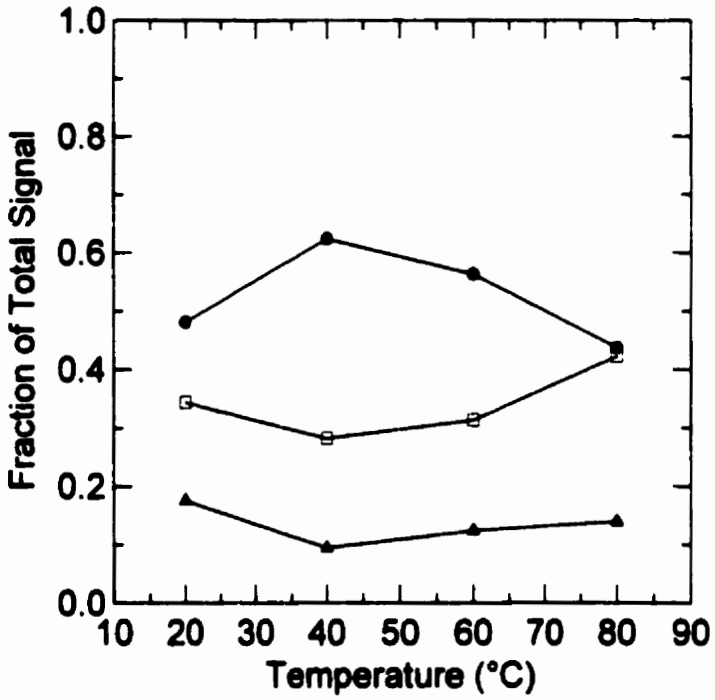

Figure 3.2.3-f Relative amounts of each oxygen species apparent in the surface of a Ti-16 electrode after exposure to deaerated 0.27 mol·dm^{-3} NaCl at various temperatures, as determined by deconvolution of the O_{1s} XPS band; water (□), Ti-OH (▲), and Ti=O (●).

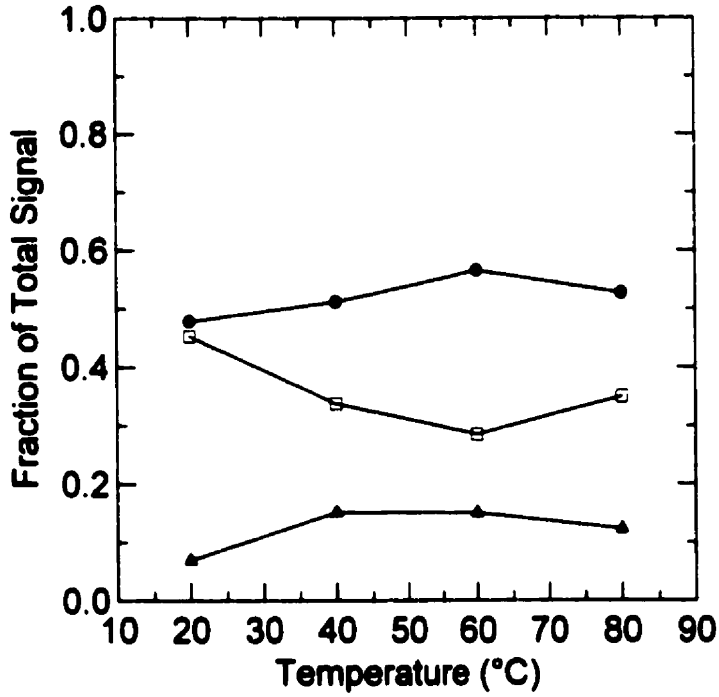

Figure 3.2.3-g Relative amounts of each oxygen species apparent in the surface of a Ti-0.1Ru electrode after exposure to deaerated 0.27 mol·dm^{-3} NaCl at various temperatures, as determined by deconvolution of the O_{1s} XPS band; water (□), Ti-OH (▲), and Ti=O (●).

Distinct changes with both temperature and alloy type were observed in the O_{1s} band. Above 40°C, the amount of oxygen associated with bound water increased with increasing temperature, except for films grown on the high purity Ti, which showed the opposite trend, and on Ti-0.1Ru, on which it remained relatively constant. An increase in the amount of bound water in anodic Ti oxide films with increasing temperature was also observed by XPS by Shibata and Zhu [84]. These authors found a steady increase in the water content of anodic films formed in 0.5 mol·dm^{-3} H_2SO_4 at temperatures below 70°C and a marked increase above 70°C.

The amounts of water in the oxide films grown at 20°C, except on Ti-12, appear surprisingly high. The reason for the higher water contents in films grown at 20°C is not known; however, it may be that these films had not yet established a steady-state composition during their 16-30 h of exposure to solution, perhaps due to slow kinetics at this lower temperature. This idea is supported, albeit weakly, by the non-steady state nature of the E_{oc} transients in these exposures. The equivalent circuit element values derived from EIS experiments at 20°C also sometimes appeared "out of line" with the trends shown by the data from other temperatures.

The Ti-OH contents were remarkably similar for all alloys and all electrolyte temperatures, contributing 5-20% of the total O_{1s} signal. Other researchers [84, 96] have noted that the distinction between bound water and hydrated metal (Ti-OH) species by XPS is difficult and have dealt with these two components as a single combined contribution. If the same is done with the current results (*i.e.*, summing the H_2O and Ti-

OH contributions), the temperature-related trends in the data remain as described above for the bound water component, as seen in Figure-3.2.3-h.

Figure 3.2.3-i demonstrates the deconvolution of the $Ti_{2p3/2}$ XPS band [93], from a spectrum acquired on freshly polished Ti-2, into components associated with Ti^{IV} species (**D**, 458.5 eV), Ti^{III} (**E**, 456.7 eV), and Ti from the substrate metal[1] (**F**, 453.5 eV). For all of the electrodes exposed at E_{oc} to the NaCl solutions, at all temperatures tested, the only Ti oxidation state detectable was Ti^{IV}. From the levels of noise in the experimental spectra in the vicinity of the $Ti_{2p3/2}$ band, it was estimated that the detection limits for Ti^{III} and metallic Ti were on the order of 10-15% of the total $Ti_{2p3/2}$ signal.

In addition to the examinations of electrodes after exposure to solution, XPS analyses were performed on freshly polished disks of each material. The latter specimens were wet-polished and rinsed (at room temperature) before XPS, but not exposed to any saline solutions. Freshly polished samples displayed observable levels of Ti^{III} and metallic Ti, unlike the electrodes that had been exposed to solution. This difference was probably due to the thinness of the oxide film immediately after polishing and the oxidation of lower-valence Ti species with time during exposure to aqueous solution. The relative amounts of Ti^{IV}, Ti^{III}, and metallic Ti measured on freshly polished disks of each alloy are plotted in Figure 3.2.3-j.

The water and Ti-OH contents of freshly polished specimens of each alloy are plotted in Figure 3.2.3-k. The high purity Ti, Ti-2 and Ti-12 samples had quite similar total water

[1] A good description of the extent to which sub-surface species can contribute to the XPS spectrum and how the intensity of the photoelectron signal from the underlying metal can be used to estimate the thickness of the oxide film on Ti alloys has been written by Stephen Yu [72].

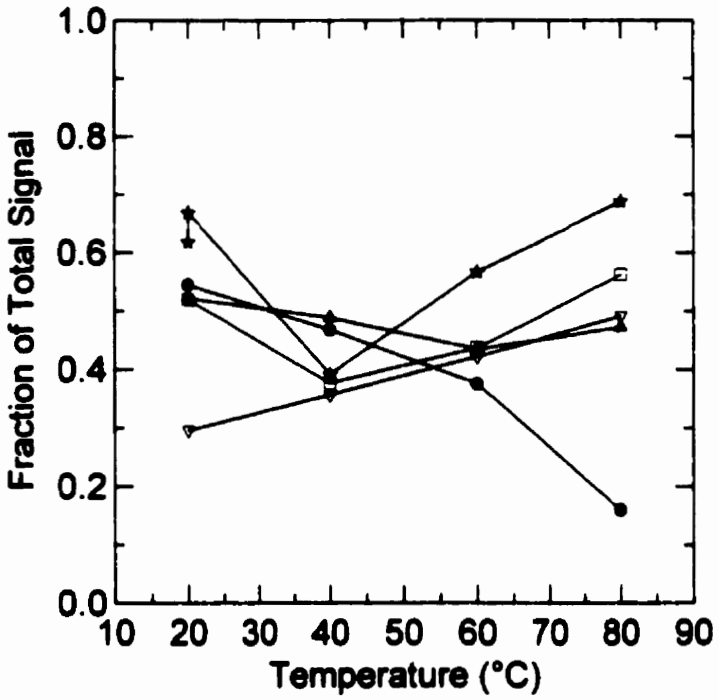

Figure 3.2.3-h Sum of water and Ti-OH components as a fraction of the total amount of oxygen species in the surfaces of Ti alloy electrodes after exposure to deaerated 0.27 mol·dm^{-3} NaCl at various temperatures, as determined by deconvolution of the O_{1s} XPS band; high purity Ti (●), Ti-2 (★), Ti-12 (▽), Ti-16 (□), Ti-0.1Ru (▲).

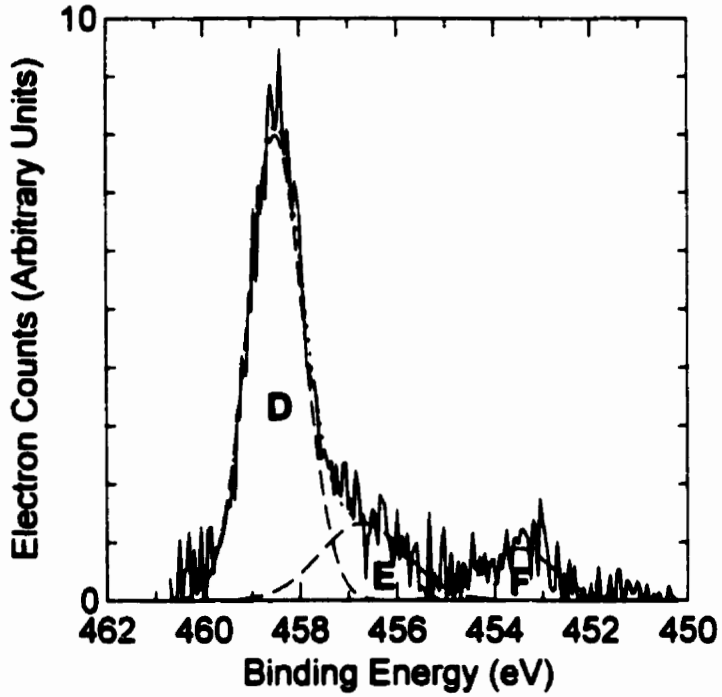

Figure 3.2.3-i $Ti_{2p3/2}$ *band from the high-resolution XPS scan of a Ti-2 electrode immediately following wet polishing and its deconvolution into components attributable to* Ti^{IV} *(D),* Ti^{III} *(E), and metallic Ti (F); experimental data (———), deconvoluted component peaks (— — —), and sum of fitted component peaks (· · · · · · ·).*

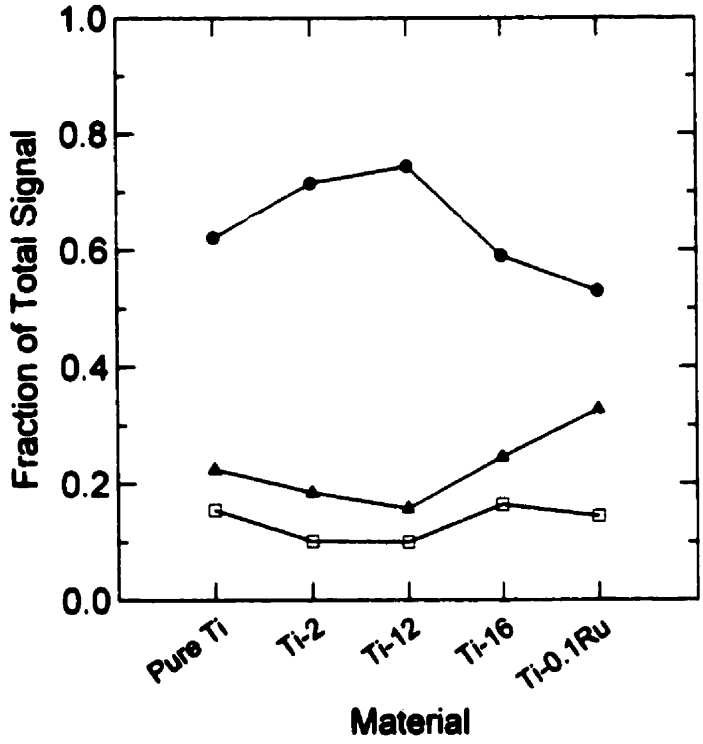

Figure 3.2.3-j Relative amounts of Ti in each oxidation state apparent in the surfaces of freshly polished Ti alloy electrodes (wet polished, without exposure to saline solution), as determined by deconvolution of the $Ti_{2p3/2}$ XPS band; metallic Ti (□), Ti^{III} (▲), and Ti^{IV} (●).

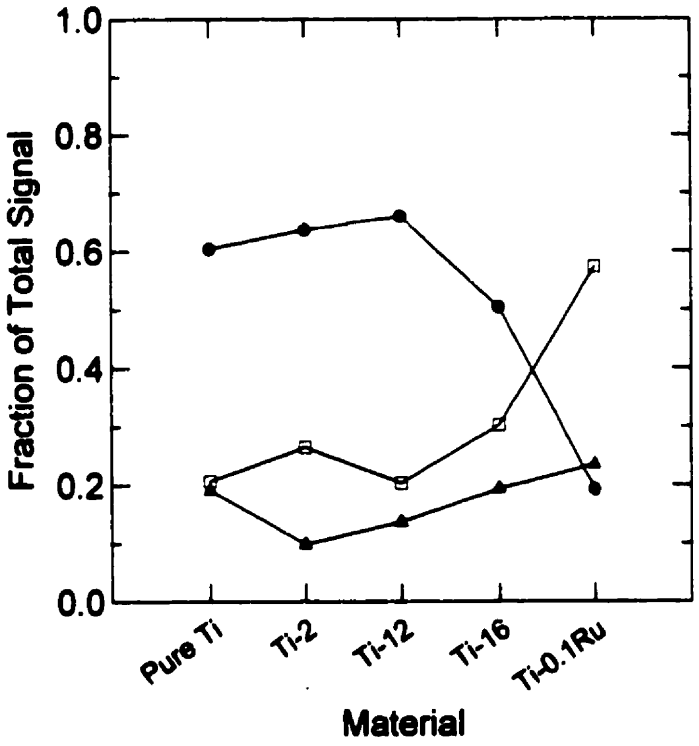

Figure 3.2.3-k Relative amounts of each oxygen species apparent in the surfaces of freshly polished Ti alloy electrodes (wet polished, without exposure to saline solution), as determined by deconvolution of the O_{1s} XPS band; water (□), Ti-OH (▲), and Ti=O (●).

and Ti-OH contents, while those of Ti-16 and Ti-0.1Ru were much higher. This may be coincidental, since such comparisons are not consistent among the samples exposed to NaCl solutions, as seen in Figure 3.2.3-h.

Some concern over the possibility that absorbed water and OH could be extracted from these oxide films on prolonged exposure to the ultra high vacuum (UHV) of the XPS system led to an investigation of the time-dependence of the corresponding signals. A Ti-2 sample that had been exposed to 40°C NaCl solution and examined by XPS according to the procedure used for all of the XPS analyses reported above was left in the UHV system and re-analyzed several times by XPS over a period of seven days. The water, Ti-OH and Ti=O contents measured after 3 h, 18 h, 42 h, and 168 h are presented in Figure 3.2.3-l and show the fraction of the O_{1s} signal corresponding to water decreasing with time while the other two components increase. Detailed examination of these results reveals, however, that the apparent time-dependence cannot be explained as a simple loss of water from the surface, because the ratio of Ti-OH to Ti=O increases with time (it would remain constant if water loss was the only process occurring, or decrease if OH was abstracted as well). Instead of vacuum desiccation, it is likely that at least some of the changes observed were caused by repeated exposure to the X-ray beam, and possible that the presence of the specimen in the vacuum chamber while other unrelated specimens were analyzed resulted in further damage. The influence of the effects shown in Figure 3.2.3-l in the rest of the XPS data is expected to be minimal, since the electrodes were analyzed within a few hours of entry into the UHV chamber, and few or no other analyses were performed during this period, nor were repeated analyses of the same specimen.

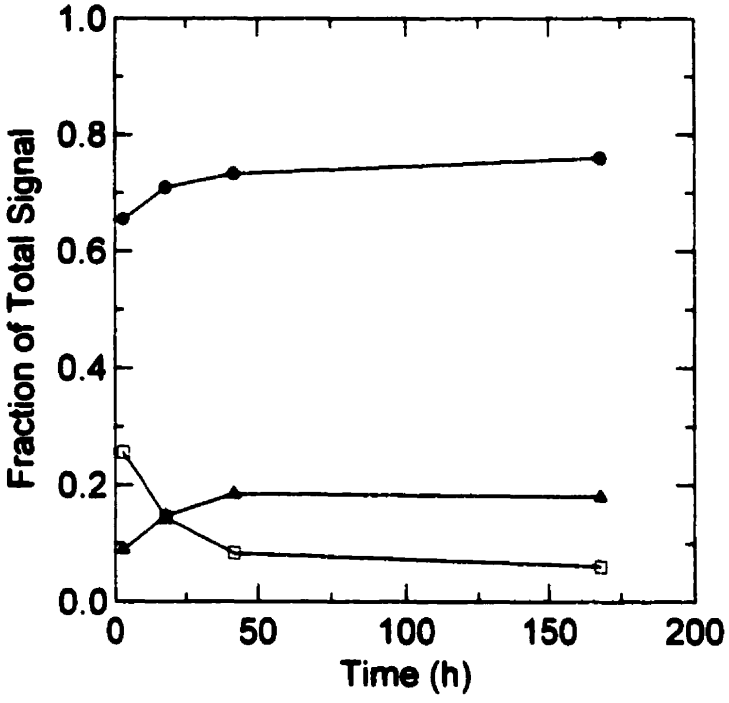

*Figure 3.2.3-l Relative amounts of each oxygen species apparent in the surface of a Ti-2 electrode after exposure to deaerated 0.27 mol·dm^{-3} NaCl at 40°C, as determined by deconvolution of the O_{1s} XPS band; water (□), Ti-OH (▲), and Ti=O (●). The speciation data are plotted as a function of the time that the sample was held under vacuum (*i.e., *the same specimen was left inside the UHV system and re-analyzed several times over a period of seven days).*

Angle-resolved XPS was employed to determine the location of the bound water and Ti-OH within the passive film on solution-exposed Ti. Angle-resolved XPS relies on the very short inelastic mean free path of low-energy electrons in condensed matter (<60 Å)[175] to provide information on the location of an element within the sample. Photoelectrons emitted from deeper within the sample have much less likelihood of escaping the surface at shallow angles than they do at high angles, due to the difference in the escape path length through the sample, as described in Section 2.1.2. Examples of the use of angle-resolved XPS for determining the depths of species within sample surfaces can be found in the following references: [72, 96, 199, 200].

Figure 3.2.3-m shows the sum of bound water and Ti-OH components in the film (as a fraction of the total O_{1s} signal) as a function of the angle between the plane of the sample surface and the electron analyzer. The decrease in H_2O and Ti-OH (*i.e.*, increase in Ti=O) with increasing analyzer angle indicates that the proportion of H_2O and Ti-OH relative to Ti=O decreases with increasing depth into the oxide film. This observation is consistent with the angle-resolved XPS results of Pan *et al.* [96] on Ti-2 in NaCl solution containing pH 7 phosphate buffer.

3.2.4 Neutron reflectometry

The neutron reflectometry experiments began with a characterization of the as-prepared sample. Neutron reflectometry scans were acquired in air with the as-prepared sample mounted in two orientations: first, with the neutrons incident from the air side of the Ti, and second, from the Si side as illustrated in Figure 2.6.5-b. This second orientation was

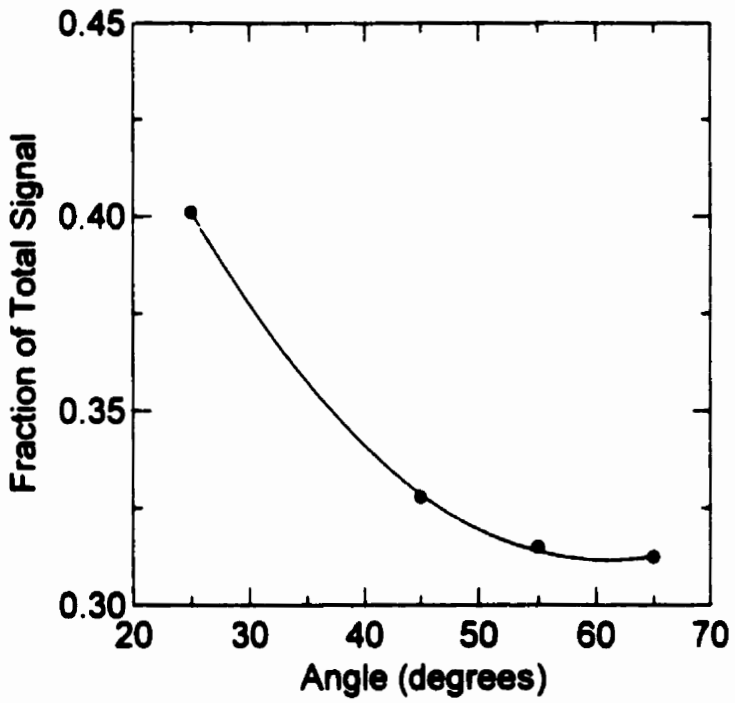

Figure 3.2.3-m Angle-resolved XPS measurement showing the sum of the O_{1s} signals from water and Ti-OH as a fraction of the total O_{1s} signal from a Ti-2 electrode after exposure to deaerated 0.27 mol·dm^{-3} NaCl solution at 40°C. The decrease in the signal fraction with increasing angle implies a decrease in the amount of water and OH with increasing depth into the passive oxide film.

also used for *in situ* reflectometry, except that the last medium (air) was replaced with an aqueous electrolyte.

The single-crystal Si substrate was highly transparent to neutrons; the loss of neutron flux due to neutrons having to traverse the entire diameter of the substrate was only ~ 17%. The neutron losses in the Si substrate arise mainly out of neutron absorption by the Si, in accordance with its neutron absorption cross section.

The counts of reflected neutrons from the reflectometry scans of the as-prepared sample are shown, together with the calculated reflectivity, $R_S(Q)$, scaled to the observed counts, in Figures 3.2.4-a and 3.2.4-b for the two orientations used (*i.e.*, with the neutrons incident from the air side and from the Si side, respectively). The values of $R_S(Q)$ in Figure 3.2.4-b were determined based on the least-squares fitted model illustrated in Figure 3.2.4-c. The agreement between the experimental data and $R_S(Q)$ was good and without any systematic residual disagreement. An equally good agreement was achieved between the experimental reflectivity data acquired on the as-prepared sample in air, in the other orientation, and the $R_S(Q)$ values derived from a model with the same layers and thicknesses found in the above model, but arranged in the opposite order.

The reader is cautioned again, just as in the case of EIS modeling reported in Section 3.2.2, that a favourable comparison between experimental data and values calculated from a model ($R_S(Q)$ in this case) does not necessarily mean the model is correct. Since the model-data agreement is obtained by fitting the initial model, there remains the possibility that a different initial model would have given a better fit. Therefore, in analyzing reflectometry data, as in other modeling, one always has to consider whether the model is reasonable. The approach used here was to begin with the

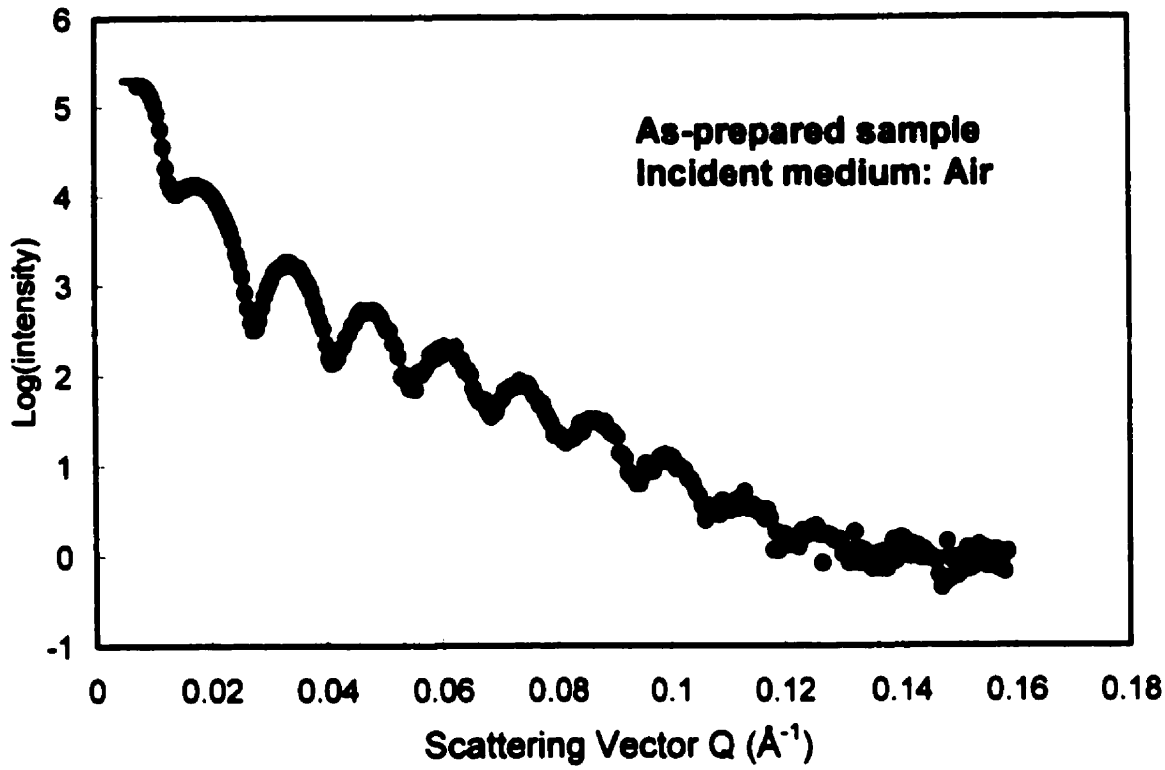

Figure 3.2.4-a Observed neutron counts specularly reflected by the as-prepared sample (●) and the calculated specular reflectivity, scaled to the observed intensities (———). Neutrons were incident on the Ti film from the air side.

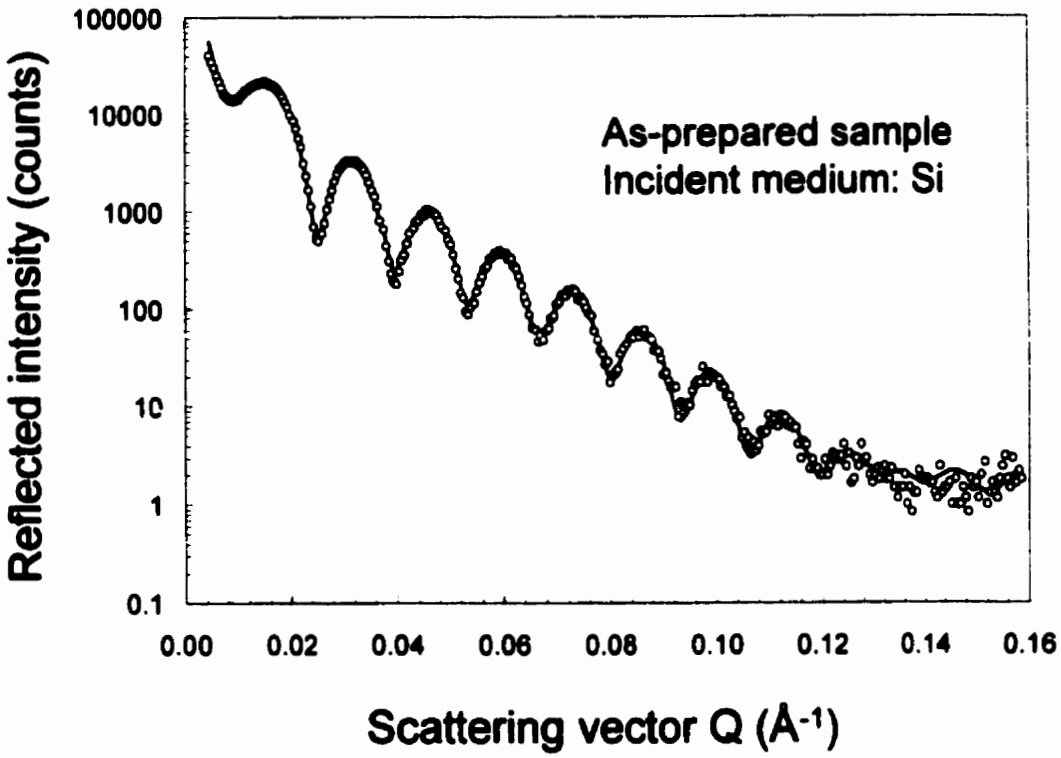

Figure 3.2.4-b Observed neutron counts specularly reflected by the as-prepared sample (°) and the calculated specular reflectivity, scaled to the observed intensities (———). Neutrons were incident on the Ti film from the Si side.

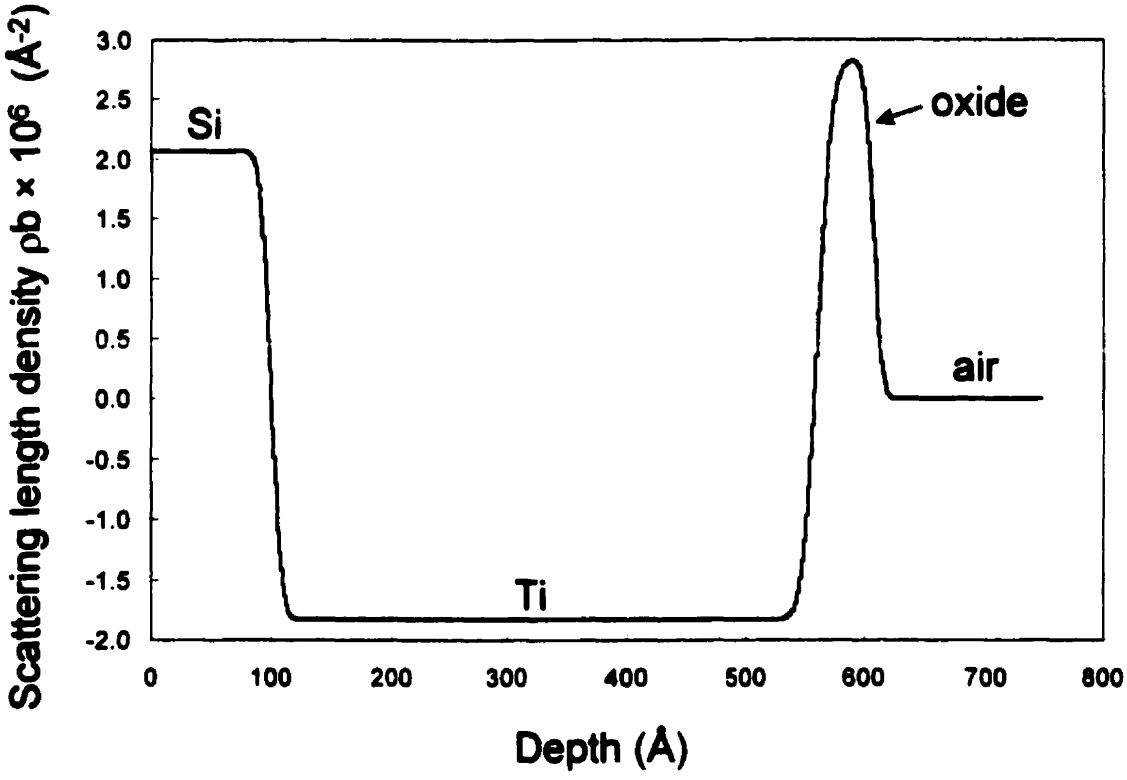

Figure 3.2.4-c Least-squares fitted SLD layer profile of the as-prepared thin film electrode. The numerical values of the model parameters are given in Table 3.2.4-b, the model consisting of layers of four distinct media: Si, Ti, titanium oxide, and air. The gradual interfaces between layers are represented by hyperbolic tangent functions.

simplest model possible for the system under study and to add no supplementary feature unless it led to a significantly better fit, and made physical and chemical sense.

After least-squares fitting, the final scattering length density (SLD) value estimates for each layer were compared to the independently calculated[1] SLD values for the materials expected to be present. The coherent neutron scattering lengths (for elements) or effective scattering lengths (for multinuclear species), number densities of atoms or molecules, and scattering length densities of materials that *could* be relevant to Ti thin film electrodes are listed in Table 3.2.4-a.

The SLD values listed in the Table were calculated assuming that the layers within the thin-film electrode were of densities equivalent to those of the corresponding bulk materials (*e.g.*, bulk single-crystal Ti metal). If the layers were defective or porous, or if the crystal structures of the thin films were different from those of the corresponding bulk materials, the actual SLD values for the layers could be lower or higher than the calculated estimates, depending on whether the pores were vacant or filled (and what they were filled with) or on whether the thin film was more or less dense than the bulk material. The model shown in Figure 3.2.4-c is the simplest layer profile that one could reasonably propose for the as-prepared Ti thin film electrode. It consists of the Si slab as the incident medium (only 100 Å shown in the Figure), a layer of metallic Ti, an oxide layer, and air (only 100 Å shown in the Figure). The thicknesses of the metal and oxide

[1] Calculated using tabulated values of b [179], and values of ρ calculated from the bulk densities [8] (see Section 2.1.4).

Table 3.2.4-a Coherent Neutron Scattering Lengths or Effective Scattering Lengths, Number Densities, and Scattering Length Densities of Materials that Could be Relevant to Ti Thin Film Electrodes.

Element, Compound, or Functional Group	(Effective) Coherent Neutron Scattering Length[a], b (fm)	Number Density[b], ρ ($Å^{-3}$)	SLD, ρb ($Å^{-2}$)
Si	4.1491	4.996×10^{-2}	2.07×10^{-6}
Ti	-3.438	5.670×10^{-2}	-1.95×10^{-6}
O	5.803	N/A	N/A
H	-3.7390	N/A	N/A
Na	3.63	N/A	N/A
Cl	9.5770	N/A	N/A
Fe	9.45	N/A	N/A
H_2O	-1.675	3.343×10^{-2}	-0.56×10^{-6} @ 20°C
SiO_2 (cristobalite)	15.7551	2.325×10^{-2}	3.66×10^{-6}
SiO_2 (amorphous)	15.7551	2.205×10^{-2}	3.47×10^{-6}
SiO_2 (quartz)	15.7551	2.666×10^{-2}	4.20×10^{-6}
TiO_2 (rutile)	8.168	3.211×10^{-2}	2.62×10^{-6}
TiO_2 (anatase)	8.168	2.894×10^{-2}	2.40×10^{-6}
TiO_2 (brookite)	8.168	3.143×10^{-2}	2.56×10^{-6}
TiH_2	-10.916	4.705×10^{-2}	-5.14×10^{-6}
-OH group	2.064	N/A	N/A
Air	~17	$\sim 2.5 \times 10^{-5}$	Negligible

[a] Taken or calculated from the data published by Sears [179].

[b] Calculated from published bulk density values [8].

layers have been refined by the fitting procedure, along with their SLD values and the widths of the interface regions.

One obvious omission from this "simplest" model is the layer of silicon dioxide that would have been present on the Si slab surface before the Ti film was deposited, and which one could reasonably expect to have remained at the Si/Ti interface. In fact, a region of increased oxygen concentration *was* observed at the Si/Ti interface by the Auger depth profiling performed after all neutron reflectometry and electrochemical experiments were completed (see Figure 3.2.4-d). As it seems unlikely that the oxygen

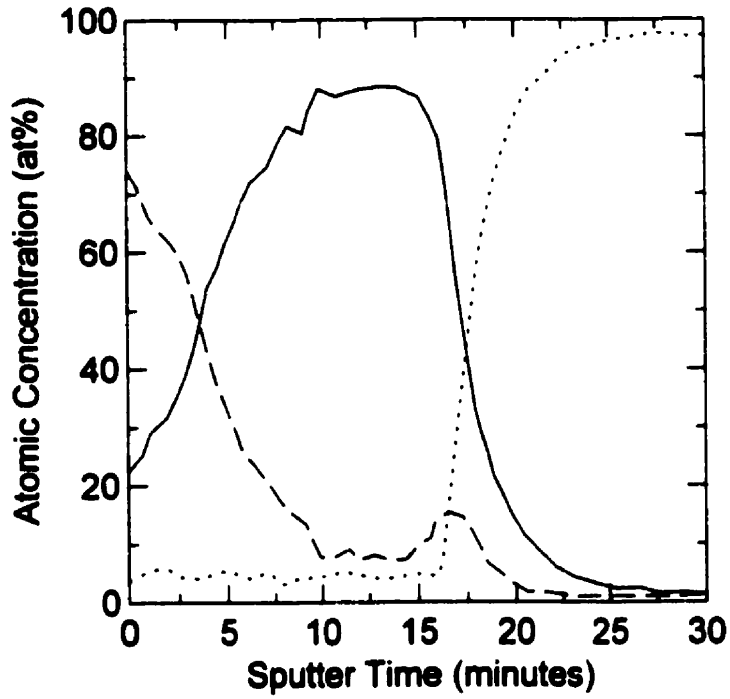

Figure 3.2.4-d Auger depth profile of Ti thin film electrode after completion of all in situ *electrochemistry/neutron reflectometry experiments, showing the concentrations of Ti (————), O (— — — —), and Si (· · · · · · · · ·) calculated as if these were the only elements present* (i.e., *ignoring the presence of hydrogen, which cannot be seen by AES). Note that the zero depth* (i.e., *zero time) and orientation of the sample in this profile are different than those of the profiles from neutron reflectometry. This is a consequence of the AES profiling technique, which looks at the outermost surface of the thin film* in vacuo.

concentration at the Si/Ti interface below an intact Ti film would have been significantly altered by the electrochemical treatments applied to the electrode, the observed region of increased oxygen concentration can be construed as the expected SiO_2 layer that would have existed since before the Ti was deposited. However, attempts to include this layer in the model did not lead to a significantly better fit (one of the important modeling criteria), so it was omitted.

Since there is a very large contrast in SLD between Si and SiO_2 and also between SiO_2 and Ti (see Table 3.2.4-a), it is, perhaps, surprising that a significantly better agreement between data and model was not obtained by including this layer, and one might initially consider the possibility that the good fit of the model in Figure 3.2.4-c was the product of a false least-squares minimum. However, the Auger electron spectroscopy depth profile[1], performed after all reflectometry experiments were finished, (Figure 3.2.4-d) revealed a significant interlayer diffusion of Ti into the Si slab that extended well beyond the depth of the oxygen-enriched region. The presence of significant amounts of Ti in Si reduces the average SLD in the mixed region well below that of pure Si, masking the increase in average SLD due to the presence of oxygen. This explains why the model does not require a region of increased SLD (corresponding to SiO_2) at the Si/Ti interface. Strictly speaking, the model of Figure 3.2.4-c is incorrect (because it omits the thin SiO_2 layer), but its features away from the Si/Ti interface are reliable. The numerical values of the layer and interface thicknesses and scattering length densities for the fitted model

[1] The Auger sputter profile is discussed at the end of this Section.

(Figure 3.2.4-c) are given in Table 3.2.4-b for comparison with calculated (Table 3.2.4-a) and literature values.

Thicknesses of air-formed oxide films on Ti have been measured by several authors [71, 107, 108]. Optical polarization measurements by Andreeva [71] indicated that upon exposure to air at room temperature the oxide layer on a freshly prepared Ti surface grows for a very long period, reaching ~50 Å after two months and ~250 Å after four years. At the time of the neutron reflectometry experiment, the thin film electrode had been exposed to ambient air for 5-6 weeks, so the measured oxide film thickness, 47 Å, agrees with Andreeva's results. An even more direct comparison can be made with the neutron reflectometry work of Wiesler and Majkrzak on Ti thin film electrodes [107, 108]. They also found 47 Å of oxide on their as-prepared electrodes.

Table 3.2.4-b Numerical Values of the Fitted Layer and Interface Thicknesses and Scattering Length Densities for the As-Prepared Thin Film Electrode Model Shown in Figure 3.2.4-c.

Layer	SLD ($Å^{-2}$)	Thickness (Å)	InterfaceWidth (Å)
Si	2.07×10^{-6}	∞	16.5
Ti	-1.83×10^{-6}	461	23.4
oxide	2.83×10^{-6}	47.0	13.5
air	0	∞	

On the other hand, several important differences between the SLD values gleaned from the present experiment, those determined by Wiesler and Majkrzak, and the calculated values (Table 3.2.4-a) are apparent. The SLD of the Ti film was ~6% higher[1] than that calculated for bulk Ti, whereas Wiesler and Majkrzak obtained a value ~15% lower than that of bulk Ti. The SLD of the air-formed oxide layer was ~8% higher than that expected for rutile, the highest density phase of TiO_2, while Wiesler and Majkrzak's value was close to that of rutile.

Wiesler and Majkrzak attributed their low Ti film SLD to the presence of interstitial hydrogen incorporated into the metal film during sputtering. In the present case, the most likely cause for the high Ti film SLD is the presence of metallic impurities or O. Since the sputtering target used to prepare the thin film electrodes was commercial-grade Ti, the presence of sufficient metallic impurities to generate the observed result is plausible. For instance ~1 at.% Fe impurity in the Ti would give the observed SLD shift. The incorporation of oxygen into the metal layer during sputtering is also a strong possibility, since it is well known that Ti has a high affinity for oxygen. In fact, this reactivity is the basis for UHV pumping by oxygen gettering using a titanium sublimation pump. Indeed it is also possible that oxygen was absorbed into the Ti film during surface oxidation upon exposure to air after sputtering. To obtain the observed value of the metal layer SLD, 3.5 at.% oxygen would be required.

After reflectometry measurements were completed on the thin film electrode in its as-prepared condition, it was mounted on the purpose-built electrochemical cell for *in situ*

[1] Note that for Ti, with its negative SLD, "higher" means lower in magnitude.

electrochemistry/neutron reflectometry. Figure 3.2.4-e shows the layer profiles obtained by least-squares fitting of the data measured with the electrode at E_{oc} in the electrolyte solution and after achieving a steady-state condition at an applied potential of +2 V. The profile taken with the electrode at E_{oc} is similar to that for the as-received electrode, seen in Figure 3.2.4-c, indicating that the sample did not change when simply exposed, at E_{oc}, to unbuffered, deaerated 0.27 mol·dm^{-3} NaCl at room temperature, over the two-day exposure period.

The Figure shows the following effects of anodization to +2 V:

1) The oxide layer thickened from 47 Å to 113 Å.

2) The metallic Ti layer was thinned by 38.0 Å.

3) The original, uniform-looking oxide layer was converted into an anodic film consisting of two distinct regions: an inner high-SLD region and an outer low-SLD region.

4) There was a small increase in the SLD of the metallic Ti (*i.e.*, the value became less negative).

The Si/Ti interface was little affected by anodization. The corresponding anodization ratio in this experiment was

$$\frac{\Delta d}{E - E_{oc}} = \frac{112\,\text{Å} - 47.0\,\text{Å}}{2.00\,\text{V} - (-0.56\,\text{V})} = 25.4\,\text{Å}\cdot\text{V}^{-1} \qquad \textbf{(3.2.4-a)}$$

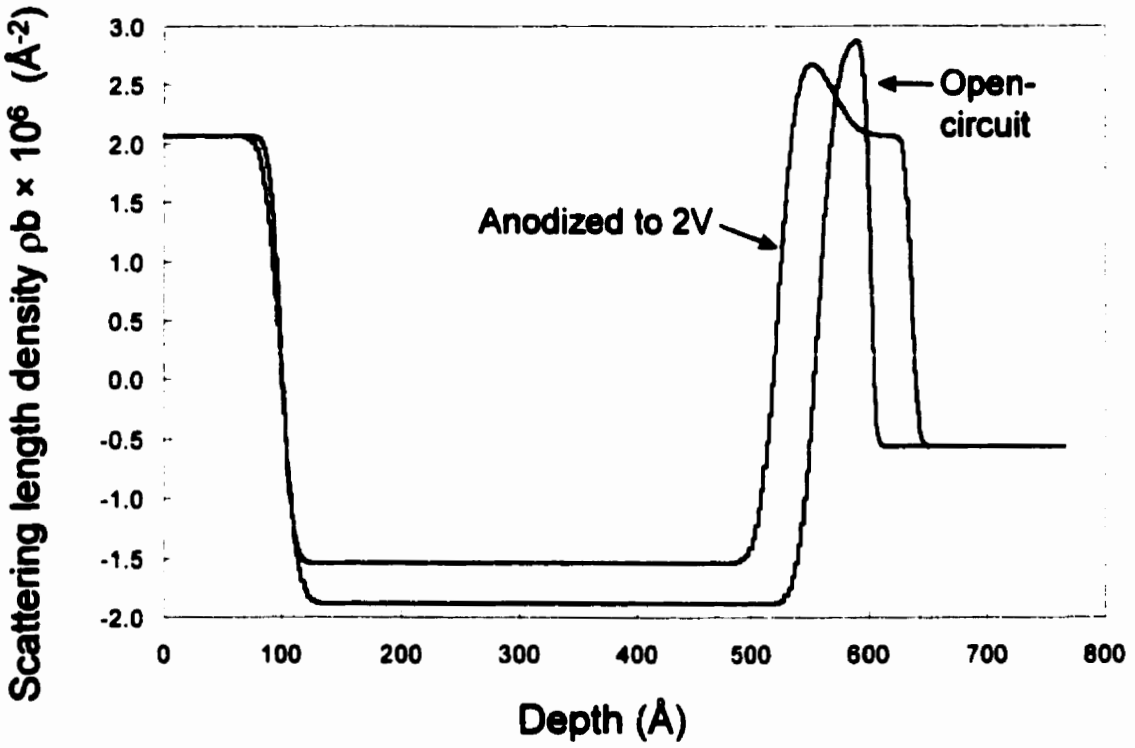

Figure 3.2.4-e SLD profiles of the Ti thin film electrode in solution at E_{oc} (= -0.56 V) before anodization, and at +2 V, after a steady state was reached.

where Δd is the change in film thickness upon anodization. This value agrees very well with the 25 ± 5 Å·V^{-1} frequently quoted for Ti in the literature [84, 85, 87, 104, 105, 114, 118, 127, 131, 135].

By contrast, Wiesler and Majkrzak [107] determined an anodization ratio of only 14 Å·V^{-1} for a Ti film in H_2SO_4 solution, but there is a good argument that can be made for the difference. The oxide film thickness at any potential will be determined by the point at which the electric field within the oxide film can no longer drive solid-state ion transport[1] or, if the oxide is dissolving simultaneous with the growth, the point at which the oxide's growth rate is equal to its dissolution rate (see Sections 1.3.4 and 1.3.5). In near-neutral pH solution such as was used in the present study, the solubility of Ti ions is low, so the former condition would likely apply, but in dilute acidic solution such as that used by Wiesler and Majkrzak, oxide film dissolution takes place at ~0.7 Å·h^{-1}, and the latter condition probably takes precedence. Blackwood *et al.* [116] found even higher oxide dissolution rates (5.8-6.8 Å·h^{-1}) in 3 mol·dm^{-3} H_2SO_4.

The thinning of the metal film and thickening of the oxide layer resulted in the inward movement of the metal/oxide interface by a distance $f_i = 38.0$ Å with respect to the Si/Ti interface, and the outward extension of the oxide/electrolyte interface by a distance $f_o = 27.3$ Å. For thin films with a constant surface area, f_i and f_o are related to the Pilling-Bedworth ratio, $\Re_{PB}$, the factor by which the volume of a metal swells when it is oxidized (see Section 1.3.4). In this case:

[1] According to FAIT theory, this never happens, growth just becomes slower.

$$\Re_{PB} = 1 + \frac{f_o}{f_i} = 1.72 \pm 0.04 \qquad \textbf{(3.2.4-b)}$$

$\Re_{PB}$ for the various polymorphs of TiO_2 can be calculated from crystallographic lattice parameters, or from their densities and that of bulk Ti [8], yielding values of 1.77, 1.82, and 1.96, respectively, for the rutile, brookite, and anatase structures. The observed $\Re_{PB}$ clearly indicates that the anodic oxide was packed as densely as rutile, even slightly more so. The only other explanation possible for such a low $\Re_{PB}$ value is that some material was lost to dissolution, which is highly unlikely, given the near-neutral pH of the electrolyte solution used.

The fact that the observed value of $\Re_{PB}$ was close to the bottom end of the expected range suggests that the oxide was densely packed and free from pores. This must have been the case even for the low-SLD region of the oxide, since loose packing or porosity anywhere within the film would have led to a larger $\Re_{PB}$ value. The unexpectedly low value of $\Re_{PB}$ could potentially have been the result of the presence of some suboxides or packing defects that increased the density the high-SLD oxide. Another possibility is that such a thin film does not behave entirely like the bulk material to which it is being compared here. Likewise, it is not unreasonable that some of the uncertainties regarding the structure and composition of the passive film on Ti (see Section 1.3) arise from differences in properties between the thin films analyzed and the corresponding bulk materials.

That an anodization ratio in agreement with the literature and a sensible value of $\Re_{PB}$ were obtained suggest that this thin film sample behaved similar to electrodes made of

bulk Ti metal. This conclusion is supported by the observation (point 1 above) that, for the potential applied, the metal film was sufficiently thick that the surface anodization did not affect the Si/Ti interface.

From the detailed shape of the SLD profile, further aspects of the structure and composition of the anodic oxide can be inferred. The inner high-SLD region of the oxide displayed a SLD value similar to, but slightly lower than, that of the original air-formed oxide. The formation of a small amount of suboxide after anodization is one of the possibilities that could account for this difference. Such an explanation would be consistent with the observation of the low $\Re_{PB}$ value, as discussed above.

The SLD value of the outer low-SLD region was well below that of anatase, the lowest-density form of TiO_2 (see Table 3.2.4-a). As argued above on the basis of $\Re_{PB}$ values, loosely packed oxide cannot be invoked as the reason for this discrepancy. Neither can the presence of oxygen-deficient suboxides explain this low SLD value, since oxygen deficiency, if any, should occur deep within the oxide layer, adjacent to the metal/oxide interface.

It is proposed here that the oxide layer SLD was low near the aqueous electrolyte because the oxide in this region incorporated a significant amount of hydrogen from solution during its growth, probably in the form of Ti-OH species or bound water. Hydrogen, with its strong negative scattering length (see Table 3.2.4-a), can lower the SLD of a material without causing much swelling. Incorporation of hydrogen into anodic oxides on Ti has been reported by Ohtsuka *et al.* [85] and the formation of hydroxyl bridges suggested. Perhaps this bridge bonding helps eliminate any need for a volume increase.

Knowing $\Re_{PB}$ for formation of this oxide, one can calculate the number density of Ti atoms. Assuming the Ti is present as Ti(IV) (a very reasonable assumption, especially given the XPS results in Section 3.2.3), the composition of the oxide can then be determined from the number density of Ti atoms and the SLD value. The SLD value of the plateau part of the low-SLD region corresponds roughly to composition $TiO_2 \cdot H_2O$. It could as well be the compound $TiO(OH)_2$, which would have essentially the same SLD[1], provided it could be packed with the Ti atoms at the appropriate number density. In other words, the stoichiometry corresponds to one water molecule per TiO_2 unit.

The observation of two distinct strata within the oxide film is consistent with the angle-resolved XPS results (Section 3.2.3), which indicated that OH species, in the form of H_2O or Ti-OH, were present at the surface of solution-grown oxides in greater concentrations than were found deeper into the oxide layer. The hydration of solution-grown oxide films on Ti and other metals has been observed by others [84, 85, 93-96, 105, 135, 201].

Finally, it is reasonable to postulate that the small overall increase in the SLD of the metallic Ti observed after anodization was due to diffusion of a small amount of oxygen into the metal during anodization. It is interesting to note, however, that the width of the metal/oxide interface region remained constant (within the limits of the experimental error) during anodization. No detectable roughening occurred.

The presence and location of the high-SLD region of the oxide film leads to contemplation of the mechanism of oxide film growth. Figure 3.2.4-e shows that the

[1] According to Dr. Zin Tun of the Neutron Program for Materials Research, Chalk River, ON (personal communication, 1998), this is the first account of neutron reflectometry being used to determine the composition of an unknown phase.

peak SLD value of the high SLD region is very close to that of the original air-grown oxide. Moreover, the least-squares fitted width of this region given by MLAYER [187] is 45 Å -essentially the same as that of the original oxide. One could postulate that these similarities suggest that the high-SLD region is indeed the original oxide that simply "sank" closer to the Si/Ti interface because some amount of metal was removed and transported across the original oxide to form new oxide at the oxide/electrolyte interface. This interpretation, however, is not consistent with the transport numbers reported by Khalil and Leach [135], since it would imply very little oxygen mobility during the anodization of Ti (*i.e.*, $t_m = 1$ and $t_O = 0$).

Using α-particle emitters implanted into an oxide film on Ti prior to anodization, Khalil and Leach [135] determined from the energy-loss spectrum that the emitter layer was buried deeper below the oxide surface, after anodization, by a depth equal to 35% of the increase in oxide layer thickness. This corresponds to $t_m = 0.35$ and $t_O = 0.65$ for anodic oxide growth on Ti metal initially covered with an air-formed oxide film. The anodization conditions used by these authors were very different from those employed here, however, both experiments were carried out at room temperature in aqueous solution, and the current densities were kept low to give a nearly 100% oxide growth efficiency. Assuming similar transport numbers for the current anodization, the present results can be interpreted differently for the two leading proposed oxide film growth mechanisms (FAIT and PDM) as explained below (see also Section 1.3.4).

According to FAIT theory, $t_m = 0.35$ implies 35% of the newly formed oxide grows on the electrolyte side of the original oxide layer, while 65% of growth occurs on the metal

side. Ignoring the observation that a small amount of oxygen migrated into the metal layer during anodization, in this experiment 23 Å of new oxide should have grown at the oxide/electrolyte interface, while 42 Å should have grown at the metal/oxide interface, according to FAIT theory and the transport numbers measured by Khalil and Leach [135]. The region between these boundaries would correspond to the original oxide.

The SLD profile shows that the portion of the oxide film corresponding to what would have been the outer fraction of new oxide (if FAIT was the active mechanism) was uniformly hydrated (a plateau in SLD), while the portion of the film that would be the inner fraction of new oxide contained far less hydrogen. The part of the oxide corresponding to what would have been the original air-formed oxide contained much more hydrogen than did the original film. These observations could be rationalized under the FAIT mechanism by assuming that hydrogen from the water was incorporated along with oxygen during anodization, and invoking restrictions on the mobile oxygen species; specifically that the species that crossed the original oxide layer most readily were hydrogen-free. The hydrogenation of the original oxide might then have occurred by stripping of hydrogen from OH species as they travelled toward the metal/oxide interface to form new oxide, or by exchange of OH with oxygen in the original oxide lattice, the latter becoming the mobile species that went on to create new oxide at the metal/oxide interface. The mobile oxygen species arriving at the metal/oxide interface would then have been hydrogen-free. This conversion of high-SLD to low-SLD oxide is a critical step in this mechanism if the amount of high-SLD oxide is to be conserved. Such details were not part of the FAIT model originally [120], but there does not appear to be any obvious reason why such a mechanism could not proceed in this case.

Within the framework of the PDM, the location of original oxide after anodization is an inappropriate question, since the original oxide layer would no longer exist. The constituents of the oxide would move in different directions during film thickening. The oxygen anions that comprised the original oxide would end up located adjacent to the metal, while the metal cations with which they were originally associated would be found adjacent to the electrolyte. In this picture, the high-SLD region of the anodic oxide would have been formed from the "hydrogen-free" oxygen anions of the original air-grown oxide, combined with freshly oxidized metal cations. In contrast, the low-SLD oxide would have grown from the metal ions of the original oxide, combined with newly supplied oxygen ions from the electrolyte. This supply from aqueous solution would unavoidably contain OH ions, and some of these would be incorporated into the oxide, leading to the low-SLD of this region.

Thus, it is possible to interpret the current results in terms of either model. The transport numbers measured by Khalil and Leach [135] are equally valid, and their definition in terms of the relative ionic mobilities would be the same in either case; however, the outward significance of the transport numbers [122] is somewhat more subtle in the PDM case because the distinction between newly formed and pre-existing oxide would be lost. Both of these hypothetical mechanisms predict a bilayer structure for the anodic oxide, with a hydrated outer layer and a "dry" inner layer; the thickness of the latter would be conserved in either case. The distinguishing characteristic between the two mechanisms is the position at which new atoms of each component would be incorporated into the oxide. The FAIT mechanism would have 65% of the newly oxidized Ti , along with 65% of the newly incorporated oxygen anions, adjacent to the metal surface, and 35% of each

of the freshly introduced oxygen and Ti ions adjacent to the oxide/solution interface. The ions residing in the oxide for the longest time, including those of the original oxide layer, would be located in the middle of the oxide film. By contrast, in an oxide film growing via the PDM, the duration of residence within the oxide for each ion would be ordered by depth, the most recently incorporated metal ions being located closest to the metal surface and the earliest incorporated occupying the positions closest to the oxide/solution interface. The opposite ordering would apply to the oxygen anions, with the duration of occupancy increasing from the oxide/solution interface to the metal surface.

Unfortunately, one crucial piece of information that the neutron reflectometry profiles from this experiment cannot provide directly is the location of the original native oxide within the thickened oxide layer. Further experiments are needed in order to fully distinguish between the two models. The details of such experiments will be discussed in Section 4.

After anodization at +2 V, the thin film electrolyte was polarized to a series of lower potentials, with neutron reflectometry scans performed *in situ* at each fixed potential in the series. The current density measured during the neutron scans is plotted as a function of the applied potential in Figure 3.2.4-f. For applied potentials down to and including -1.0 V, the cathodic current on the thin film electrode approached a steady-state value after an initial increase in magnitude. This behaviour began to change significantly at -1.2 V; although the current density decreased in magnitude over the first few hours it increased again later. Similar behaviour, although on a shorter time-scale, was observed

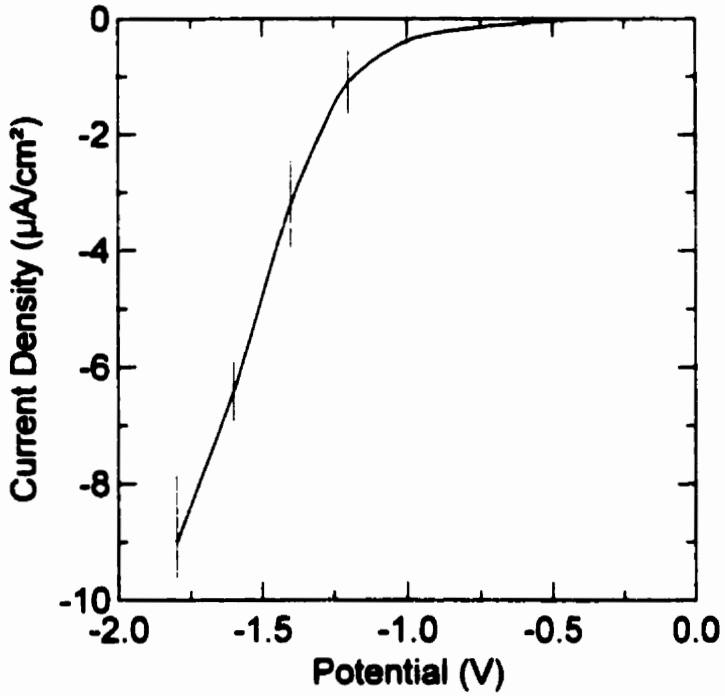

Figure 3.2.4-f Polarization data recorded on a Ti thin film electrode during in situ *neutron reflectometry scans. The vertical lines indicate the ranges of fluctuating currents at each applied potential.*

previously in cathodic polarizations of Ti-2 disk electrodes in HCl solutions (see Section 3.1.2.2), and by Arsov [152] at applied potentials < -0.75 V.

The observed increase in the magnitude of the cathodic current density was accompanied by "noisy" excursions (the current ranges of which are indicated by the vertical bars in Figure 3.2.4-f). These fluctuations, with periods on the order of ~1 h, did not subside during the 24 h period required for the reflectometry scans at each potential; however, the reflectivity did come to a steady-state condition, typically after 12 h, suggesting that the continuing changes responsible for the current excursions were too small to be seen with the maximum reflectometry scan range used.

During the measurements at -1.6 V, the presence of a very fine white suspension was observed in the electrolyte solution. The amount of suspended material increased gradually until the end of the experiment. When the thin film electrode was removed from the cell, small circular areas (diameter 0.04 - 0.5 mm) of Ti film were observed to have delaminated from the Si substrate. Under an optical microscope, these circular areas appeared as if created by gas bubbles formed between the film and the substrate, the metal immediately above the blisters being removed when they burst (see Figure 3.2.4-g). Indeed, some of these areas were ringed by tattered remnants of the Ti film. The white material suspended in the solution was not analyzed for chemical composition; however, it seems likely that this substance was a corrosion product of the fresh Si surface that was exposed at ruptured blister sites.

The model layer profiles given in Figures 3.2.4-h and 3.2.4-i show how the thin film electrode evolved when the cell potential was set to each potential in a series of lower

Figure 3.2.4-g Optical micrograph of a portion of the thin film electrode surface after completion of all in situ *electrochemistry/neutron reflectometry experiments.*

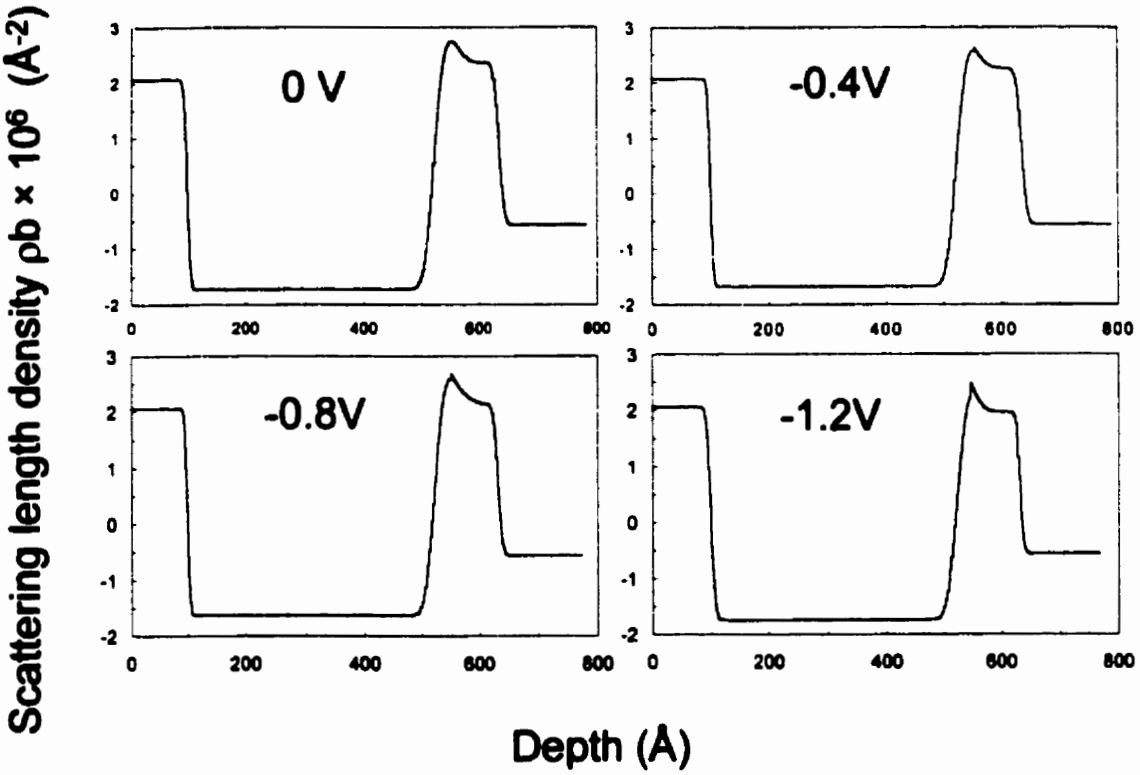

Figure 3.2.4-h SLD profiles recorded at various potentials applied after anodization at +2 V. The overall thickness of the oxide layer did not change significantly, but the peak height and the extent of the high-SLD region decreased progressively as lower potentials were applied.

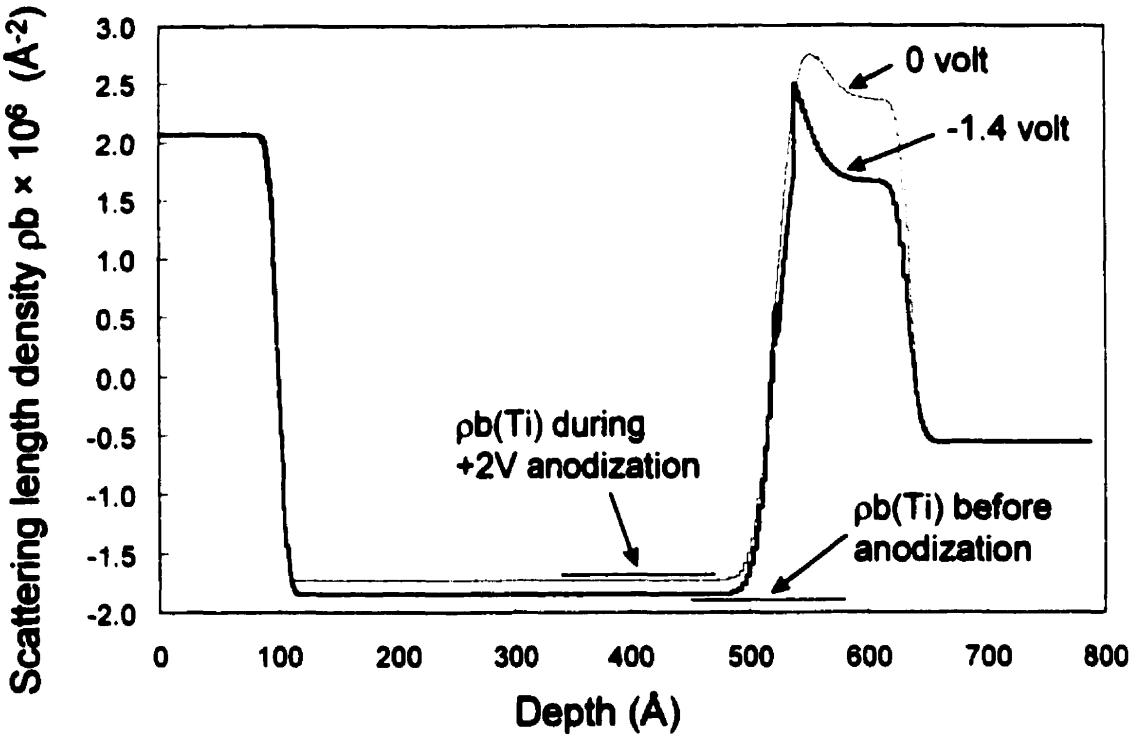

Figure 3.2.4-i SLD profiles least-squares fitted to the specular reflectivity data measured at applied potentials of 0 V and -1.4 V on a Ti thin film electrode previously anodized at +2 V, highlighting the extent of change in the oxide layer SLD with decreasing applied potential and the constancy of the oxide thickness. The short horizontal lines in the 500 Å and 400 Å regions mark the observed SLD values of the metallic layer at E_{oc} (before anodization) and at a potential of +2 V, after a steady state was reached, respectively.

potentials after anodization. The sequence of layer profiles in Figure 3.2.4-h spans the potential range from 0 to -1.2 V. Figure 3.2.4-i shows the profile fitted to the data measured with the electrode polarized to -1.4 V, superimposed on a re-plot of the first panel of Figure 3.2.4-h (E = 0 V). For the sake of comparison, Figure 3.2.4-i also includes horizontal lines showing the SLD values of the metal region before anodization and after a steady state was reached with the electrode at the anodization potential of +2 V.

The apparent effects of applying increasingly lower potentials, seen in the Figures, were:

1) The overall shape of the oxide SLD profile changed dramatically with the application of increasingly lower potentials. The SLD decreased generally over the entire oxide layer.

2) The low-SLD region became thicker at the expense of the high-SLD oxide. At -1.4 V the remaining high-SLD region was very thin; the FWHM of the SLD spike in Figure 3.2.4-i is 15 Å, corresponding to only about six atomic layers.

3) The *total* oxide thickness remained unchanged at all potentials applied after the anodization treatment.

4) The SLD of the metal region decreased (*i.e.*, became more negative), but the change was small and clearly noticeable only at -1.4 V. There was no potential at which the metal SLD dropped abruptly.

5) When the applied potential reached -1.6 V the reflectometry scans were seriously degraded, probably because the Ti film was ruptured or delaminated.

There are only a few mechanisms that can lead to a relatively large drop in the SLD of an oxide film without a change in thickness. One possibility is the formation of voids, pits, or pores that either remain vacant or fill with H_2O or H_2 molecules; however, given that TiO_2 is highly insoluble in the electrolyte used, this is not likely to have been the case. Pitting of the oxide layer during cathodic polarization was seen by Wiesler and Majkrzak [107, 108], but the detailed features of their results were different than those reported here. These authors used dilute sulphuric acid electrolyte and observed dissolution of oxide at a rate of ~0.7 $Å \cdot h^{-1}$, with an associated increase in surface roughness that broadened the oxide/electrolyte interface. In the present experiments the interface remained well-defined; only the magnitude of the oxide SLD was decreased. Again, this stability of the oxide film can be attributed to the use of a neutral, rather than an acidic, electrolyte.

Another possible explanation for the drop in oxide layer SLD, which seems more likely, is the incorporation of hydrogen into the oxide layer, either as interstitial atoms or as Ti-OH species, perhaps in the form of the alleged compound TiO(OH) [150]. (It should be noted here that hydrogen cannot be observed directly by AES, so the Auger depth profile of Figure 3.2.4-d is of no assistance in detecting hydrogen ingress.) Hydrogen absorption may also explain the decrease in the metal layer SLD and the eventual destruction of the thin film electrode by gas bubble formation.

According to Ohtsuka *et al.* [150], TiO_2 can be reduced to TiO(OH) by the application of cathodic charge. In acidic solution this dissolves even faster than TiO_2, but in neutral solution reduction does not lead to dissolution [150]. The added hydrogen yields electron donor states, increasing the conductivity of the oxide. As this conversion takes place, the oxide seems to become permeable to hydrogen atoms, which can traverse the oxide and become absorbed into the underlying metal. The present results are consistent with this idea, because the reduction to TiO(OH) would yield a lower SLD for the oxide. There was also no change in oxide layer thickness; if no dissolution took place then the reductive conversion of the oxide appears not to involve a volume change. Finally, there was an increase in current density with decreasing potential, suggesting the conductivity of the film increased with decreasing potential (as more donor states were introduced into the oxide by reduction).

The layer profile corresponding to an applied potential of -1.4 V, shown in Figure 3.2.4-i, was the last model for which a satisfactory fit to the data could be obtained. The reflectivity data measured with the electrode held at -1.6 V and -1.8 V contained intensity minima that were too shallow to be successfully reproduced by the trial layer profiles for which fitting was attempted. The cause of this failure is suggested to be the roughening of the sample surface by gas-induced blistering of the metal film, observed later by optical microscopy, (Figure 3.2.4-g). It seems reasonable to think that the destruction of the thin metal film coincided with the entry of large amounts of hydrogen into the metal and was facilitated by the deleterious effects of hydrogen on the mechanical properties of Ti. Unfortunately, this hypothetical film destruction mechanism could not be verified, due to the deterioration of the quality of the reflectometry data at this point; however it

should be emphasized that an abrupt increase of hydrogen absorption into the metal was not observed up to this juncture.

The atomic concentration profile as a function of sputter time, determined by AES at a point within ~1 cm of the edge of the sample after completion of all reflectometry experiments, is shown in Figure 3.2.4-d. This profile is given as a function of sputter time, rather than sputter depth, due to difficulties in determining the sputter rate. Attempts were made to calculate an approximate depth profile based on literature data on sputtering yields, but the results were quite variable, depending on the sputtering data used. The major problem was that no data could be found that were acquired under equivalent conditions and on the same materials used here, so no accurate sputtering depth scale could be estimated.

In spite of the lack of a depth scale for this profile, a couple of important qualitative observations can be taken. In particular, the boundaries between oxide and metal, and between metal and substrate, appear very gradual[1] in this AES profile. Also, a small peak in oxygen concentration was observed at the metal/substrate interface. This may correspond to a thin passive Si oxide present on the slab since before the Ti film was deposited, as discussed above.

[1] Although "gradual" as a function of distance is not discernible directly in this Figure, one can get a qualitative estimate of the relative interface thicknesses as a fraction of the layer thicknesses by comparing the sputter times for the interfacial regions with those for the "bulk" of the layers.

3.3 Crevice corrosion initiation

A number of crevice corrosion-type experiments were performed on Ti-2 in which the temperature was rapidly raised to 100°C, but then the tests were halted before the onset[1] of crevice corrosion. Subsequent inspection of the electrode surfaces where they were in contact with the crevice former showed general acid etching of the metal surface within the occluded area (Figure 3.3-a). Similar acid etching was observed in both 0.27 mol·dm^{-3} NaCl and "chloride-free" 0.14 mol·dm^{-3} Na_2SO_4 solutions. Likewise, etching has been observed (in other experiments) on the boldly exposed surfaces of severely crevice-corroded coupons, in regions adjacent to the crevice mouth where acidic solution from the crevice interior flowed out over the surrounding surfaces. The observed etching pattern is a clear indication of acid attack on the passive oxide film.

In other similar short-term experiments on Ti-2 in 0.27 mol·dm^{-3} NaCl that were halted shortly *after* small increases in the coupled current[2] and the appearance of electrochemical noise transients (Figure 3.3-b), visual inspection of the occluded metal surfaces yielded clear evidence of true localized attack of the electrodes (*i.e.*, more than just mild etching). Based on these results, one can conclude that a general oxide dissolution process, caused by the development of acidity within the occluded region, precedes the initiation of crevice corrosion. This is consistent with the results of

[1] The onset of crevice corrosion was indicated by an increase in current flow between the creviced electrode and the counter electrode and the commencement of electrochemical "noise" transients in the measured current and potential signals.

[2] The measured currents in these crevice corrosion experiments were those flowing between the artificially creviced electrode and the electrically coupled counter electrode.

Figure 3.3-a Photomicrograph of a Ti-2 crevice coupon previously exposed to 0.27 mol·dm^{-3} NaCl at 100°C, showing the acid etching that occurred in the occluded region (stained area around centre of coupon) before crevice corrosion initiation. The acid etching was widespread and general, but not homogeneous across the entire occluded region; the central area of the occluded region, for example, was not stained.

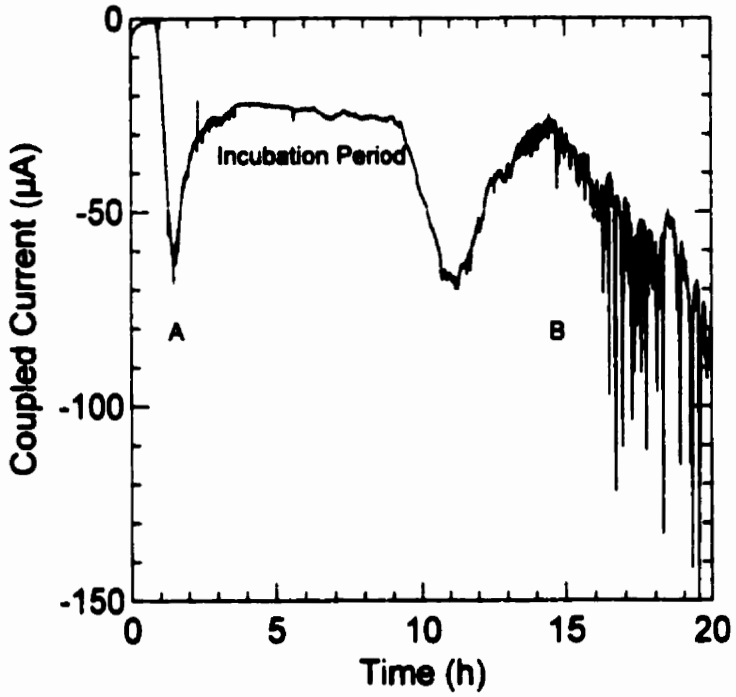

Figure 3.3-b Coupled crevice corrosion current versus time for Ti-2 in 0.27 mol·dm^{-3} NaCl, showing a short-lived current transient during the heating period (A), the low-current "incubation period", and the commencement of crevice corrosion, as indicated by increasing coupled currents and current "noise" transients (B).

Blackwood *et al.* [104], which showed that the dissolution of oxide films on Ti in acidic solutions occurs generally, not locally.

Therefore, the "waiting period" between the temperature increase and the onset of current flow represents a largely deterministic "incubation" period, rather than an "induction" period as often seen in apparently stochastic processes such as pitting or the nucleation of growth centres in electrocrystallization. During this incubation period, acidity builds up inside the crevice before crevice corrosion initiation takes place. Crevice corrosion initiation typically took between 5 and 10 h on coupons heated rapidly to 100°C in oxygenated 0.27 $mol \cdot dm^{-3}$ NaCl.

Although crevice acidification resulting in surface etching was observed on Ti-2 in both 0.27 $mol \cdot dm^{-3}$ NaCl and "chloride-free" 0.14 $mol \cdot dm^{-3}$ Na_2SO_4 solutions at 100°C, the subsequent initiation of crevice corrosion did not occur on specimens maintained at 100°C in sulphate solutions, even after an exposure period of several weeks. These results are in stark contrast with those obtained in chloride-containing solutions, in which crevice corrosion initiated within a matter of hours (Figure 3.3-b). The nature of the electrolyte anion clearly influences the crevice corrosion initiation process. These results indicate that the pH generated inside the crevice was acidic even in sulphate solution. It is possible that the difference between crevice corrosion initiation in chloride-containing solution and in sulphate solution at 100°C is that the pH in the sulphate solution may not have been sufficiently low to initiate crevice corrosion, perhaps due to the ability of sulphate to complex Ti cations and thereby limit the amount of hydrolysis. Alternatively, or additionally, the difference in the ability of the two solutions to initiate crevice attack

may arise from the stronger ability of chloride ions to attack and disrupt whatever remains of the oxide film on the Ti surface under these conditions, especially once the oxide film is thinned (perhaps to monolayer thickness [10]) by the acidity. Another possibility is Kelly's autopassivation effect [10, 11], by which Ti^{IV} species act as oxidants within the crevice and reinforce passivity. This effect was noted to require 10.5 times more Ti^{IV} in chloride solutions than in sulphate. The ability of sulphate to lower the electrical resistivity of the oxide film (see Section 3.2.2) does not seem to result in an enhancement of crevice corrosion in sulphate solutions under these conditions.

In another set of experiments, the potentials of planar and artificially creviced electrodes in 0.27 $mol \cdot dm^{-3}$ NaCl were compared as the temperature was very gradually increased (0-10 Celsius degrees per day), starting from 55°C. While slightly different in value, the two potentials both changed in a parallel fashion as the temperature increased, until a certain temperature was achieved: 72°C for Ti-2 (Figure 3.3-c) and 67°C for Ti-12 (Figure 3.3-d). At this point, the two potentials ceased to move in the same direction and a small but increasing current attributable to the onset of crevice corrosion, as well as current "noise" transients, were recorded.

These crevice corrosion initiation temperatures are consistent with the accepted value of the critical crevice corrosion initiation temperature for Ti (~70°C) [40]. They are also near the temperature at which breakdown crystallization is believed to occur [84, 140], near the temperature at which the oxide film impedance decreases (see Section 3.2.2), and near [84] or slightly above (see Section 3.2.3) the temperature at which the incorporation of OH or water into the oxide film on Ti increases substantially.

a)

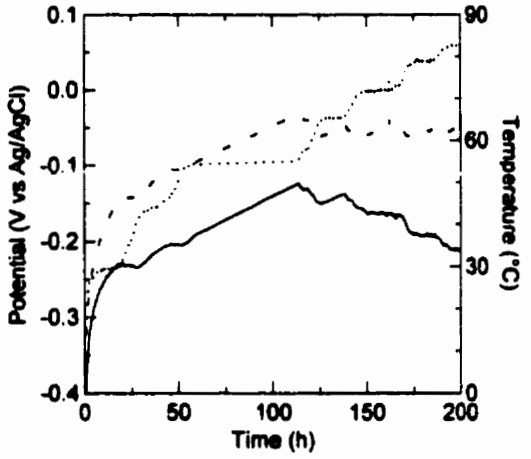

b)

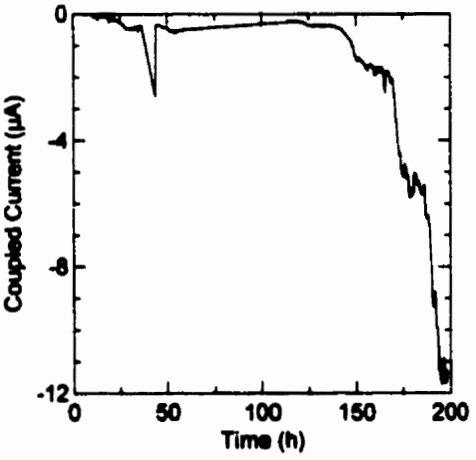

Figure 3.3-c Data collected during a crevice corrosion initiation experiment on Ti-2 in 0.27 mol·dm^{-3} NaCl in which the temperature was slowly increased to estimate a critical temperature for initiation: a) temperature (· · · · ·), planar electrode potential (- - - - -), and crevice electrode potential (————); b) coupled current. Note that the planar and crevice electrode potentials ceased moving in the same direction at the same time that the coupled current began to increase in magnitude (~150 h). The temperature at this point was ~72°C.

a)

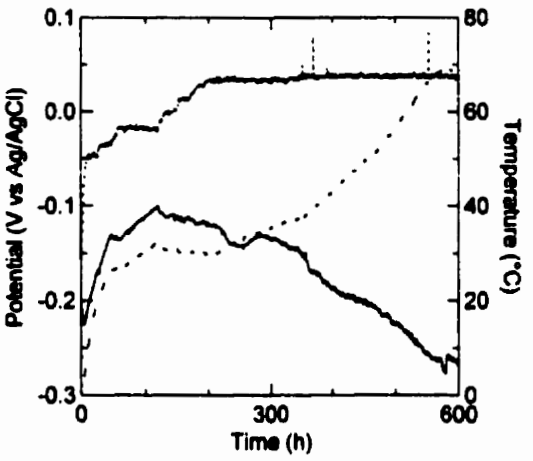

b)

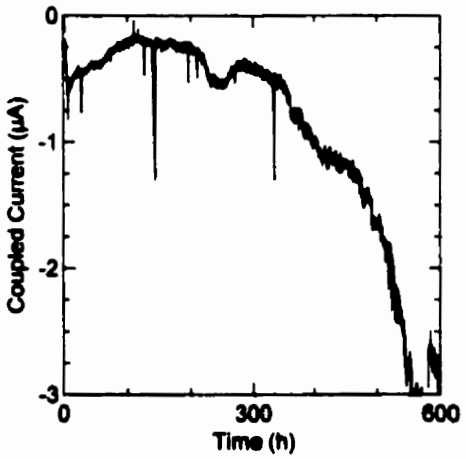

Figure 3.3-d Data collected during a crevice corrosion initiation experiment on Ti-12 in 0.27 mol·dm^{-3} NaCl in which the temperature was slowly increased to estimate a critical temperature for initiation: a) temperature (· ·····), planar electrode potential(- - - - -), and crevice electrode potential (————); b) coupled current. Note that the planar and crevice electrode potentials ceased moving in the same direction at the same time that the coupled current began to increase in magnitude (~200 h). The temperature at this point was ~67°C.

The data reported in this Thesis can be used to develop an hypothesis to explain the underlying reasons why the empirically measured crevice corrosion initiation temperature of 70°C [40] is valid. It seems a good bet that the large changes in the passive film on Ti as the temperature increases beyond 70°C, namely breakdown crystallization and water/OH uptake, corrupt the oxide sufficiently to permit some oxidation of the underlying metal. On boldly exposed surfaces in "high" pH (≥ 3) solution this would probably only result in some film thickening and self-repair and, perhaps, a higher susceptibility to general corrosion if the pH were subsequently lowered. On occluded surfaces, this oxidation of a small amount of the underlying Ti and the subsequent hydrolysis of the metal cations in solution would produce acidity that could not be easily dispersed into the bulk of the solution because of the restricted mass transport. The accumulation of acidity would begin to cause the dissolution of the passive film, as seen in activation experiments (see Figure 3.1.1-a) and the crevice corrosion initiation experiments (Figure 3.3-a). The development of acidity within a crevice is insufficient to cause crevice corrosion initiation; it appears that for this process to evolve into active crevice corrosion at 100°C, an aggressive anion such as chloride is required to complete the breakdown of the remaining surface film (Figures 3.3-a and 3.3-b).

Although the artificial crevice design (see Figures 2.3.1-b, 2.3.1-d, and 2.4.3-a) actually contained more than ten reasonably tight occluded regions (the two PTFE-metal crevices, along with four metal-to-metal crevices between the coupons and the nuts, four between the nuts and bolts (in the threads), and possibly others between the bolts and coupons), crevice corrosion occurred reliably and exclusively within the PTFE-metal crevices. This observation is consistent with the results of Satoh *et al.* [48], who investigated the effects

of different crevice former materials on crevice corrosion initiation on Ti and found that initiation was much more probable in PTFE-Ti crevices than in metal-to-metal Ti crevices.

3.4 Hydrogen absorption

3.4.1 Normalization and data presentation

The absorbed hydrogen and charge data presented in this section have been area-normalized and are reported in units of $mg \cdot cm^{-2}$ and $C \cdot cm^{-2}$, respectively, to facilitate comparisons with values recorded on samples with different surface areas in other experiments and by different researchers. Some problems in comparing amounts of absorbed hydrogen may still exist, however. In addition to the exposed surface area, the overall electrode geometry may be important to the relationship between the amount of absorbed hydrogen and the total charge passed. Different surface area-to-volume ratios could result in different hydrogen concentration profiles within the metal, which might influence the absorption characteristics.

For the parallelepiped-shaped hydrogen absorption coupons used in these experiments there are two ways in which the geometry could influence the hydrogen concentration profiles: in the vicinity of the corners, the hydrogen atoms absorbed on different faces of the metal will encounter each other; and, if enough hydrogen is absorbed relative to the coupon thickness, hydrogen atoms absorbed at opposite faces of the coupon will meet in the centre of the coupon. Either of these occurrences would perturb the hydrogen concentration profile within the metal, although the effects of such a perturbation on the hydrogen absorption behaviour are uncertain.

One could expect the overall influence of the "corner regions" on the hydrogen absorption behaviour to be small since they would comprise a relatively small fraction of the total coupon area, but the "corner effects" would increase in importance with time

since the area of the sample that would have to be considered part of the corner regions would increase as more hydrogen was absorbed. The perturbation of the hydrogen concentration profiles due to hydrogen penetrating the coupon from opposite faces in a planar region of the coupon away from the corners would be insignificant at first, but would increase in importance once enough hydrogen was absorbed. How much hydrogen is enough to cause an effect on the absorption rate would depend on the coupon thickness and the rate of hydrogen redistribution within the metal (J_H) (see Figure 1.4.1-a). Given the dimensions of the hydrogen absorption coupons used, for the purposes of these experiments these geometric effects have been assumed to be negligible.

To facilitate comparisons between amounts of hydrogen absorbed by coupons charged at different cathodic current densities or for differing periods of time, hydrogen absorption data have also been reported in the form of average hydrogen absorption efficiencies. The hydrogen absorption efficiency can be defined as the fraction of all the hydrogen produced at the metal surface that was absorbed into the metal, expressed as a percentage. The hydrogen absorption efficiencies reported here are *average* efficiencies because they are based on the ratio of the integral amount of hydrogen absorbed over the course of the experiment to the total amount of hydrogen produced at the electrode surface as determined from the amount of charge passed.

This method of representation emphasizes the differences in the low-charge data that are minimized by the scale of plots of the amount of absorbed hydrogen *versus* the total charge passed. Also, because the efficiency values calculated in this way are average values over the entire duration of the experiment, they become increasingly less sensitive

to change as the charge increases. The difficulty with expressing changes in the hydrogen absorption behaviour with increasing amounts of charge passed originates from the method of hydrogen analysis. Because this destructive analysis can only be performed at the end of an experiment, it only generates one value of the hydrogen concentration in the sample for each experiment. The absorbed hydrogen concentration can be converted into a total amount of hydrogen absorbed and this value can be thought of as the integral of the hydrogen absorption rate over the course of the experiment; the hydrogen absorption efficiency at any point during the experiment remains unknown.

A more sensitive estimate of the true absorption efficiency at any charge value is the calculated instantaneous hydrogen absorption efficiency. This efficiency is calculated (rather than measured) by taking the slope of the tangent to the plot of absorbed hydrogen per unit surface area versus charge passed per unit surface area. Since the average hydrogen absorption efficiencies for Ti do not appear to increase with time (see the following Sections), the calculated instantaneous absorption efficiency at any value of the charge passed must be less than or equal to the average absorption efficiency up to that point. Therefore the average absorption efficiency, the only quantity available from some types of measurements, yields an over-estimate of the material's ability to absorb hydrogen at that stage of its history. Because they come from the same set of measurements that yield the average absorption efficiency values, the calculated instantaneous hydrogen absorption efficiencies have the same lack of sensitivity at high total charge values.

The hydrogen charging experiments reported here were conducted in acidic, deaerated solutions to simulate the conditions for hydrogen absorption occurring on nuclear waste containers during periods of active crevice corrosion. These solutions only roughly approximate the crevice anolyte solutions by their acidity and low oxygen concentrations; the exact pH, oxygen concentration, chloride ion concentration and other conditions inside a corroding crevice have not yet been determined. The rate of hydrogen absorption by Ti during crevice corrosion is much higher than that during uniform corrosion in neutral solution, where absorption must occur through a passive oxide film; therefore hydrogen absorption accompanying crevice corrosion threatens to limit the lifetimes of nuclear waste containers more than hydrogen absorption occurring during a period of uniform corrosion.

All hydrogen charging experiments reported herein were conducted without the application of stresses, on planar specimens expected to have low, if any levels of residual stresses.

3.4.2 Galvanostatic hydrogen charging on Ti-2 at 25°C

A plot of the hydrogen absorption behaviour of Ti-2 is shown in Figure 3.4.2-a for galvanostatic charging experiments conducted in 0.1 mol·dm^{-3} HCl + 0.27 mol·dm^{-3} NaCl with an applied cathodic current density of 190 μA·cm^{-2} at 25°C. The Figure shows that the amount of hydrogen absorbed into the metal is a function of the total amount of hydrogen produced at the sample surface (as represented by the charge passed), but there are insufficient data, especially in the 100 to 200 C·cm^{-2} charge range, to determine whether the function increases linearly with the charge passed or whether its slope

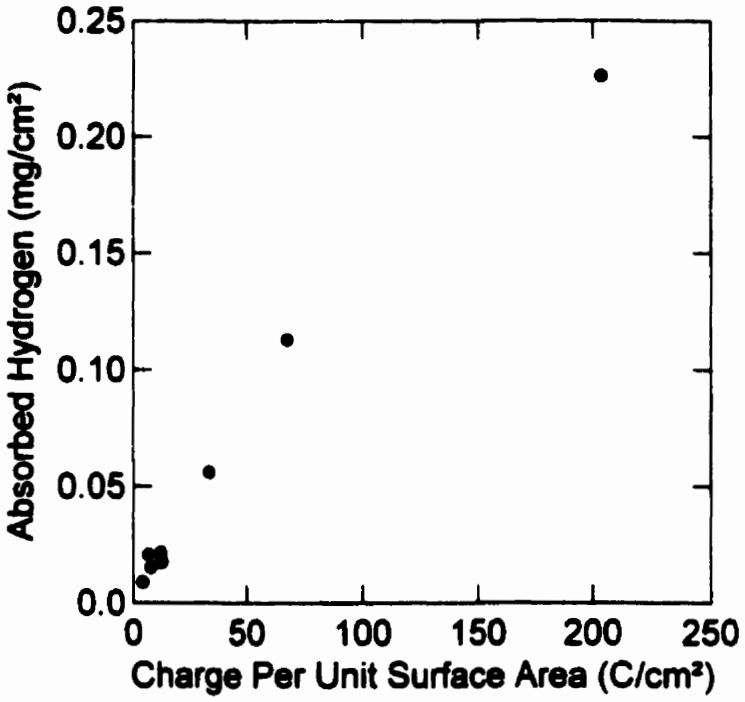

Figure 3.4.2-a Amount of hydrogen absorbed per unit surface area as a function of charge passed per unit surface area for Ti-2 in 0.1 mol·dm^{-3} HCl + 0.27 mol·dm^{-3} NaCl at 25°C with an applied cathodic current density of 190 μA·cm^{-2}.

decreases as more charge is passed. A linear dependence on the charge passed would mean a constant absorption efficiency, and would lead to predictions of very large amounts of hydrogen absorption over long time periods; an asymptotic relationship would mean that the absorbed hydrogen concentration would eventually reach a maximum value. Intermediate to these two extremes are the cases in which the hydrogen absorption efficiency would decrease with increasing amounts of charge passed, but the total amount of absorbed hydrogen would have no upper limit (until the metal was all converted to hydride).

The data from Figure 3.4.2-a are re-plotted in the form of average hydrogen absorption efficiencies in Figure 3.4.2-b. Figure 3.4.2-b seems to indicate that the material's ability to absorb hydrogen initially decreases with increasing amounts of charge passed, but it does not clarify the trend in the higher-charge range. (No plot of the calculated instantaneous hydrogen absorption efficiency for the data of Figure 3.4.2-a is given since the form of the integral absorption function is uncertain. The calculated instantaneous hydrogen absorption efficiencies for the 95°C experiments are given in Section 3.4.3.)

Figure 3.4.2-c shows a plot of the amount of hydrogen absorbed as a function of the charge passed for Ti-2 at 25°C with different applied cathodic current densities between 190 $\mu A \cdot cm^{-2}$ and 1.9 $mA \cdot cm^{-2}$, as indicated in the figure caption. From this graph, it appears that the amount of hydrogen absorbed depended only on the *amount* of hydrogen produced at the metal surface (*i.e.*, the charge passed) and weakly, if at all, on the *rate* of hydrogen production at the surface (*i.e.*, the applied current density). In other words, over the investigated range of hydrogen production rates, the hydrogen absorption efficiency

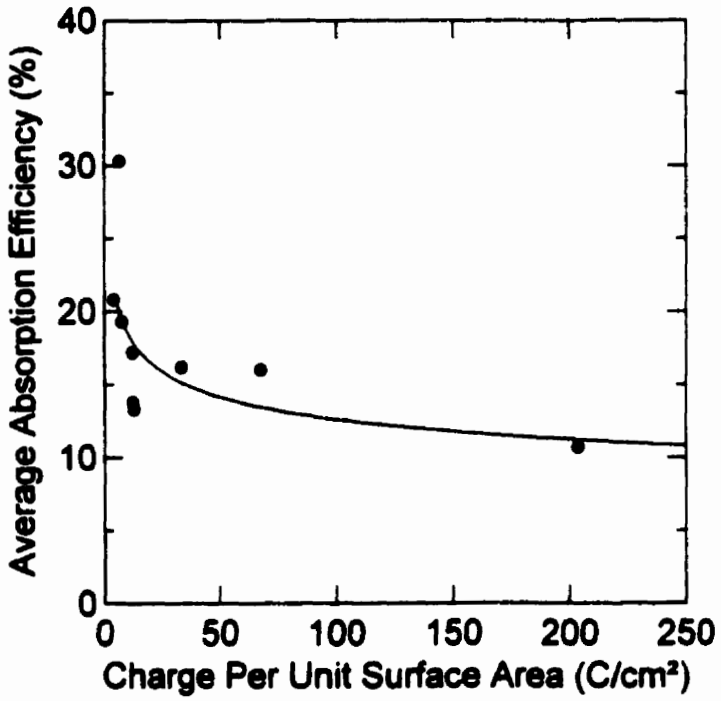

Figure 3.4.2-b Average hydrogen absorption efficiency as a function of charge passed per unit surface area for Ti-2 in 0.1 mol·dm^{-3} HCl + 0.27 mol·dm^{-3} NaCl at 25°C with an applied cathodic current density of 190 μA·cm^{-2}. The solid curve represents a power series fit to the existing data, but the trend at charges above ~50 C·cm^{-2} is uncertain due to the dearth of measurements in this range.

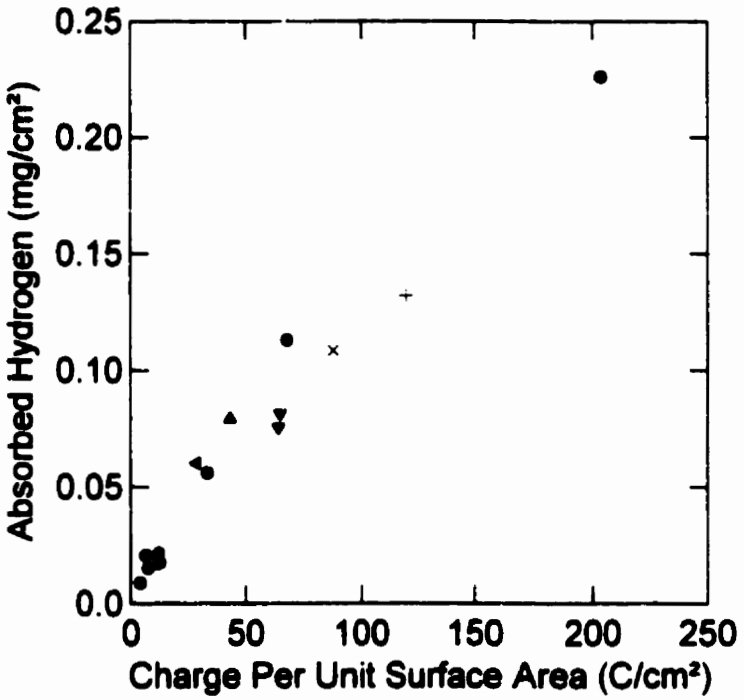

Figure 3.4.2-c Amount of absorbed hydrogen per unit surface area as a function of charge passed per unit surface area for Ti-2 in 0.1 mol·dm^{-3} HCl + 0.27 mol·dm^{-3} NaCl at 25°C for different applied cathodic current densities: (●) 190 μA·cm^{-2}, (◁) 380 μA·cm^{-2}, (▲) 770 μA·cm^{-2}, (▼) 1.2 mA·cm^{-2}, (×) 1.5 mA·cm^{-2}, (+) 1.9 mA·cm^{-2}.

for a given value of the charge passed was independent of, or only slightly dependent on, the hydrogen generation rate. Thus, a certain fraction of all hydrogen generated at the titanium surface was absorbed by the metal, that fraction being determined by the previous history of the sample (*i.e.*, how much cathodic charge was passed already). In contrast, Okada [162] and Phillips *et al.* [169] found that hydrogen absorption efficiencies *were* current-dependent; however, it should be noted that their experiments were conducted in sulphate solutions, not chloride solutions as used here.

3.4.3 Galvanostatic hydrogen charging onTi-2 at 95°C

Figure 3.4.3-a displays an optical micrograph of a cross-section of a titanium specimen after galvanostatic charging at a cathodic current density of 5.4 $mA \cdot cm^{-2}$ to a total of 1575 $C \cdot cm^{-2}$ in 0.1 $mol \cdot dm^{-3}$ HCl + 0.27 $mol \cdot dm^{-3}$ NaCl at 95°C. The exposed surface was polished and etched to highlight the locations of precipitated titanium hydrides. These appear in the micrograph in three ways: as dark needles located mainly at grain boundaries throughout the specimen, as a dense band of needles at a depth of about 100 μm from the surface, and as a homogeneous dark band in a 100 μm thick layer beginning at the sample surface. This dense hydride layer displays a number of segmented cracks, consistent with brittle rupture.

Figure 3.4.3-a shows that, after a significant amount of cathodic charge was passed, most of the absorbed hydrogen had accumulated just below the sample surface, while a small fraction was distributed deeper into the bulk of the specimen. This means that the rate of hydrogen absorption was greater than the rate of redistribution of hydrogen within the metal (*i.e.*, $R_{HA} > J_H$, Figure 1.4.1-a) under these conditions. Under conditions where

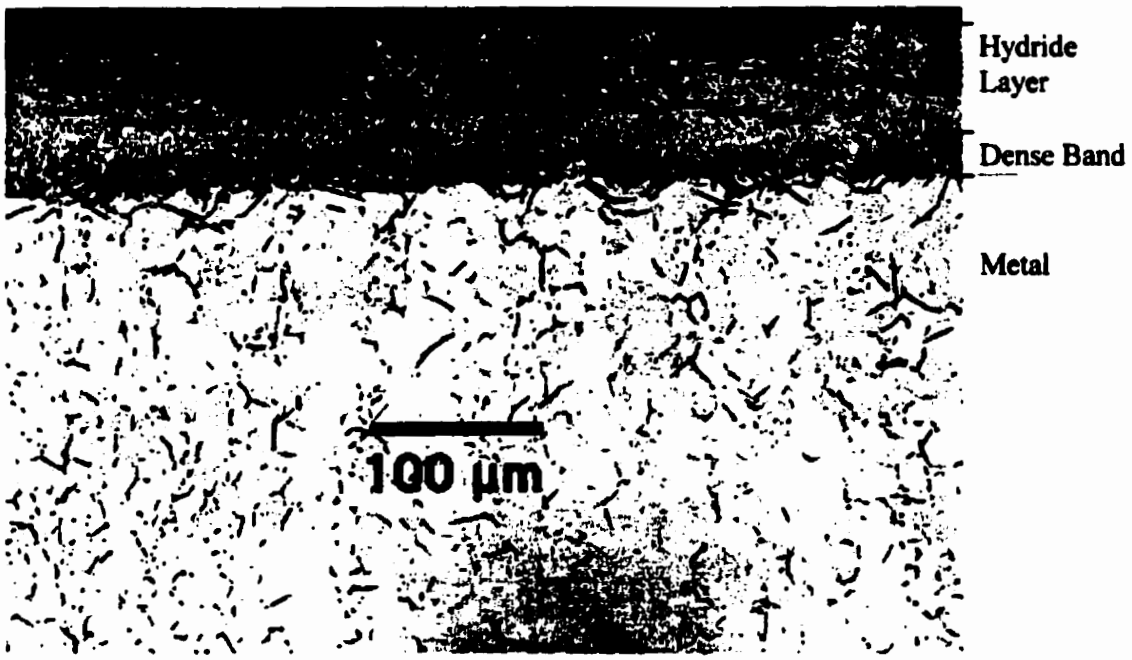

Figure 3.4.3-a Optical micrograph of a cross section of a Ti-2 hydrogen absorption coupon after charging (1575 $C \cdot cm^{-2}$) in 0.1 $mol \cdot dm^{-3}$ HCl + 0.27 $mol \cdot dm^{-3}$ NaCl at 95°C with an applied cathodic current density of 5.4 $mA \cdot cm^{-2}$. The specimen was polished and etched to highlight the locations of precipitated hydrides (dark needles).

the hydrogen generation or absorption rates were very low, one might expect to find a more uniform distribution of hydrides throughout the metal since redistribution of absorbed hydrogen would become more important. If the presence of the hydride layer is important to the hydrogen absorption mechanism, the absorption efficiency may not decrease in the same way with increasing charge in the absence of the hydride layer.

Figure 3.4.3-b depicts the relationship between the amount of absorbed hydrogen and the charge passed for Ti-2 in 0.1 mol·dm^{-3} HCl + 0.27 mol·dm^{-3} NaCl at 95°C with an applied cathodic current density of 5.4 mA·cm^{-2}. Compared to the 25°C case (Figure 3.4.2-a), much larger charges were passed in some of the 95°C experiments, so the data in this case leave no doubt that the instantaneous hydrogen absorption efficiency decreased substantially with increasing charge passed. Again, more data would increase confidence in the function determined to define the relationship between the amount of absorbed hydrogen and the amount of charge passed; however, a reasonable least-squares fit is obtained for the parabolic relationship:

$$H = k\sqrt{Q_H} \qquad \textbf{(3.4.3-a)}$$

where H represents the amount of absorbed hydrogen in units of mg·cm^{-2}, Q_H represents the total charge passed due to proton reduction, in units of C·cm^{-2}, and k is a constant equal to 0.0134 mg·cm^{-1}·C$^{-0.5}$ for this fit. The expression for the instantaneous absorption efficiency, ξ, (as a percentage) would then be given by the derivative of this function with respect to charge (converted to appropriate units):

$$\xi = 100\frac{nF}{M}\frac{dH}{dQ_H} = 50\frac{nFk}{M\sqrt{Q_H}} \qquad \textbf{(3.4.3-b)}$$

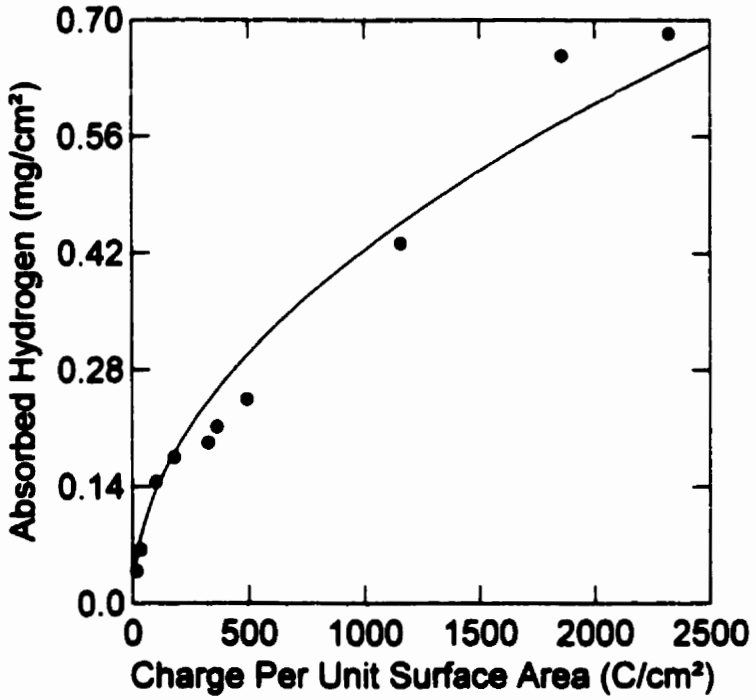

Figure 3.4.3-b Amount of hydrogen absorbed per unit surface area as a function of charge passed per unit surface area for Ti-2 in 0.1 mol·dm^{-3} HCl + 0.27 mol·dm^{-3} NaCl at 95°C with an applied cathodic current density of 5.4 mA·cm^{-2}. The curve represents a least squares fitted parabola (see Equation 3.4.3-a).

where $n = 1$ equivalent·mole^{-1} for proton reduction to hydrogen atoms, F is Faraday's constant (96 485 C·equivalent^{-1}), and M represents the molar mass of hydrogen atoms (1007.97 mg·mole^{-1}). This result is plotted as the dotted curve in Figure 3.4.3-c. Such an expression for the ξ *vs.* Q_H relationship places no mathematical limit on the total amount of hydrogen that may be absorbed as the charge passed tends to infinity, but does push the absorption efficiency toward a limit of zero at infinite charge passed. Compare the lower values of the instantaneous hydrogen absorption efficiency to the higher values of the average hydrogen absorption efficiency (also shown in Figure 3.4.3-c) for a given charge value.

The average hydrogen absorption efficiency is given (from the fitted parabola, Equation 3.4.3-a) by:

$$\bar{\xi} = 100\frac{nFH}{MQ_H} = 100\frac{nFk}{M\sqrt{Q_H}} \qquad \textbf{(3.4.3-c)}$$

Therefore, one can see that the ratio between the average and the calculated instantaneous hydrogen absorption efficiencies is:

$$\frac{\bar{\xi}}{\xi} = \frac{1}{2} \qquad \textbf{(3.4.3-d)}$$

for this model. Hence, the average hydrogen absorption efficiency overestimates the instantaneous hydrogen absorption efficiency by a factor of two, in this case.

In general, the relationship between the average and instantaneous hydrogen absorption efficiencies is given by

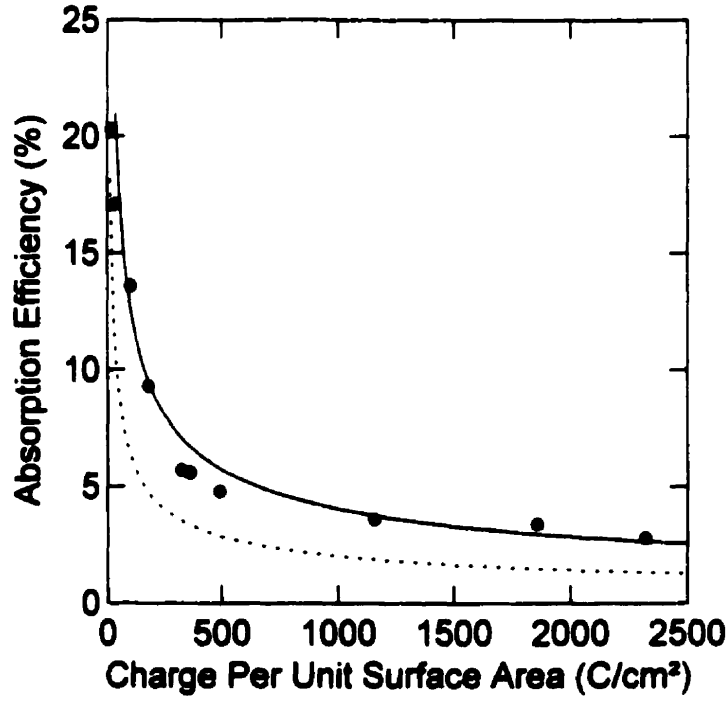

Figure 3.4.3-c Hydrogen absorption efficiency as a function of charge passed per unit surface area for Ti-2 in 0.1 mol·dm^{-3} HCl + 0.27 mol·dm^{-3} NaCl at 95°C: (●) average absorption efficiencies from galvanostatic experiments at an applied cathodic current density of 5.4 μA·cm^{-2}, (———) average absorption efficiency calculated from Equation 3.4.3-a (see Equation 3.4.3-c), (·····) calculated instantaneous absorption efficiency from Equation 3.4.3-a (see Equation 3.4.3-b).

$$\bar{\xi} = \frac{\int I_H \xi dt}{\int I_H dt} \qquad \textbf{(3.4.3-e)}$$

where I_H is the instantaneous hydrogen production rate, expressed as a current, and t is the time. Unfortunately, in most practical situations it is difficult, or impossible, to measure I_H or ξ, both of which may change over time.

Charging experiments at 95°C were also performed at a variety of applied current densities. The data acquired after applying a cathodic current density of 5.4 $mA \cdot cm^{-2}$ were shown in Figures 3.4.3-b and 3.4.3-c because they were the most reproducible. Figure 3.4.3-d shows the full set of data collected after applying cathodic current densities ranging from 190 $\mu A \cdot cm^{-2}$ to 19 $mA \cdot cm^{-2}$ at 95°C. One can see that a number of the data points from experiments with applied cathodic current densities differing from 5.4 $mA \cdot cm^{-2}$ still follow the same relationship between the amount of absorbed hydrogen and the charge passed as data from 5.4 $mA \cdot cm^{-2}$ experiments. This is comparable to the previously discussed observation that the applied current density appeared to have little, if any, effect on the hydrogen absorption characteristics at 25°C.

At 95°C, however, there is an additional complication. In some experiments no hydrogen absorption was detected (see Figure 3.4.3-d). Why certain experiments did not result in hydrogen absorption can be rationalized with reference to the potentiostatic polarization curves recorded at 95°C (Figure 3.1.2.2-f). Hydrogen absorption at 95°C was observed in experiments in which the electrode potential during cathodic charging adopted a value on the negative potential side of the cusp point in the polarization curve, *i.e.*, in region B (Figure 3.1.2.2-f). Such behaviour was observed in experiments with very large applied

a)

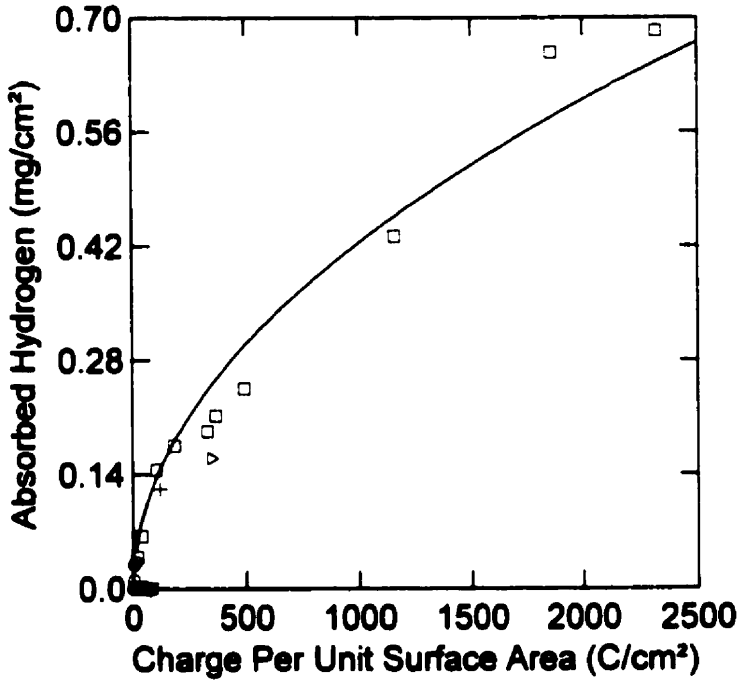

Figure 3.4.3-d a) Amount of absorbed hydrogen per unit surface area as a function of charge passed per unit surface area on Ti-2 in 0.1 mol·dm^{-3} HCl + 0.27 mol·dm^{-3} NaCl at 95°C for different applied current densities: (○) 190 μA·cm^{-2}, (◁) 380 μA·cm^{-2}, (△) 770 μA·cm^{-2}, (▽) 1.2 mA·cm^{-2}, (×) 1.5 mA·cm^{-2}, (+) 1.9 mA·cm^{-2}, (□) 5.4 mA·cm^{-2}, (▷) 19 mA·cm^{-2}, (————) fitted parabola from Equation 3.4.3-a.

b)

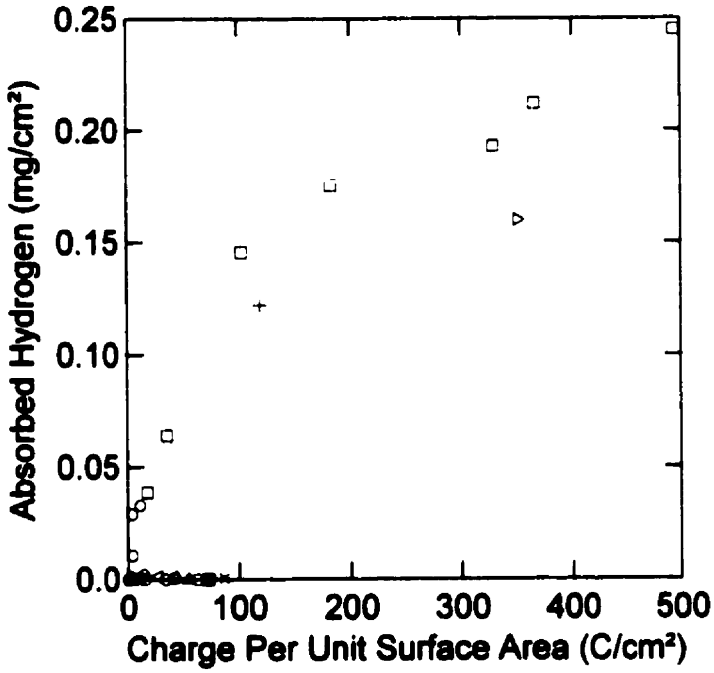

b) Expansion of low-charge region from a).

cathodic currents and in an experiment with an applied cathodic current density of only 190 $\mu A \cdot cm^{-2}$ that displayed the "unusual" form of the activation transient (*i.e.*, the electrode activated and remained active instead of undergoing "activation rebound", see Figure 3.1.1-g) and therefore adopted a potential negative of the cusp potential when cathodically polarized. The latter experiment yielded a surprising 70% average hydrogen absorption efficiency over its 5.39 C of cathodic charging.

Conversely, no hydrogen absorption was observed on Ti-2 at 95°C in experiments in which the potential adopted a value on the positive side of the cusp potential during cathodic charging. This condition normally occurred when the electrode displayed the "usual" open circuit behaviour (*i.e.*, activation-rebound, see Section 3.1.1) and then a low cathodic current density was applied during the charging period (Figure 3.4.3-d).

The polarization curve (Figure 3.1.2.2-f) indicates a range of currents over which the same current could be achieved at two or three different potentials, one negative, and the others positive, of the cusp point. The current-potential relationship also evolved with time under potentiostatic conditions, as shown in Figures 3.1.2.2-g, 3.1.2.2-h, and 3.1.2.2-i. This apparent multiplicity of states was also observed in the galvanostatic experiments. Often, when low or intermediate cathodic currents were applied at 95°C, the potential transients were relatively unstable. In two experiments with an applied cathodic current density of 190 $\mu A \cdot cm^{-2}$, the potential achieved during the galvanostatic charging period was negative of the cusp point for at least a portion of the charging period. In one case, the potential remained negative of the cusp point for the duration of the charging period and the average hydrogen absorption efficiency after 11.71 $C \cdot cm^{-2}$ of

cathodic charge had passed was 26.9% (0.33 $mg \cdot cm^{-2}$); in the other case, the potential during galvanostatic charging fell below -0.6 V for 9442 s, but then increased positive of -0.6 V for the remaining 10 797 s, achieving a final value of about -0.45 V (see Figure 3.4.3-e). In this experiment, the average hydrogen absorption efficiency was 24.0% (0.011 $mg \cdot cm^{-2}$) after 4.25 $C \cdot cm^{-2}$ had passed. If one assumed that hydrogen absorption only occurred when the potential was negative of -0.6 V and only included in the calculation the 9442 s during which this condition was satisfied, then the revised average hydrogen absorption efficiency would be 54.3% (of the 1.83 $C \cdot cm^{-2}$ that passed while the potential was negative of -0.6 V).

Figure 3.4.3-f shows the hydrogen absorption data for the 25°C and 95°C experiments on Ti-2 at all cathodic current densities applied. The Figure shows that the relationship between the amount of absorbed hydrogen and the cathodic charge passed is independent of temperature. This temperature-independence agrees with the results of Okada [162] and therefore disagrees with those of Phillips *et al.* [170].

Figures 3.4.3-e, 3.4.3-g, 3.4.3-h, and 3.4.3-i show the time evolution of the potential during galvanostatic charging. Initially, the potential underwent large changes, but over time a more gradual drift in the positive direction was observed. An early fall and rise of the potential before the more gradual drift was observed in experiments at 95°C with an applied cathodic current density of 5.4 $mA \cdot cm^{-2}$. This feature was very reproducible. The fast-rising transient potentials observed in the first 5000 s of the galvanostatic charging experiments (Figures 3.4.3-g and 3.4.3-i) may, like the current transients observed in the polarization curves (see Figures 3.1.2.2-g, 3.1.2.2-h, and 3.1.2.2-i), correspond to

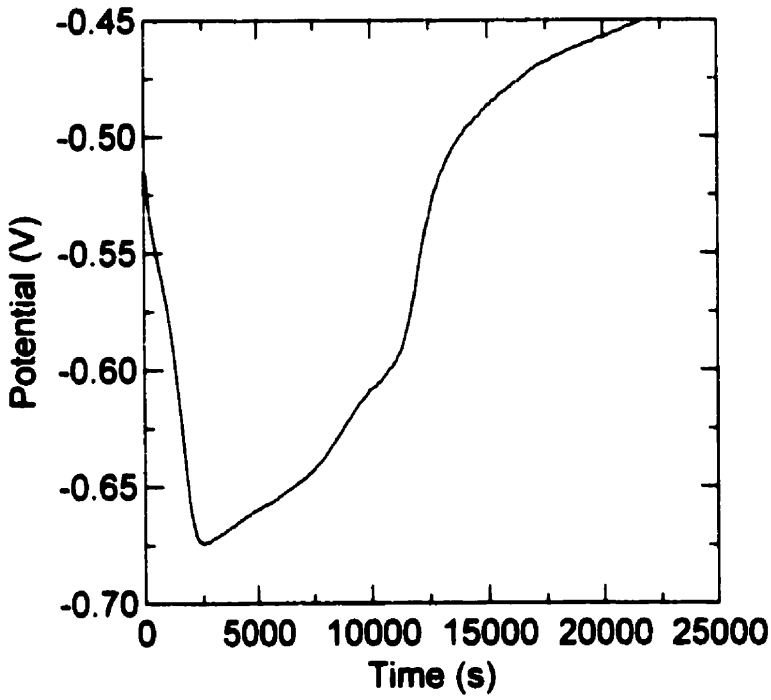

Figure 3.4.3-e Potential transient recorded on Ti-2 during galvanostatic charging in 0.1 mol·dm^{-3} HCl + 0.27 mol·dm^{-3} NaCl at 95°C with an applied cathodic current density of 190 μA·cm^{-2}, showing a large potential shift from below to above the cusp potential (~ -0.6 V).

a)

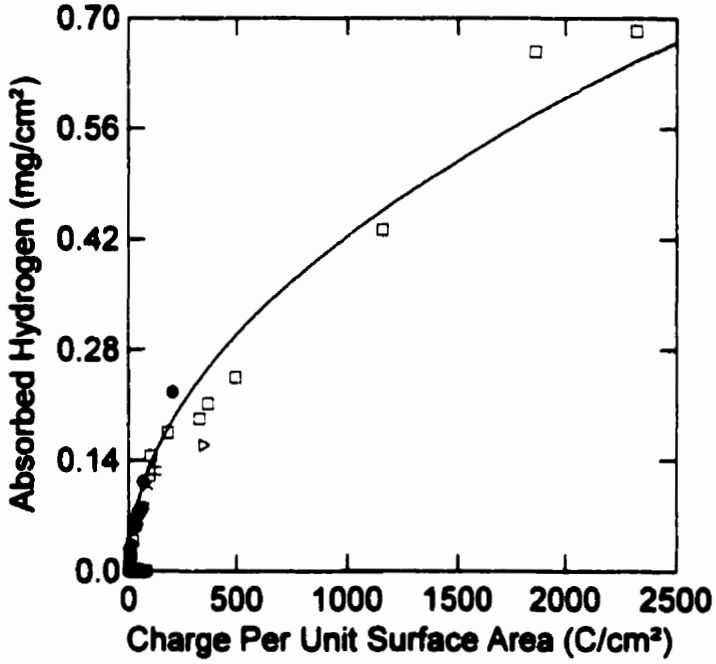

Figure 3.4.3-f a) Amount of absorbed hydrogen per unit surface area as a function of charge passed per unit surface area on Ti-2 in 0.1 mol·dm^{-3} HCl + 0.27 mol·dm^{-3} NaCl at 25°C (filled symbols) and 95°C (open symbols) for different applied current densities: (○) 190 μA·cm^{-2}, (◁) 380 μA·cm^{-2}, (△) 770 μA·cm^{-2}, (▽) 1.2 mA·cm^{-2}, (×) 1.5 mA·cm^{-2}, (+) 1.9 mA·cm^{-2}, (□) 5.4 mA·cm^{-2}, (▷) 19 mA·cm^{-2}, (————) fitted parabola from Equation 3.4.3-a.

b)

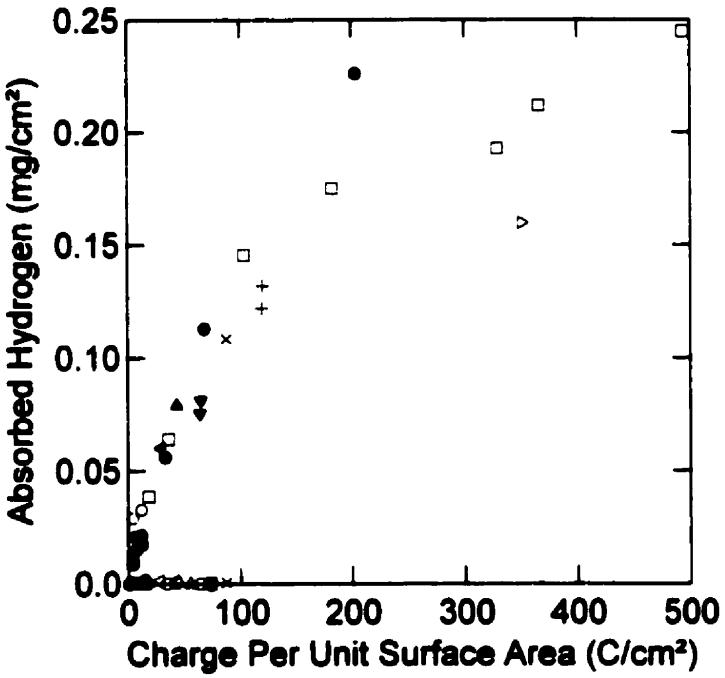

b) Expansion of low-charge region from a).

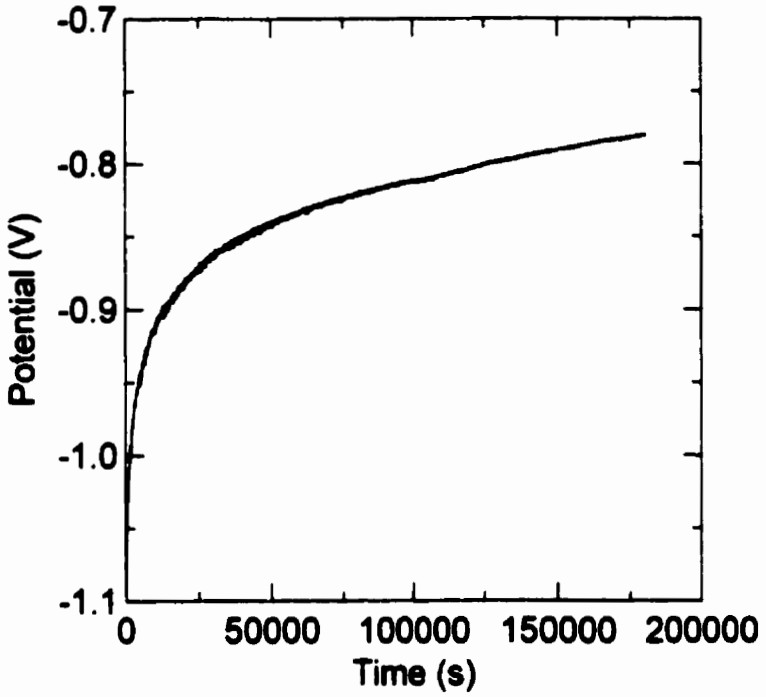

Figure 3.4.3-g Potential transient recorded during galvanostatic charging of Ti-2 in 0.1 mol·dm^{-3} HCl + 0.27 mol·dm^{-3} NaCl at 25°C with an applied cathodic current density of 190 μA·cm^{-2}.

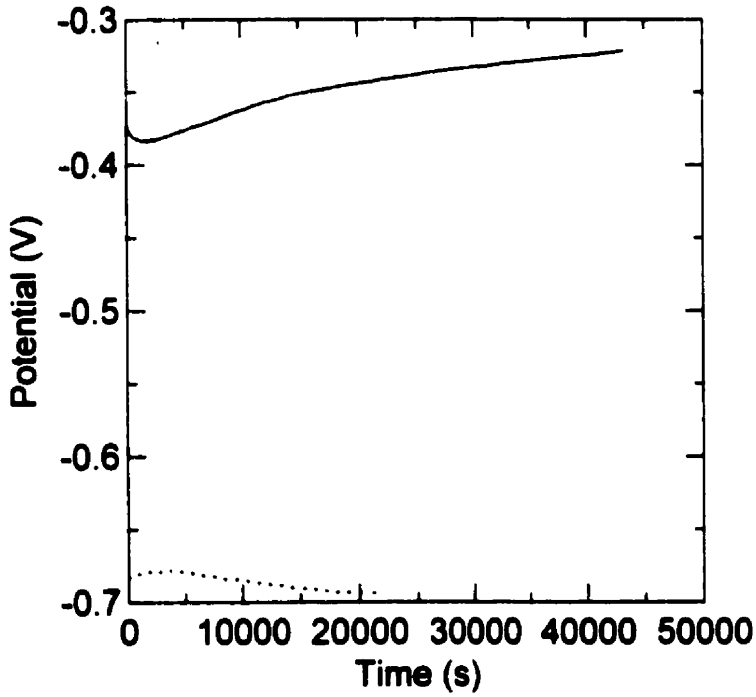

Figure 3.4.3-h Potential transients recorded during galvanostatic charging of Ti-2 in 0.1 mol·dm^{-3} HCl + 0.27 mol·dm^{-3} NaCl at 95°C with an applied cathodic current density of 190 μA·cm^{-2}: (————) polarized after activation and potential rebound at E_{oc} (see Section 3.1.1) ($\bar{\xi} = 0$), and (· · · · ·) polarized after the activation event that was not followed by potential rebound ($\bar{\xi}$ = 69.9%).

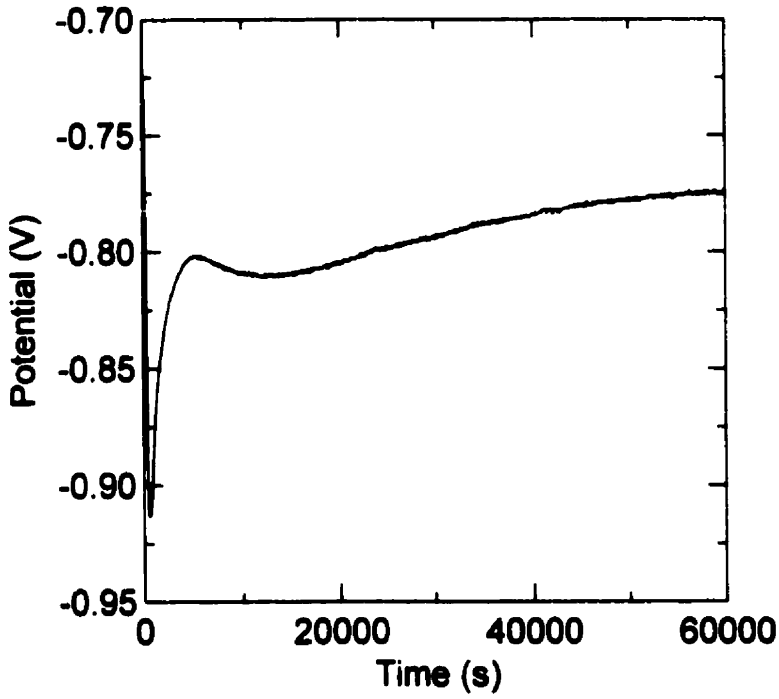

Figure 3.4.3-i Potential transient recorded during galvanostatic charging of Ti-2 in 0.1 mol·dm^{-3} HCl + 0.27 mol·dm^{-3} NaCl at 95°C with an applied cathodic current density of 5.4 mA·cm^{-2}.

adjustments in the electrode surface state that precede or accompany hydrogen absorption. In some instances, during galvanostatic charging at 95°C with low applied cathodic current densities, the potential underwent significant changes (Figure 3.4.3-h) and hydrogen absorption was observed only if the potential achieved values negative of the cusp point (see Figure 3.1.2.2-f).

3.4.4 Galvanostatic hydrogen charging on Ti-12 at 95°C

Hydrogen absorption experiments on Ti-12 in 0.1 $mol \cdot dm^{-3}$ HCl + 0.27 $mol \cdot dm^{-3}$ NaCl at 95°C proved to be much less reproducible than the similar experiments on Ti-2 reported above. Plots of the amount of hydrogen absorbed and the net absorption efficiency *versus* the charge passed per unit surface area are given in Figures 3.4.4-a and 3.4.4-b, respectively. From these results one can see that the hydrogen absorption behaviour of Ti-12 under these conditions was not determined primarily by any of the controlled variables (time, current density, or total charge); even nominally identical repeat experiments yielded dramatically different results.

The observation of an apparent threshold potential for hydrogen absorption on Ti-2 under these conditions, as well as an examination of the potential transients during the galvanostatic charging of the Ti-12 coupons (Figures 3.4.4-c and 3.4.4-d), provide the basis for a hypothesis that may begin to explain the variability in hydrogen absorption by Ti-12. The transients of Figures 3.4.4-c and 3.4.4-d show that large variations in the potential of the Ti-12 coupons occurred during galvanostatic charging. These resemble the changes observed during the galvanostatic polarization of one Ti-2 hydrogen absorption coupon, shown in Figure 3.4.3-e and discussed in Section 3.4.3. It seems

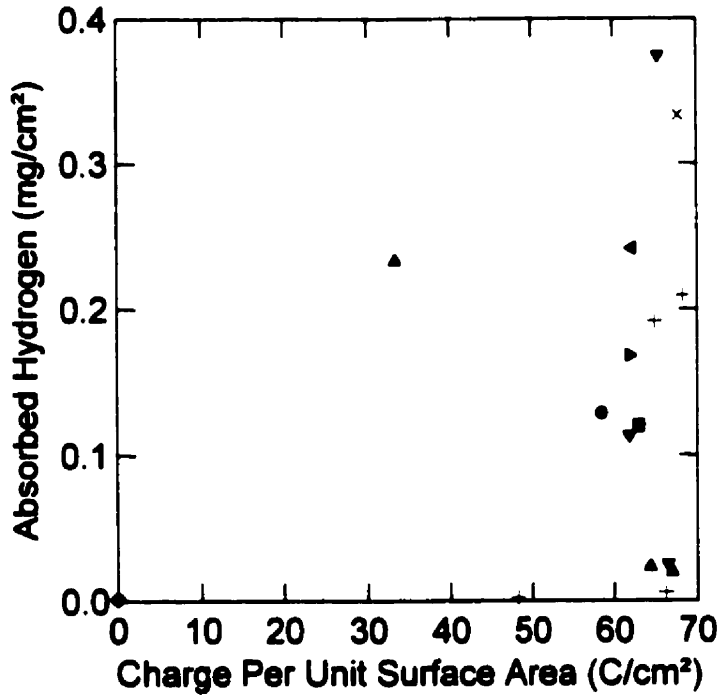

Figure 3.4.4-a Amount of hydrogen absorbed per unit surface area as a function of the charge passed per unit surface area on Ti-12 in 0.1 mol·dm^{-3} HCl + 0.27 mol·dm^{-3} NaCl at 95°C for different applied cathodic current densities: (◆) open circuit (i.e., zero current), (+) 190 μA·cm^{-2}, (▲) 380 μA·cm^{-2}, (▼) 700 μA·cm^{-2}, (×) 1.9 mA·cm^{-2}, (◀) 2.1 mA·cm^{-2}, (▶) 4.8 mA·cm^{-2}, (■) 7.0 mA·cm^{-2}, (●) 16 mA·cm^{-2}.

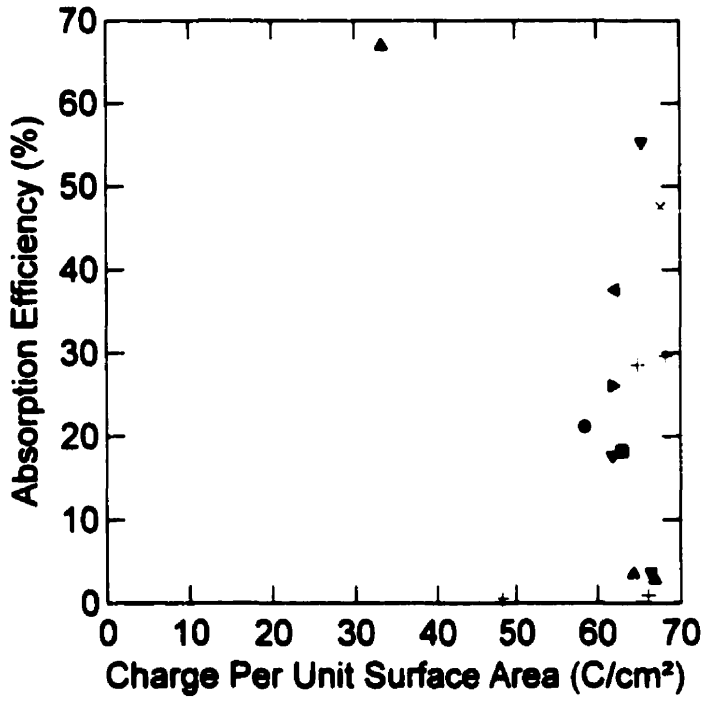

Figure 3.4.4-b Average hydrogen absorption efficiency as a function of the charge passed per unit surface area on Ti-12 in 0.1 mol·dm^{-3} HCl + 0.27 mol·dm^{-3} NaCl at 95°C for different applied cathodic current densities: (+) 190 μA·cm^{-2}, (▲) 380 μA·cm^{-2}, (▼) 700 μA·cm^{-2}, (×) 1.9 mA·cm^{-2}, (◁) 2.1 mA·cm^{-2}, (▷) 4.8 mA·cm^{-2}, (■) 7.0 mA·cm^{-2}, (●) 16 mA·cm^{-2}.

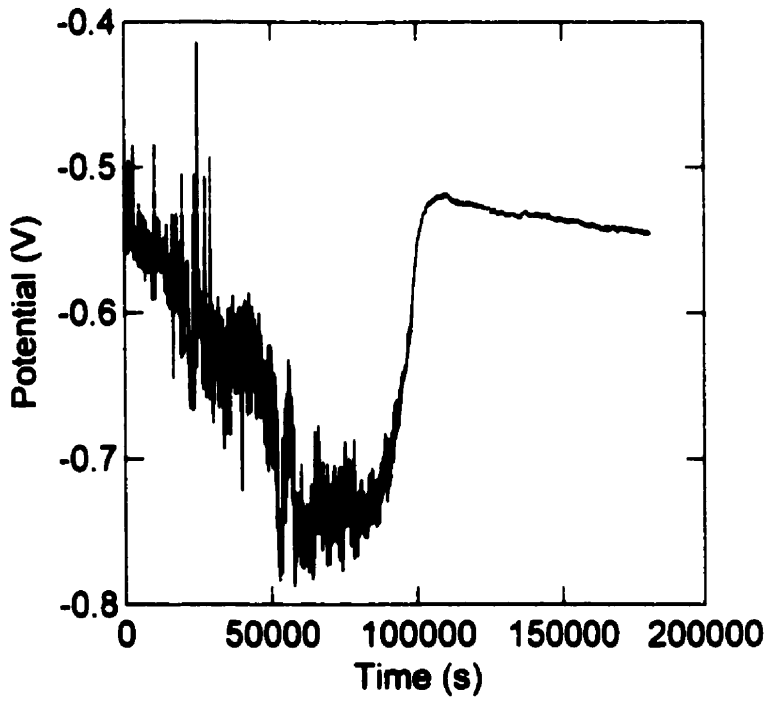

Figure 3.4.4-c Potential transient recorded on Ti-12 during galvanostatic charging in 0.1 mol·dm^{-3} HCl +0.27 mol·dm^{-3} NaCl at 95°C with an applied cathodic current density of 380 μA·cm^{-2}, showing large potential shifts and high frequency fluctuations. The average hydrogen absorption efficiency over the duration of this test was 3.5%.

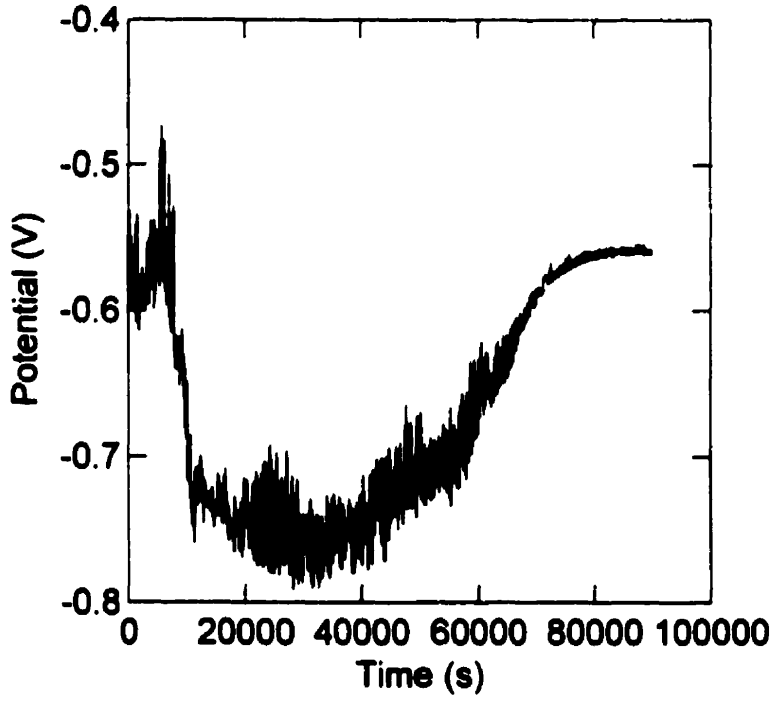

Figure 3.4.4-d Potential transient recorded on Ti-12 during galvanostatic charging in 0.1 mol·dm^{-3} HCl +0.27 mol·dm^{-3} NaCl at 95°C with an applied cathodic current density of 700 μA·cm^{-2}, showing large potential shifts and high frequency fluctuations. The average hydrogen absorption efficiency over the duration of this test was 3.7%.

reasonable that a threshold potential for hydrogen absorption may exist on Ti-12, just as on Ti-2, and that the amount of hydrogen absorbed by the Ti-12 coupons may have been determined not by the amount of charge passed, but rather by the amount of charge passed while the potential was below the threshold. If that is indeed the case, then potentiostatic charging experiments may yield more reproducible results, especially if (like for Ti-2) hydrogen absorption on Ti-12 depends on the potential and the total charge passed and is insensitive to the cathodic current density.

High frequency fluctuations in the potential are also clear in Figures 3.4.4-c and 3.4.4-d. Although some instability in the potential transients during galvanostatic polarization of Ti-2 was noted, fluctuations of the frequency and amplitude observed on Ti-12 did not occur. The amplitude of these noise-like transients decreased with time; their frequency was higher than the Nyquist limit for the sampling frequency employed (~0.017 Hz), and therefore cannot be assigned any meaningful value. Their cause is uncertain; however, they were not caused by bubble detachment, since continuous bubbling occurred all throughout these experiments and also during those on Ti-2, in which such fluctuations were not observed. Nor can they be reasonably explained as consequences of poor electrical connections or external noise pick-up since they did not endure throughout the duration of the tests, and were not observed with identically treated Ti-2 coupons. It is noteworthy that rapid current fluctuations (also of undetermined frequency) were observed during cathodic potentiostatic polarization of the Ti thin film electrode during neutron reflectometry experiments, but no relationship between the "noise" in these two different systems undergoing hydrogen evolution has yet been shown.

3.4.5 Interpretation of hydrogen absorption data

It is tempting to speculate that the existence of a hydrogen absorption threshold potential is a consequence of the state of the electrode surface (perhaps a surface film or type of absorption site present on the titanium surface only on one side of the cusp point). A good argument can be made for control of hydrogen absorption by the properties of an oxide film on the Ti. For an oxide-covered Ti surface, polarization negative of the oxide's flatband potential would lead to electronic degeneracy in the surface of the oxide, the conversion of Ti^{IV} to Ti^{III} in the oxide, incorporation of hydrogen into the oxide [148-150], and, finally, hydrogen absorption by the metal. Polarization positive of the flatband potential would lead to the formation of a space charge layer in the oxide, the stabilization of Ti^{IV}, and the loss of the Helmholtz potential necessary for hydrogen absorption. The oxide would then function as a barrier to hydrogen absorption and the threshold potential for hydrogen absorption would, effectively, be defined by the flatband potential.

According to Ohtsuka *et al.* [150] TiO_2 can be reduced to TiO(OH) by the application of cathodic charge. In acidic solution this dissolves even faster than TiO_2, but in neutral solution reduction does not lead to dissolution [150]. The added hydrogen yields electron donor states, increasing the conductivity of the oxide. As this conversion takes place, the oxide seems to become permeable to hydrogen atoms, which can traverse the oxide and become absorbed into the underlying metal.

The neutron reflectometry results (Section 3.2.4), recorded in experiments involving neutral pH solution, were consistent with the ellipsometry results of Ohtsuka *et al.* [150]. Similarly, for the galvanostatic hydrogen absorption experiments, assuming that a very

thin oxide film is always present even in acidic solutions [10], one can hypothesize that the threshold potential for hydrogen absorption was determined by the oxide's flatband potential. The position of the observed hydrogen absorption threshold (at the "cusp" potential, E ~ -0.6 V) is just below the reported value of the flatband potential for TiO_2 (E_{fb} = -0.54 V [130]).

In galvanostatic polarizations, the polarization potential is determined by how easy or difficult it is to pass the required current, and in these experiments, the polarization potential determined whether or not hydrogen absorption would occur. The conditions that result in low potentials being achieved in the galvanostatic polarizations (necessary for hydrogen absorption to occur) appear to be established while the electrode is at its open circuit potential at 25°C and, on infrequent occasions, at 95°C (dotted curve, Figure 3.1.1-g). This variability at 95°C suggests that the alteration of the air-formed film on the Ti-2 surface, which occurs on immersion of the electrode in the acidic solution, leads to formation of a highly active surface that can react unpredictably. With the electrode at its open circuit potential at 95°C, the establishment of a surface that is not prone to hydrogen absorption without very strong cathodic polarization predominates, whereas, at 25°C (and infrequently at 95°C), the formation of the surface state that *does* subsequently lead to the absorption of hydrogen (under mild conditions of cathodic polarization) occurs under open circuit conditions.

Ti-12, as a cathodically modified alloy, offers a surface upon which the reduction of hydrogen is expected to be catalyzed (*i.e.*, the same cathodic current can be achieved at a higher potential than on Ti-2). One would expect this to result in less hydrogen

absorption on Ti-12 coupons than is observed on equivalently treated Ti-2 coupons, since the applied potential would not need to be so low on Ti-12. The difficulty in achieving reproducibility in the amount of hydrogen absorption by Ti-12 reported in Section 3.4.4 suggests additional complexity, probably related to the large variability in the potentials attained by the Ti-12 coupons during the galvanostatic polarizations.

One possible explanation for the large potential shifts during the galvanostatic experiments with Ti-12 is that the catalytic sites on the Ti-12 surfaces were not exposed to solution sufficiently well to perform the amount of catalysis required to lift the potential above the threshold potential at first, but after some time and cathodic polarization, the oxide, metal, or other debris that was blocking these sites was dissolved or removed, allowing the reduction reaction to proceed more easily and the potential to rise.

A second possibility questions the catalytic activity of the as-produced Ti-12 surface. It is possible that the catalysis of proton reduction expected to generate polarization potentials above the hydrogen absorption threshold value during galvanostatic experiments is not provided by Ti_2Ni intermetallic precipitates themselves (or not provided to a sufficient level), but rather by some surface species that forms during the course of the experiment, such as a catalytic surface hydride. The presence of the intermetallic particles may simply provide "windows" in the surface film at which this hydride or other catalytic species can grow.

There is a danger too that intermetallic precipitates may also provide windows in the protective oxide that defeat the hydrogen barrier afforded by the oxide and allow

hydrogen to enter the alloy at potentials above the absorption threshold potential observed on Ti-2. This is a concern not only for Ti-12, but also for the other cathodically modified alloys. One might even expect it to be a bigger danger on Ti-16 and Ti-0.1Ru than on Ti-12, since the EIS results showed that the former alloys offer the electrolyte solution greater access to the metal surface than does Ti-12 (*i.e.*, they had lower overall pore resistances, R_{pore}, than did Ti-12). Furthermore, Pd, the alloying element in Ti-16, is a well known[1] absorber of hydrogen. Under natural corrosion conditions, though, even if the hydrogen absorption *efficiency* was higher on a cathodically modified alloy than on Ti-2, the hydrogen absorption *rate* would probably be much lower on the cathodically modified alloy since the corrosion rate, and therefore the hydrogen reduction rate, would be much lower on this surface.

It is noteworthy that the transition potential between regions A and B (cusp potential) also coincides with the switch from decreasing to increasing cathodic current transients in the polarization curves (see Figures 3.1.2.2-g, 3.1.2.2-h, and 3.1.2.2-i). The transient currents may also be related to the establishment of the surface state required to prevent or permit hydrogen absorption in each region (*e.g.*, formation of catalytic surface hydride sites). For example, in galvanostatic charging experiments at 95°C after a "usual" open circuit potential transient, hydrogen absorption would probably proceed during the galvanostatic polarization in every experiment if a cathodic current density sufficient to push the potential negative of the cusp potential was applied.

[1] Especially because of its association with the "cold fusion" excitement that began in 1989.

In proposing a mechanism for hydrogen entry into Ti-2 under the conditions used in these experiments, one must consider that the hydrogen absorption efficiency appears to be dependent on the total amount of cathodic charge passed, but independent of the hydrogen production rate at the metal surface (*i.e.*, the current), independent of potential at potentials below the threshold potential (different potentials were achieved at different applied current densities), and independent of time (different times are required to pass the same amount of charge with different applied currents). The apparent current-independence observed in these experiments contrasts with the results of experiments performed by Okada [162, 168] and Phillips *et al.* [169, 170], which indicated that the absorption efficiency depended on the applied current. At the moment, the reasons for the differences in current dependence are unknown; however, it should be noted that the experiments of Okada and Phillips *et al.* were conducted in sulphate solutions, these in chloride solutions.

Two possible explanations for the lack of current dependence are that hydrogen is absorbed at specific surface sites or "windows", or that the hydrogen absorption behaviour is controlled by a hydride layer growth process within the metal. In considering the first mechanism, one can imagine a surface carrying some limited number of "windows" (*i.e.*, regions of very high hydrogen permeability) that cover a fraction of the sample surface, and which act as entry points for the hydrogen atoms that contact them. The rest of the surface must then have a much lesser propensity for hydrogen permeation, such that absorption from these regions does not significantly influence the net absorption efficiency. The latter regions must still be capable of passing cathodic charge. These windows at which hydrogen absorption takes place could consist of

islands of hydride on the surface, precipitated intermetallic impurity compounds, or simply a particular type of adsorption site on the metal, hydride or oxide surface layer. Protons reduced at these particular sites may be injected into the surface while those reduced at other surface sites of different geometry or composition are evolved as gas. The increasing cathodic current transients shown in Figures 3.1.2.2-b and 3.1.2.2-i imply an enhancement (over relatively short periods of time) of the electrode's ability to reduce protons and may indicate the opening of the windows, perhaps by film growth, film removal or favourable lattice distortions caused by the initial hydrogen absorption. The decline in absorption efficiency with increasing charge could be a result of the gradual blocking of absorption windows by hydride layer formation, oxide film growth, or accumulation of impurities.

If the second explanation, the hydride layer growth mechanism, were correct, the hydrogen absorption rate would be directly proportional to the "free" hydrogen concentration gradient between the sample surface and the bulk metal, which, in turn, would be proportional to the current. This would yield a constant hydrogen absorption efficiency at a given charge value for any current. Absorbed hydrogen would contribute to the hydride layer thickness, thereby decreasing the concentration gradient[1], and the absorption rate and efficiency, with increasing amounts of charge passed. The thickness of this layer would be determined by the amount of hydrogen reduced at the sample surface (*i.e.*, the total charge passed up to that point) and would be the same irrespective of time and growth rate.

[1] Provided hydrogen bound up in the form of hydride is not part of the "free" hydrogen concentration gradient.

The presence of a relatively thick sub-surface hydride layer is shown in Figure 3.4.3-a, but it is not yet clear whether this layer was created through a film growth mechanism or by hydrogen accumulation beneath many closely spaced absorption windows. Some distinction between the two mechanisms offered for consideration may be possible by examining the hydride layer thickness as a function of the total charge passed and of the applied current density to see if it matches the absorbed hydrogen concentration *vs.* charge profiles (Figures 3.4.2-a, 3.4.2-c, 3.4.3-b, 3.4.3-d, and 3.4.3-f).

Regardless of the mechanism of hydrogen entry into Ti, the rate and extent of hydrogen absorption will be extremely low on a passive Ti surface freely corroding under mild pH (≥ 3) conditions since the passive oxide is an impermeable barrier to hydrogen absorption and the hydrogen production rate, which is controlled by the corrosion rate, will be extremely low. However, under acidic, active crevice corrosion conditions, metal dissolution is supported predominantly by proton reduction and considerable amounts of hydrogen can be absorbed into the metal [18, 202].

The primary reason for measuring hydrogen absorption efficiencies is to obtain a value that can be used to predict the rate of hydrogen absorption (R_{HA}) (Figure 1.4.1-a) under crevice corrosion conditions and determine the useful lifetime of Ti structures. Recently, it was suggested [18] that the rate of hydrogen absorption is proportional to the rate of crevice corrosion propagation,

$$R_{HA} = f_H(R_{CC} - I_C) = \frac{f_H I_C Q_H}{Q_C} \qquad \textbf{(3.4.5-a)}$$

where f_H is the fraction of available hydrogen absorbed by the metal, R_{CC} the rate of crevice corrosion in units of current, I_C the measured coupled current in electrochemically monitored crevice corrosion experiments and R_{HA} is in units of current. This expression was written with the provision that f_H does not change over the duration of the crevice corrosion process. The galvanostatic hydrogen absorption experiments reported in this Thesis, however, suggest that f_H does change as more cathodic charge is passed (*i.e.*, ξ is not constant). Hence, equation 3.4.5-a should be revised slightly by substituting $\frac{\xi}{100}$ for f_H:

$$R_{HA} = \frac{\xi I_C Q_H}{100 Q_C} \qquad \textbf{(3.4.5-b)}$$

This leads to the following expression for the rate of hydrogen absorption by Ti-2 at 95°C,

$$R_{HA} = \frac{nFkI_C\sqrt{Q_H}}{2MQ_C} \qquad \textbf{(3.4.5-c)}$$

provided the fitted relationship from equation 3.4.3-a holds.

A value of $\bar{\xi} = 10\%$ was claimed to be appropriate to represent the average hydrogen absorption efficiency achieved by Ti-2 during a period of crevice corrosion at 100°C [203]. The galvanostatic results presented in this Thesis show that, for large amounts of charge passed (equivalent to extensive crevice propagation), the value of $\bar{\xi}$ falls to about 2 to 3%. These values are significantly lower than the average value of 8 to 14% obtained in the crevice corrosion experiments [202, 203]. The apparent disparity between

the galvanostatic results and the crevice corrosion results could have a number of causes. One source of difference that is of unknown, and potentially major, significance is the assumption that the 0.1 $mol \cdot dm^{-3}$ HCl + 0.27 $mol \cdot dm^{-3}$ NaCl solutions used in the galvanostatic experiments were representative of the solutions present in the interior of a corroding crevice. The makeup of the latter is unknown at present but almost certainly is lower in pH and changes with time and position within an actively corroding crevice. The interfacial potential drop at each point on the metal surface within the crevice is likewise unknown, and would vary according to location due to IR drop and variations in the solution composition. As shown in the galvanostatic experiments, the potential is of major relevance, because of the existence of a threshold potential for hydrogen absorption. Measurements of the pH, solution composition, and potential within an actively corroding crevice would be extremely useful.

Physical effects of the crevice geometry may also influence the hydrogen absorption process. The restricted mass transport within the occluded cell could hinder the escape of hydrogen from the metal surface into the solution, thereby enhancing hydrogen absorption in comparison with the boldly exposed electrodes used in galvanostatic tests. Pressure build-up within the crevice (caused by deposition of corrosion products and forceful enough to bend 6 mm thick Ti-2 plate material) may help drive more hydrogen into the surface of crevice corrosion coupons than did the atmospheric pressure to which the hydrogen absorption coupons were subjected in the hydrogen charging experiments reported here.

Other contributions to the differences in the apparent hydrogen absorption efficiencies between the galvanostatic and crevice corrosion experiments [202] may arise from difficulties in quantifying the results of the crevice corrosion experiments. Sources of uncertainty in the crevice corrosion experiments included: errors in the amount of charge attributable to hydrogen reduction because of oxygen consumption by reaction with the vessel wall or the boldly exposed surfaces of the crevice coupons, or due to homogeneous oxidation of Ti^{III} species in solution, loss of hydride due to dissolution (*i.e.*, corrosion) in the crevice, loss of hydrogen contained within corrosion product deposits that were removed before hydrogen analysis, and lack of knowledge of the proton reduction current density (neither the corroding area nor the proton reduction current were known).

In spite of the recognized differences between the conditions used in these experiments and those arising in actual crevice corrosion circumstances, and the resulting incongruity of the average hydrogen absorption rates measured, this work represents solid progress in the development of a technique to provide hydrogen absorption data for models to estimate the useful lifetimes of Ti structures before failure by hydrogen induced cracking. Further experiments are still required to assess the pH dependence, to resolve the degree of current-dependence, and to explore the effect of alloying on the hydrogen absorption efficiency of titanium.

4 Summary and Conclusions

4.1 Overview

The objective of this summary is to link together the wide range of different individual types of experiments reported in Section 3 and forge a more cohesive account of the electrochemistry of titanium corrosion in terms of passive film growth and film breakdown on, and hydrogen absorption into, Ti and some of its dilute alloys. In brief, the open circuit potential measurements, EIS, XPS, and neutron reflectometry experiments in neutral solutions were all aimed at exploring the nature and protectiveness of the oxide film on Ti under passive conditions, and the influence of alloy composition on the passivity, to aid in understanding the ability of Ti alloys to resist crevice corrosion and anodic pitting. The open circuit potential measurements, EIS, and XPS performed on electrodes that were exposed to solutions at elevated temperatures, activation experiments in acidic solutions, polarization curves, and crevice corrosion initiation experiments all served to probe the conditions necessary for the dissolution or breakdown of the passive oxide film leading to crevice corrosion, and the response of the metal to the development of acidity within a corroding crevice. Finally, the hydrogen absorption experiments were intended to determine the conditions required for hydrogen uptake in deaerated, acidic solutions designed to simulate the anolyte solution inside a propagating crevice, and to provide data that could be used to evaluate how much hydrogen could potentially be absorbed during a period of active crevice corrosion. The activation, polarization, and possibly the crevice corrosion behaviour of Ti seem also to be influenced by the presence of hydrogen in the metal surface. An understanding of all of these aspects of the

corrosion response of Ti and certain of its alloys is important to the evaluation of Ti as a possible construction material for nuclear waste containers to be used under Canadian nuclear fuel waste disposal vault conditions, as described briefly in Section 1.1, or as a structural metal for other industrial applications.

When specifying the suitability of Ti alloys for specific industrial applications, guidelines based on practical experience are commonly employed. Thus, it is generally accepted that crevice corrosion will not occur on Ti at temperatures lower than 70°C, regardless of solution pH or chloride concentration [40]. For hydrogen absorption leading to HIC, it is considered that the following three general conditions must exist simultaneously: a source of atomic hydrogen, a temperature >80°C and, for neutral solution, an impressed potential negative of -1 V (SCE) [40], although a threshold potential of -0.7 V is sometimes quoted. Industrial experience indicates that hydrogen absorption at moderate potentials in the neighbourhood of -0.7 V generally produces a thin surface hydride layer [40] that is not usually of any mechanical significance in common industrial situations; however the extremely long containment periods required for disposal of nuclear fuel waste may make the entry of any hydrogen, even as thin surface hydrides, significant to the overall container lifetime. The work presented in this Thesis helps to elucidate the underlying chemical and physical reasons why these empirically developed guidelines work very well.

4.2 The passive oxide film

The neutron reflectometry experiments showed the presence of a passive oxide film on a sputtered Ti layer that was exposed to air for a two-month period. This air-formed film

had a thickness of 47 Å, in agreement with the results of at least two other research groups looking at similar air-formed oxides on Ti [71, 107, 108]. It also had a scattering length density comparable to (slightly higher than) that of rutile, the highest-density crystalline phase of TiO_2. Although neutron reflectometry does not measure crystal structures directly, if one assumes that the film composition was TiO_2, the high SLD value indicates that the film structure was either rutile-like or an amorphous phase with a packing density similar to or higher than that of rutile.

Some evidence that the air-formed film composition really was TiO_2 was inferred from XPS experiments on other electrodes that showed that, except for the case of some very freshly polished Ti surfaces, all surface Ti was in the +4 oxidation state in solution-grown oxide films on Ti. Also, if the air-formed oxide layer contained any suboxides, bound water, or Ti-OH species, the SLD value from the reflectometry would have been lower than what was observed. The questions of titanium oxide composition and crystal structure for thin oxide films grown on Ti metal in solutions have also been addressed in the literature (see Section 1.3), and, although many different experiments have been performed, are still open to debate. The bulk of the evidence suggests that the composition of at least the outermost part of such films is TiO_2. Since the neutron reflectometry results indicated a constant composition throughout the oxide (which also was not a solution-grown film), if the outermost part of the oxide was TiO_2, it would be difficult to reasonably claim a composition other than TiO_2 for the entire oxide layer.

Neither the structure nor the composition of the air-formed oxide changed detectably when it was immersed at E_{oc} in deaerated, 0.27 mol·dm^{-3} NaCl solution at room

temperature (*e.g.*, no water was absorbed). Oxide films *grown* in the same type of solution, either by exposing freshly polished Ti (see XPS results) or by anodizing Ti already covered by an air-formed oxide layer (see neutron reflectometry results), however, incorporated large amounts of hydrogen as Ti-OH species or bound water. In fact, the oxide that was thickened by anodization developed a two-layer structure comprising an inner "dry" or hydrogen-free layer with a thickness corresponding to that of the original hydrogen-free air-formed oxide and an outer "wet" or hydrated layer that was determined to have a composition of (roughly) $TiO_2 \cdot H_2O$ or, equivalently, $TiO(OH)_2$ and had a thickness equal to the increase in the overall oxide layer thickness due to anodization. A decrease in bound water and/or Ti-OH species with depth into the oxide film was also noted by angle-resolved XPS on oxide films grown in solution on freshly polished electrodes left at E_{oc}.

The anodization ratio for Ti measured by *in situ* neutron reflectometry (25 $Å \cdot V^{-1}$) is in excellent agreement with the values reported in the literature. One of the most surprising results of this work was that the Pilling Bedworth ratio for the anodized oxide was close to (even slightly *less* than) that of rutile, in spite of the difference in composition. Intuitively, one might expect the addition of one oxygen atom and two hydrogen atoms per TiO_2 unit in the oxide would require a volume increase. Apparently it does not. The reason for this is not known; however one could speculate that, if the incorporation of OH into the oxide results in the formation of hydroxyl bridges, as suggested by Ohtsuka [85], the hydroxyl bridge bonding structure may mitigate against the need for a volume increase.

These observations, *i.e.*, that the anodic oxide has two compositionally different layers and is *like* rutile, yet *not* rutile, may help explain why so much contradictory information has been published concerning the composition and structure of oxide films on Ti. It has been shown that the air-formed oxide is different from solution-grown oxides. Anodic films may also be different than oxides grown at E_{oc} on freshly polished Ti. When different research groups explore these different films with the same technique, different conclusions may be drawn. Furthermore, this rutile-like nature of the anodic oxide, and the existence of two layers within it, might invite different conclusions about the *same* oxide film examined by different techniques.

The apparent conservation of "dry" or hydrogen-free oxide during anodization of Ti originally covered by an air-formed oxide layer draws attention to the question of the oxide growth mechanism. The similarity in thickness and SLD of the air-formed oxide and the inner layer in the anodized film tempts the observer to think that the two are one in the same, but the idea that all of the oxide formed during anodization grows on top of the pre-existing oxide denies the validity of the transport number measurements of Khalil and Leach [135]. These imply that ~35% of the newly formed oxide should grow by metal cation movement out toward the solution and 65% by oxygen anion movement in toward the metal surface.

The FAIT mechanism could account for the transport numbers of metal and oxygen, but would require special conditions to explain a constant thickness of "dry" oxide. Under the traditional FAIT mechanism, both the inner and outer layers should increase in thickness in proportion to the transport numbers. Somehow, perhaps by stripping

hydrogen from mobile OH species or exchanging one O^{2-} for every two OH^- species, the existing hydrogen-free oxide would have to be converted to hydrated or "wet" oxide at a rate matching the rate of formation of new "dry" oxide.

The conservation of dry oxide would be a natural consequence of oxide thickening via a PDM mechanism. The amount of hydrogen-free oxygen species would be fixed by the thickness of the air-formed oxide. During film growth, according to the PDM, atoms of each type would retain their positions with respect to other atoms of the same type, but metal cations would move out, away from the metal surface and oxygen anions would move in, towards the metal surface. The ionic transport numbers would still be valid, although their influence would be somewhat more subtle than in the FAIT mechanism. The original air-formed film would cease to exist as such within the anodic oxide film. The oxygen anions of the original oxide would move inward and continue to be found adjacent to the metal surface, combined with the most recently oxidized metal cations. The metal cations of the original oxide would move outward and continue to be found adjacent to the oxide/solution interface, combined with the oxygen anions that entered the oxide most recently.

The PDM seems the most likely route since it does not require exemptions or special circumstances to yield the observed results, but the other pathways cannot be ruled out without further data (see Section 4.5).

The results of the EIS measurements on the various alloys under passive conditions at 20°C indicated that the passive oxide film on high purity Ti and Ti-2 is continuous and without accessible low-impedance "shortcuts" such as pores, cracks, or active grain

boundaries. On Ti-12, Ti-16, and Ti-0.1Ru, low impedance pathways through (or around) the oxide do exist, suggesting that the oxide films does not form its usual protective, passive layer over certain sites on the metal surface. Presumably these sites correspond to the locations of intermetallic precipitates in the alloy. This should not be very surprising, since these sites, also thought to be the catalytic sites (for the cathodic half-reaction) that give the alloy corrosion resistance by "cathodic modification", would have to be exposed easily to the electrolytic solution to be effective cathodic modifiers.

4.3 Oxide film breakdown and dissolution

The oxide film on Ti protects against corrosion over a very wide range of conditions, but even so, has its limits. There are two ways in which the oxide loses its protectiveness against corrosion. One is by a breakdown process thought to involve the formation of cracks, pores, or conductive regions (perhaps along grain boundaries) under severe conditions of temperature or applied potential[1] that induce crystallization in the oxide layer, thus the term "breakdown crystallization". The other is by simple oxide film thinning due to dissolution in acidic solution. (Loss of protection against hydrogen ingress is included in Section 4.4). In this Thesis project, breakdown crystallization is expected at temperatures of 70°C or above, or potentials of 7 V or above [40]. The actual "breakdown crystallization" process was not directly observed in the sense of measuring structural changes in the oxide that would show whether or not crystallization had occurred. Instead, the conditions necessary for breakdown to occur, the effects of the

[1] Not tested in this Thesis project.

breakdown on the protectiveness of the oxide, and the compositional changes occurring in the film under conditions close to the conditions required for breakdown were measured.

The slow heat-up experiments with crevice coupons demonstrated that for oxide breakdown leading to crevice corrosion in 0.27 $mol \cdot dm^{-3}$ NaCl solution, temperatures of 72°C and 67°C were required for Ti-2 and Ti-12 coupons respectively. Rapid heat-up crevice corrosion experiments demonstrated, however, that achieving the oxide film breakdown temperature was not sufficient to cause crevice corrosion initiation by itself. After being maintained at a temperature of 100°C, crevice corrosion coupons exposed to 0.27 $mol \cdot dm^{-3}$ NaCl and those exposed to 0.27 $mol \cdot dm^{-3}$ Na_2SO_4 both showed signs of oxide film breakdown, *i.e.*, the occluded surfaces were stained from acid attack. The acidity was probably generated when breakdown crystallization caused an increase in the Ti dissolution rate, leading to acid-producing metal cation hydrolysis. Only in the NaCl solution, however, did crevice corrosion initiate. It seems that crevice corrosion initiation may be facilitated by chloride ions, perhaps due to attack of any residual thin oxide layer present on the Ti by chloride ions.

Changes in the oxide film on Ti with increasing temperature were also observed by EIS and XPS. EIS experiments showed a decrease in the pore resistances or oxide film resistances of all the Ti alloys, except Ti-0.1Ru, at temperatures greater than 40-60°C, implying the development of lower-resistance charge transport pathways through the film. This loss of resistivity is consistent with the appearance of cracks, pores, or grain boundaries within the oxide, perhaps a consequence of breakdown crystallization. XPS measurements of the amount of Ti-OH and water in the oxide film also show significant

increases with increasing temperature (except on high purity Ti). It is possible that OH incorporation into the oxide is responsible or partly responsible for the apparent thermally induced breakdown crystallization that occurs in the temperature range 40-60°C. It could also be an *effect* of breakdown crystallization, rather than a *cause*. The neutron reflectometry experiments showed that titanium oxide *grown* in aqueous solution contains large amounts of OH species. On the oxides observed by XPS, breakdown crystallization may have enhanced oxide film thickening by increasing, at least temporarily, the metal oxidation rate. This "solution-grown" oxide may have formed with large amounts of incorporated OH species.

Activation experiments carried out in acidic solution showed that a pH of less than ~2 was required to prevent Ti-2 from passivating in 1.0 $mol \cdot dm^{-3}$ chloride solutions at 25°C. The time required for the open circuit potential to drop from the passive potential region to the active region in activation experiments on Ti-2 in 1.0 $mol \cdot dm^{-3}$ HCl was increased by increasing the time that the Ti surface was exposed to ambient air at room temperature, and thereby allowing thicker, less defective oxide films to form. This was taken as evidence that the activation process involves the thinning of the passive oxide by dissolution in acid. Such acid attack on the existing oxide was also noted to be a precursor for crevice corrosion initiation.

Activation of Ti-12 in acid appeared to demonstrate the effects of cathodic modification. An initial potential drop, followed by a rapid and lasting return of the open circuit potential to the passive potential region, was noted to be consistent with the notion that the exposure of a sufficient number of catalytic sites for the proton reduction reaction

could drive the potential into the passive region. The initial potential drop was interpreted as the result of a brief period of active corrosion leading to the exposure of a significant number of Ti_2Ni intermetallic precipitates or other catalytic sites on the electrode surface to drive repassivation via enhanced cathodic kinetics.

4.4 Hydrogen absorption

Activation experiments on Ti-2 in deaerated acidic solutions showed two general types of behaviour: either the open circuit potential dropped from the passive to the active potential region and remained there indicating a thinning of the passive film and the beginning of active corrosion, or the open circuit potential decreased initially but "rebounded" to the passive potential range. The latter behaviour was termed "activation - rebound". The potential transients associated with activation-rebound were found to be quite similar in appearance to the open circuit potential transients recorded on Ti-12 in the same solution. In the case of Ti-12, the activation-rebound-like behaviour was attributed to an initial surface attack by the acid (activation) leading to the exposure of sufficient catalytic surface sites (possibly Ti_2Ni intermetallic particles) to enhance the cathodic half reaction (proton reduction) such that the potential would be driven into the passive region (rebound). The addition of Ni to the alloy is said to result in "cathodic modification" [54]. If the cause of activation-rebound behaviour on Ti-2 is cathodic modification as on Ti-12, the origin of the proposed effect is more subtle. The impurities in the commercial purity Ti-2 (mainly Fe and Si) are not expected to afford Ti-2 much help in catalyzing the cathodic reaction to the point of generating passivity. It was proposed, instead, that the formation of a thin surface hydride layer (which may be an actual hydride phase, or

simply an adsorbed monolayer), by adsorption or absorption of hydrogen produced by the corrosion of the Ti, generated catalytic sites for proton reduction and provided the Ti with a sort of "cathodic self-modification". TiH_2 is known to be a catalyst for proton reduction [195]. The presence of a catalytic surface, whatever its composition, after activation-rebound was demonstrated by cathodic polarization of Ti-2 electrodes before and after undergoing activation-rebound. Electrodes on which activation-rebound had occurred showed no active-to-passive transition or active regions but rather enhanced cathodic kinetics, beginning at higher potentials than on Ti-2 electrodes polarized immediately after activation in acid. This behaviour mimicked the cathodic polarization response of Ti-12. The increasing cathodic current transients recorded in polarizations of Ti-2 electrodes after activation-rebound suggest that the surface coverage by the catalytic sites increases with polarization time, perhaps by nucleation and growth of surface hydride patches at the expense of a surface oxide layer. Such effects (formation of a catalytic surface, driving the open circuit potential in the positive direction, and increasing the cathodic current with time) may be responsible, in part, for the current and potential fluctuations observed during crevice corrosion on Ti-2.

It was also noted that activation-rebound usually did not occur on electrodes that had been allowed to grow an air-formed oxide, but rather on freshly polished electrodes. The reason for this is far from certain, but it may be a consequence of the persistence of the air-formed oxide film on Ti. If a thin layer of oxide remains on the surface even in acidic solution, then this oxide may prevent the formation of the catalytic surface hydride. On freshly polished electrodes, the surface oxide may not be thick enough to resist dissolution and hydride formation, the composition of the oxide present on freshly (wet-)

polished surfaces may be different than that formed in air, leading to a difference in the ability to form catalytic surface hydride, or the surface hydride may form directly during the wet-polishing stage but be destroyed upon prolonged air exposure.

There also seems to be a fine balance point (around pH 1 in 1.0 $mol \cdot dm^{-3}$ chloride solution) between the formation of the catalytic surface leading to potential-rebound, and the achievement of long-term active corrosion behaviour. This balance may be determined by competition between the rate of catalytic surface hydride formation and the rate of hydride dissolution or oxide layer formation.

Galvanostatic hydrogen charging experiments performed on Ti-2 in 0.1 $mol \cdot dm^{-3}$ HCl + 0.27 $mol \cdot dm^{-3}$ NaCl showed that the efficiency of hydrogen absorption into the metal decreased with an increase in the amount of charge passed. The hydrogen absorption efficiency did not appear to depend on the applied current density or the temperature over the range of conditions tested. The current independence of the absorption efficiency is an unexpected observation.

One possible explanation for this behaviour is the presence of "windows" on the Ti surface, at which hydrogen absorption is rapid by comparison to hydrogen absorption elsewhere on the surface and by comparison to the rate of hydrogen production (proportional to the current). The hydrogen absorption efficiency would be proportional to the surface coverage by the "window" sites.

The amount of hydrogen absorbed by Ti-2 in deaerated 0.1 $mol \cdot dm^{-3}$ HCl + 0.27 M NaCl at 95°C was found to increase proportional to the square root of the charge passed according to

$$H = k\sqrt{Q_H} \qquad \textbf{(3.4.3-a)}$$

where H represents the amount of absorbed hydrogen, Q_H represents the total charge passed and k is a constant.

The corresponding average hydrogen absorption efficiency can be expressed as

$$\bar{\xi} = 100\frac{nFk}{M\sqrt{Q_H}} \qquad \textbf{(3.4.3-c)}$$

where n is the number of electrons (one for hydrogen), F Faraday's constant, and M the molar mass of hydrogen atoms. An instantaneous hydrogen absorption efficiency was calculated from the tangent to the plot of H *vs.* Q_H giving:

$$\xi = 100\frac{nF}{M}\frac{\partial H}{\partial Q_H} = 50\frac{nFk}{M\sqrt{Q_H}} \qquad \textbf{(3.4.3-b)}$$

One can see from the latter two expressions that the average hydrogen absorption efficiency measured in these experiments overestimates the instantaneous hydrogen absorption efficiency at any charge by a factor of about two.

The hydrogen absorption mechanism involving the "windows", mentioned above, can be used to explain the decrease in hydrogen absorption efficiency with increasing charge passed. As more hydrogen enters the metal, forming a dense layer of precipitated hydrides as observed in the metallographic cross section (Figure 3.4.3-a), some of the hydrogen absorption sites may become blocked by hydride, deformed, or otherwise rendered less able to permit hydrogen absorption. Furthermore, hydrogen absorption should become progressively more difficult as the hydrogen must travel farther through a

thickening surface hydride layer. This may eventually result in diffusion control of the absorption rate.

A threshold potential for hydrogen absorption was observed in experiments on Ti 2 at 95°C. At potentials above this threshold value, no hydrogen absorption was observed, in spite of the passage of large amounts of cathodic charge (*i.e.*, large amounts of hydrogen evolution). The threshold for hydrogen absorption coincided with a cusp in the potentiostatic polarization curve for Ti-2 and a shift from decreasing cathodic current transients above the threshold potential to increasing cathodic current transients at potentials below it. The threshold was also found to sit just below the flatband potential for TiO_2.

It was suggested that a thin residual oxide film on the Ti may act as a barrier to hydrogen absorption, but at potentials below the flatband potential the Fermi level in the oxide surface moves into the conduction band, resulting in electronic degeneracy in the thin oxide that allows current to pass easily through it. A chemical change in the oxide accompanies degeneracy and hydrogen can penetrate the former barrier to enter the metal. Neutron reflectometry revealed the ingress of hydrogen into the oxide film in neutral NaCl solution at room temperature. The hydrogenation of the oxide film progressed across its thickness as a function of decreasing potential, and no hydrogen absorption into the metal was observed before the entire oxide layer was hydrogenated. Unfortunately, hydrogen entry into the metal at this stage could not be observed directly by neutron reflectometry because the metal film was physically disrupted at that point. Microscopic inspection of the film afterward revealed the delamination of the metal from the Si

substrate by blistering, probably caused by formation of hydrogen gas bubbles between the metal and substrate after hydrogen was absorbed by the metal.

Galvanostatic hydrogen absorption experiments conducted on Ti-12 at 95°C in 0.1 $mol \cdot dm^{-3}$ HCl + 0.27 $mol \cdot dm^{-3}$ NaCl solution showed large swings in the potential during polarization, and replicate experiments displayed wide variability in the amount of absorbed hydrogen. This phenomenon was rationalized in terms of the presence of a potential threshold for hydrogen absorption as seen on Ti-2 under the same conditions, complicated by the effects of cathodic modification. The sites on the Ti-12 surface that catalyze the cathodic reaction, once they became active, are thought to drive the potential to higher values while allowing the same current to flow. Hydrogen absorption on the bulk of the surface may proceed while the potential lies below the threshold value, but once the catalysis of the proton reduction allows the potential to rise above the threshold value, hydrogen absorption at the bulk of the surface ceases (although it may continue to some extent at the catalytic sites).

The suggested hypothesis summarizing the potential dependence of the hydrogen absorption behaviour can be briefly stated as follows. For potentials positive of the hydrogen absorption threshold potential, proton reduction occurs on exposed intermetallic particles or hydride-covered catalytic sites. These sites are much more efficient at evolving hydrogen than absorbing it, and are capable of sustaining large cathodic current densities. The transient currents fall as these sites become blocked or damaged. At potentials negative of the threshold, the oxide becomes reducible and, in acidic solutions, may dissolve, allowing the growth of a layer of hydrides laterally across the surface. This

leads to an expansion of the cathodically active surface area that results in increasing transient cathodic currents and the absorption of hydrogen. The efficiency of hydrogen absorption under these conditions decreases with time as the hydride layer at the metal surface thickens, creating a longer diffusion pathway for hydrogen atoms to enter the underlying metal.

4.5 Future work

The experiments performed in this Thesis project have led to many more questions and hint at the type of work required to solve some of the existing ones. A collection of some of the ideas for future experiments and research directions is presented below.[1]

In order to verify the neutron reflectometry results showing hydrogen incorporation into the oxide on Ti during anodization, these experiments can be repeated in D_2O instead of H_2O. Because of the large contrast in coherent neutron scattering length of H and D, and the expected identical chemical behaviour in this system, the neutron reflectometry results should be much different in D_2O than they were in H_2O, but the differences should be predictable. The neutron reflectometry results can also be confirmed qualitatively using secondary ion mass spectrometry (SIMS) to detect the elements present in the thin film electrode as a function of depth combined with profilometry to measure the layer thicknesses at the SIMS sputtering craters[2]. Provided that the destruction of the Ti film upon hydrogen absorption can be overcome (perhaps by using thicker Ti layers), neutron

[1] In the interests of not unnecessarily lengthening this already lengthy document, this list is far from complete.

[2] At the time of this writing the neutron reflectometry and SIMS experiments have been performed but the results have not yet been analyzed.

reflectometry in acidic solutions should be helpful in investigating the state of the Ti surface near the hydrogen absorption threshold.

Neutron reflectometry may also be useful in distinguishing between the FAIT and PDM theories of anodic oxide film growth. These two models predict different locations within the oxide for freshly oxidized Ti cations. By using a dual-layer Ti film composed of a natural abundance Ti and a layer of isotopically separated Ti, one could take advantage of the large difference between the coherent neutron scattering lengths of natural Ti (largely ^{48}Ti) and the less common isotopes (^{46}Ti, ^{47}Ti, ^{49}Ti, and ^{50}Ti) to track the positions of certain Ti cations as they enter the oxide, and as the oxide thickens around them.

The EIS work in this project suggested that the cathodically modified Ti alloys have holes in their passive oxide layers, and it is suspected that an intermetallic precipitate lies at the base of each pore. These ideas could be checked using scanning tunnelling or atomic force microscopies to look for holes in the oxide and SIMS microscopy or scanning Auger microscopy to look for intermetallic particles at the base of each hole. Another important question is whether such holes in the oxide represent a danger to the longevity of the material, either as active sites for localized corrosion or points of entry for hydrogen. Future experiments should examine the local corrosion resistance of these materials (perhaps best done in acidic solution using EIS or, even better, localized EIS (LEIS)) and their long term resistance to hydrogen absorption.

The EIS and XPS measurements of oxide films grown in aqueous solutions at various temperatures could be repeated in acidic solutions to determine whether it is possible to observe Ti in the oxide at oxidation states lower than +4 and to probe the possibility of

initiating localized corrosion at the bases of the cracks that develop in the oxide after breakdown crystallization.

The development of acidity within a crevice before crevice corrosion initiation and the influence of the anion on initiation have been demonstrated. A next step in this research area would be to determine the pH, potential and chloride ion concentration within a crevice as it undergoes crevice corrosion initiation, propagation, and repassivation. These data would also be useful in corrosion rate measurements and hydrogen absorption efficiency tests to better define appropriate "simulated crevice chemistry conditions". The internal crevice chemistry might be measurable using a microelectrode array integrated into the crevice former. While other researchers [3] have already inserted microelectrode probes into corroding crevices, they have tended to use wide-gap crevices (not a possibility for Ti) or insertion channels in the crevice former (which do not really allow them to probe the conditions in the true (tight) crevice gap). A microelectrode array would also help link together the local crevice chemistry with the physical corrosion damage done to the metal surface and the fluctuating potential and current signals observed during crevice corrosion (corrosion noise).

Finally, the breakdown of the oxide film on Ti with increasing potential, which was mentioned in the Introduction (Section 1.3) but not investigated in this Thesis project, could be examined. Neutron reflectometry and atomic force microscopy applied to examine oxide films of Ti near the breakdown potential may yield valuable information regarding structural changes in the oxide film at the breakdown point. The possibility that the corrosion-resistant alloy components could lead to easier film breakdown or

could be oxidized from the Ti at high potentials, leaving the material susceptible to corrosion, could also be explored.

According to the neutron reflectometry measurements, neither the structure nor the composition of the air-formed oxide changed detectably when it was immersed in deaerated, neutral pH 0.27 $mol \cdot dm^{-3}$ NaCl solution at E_{oc}. This result contrasts somewhat with the XPS results showing differences in the oxide films on freshly polished (air exposed) Ti alloy electrodes and those exposed to NaCl solution at 20°C. The difference is probably related to the fact that an oxide was still forming on the freshly polished surfaces at the time of immersion, whereas the surface of the thin film electrode had been exposed to air for several weeks and had probably formed a reasonably stable oxide layer before immersion and no further oxide film growth occurred upon exposure to the solution.

That the development of acidity and thinning of the oxide layer took place both in chloride and in sulphate solutions, but led to crevice corrosion only in the chloride solutions (at 100°C), indicates that crevice corrosion initiation may require at least one further step involving the anion. The introduction of ionic diffusion pathways into the recrystallized oxide may allow transport of chloride ions through the thin residual film, leading to crevice corrosion initiation. While the presence of sulphate ions does not lead to crevice corrosion, the observation of etching within the occluded area in chloride-free sulphate solutions clearly indicates that it is the change in the properties of the oxide with temperature that is responsible for the 70°C threshold for crevice corrosion.

5 References

[1] AECL, "Environmental impact statement on the concept for disposal of Canada's nuclear fuel waste", Atomic Energy of Canada Limited Report, AECL-10711, COG-93-1. AECL. Pinawa, MB. 1994.

[2] D.W. Shoesmith, B.M. Ikeda, M.G. Bailey, M.J. Quinn, and D.M. LeNeveu, "Lifetime model for Grade-2 titanium containers for nuclear waste", Atomic Energy of Canada Limited Report, AECL-10973, COG-94-558. AECL. Pinawa, MB. 1994.

[3] L. Yao, F. Gan, Y. Zhao, C. Yao, and J.L. Bear, "Microelectrode monitoring the crevice corrosion of titanium", *Corrosion*, **47**(1991)420-423.

[4] R. Greef, R. Peat, L.M. Peter, D. Pletcher, and J. Robinson, "Instrumental Methods in Electrochemistry", Ellis Horwood Ltd. Chichester, England. 1990.

[5] D.W. Shoesmith, B.M. Ikeda, F. King, and S. Sunder, "Prediction of long-term behaviour for nuclear waste disposal", Atomic Energy of Canada Limited Report, AECL-11580, COG-96-187, AECL, Pinawa, MB. 1996.

[6] B.A. Cheadle, C.E. Ells, E.F. Ibrahim, R.A. Holt, C.E. Coleman, R.W. Gilbert, D.O. Northwood, W.J. Langford, and R.R. Hosbons, "The physical metallurgy of zirconium alloys", W. Evans and J. A. L. Robertson, eds. Atomic Energy of Canada Limited Report, CNRL-1208. AECL. Chalk River, ON. 1975.

[7] N.A. Lange, "Lange's Handbook of Chemistry", Eleventh Edition. J.A. Dean, ed. McGraw-Hill. New York. 1973.

[8] "CRC Handbook of Chemistry and Physics", 60th Edition. R.C. Weast, ed.CRC Press. Boca Raton, FL. 1997

[9] B.M. Ikeda and D.W. Shoesmith, "Industrial experience with titanium", Atomic Energy of Canada Limited Report, AECL 11750, COG-97-4I. AECL. Pinawa, MB. 1997.

[10] E.J. Kelly, "Electrochemical Behavior of Titanium", In Modern Aspects of Electrochemistry. J.O. Bockris, B.E. Conway, and R.E. White, eds. Plenum Press. New York. (1982) Vol. 14, pp 319-424.

[11] E.J. Kelly, "Anodic dissolution and passivation of titanium in acidic media", *J. Electrochem. Soc.*, **126**(1979)2064-2074.

[12] J.O. Bockris and A.K.N. Reddy, "Modern Electrochemistry", Plenum Press. New York. (1970) Vol. 2.

[13] M.G. Fontana, "Corrosion Engineering", Third Edition. M. B. Bever, S. M. Copley, M. E. Shank, C. A. Wert, and G. A. Wilkes, eds. McGraw-Hill Series in Materials Science and Engineering. McGraw-Hill, Inc. Toronto. 1986.

[14] E.J. Kelly, "Anodic dissolution of titanium in acidic sulfate solutions", *J. Electrochem. Soc.*, **123**(1976)162-170.

[15] N.T. Thomas and K. Nobe, "Electrochemical behavior of titanium", *J. Electrochem. Soc.*, **119**(1972)1450-1456.

[16] B.M. Ikeda, M.G. Bailey, C.F. Clarke, and D.W. Shoesmith, "Crevice corrosion of titanium under nuclear fuel waste conditions", Atomic Energy of Canada Limited Report, AECL-9568. AECL. Pinawa, MB. 1989.

[17] B. De Force and H. Pickering, "A clearer view of how crevice corrosion occurs", *JOM*, **47**(1995)22-27.

[18] D.W. Shoesmith, M.G. Bailey, J.J. Noël, and B.M. Ikeda, "Electrochemical studies of hydrogen absorption by titanium", In Proc. Symp. Electrochemistry and Materials Science of Cathodic Hydrogen Absorption and Adsorption, San Francisco, CA, May 22-27, 1994. B.E. Conway and G. Jerkiewicz, eds. The Electrochemical Society, Inc. Pennington, NJ. (1995) Vol. 94-21, pp 120-136.

[19] P. McKay and D.B. Mitton, "An electrochemical investigation of localized corrosion on titanium in chloride environments", *Corrosion*, **41**(1985)52-62.

[20] B.M. Ikeda, M.G. Bailey, M.J. Quinn, and D.W. Shoesmith, "The development of an experimental data base for the lifetime predictions of titanium nuclear waste containers", In Application of Accelerated Corrosion Tests to Sevice Life Prediction of Materials, Proc. ASTM Symp., Miami, FL, November 16-17, 1992. G. Cragolino and N. Sridhar, eds. American Society for Testing and Materials. Philadelphia, PA. (1994)126-142.

[21] P. McKay, "Crevice-corrosion kinetics on titanium and a Ti-Ni-Mo alloy in chloride solutions at elevated temperature", In Proc. Corrosion Chemistry within Pits, Crevices and Cracks, Teddington, UK, October 1-3, 1984. A. Turnbull, ed. Her Majesty's Stationary Office. London. (1987)107-128.

[22] B.M. Ikeda, M.G. Bailey, M.J. Quinn, and D.W. Shoesmith, "The effect of temperature on crevice corrosion of titanium", In Proc. 11th Int. Corrosion Cong., Florence, Italy, April 2-6, 1990. Associazione Italiana di Metallurgia. Milan, Italy. (1990) Vol. 5, pp 5.371-5.378.

[23] A.D. Davydov, "Limiting currents of anodic metal dissolution", *Elektrokhimiya*, **27**(1990)947-960.

[24] H.S. Harned and B.B. Owen, "The Physical Chemistry of Electrolytic Solutions", W. A. Hamor, ed. American Chemical Society Chemical Monographs Series. Reinhold Publishing Corporation. New York. (1958) Vol. 3, p. 748.

[25] B.M. Ikeda, "The effect of gamma radiation on the electrochemistry of candidate container materials", In The Corrosion Performance of Nuclear Fuel Waste Containers. K. Nuttall and P. McKay, eds. Atomic Energy of Canada Limited Report, TR-340. AECL. Pinawa, MB. (1985)87-94.

[26] S.R. Ryan, C.F. Clarke, B.M. Ikeda, F. King, C.D. Litke, P. McKay, and D.B. Mitton, "An investigation of the long-term corrosion behaviour of selected nuclear fuel waste container materials under possible disposal vault conditions", Atomic Energy of Canada Limited Report, TR-489, COG-94-55. AECL. Pinawa, MB. 1994.

[27] M.G. Bailey, B.M. Ikeda, M.J. Quinn, and D.W. Shoesmith, "Crevice corrosion behaviour of titanium Grades-2 and -12 in hot aqueous chloride solution -the effect of chloride concentration", Atomic Energy of Canada Limited Report, AECL-10971, COG-95-279. AECL. Pinawa, MB. 1996.

[28] F.A. Posey and E.G. Bohlmann, "Pitting of titanium alloys in saline waters", *Desalination*, 3(1967)269-279.

[29] D.W. Shoesmith, B.M. Ikeda, D. Hardie, M.G. Bailey, and C.F. Clarke, "Impact of various parameters on the corrosion of titanium nuclear fuel waste containers under disposal vault conditions." In Proc. Topical Meeting Nuclear Waste Packaging, Focus '91, Las Vegas, NV, Sept. 29-Oct. 2, 1991. American Nuclear Society, Inc. La Grange Park, IL. (1992)193-200.

[30] F. King, B.M. Ikeda, and D.W. Shoesmith, "Nuclear waste: can we contain it?", *Chemtech*, 22(1992)214-219.

[31] D.W. Shoesmith, B.M. Ikeda, and D.M. LeNeveu, "Lifetime predictions for titanium nuclear waste containers", Proc. Int. Conf. Life Prediction of Corrodible Structures, Cambridge, UK, Sept. 23-26, 1991, NACE. Houston, TX. (1991)484.

[32] P. McKay, "Crevice corrosion of Ti-0.3% Ni-0.3% Mo alloy (ASTM Grade-12) in chloride environments at elevated temperature", In Proc. 9th Int. Cong. Metallic Corrosion, Toronto, June 3-7, 1984. NRC. Ottawa, ON. (1984) Vol. 3, pp 288-297.

[33] B.M. Ikeda, M.G. Bailey, M.J. Quinn, and D.W. Shoesmith, "The effect of chloride concentration on the crevice corrosion of grade-2 titanium", In Critical Factors in Localized Corrosion. G. S. Frankel and R. C. Newman, eds. The Electrochemical Society Inc. Pennington, NJ, (1992) Vol. 92-9, pp 431-447.

[34] B.M. Ikeda, M.G. Bailey, D.C. Cann, and D.W. Shoesmith, "Effect of iron content and microstructure on the crevice corrosion of Grade-2 titanium under nuclear waste vault conditions", In Advances in Localized Corrosion: Proc. Int. Conf. Localized Corrosion, Orlando, FL, June 1-5, 1987. NACE-9. H.S. Isaacs, U. Bertocci, J. Kruger, and S. Smialowska, eds. NACE. Houston, TX. (1990)439-444.

[35] B.M. Ikeda, M.G. Bailey, C.F. Clarke, and D.W. Shoesmith, "Crevice corrosion and hydrogen embrittlement of Grades-2 and -12 titanium under Canadian nuclear waste vault conditions", In Corrosion of Nuclear Fuel Waste Containers: Proceedings of a Workshop, Winnipeg, MB, February 9-10, 1988. D. W. Shoesmith, ed. Atomic Energy of Canada Limited Report, AECL-10121. AECL. Pinawa, MB. (1988)45-66.

[36] D.W. Shoesmith, W.H. Hocking, B.M. Ikeda, F. King, J.J. Noël, and S. Sunder, "Application of electrochemical methods in the development of models for fuel dissolution and container corrosion under nuclear waste disposal conditions", *Can. J. Chem.* 75(1997)1566-1584.

[37] B.M. Ikeda, J.J. Noël, and D.W. Shoesmith, "Crevice corrosion and the lifetime performance of titanium nuclear waste containers", Atomic Energy of Canada Limited Report, AECL-11823, COG-97-061-I. AECL. Pinawa, MB. 1997.

[38] R.W. Schutz, "Understanding and preventing crevice corrosion of titanium alloys: part I", *Mater. Perf.*, October(1992)57-62.

[39] R.W. Schutz, "Understanding and preventing crevice corrosion of titanium alloys: part II", *Mater. Perf.*, November(1992)54-56.

[40] R.W. Schutz and D.E. Thomas, "Corrosion of titanium and titanium alloys", In Metals Handbook, Ninth Edition. ASM International. Metals Park, OH. (1987) Vol. 13, pp 669-706,

[41] B.M. Ikeda and C.F. Clarke, "Titanium corrosion under Canadian nuclear fuel waste disposal conditions", In Proc. 2nd Int. Conf. Radioactive Waste Management, Winnipeg, MB, Sept. 7-11, 1986. Canadian Nuclear Society. Toronto, ON. (1986)605-610.

[42] R.W. Schutz, "Recent titanium alloy and product developments for corrosive industrial service", In NACE Corrosion '95. NACE. Houston. (1995) Paper #244, pp 244/1-244/20.

[43] J.A. Hall, D. Banerjee, and T.L. Wardlaw, "The relationships of structure and corrosion behaviour of Ti-0.3Mo-0.8Ni (TiCode-12)", In Titanium Science and Technology '84, Proc. 5th Int. Conf. Titanium, Munich, Sept. 10-14, 1984.)", G. Lütjering, U. Zwicker, and W. Bunk, eds. Deutsche Gesellschaft fur Metallkunde e.V. (1984) Vol. 4, pp 2603-2610.

[44] B.M. Ikeda, R.C. Styles, M.G. Bailey, and D.W. Shoesmith, "The effect of material purity on crevice corrosion of titanium in NaCl solution", Proc. Symp. Compatability of Biomedical Implants, San Francisco, CA, May 22-27, 1994. P. Kovacs and N. S. Istephanous, eds. The Electrochemical Society, Inc. Pennington, NJ. (1994) Vol. 94-15, pp 368-380.

[45] B.M. Ikeda, J.J. Noël, and D.W. Shoesmith, "Summary report of the experimental evaluation of titanium as a nuclear fuel waste container", Ontario Hydro Report, 06819-REP-01200-0025-Roo. Ontario Hydro. Toronto, ON. 1999.

[46] A. Caprani, J.P. Frayret, R. Pointeau, S.K. Marya, and F. Le Maitre, "On the corrosion resistance of the submerged arc welded titanium in concentrated hydrochloric acid 8N", *Electrochim. Acta*, **28**(1983)141-147.

[47] T. Fukuzuka, K. Shimogori, H. Satoh, and F. Kamikubo, "Effects of heat treatments on corrosion resistance and hydrogen absorption of commercially pure titanium", In Titanium '80: Proc. 4th Int. Conf. Titanium, Kyoto, Japan, May 19-22, 1980. H. Kimura and O. Izumi, eds. The Minerals, Metals, and Materials Society. Warrendale, PA. (1980) Vol. 4, pp 2685-2693.

[48] H. Satoh, F. Kamikubo, and K. Shimogori, "Effect of gasket materials on crevice corrosion of titanium", In Titanium Science and Technology '84, Proc. 5th Int. Conf. Titanium, Munich, Sept. 10-14, 1984.)", G. Lütjering, U. Zwicker, and W. Bunk, eds. Deutsche Gesellschaft fur Metallkunde e.V. (1984) Vol. 4, pp 2633-2639.

[49] N. Sridhar and D.S. Dunn, "Effect of applied potential on changes in solution chemistry inside crevices on type 304L stainless steel and alloy 825", *Corrosion*, **50**(1994)857-872.

[50] G.T. Burstein and R.M. Souto, "Observations of localised instability of passive titanium in chloride solution", *Electrochim. Acta*, **40**(1995)1881-1888.

[51] R.W. Schutz and L.C. Covington, "Effect of oxide films on the corrosion resistance of titanium", *Corrosion*, **37**(1981)585-591.

[52] D.W. Shoesmith and B.M. Ikeda, "The resistance of titanium to pitting, microbially induced corrosion and corrosion in unsaturated conditions", Atomic Energy of Canada Limited Report, AECL-11709, COG-96-557-I. AECL. Pinawa, MB. 1997.

[53] M. Stern and H. Wissenberg, "The influence of noble metal additions on the electrochemical and corrosion behaviour of titanium", *J. Electrochem. Soc.*, **106**(1959)759-764.

[54] E. van der Lingen and H. de Villiers Steyn, "The potential of ruthenium as an alloying element in titanium", In Proc. Titanium Applications Conference, Boulder, CO, Oct. 2-5, 1994. Titanium Development Association. Boulder, CO. (1994)450-461.

[55] L.P. Kornienko, A.E. Gitlevich, P.A. Topala, G.P. Chernova, R.K. Zalavutdinov, G.M. Plavnik, G.N. Khrustaleva, and N.D. Tomashov, "Electrochemical and corrosive behavior of titanium with electrospark Pd and Cr-Pd coatings", *Z. Metallov*, **29**(1993)351-358.

[56] N.D. Tomashov, G.P. Chernova, Y.S. Ruscol, and G.A. Ayuyan, "The passivation of alloys on titanium bases", *Electrochim. Acta*, **19**(1974)158-172.

[57] A.J. Sedriks, "Corrosion resistance of titanium-ruthenium alloys", *Corrosion*, **31**(1975)60-65.

[58] A.J. Sedriks, J.A.S. Green, and D.L. Novak, "Electrochemical behavior of Ti-Ni alloys in acidic chloride solutions", *Corrosion*, **28**(1972)137-142.

[59] R.S. Glass and Y.K. Hong, "Transpassive behaviour of titanium-molybdenum alloys in 1N H_2SO_4 ", *Electrochim. Acta*, **29**(1984)1465-1470.

[60] R.W. Schutz, "Ruthenium enhanced titanium alloys: minor ruthenium additions produce cost effective corrosion resistant commercial titanium alloys", *Platinum Metals Rev.*, **40**(1996)54-61.

[61] R.W. Schutz and M. Xiao, "Optimized lean-Pd titanium alloys for aggressive reducing acid and halide service environments", In Proc. 12th Int. Corr. Cong., 3A, Sept., 1993, NACE. Houston, TX, (1993)1213-1225.

[62] T. Fukuzuka, K. Shimogori, and H. Satoh, "Role of palladium in hydrogen absorption of Ti-Pd alloy", In Titanium '80: Proc. 4th Int. Conf. Titanium, Kyoto, Japan, May 19-22, 1980. H. Kimura and O. Izumi, eds. The Minerals, Metals, and Materials Society. Warrendale, PA. (1980) Vol. 4, pp 2695-2703.

[63] R.D. Armstrong, R.E. Firman, and H.R. Thirsk, "Ring-disc studies of titanium-palladium alloy corrosion", *Corr. Sci.*, **13**(1973)409-420.

[64] T. Kido and S. Tsujikawa, "Effects of Ni and Mo on critical conditions for crevice corrosion of low alloy titanium", *Tetsu to Hagane*, **75**(1989)1332-1337.

[65] T. Fukuzuka, K. Shimogori, H. Satoh, and F. Kamikubo, "Protection of titanium against crevice corrosion by coating with palladium oxide", In Titanium '80: Proc. 4th Int. Conf. Titanium, Kyoto, Japan, May 19-22, 1980. H. Kimura and O. Izumi, eds. The Minerals, Metals, and Materials Society. Warrendale, PA. (1980) Vol. 4, pp 2631-2638.

[66] L.P. Kornienko, N.D. Tomashov, and G.P. Chernova, "Electrochemical and corrosive behavior of intermetallic phases with composition Ti_2Pd and TiPd and titanium with electrospark palladium coatings", *Z. Metallov*, **29**(1992)359-367.

[67] T. Watanabe, T. Shindo, and H. Abo, "Corrosion and corrosion resistance of high-strength low-alloy titanium (Ti-O-N-Fe system)", In Proc. 11th Int. Corrosion Cong., Florence, Italy, April 2-6, 1990. Associazione Italiana di Metallurgia. Milan, Italy. (1990)

[68] R.S. Glass, "Effect of intermetallic Ti_2Ni on the electrochemistry of TiCODE-12 in hydrochloric acid", *Electrochim. Acta*, **28**(1983)1507-1513.

[69] N.D. Tomashov, R.M. Altovsky, and G.P. Chernova, "Passivity and corrosion resistance of titanium and its alloys", *J. Electrochem. Soc.*, **108**(1961)113-119.

[70] D.G. Kolman and J.R. Scully, "Electrochemistry and passivity of a Ti-15Mo-3Nb-3Al beta-titanium alloy in ambient temperature aqueous chloride solutions", *J. Electrochem. Soc.*, **140**(1993)2771-2779.

[71] V.V. Andreeva, "Behaviour and nature of thin oxide films on some metals in gaseous media and in electrolyte solutions", *Corrosion*, **20**(1964)35t-46t.

[72] S.Y. Yu, "Mechanisms for Enhanced Active Dissolution Resistance and Passivity of Ti Alloyed with Nb and Zr", Ph.D. Thesis. University of Virginia. Charlottesville, VA. 1998.

[73] H. Ezaki, M. Morinaga, and S. Watanabe, "Hydrogen overpotential for transition metals and alloys, and its interpretation using an electronic model", *Electrochim. Acta*, **38**(1993)557-564.

[74] C.E. Mortimer, "Chemistry: A Conceptual Approach", Reinhold Publishing Corporation, New York. (1967)76.

[75] K. Shimogori, H. Satoh, H. Tomari, and A. Ooki, "Analysis of passive film on titanium formed in dilute HCl solutions at elevated temperatures", In Titanium and Titanium Alloys: Scientific and Technological Aspects, Proc. 3rd Int. Conf. Titanium, Moscow State University, May 18-21, 1976. J. C. Williams and A. F. Belov, eds. Plenum Press. New York. (1976)881-890.

[76] J.C. Griess, "Crevice corrosion of titanium in aqueous salt solutions", *Corrosion*, **24**(1968)96-109.

[77] L. Lunde and R. Nyborg, "Hydrogen absorption of titanium alloys during cathodic polarization", In Proc. Conf. Engineering Solutions to Industrial Corrosion Problems, Sandefjord, Norway, June 7-9, 1993. NACE. Houston, TX. (1993)5/1-5/9.

[78] P.Y. Park, E. Akiyama, H. Habazaki, A. Kawashima, K. Asami, and K. Hashimoto, "The corrosion behaviour of sputter-deposited Mo-Ti alloys in concentrated hydrochloric acid", *Corr.Sci.*, **38**(1996)1649-1667.

[79] P. Marcus, "On some fundamental factors in the effect of alloying elements on passivation of alloys", *Corr.Sci.*, **36**(1998)2155-2158.

[80] J.B. Cotton, "Using titanium in the chemical plant", *Chem. Eng. Prog.*, **66**(1970)57-62.

[81] L.C. Covington and R.W. Schutz, "The effects of iron on the corrosion resistance of titanium", In Titanium '80: Proc. 4th Int. Conf. Titanium, Kyoto, Japan, May 19-22, 1980. H. Kimura and O. Izumi, eds. The Minerals, Metals, and Materials Society. Warrendale, PA. (1980) Vol. 4, pp 2669-2676.

[82] S. Tsujikawa and Y. Kojima, "Repassivation method to predict long term integrity of low alloy titanium for nuclear waste package", In Scientific Basis for Nuclear Waste Management XIV: Mat. Res. Soc. Symp. Proc., Boston, Nov. 26-29, 1990. T. J. Abrajano and L. H. Jonhson, eds. Materials Research Society. Pittsburgh, PA. (1991) Vol. 212, pp 261-268.

[83] J.S.L. Leach and B.R. Pearson, "Crystallization in anodic oxide films", *Corr. Sci.*, **28**(1988)43-56.

[84] T. Shibata and Y. Zhu, "The effect of film formation conditions on the structure and composition of anodic oxide films on titanium", *Corr. Sci.*, **37**(1995)253-270.

[85] T. Ohtsuka, M. Masuda, and N. Sato, "Ellipsometric study of anodic oxide films on titanium in hydrochloric acid, sulfuric acid, and phosphate solution", *J. Electrochem. Soc.*, **132**(1985)787-792.

[86] T. Ohtsuka, J. Guo, and N. Sato, "Raman spectra of the anodic oxide film on titanium in acidic sulphate and neutral phosphate solutions", *J. Electrochem. Soc.*, **133**(1986)2473-2476.

[87] C.K. Dyer and J.S.L. Leach, "Breakdown and efficiency of anodic oxide growth on titanium", *J. Electrochem. Soc.*, **125**(1978)1032-1038.

[88] M. Mikula, J. Blecha, and M. Ceppan, "Photoelectrochemical properties of anodic TiO_2 layers prepared by various current densities", *J. Electrochem. Soc.*, **139**(1992)3470-3474.

[89] K. Leitner, J.W. Schultze, and U. Stimming, "Photoelectrochemical investigations of passive films on titanium electrodes", *J. Electrochem. Soc.*, **133**(1986)1561-1568.

[90] L.D. Arsov, C. Kormann, and W. Plieth, "In situ Raman spectra of anodically formed titanium dioxide layers in solutions of H_2SO_4, KOH, and HNO_3", *J. Electrochem. Soc.*, **138**(1991)2964-2970.

[91] M. Pankuch, R. Bell, and C.A. Melendres, "Composition and structure of the anodic films on titanium in aqueous solutions", *Electrochim. Acta*, **38**(1993)2777-2779.

[92] C.E. Vallet, A. Choudhury, P.E. Sobol, and C.W. White, "XPS characterization of anodic layers grown on Ir- and Rh-implanted titanium", *Electrochim. Acta*, **38**(1993)1313-1320.

[93] T. Shibata and Y. Zhu, "X-ray photoelectron spectroscopy analysis of anodic oxide film on titanium", *Denki Kagaku*, **61**(1993)853-856.

[94] J.L. Ong, L.C. Lucas, G.N. Raikar, and J.C. Gregory, "Electrochemical corrosion analysis and characterization of surface-modified titanium", *Appl. Surf. Sci.*, **72**(1993)7-13.

[95] N.R. Armstrong and R.K. Quinn, "Auger and X-ray photoelectron spectroscopic and electrochemical characterization of titanium thin film electrodes", *Surf. Sci.*, **67**(1977)451-468.

[96] J. Pan, D. Thierry, and C. Leygraf, "Electrochemical and XPS studies of titanium for biomaterial applications with respect to the effect of hydrogen peroxide", *J. Biomed. Mat. Res.*, **28**(1994)113-122.

[97] C. da Fonseca, S. Boudin, and M. da Cunha Belo, "Characterisation of titanium passivation films by in situ ac impedance measurements and XPS analysis", *J. Electroanal. Chem.*, **379**(1996)173-180.

[98] C.N. Sayers and N.R. Armstrong, "X-ray photoelectron spectroscopy of TiO_2 and other titanate electrodes and various standard titanium oxide materials: surface compositional changes of the TiO_2 electrode during photoelectrolysis", *Surf. Sci.*, **77**(1978)301-320.

[99] "Alfa AESAR 1997-98 Product Catalog", Johnson Matthey Catalog Company, Inc. Ward Hill, MA. (1997) p. 570

[100] J-M. Pan, B.L. Maschhoff, U. Diebold, and T.E. Madey, "Interaction of water, oxygen, and hydrogen with TiO_2(110) surfaces having different defect densities", *J. Vac. Sci. Technol. A*, **10**(1992)2470-2476.

[101] A.K. See and R.A. Bartynski, "Inverse photoemission study of the defective TiO_2(110) surface", *J. Vac. Sci. Technol. A*, **10**(1992)2591-2596.

[102] M.A. Henderson, "Mechanism for the bulk-assisted reoxidation of ion sputtered TiO_2 surfaces: diffusion of oxygen to the surface or titanium to the bulk?", *Surf. Sci.*, **343**(1995)L1156-L1160.

[103] L. Soriano, M. Abbate, J. Vogel, J.C. Fuggle, A. Fernandez, A.R. Gonzalez-Elipe, M. Sacchi, and J.M. Sanz, "Chemical changes induced by sputtering in TiO_2 and some selected titanates as observed by X-ray absorption spectroscopy ",*Surf. Sci.*, **290**(1993)427-435.

[104] D.J. Blackwood, R. Greef, and L.M. Peter, "An ellipsometric study of the growth and open-circuit dissolution of the anodic oxide film on titanium", *Electrochim. Acta*, **34**(1989)875-880.

[105] Y. Serruys, T. Sakout, and D. Gorse, "Anodic oxidation of titanium in 1M H_2SO_4, studied by Rutherford backscattering", *Surf. Sci.*, **282**(1993)279-287.

[106] K.E. Healy and P. Ducheyne, "Passive dissolution kinetics of titanium in vitro", *J. Mater. Sci.*, **4**(1993)117-126.

[107] D.G. Wiesler and C.F. Majkrzak, "Neutron reflectometry studies of surface oxidation", *Physica B*, **198**(1994)181-186.

[108] D.G. Wiesler and C.F. Majkrzak, "Growth and dissolution of protective oxide films on titanium: an in-situ neutron reflectivity study", In Scientific Basis for Nuclear Waste Management: Mat. Res. Soc. Symp. Proc. Materials Research Society. North Holland, NY. (1995) Vol. 376, pp 247-257.

[109] N. Tit, "Role of oxygen vacancies in anodic TiO_2 thin films", *Appl. Surf. Sci.*, **65/66**(1993)246-251.

[110] J.F. McAleer and L.M. Peter, "Instability of anodic films on titanium", *J. Electrochem. Soc.*, **129**(1982)1252-1260.

[111] D.G. Wiesler, M.F. Toney, M.G. Samant, O.R. Melroy, C.S. McMillan, and W.H. Smyrl, "Structure and epitaxy of anodic TiO_2/Ti(1120)", *Surf. Sci.*, **268**(1992)57-72.

[112] M.R. Kozlowski, P.S. Tyler, W.H. Smyrl, and R.T. Atanasoski, "Anodic TiO_2 thin films: photoelectrochemical, electrochemical, and structural study of heat-treated and RuO_2 modified films", *J. Electrochem. Soc.*, **136**(1989)442-450.

[113] P.S. Tyler, M.R. Kozlowski, W.H. Smyrl, and R.T. Atanasoski, "Photoelectrochemical microscopy as a probe of localized properties of thin TiO_2 films", *J. Electroanal. Chem.*, **237**(1987)295-302.

[114] S. Kudelka, A. Michaelis, and J.W. Schultze, "Effect of texture and formation rate on ionic and electronic properties of passive layers on Ti single crystals", *Electrochim. Acta*, **41**(1996)863-870.

[115] M.R. Kozlowski, P.S. Tyler, W.H. Smyrl, and R.T. Atanasoski, "Photoelectrochemical microscopy of oxide films on metals: Ti/TiO_2 interface", *Surf. Sci.*, **194**(1988)505-530.

[116] D.J. Blackwood, L.M. Peter, and D.E. Williams, "Stability and open circuit breakdown of the passive oxide film on titanium", *Electrochim. Acta*, **33**(1988)1143-1149.

[117] E. Lee and S. Pyun, "Analysis of nonlinear Mott-Schottky plots obtained from anodically passivating amorphous and polycrystalline TiO_2 films", *J. Appl. Electrochem.*, **22**(1992)156-160.

[118] G. Blondeau, M. Froelicher, M. Froment, and A. Hugot-Le Goff, "On the optical indices of oxide films as a function of their crystallization: application to anodic TiO_2 (anatase)", *Thin Solid Films*, **42**(1977)147-153.

[119] J. Yahalom and J. Zahavi, "Electrolytic breakdown crystallization of anodic oxide films on Al, Ta, and Ti", *Electrochim. Acta*, **15**(1970)1429-1435.

[120] L. Young, "Anodic Oxide Films", Academic Press. London. 1961.

[121] N. Sato, "A theory for breakdown of anodic oxide films on metals", *Electrochim. Acta*, **16**(1971)1683-1692.

[122] J.C. Nelson and R.A. Oriani, "Stress generation during anodic oxidation of titanium and aluminum", *Corr. Sci.*, **34**(1992)307-326.

[123] F. di Quarto, K. Doblhofer, and H. Gerischer, "Instability of anodically formed TiO_2 layers", *Electrochim. Acta*, **23**(1978)195-201.

[124] M. Pourbaix, "Atlas of Electrochemical Equilibria in Aqueous Solutions", Pergamon Press. Toronto. (1966) Vol. 1.

[125] N. Sato, "An overview on the passivity of metals", *Corr. Sci.*, **31**(1990)1-19.

[126] D.D. Macdonald, "The point defect model for the passive state", *J. Electrochem. Soc.*, **139**(1992)3434-3449

[127] R. Nishimura and K. Kudo, "Anodic oxidation and kinetics of titanium in 1 M chloride solutions", *Corr. Sci.*, **22**(1982)637-645.

[128] T.R. Beck, "Initial oxide growth rate on newly generated surfaces", *J. Electrochem. Soc.*, **129**(1994)2500-2501.

[129] D.J. Blackwood and L.M. Peter, "Potential modulated reflectance spectroscopy of anodic oxide films on titanium", *Electrochim. Acta*, **35**(1990)1073-1080.

[130] R.M. Torresi, O.R. Camara, C.P. De Pauli, and M.C. Giordano, "Hydrogen evolution reaction on anodic titanium oxide films", *Electrochim. Acta*, **32**(1987)1291-1301.

[131] R.M. Torresi, O.R. Camara, and C.P. De Pauli, "Influence of the hydrogen evolution reaction on the anodic titanium oxide film properties", *Electrochim. Acta*, **32**(1987)1357-1363.

[132] F.P. Fehlner and N.F. Mott, "Low-temperature oxidation", *Oxidation of Metals*, **2**(1970)59-99.

[133] N. Cabrera and N.F. Mott, "Theory of the oxidation of metals", *Rept. Prog. Phys.*, **12**(1948)163-184.

[134] "Dexter Hysol encapsulating compounds", Hysol Division Bulletin E3-100K. The Dexter Corporation. Toronto. 1989

[135] N. Khalil and J.S.L. Leach, "The anodic oxidation of valve metals -I. Determination of ionic transport numbers by α-spectrometry", *Electrochim. Acta*, **31**(1986)1279-1285.

[136] J.J. Noël, "Electrooxidation of Carbon Monoxide on Glassy $Pt_{77}Si_{23}$ and Polycrystalline Platinum", M.Sc. Thesis. University of Guelph. Guelph, ON. 1990.

[137] N. Sato and M. Cohen, "The kinetics of anodic oxidation of iron in neutral solution: I. Steady growth region", *J. Electrochem. Soc.*, **111**(1964)512-519.

[138] N. Sato and M. Cohen, "The kinetics of anodic oxidation of iron in neutral solution: II. Initial stages", *J. Electrochem. Soc.*, **111**(1964)519-522.

[139] D.D. Macdonald and B. Roberts, "A potentiostatic transient study of the passivation of carbon steel in 1 M NaOH", *Electrochim. Acta*, **23**(1978)557-564.

[140] T. Shibata and Y. Zhu, "The effect of film formation temperature on the stochastic processes of pit generation on anodized titanium", *Corr. Sci.*, **36**(1994)1735-1749.

[141] F.P. Fehlner, "Low-Temperature Oxidation: The Role of Vitreous Oxides", K. Nobe, R. T. Foley, J. Kruger, H. Leidheiser,Jr., and J. B. Wagner,Jr., eds. The Corrosion Monograph Series. John Wiley and Sons. Toronto. 1986.

[142] A.A. Ejov, S.V. Savinov, I.V. Yaminsky, J. Pan, C. Leygraf, and D. Thierry, "Ex situ scanning tunneling microscopy investigations of the modification of titanium surface due to corrosion processes", *J. Vac. Sci. Technol. B*, **12**(1994)1547-1550.

[143] S.R. Morrison, "Electrochemistry at Semiconductor and Oxidized Metal Electrodes", Plenum Press. New York. 1980.

[144] R. Fujisawa and S. Tsujikawa, "Cathodic protection for nuclear waste packaging under gamma ray irradiation by using TiO_2 coating combined with glass scintillators", In Scientific Basis for Nuclear Waste Management: Mat. Res. Soc. Symp. Proc. Materials Research Society. Pittsburgh, PA. (1995) Vol. 353, pp 735-742.

[145] P.F. Dennis and R. Freer, "Oxygen self-diffusion in rutile under hydrothermal conditions", *J. Mater. Sci.*, **28**(1993)4804-4810.

[146] P.W. Atkins, "Physical Chemistry", Second Edition. Oxford University Press. 1982.

[147] H.O. Finklea, "Titanium dioxide (TiO_2) and Strontium Titanate ($SrTiO_3$)", In Semiconductor Electrodes. H. O. Finklea, ed. Studies in Physical and Theoretical Chemistry. Elsevier Science Publishers. Amsterdam. (1988) Vol. 55, pp 43-145.

[148] M.F. Weber, L.C. Schumacher, and M.J. Dignam, "Effect of hydrogen on the dielectric and photoelectrochemical properties of sputtered TiO_2 films", *J. Electrochem. Soc.*, **129**(1982)2022-2028.

[149] C.K. Dyer and J.S.L. Leach, "Reversible reactions within anodic oxide films on titanium electrodes", *Electrochim. Acta*, **23**(1978)1387-1394.

[150] T. Ohtsuka, M. Masuda, and N. Sato, "Cathodic reduction of anodic oxide films formed on titanium", *J. Electrochem. Soc.*, **134**(1987)2406-2410.

[151] N.T. Thomas and K. Nobe, "The electrochemical behavior of titanium - effect of pH and chloride ions", *J. Electrochem. Soc.*, **116**(1969)1748-1751.

[152] L.D. Arsov, "Dissolution électrochimique des films anodiques du titane dans l'acide sulfurique", *Electrochim. Acta*, **30**(1985)1645-1657.

[153] J.W. Schultze, S. Kudelka, and A. Michaelis, "Advances in microcorrosion research: single crystal experiments on polycrystalline titanium", In Proc. Corrosion/97: Research Topical Symp. NACE. Houston, TX. (1997)121-130.

[154] A. Michaelis and J.W. Schultze, "Anisotropy micro-ellipsometry for in-situ determination of optical and crystallographic properties of anisotropic solids and layers with Ti/TiO_2 as an example", *Thin Solid Films*, **274**(1996)82-94.

[155] S. Kudelka, A. Michaelis, and J.W. Schultze, "Electrochemical characterisation of oxide layers on single grains of a polycrystalline Ti-sample", *Ber. Bunsenges. Phys. Chem.* **99**(1995)1020-1027.

[156] J. Pan, D. Thierry, and C. Leygraf, "Electrochemical impedance spectroscopy study of the passive oxide film on titanium for implant application", *Electrochim. Acta*, **41**(1996)1143-1153.

[157] C.F. Clarke, D. Hardie, and B.M. Ikeda, "Hydrogen-induced cracking of commercial purity titanium", *Corr.Sci.*, **39**(1997)1545-1559.

[158] C.F. Clarke, D. Hardie, and B.M. Ikeda, "Hydrogen induced cracking of Grade-2 titanium", Atomic Energy of Canada Limited Report, AECL-11284. AECL. Pinawa, MB. 1995.

[159] K. Shimogori, "Hydrogen embrittlement in titanium and ways to prevent it", In Materials from the 46th Corrosion Prevention Symp., Tokyo, Japan, November 12, 1982. Corrosion Prevention Society, Inc., Tokyo, Japan. (1982)23-29.

[160] Z.A. Foroulis, "Factors influencing absorption of hydrogen in titanium from aqueous electrolytic solutions", In Titanium '80: Proc. 4th Int. Conf. Titanium, Kyoto, Japan, May 19-22, 1980. H. Kimura and O. Izumi, eds. The Minerals, Metals, and Materials Society. Warrendale, PA. (1980) Vol. 4, pp 2705-2711.

[161] C.F. Clarke, B.M. Ikeda, and D. Hardie, "Effect of crevice corrosion on hydrogen embrittlement of titanium", In Environment-Induced Cracking of Metals, Proc. First Int. Conf. Environment-Induced Cracking of Metals, Kohler, Wisconsin, October 2-7, 1988. NACE-10. R. P. Gangloff and M. B. Ives, eds. National Association of Corrosion Engineers. Houston, TX. (1988)419-424.

[162] T. Okada, "Factors influencing the cathodic charging efficiency of hydrogen by modified titanium electrodes", *Electrochim. Acta*, **28**(1983)1113-1120.

[163] C. Lim and S.-I. Pyun, "Theoretical approach to faradaic admittance of hydrogen absorption reaction on metal membrane electrode", *Electrochim. Acta*, **38**(1993)2645-2652.

[164] N.T. Thomas and K. Nobe, "Kinetics of the hydrogen evolution reaction on titanium", *J. Electrochem. Soc.*, **117**(1970)622-626.

[165] K. Shimogori, "Hydrogen adsorption by titanium", *Boshoku Gijutsu*, **30**(1981)349-357.

[166] R.W. Schutz, "Titanium: Process Industry Corrosion -The Theory and Practice", NACE. Houston, TX. (1986)503-527.

[167] T. Moroishi and H. Miyuki, "Hydrogen absorption of titanium in sea water at high temperature", In Titanium '80: Proc. 4th Int. Conf. Titanium, Kyoto, Japan, May 19-22, 1980. H. Kimura and O. Izumi, eds. The Minerals, Metals, and Materials Society. Warrendale, PA. (1980) Vol. 4, pp 2713-2722.

[168] T. Okada, "The effects of surface modification of titanium on the absorption rate of hydrogen during cathodic polarization", *Electrochim. Acta*, **27**(1982)1273-1280.

[169] I.I. Phillips, P. Poole, and L.L. Shreir, "Hydride formation during cathodic plarization of Ti - I. Effect of current density on kinetics of growth and composition of hydride", *Corr. Sci.*, **12**(1972)855-866.

[170] I.I. Phillips, P. Poole, and L.L. Shreir, "Hydride formation during cathodic polarization of Ti - II. Effect of temperature and pH of solution on hydride growth", *Corr. Sci.*, **14**(1974)533-542.

[171] J.P. Frayret, A. Caprani, P. Morel, and F. Pouliquen, "Study in acidic chloride medium of the titanium-hydrogen interactions. Multisteady states at the vicinity of the corrosion potential", In Proc. 3rd Int. Cong. Hydrogen and Materials, Paris, June 7-11, 1982. pp 299-304.

[172] E. Nowicka, Z. Wolfram, and R. Dus, "Hydrogen adsorption states on surfaces of thin transition-metal films in the process of hydride formation", *Appl. Surf. Sci.*, **65/66**(1993)90-93.

[173] T. Murai, M. Ishikawa, and C. Miura, "The absorption of hydrogen into titanium under cathodic polarization", *Boshoku Gijutsu*, **26**(1977)177-183.

[174] K. Siegbahn, C. Nordling, A. Fahlman, R. Nordberg, K. Hamrin, J. Hedman, G. Johansson, T. Bergmark, S. Karlsson, I. Lindgren, and B. Lindberg, "ESCA: Atomic, Molecular, and Solid State Structure Studied by Means of Electron Spectroscopy", Nova Acta Regiae Societatis Scientiarum Upsaliensis. Almqvist and Wiksells Boktryckeri Ab. Uppsala, Sweden. 1967.

[175] J.F. Moulder, W.F. Stickle, P.E. Sobol, and K.D. Bomben, "Handbook of X-ray Photoelectron Spectroscopy", J. Chastain, ed. Perkin-Elmer. Eden-Prairie, MN. 1992.

[176] U. Bertocci, C.M. Doyle, W.J. Eggers, B. Sayers, L.L. Scribner, J.R. Scully, G.E. Stoner, and S.R. Taylor, "A Short Course on Electrochemical Impedance Spectroscopy: Theory, Applications, and Laboratory Instruction, July 31-August 4, 1995", The Center for Electrochemical Science and Engineering, University of Virginia. Charlottesville, VA. 1995.

[177] A.J. Bard and L.R. Faulkner, "Electrochemical Methods: Fundamentals and Applications", Wiley. Toronto. 1980.

[178] C. Gabrielli, "Use and applications of electrochemical impedance techniques", Schlumberger Technical Report, 12860013. Schlumberger Technologies. Farnborough, England. 1990.

[179] V.F. Sears, "Neutron scattering lengths and cross sections", *Neutron News*, 3(1992)26-37.

[180] G. Petzow, "Metallographic Etching: Metallographic and Ceramographic Methods for Revealing Microstructure", American Society for Metals. Metals Park, OH. 1978.

[181] "Specification for titanium and titanium alloy welding electrodes and rods: SFA-5.16", In 1995 ASME Boiler and Pressure Vessel Code: An Internationally Recognized Code, Part C -Specifications for Welding Rods, Electrodes, and Filler Metals, Including 1996 Addenda (Issued 1996 December). American Society of Mechanical Engineers. New York. (1996)325-334,

[182] F. King, M.G. Bailey, C.F. Clarke, B.M. Ikeda, C.D. Litke, and S.R. Ryan, "A high-temperature, high-pressure, silver-silver chloride reference electrode: a user's guide", Atomic Energy of Canada Limited Report, AECL-9890, AECL. Pinawa, MB. 1989.

[183] "McGraw-Hill Dictionary of Scientific and Technical Terms, Fourth Edition", S. P. Parker, ed. McGraw-Hill. New York. 1989.

[184] D.D. Macdonald, "Reference electrodes for high temperature aqueous systems -a review and assessment", *Corrosion*, 34(1978)75-84.

[185] M. Gascoyne, C.C. Davison, J.D. Ross, and R. Pearson, "Saline groundwaters and brines in plutons in the Canadian Shield", In Saline Water and Gases in Crystalline Rocks, P. Fritz and S.K. Frape, Eds., Geological Association of Canada Special Paper 33, (1987) pp 53-68.

[186] M.J. Quinn, M.G. Bailey, B.M. Ikeda, and D.W. Shoesmith, "Image-analysis techniques for investigating localized corrosion processes", Atomic Energy of Canada Limited Report, AECL-10966, COG-93-405, AECL. Pinawa, MB. 1993.

[187] J.F. Ankner and C.F. Majkrzak, "Subsurface profile refinement for neutron specular reflectivity", In Neutron Optical Devices and Applications: Proc. SPIE-The International Society for Optical Engineering, San Diego, CA, July 22-24, 1992. C.F. Majkrzak and J.L. Wood, eds. SPIE-The International Society for Optical Engineering. Bellingham, WA. (1992) Vol. 1738, pp 260-269.

[188] J Penfold and R.K. Thomas, "The application of the specular reflection of neutrons to the study of surfaces and interfaces", *J. Phys.: Condens. Matter*, **2**(1990)1369-1412.

[189] C.E. Mortimer, "Chemistry: A Conceptual Approach", Reinhold Publishing Corporation, New York. (1967)76.

[190] E. Brauer and E. Nann, "The electrochemical behavior of titanium", *Werkstoffe und Korrosion*, **20**(1969)676-683.

[191] D.S. Mancey, "The dissolution of magnetite films from carbon steel surfaces",M.Sc. Thesis. University of Manitoba. Winnipeg, MB. 1985.

[192] D.W. Shoesmith, T.E. Rummery, W. Lee, and D.G. Owen, "Dissolution of oxide films on iron in aqueous solutions containing complexing anions -I. Magnetite in citrate and ethylenediaminetetraacetate", *Power Ind. Res.*, **1**(1981)43-63.

[193] D.W. Shoesmith, W. Lee, and D.G. Owen, "Dissolution of oxide films on iron in aqueous solutions containing complexing anions -II. Magnetite in oxalic acid and oxalic acid plus EDTA", *Power Ind. Res.*, **1**(1981)253-267.

[194] L.I. Krishtalik, "Hydrogen overvoltage and adsorption phenomena: Part III. Effect of the adsorption energy of hydrogen on the overvoltage and the mechanism of the cathodic process", In Advances in Electrochemistry and Electrochemical Engineering, Volume 7, Electrochemistry, P.Delahay and C.W. Tobias, Eds., Interscience Publishers. Toronto. (1970) Vol. 7, pp 283-339.

[195] M. Alagia and R. Palombari, "On the electrochemical properties of titanium hydride", *J. Electroanal. Chem.*, **316**(1991)347-352.

[196] M. Fleischmann and H.R. Thirsk, "Metal deposition and electrocrystallization", In Advances in Electrochemistry and Electrochemical Engineering. P. Delahay and C. W. Tobias, eds. Wiley Interscience. New York. (1963) Vol. 3, pp 123-210.

[197] L.G. Parratt, *Phys. Rev.*, **95**(1954)359.

[198] N. Hackerman and C.D.J. Hall, "Electrochemical polarization of titanium in aqueous solutions of sodium chloride", *J. Electrochem. Soc.*, **101**(1954)321-327.

[199] S. Sunder, N.H. Sagert, D.D. Wood, and N.H. Miller, "X-ray photoelectron spectra of gamma-irradiated perfluorobenzene", *Can. J. Appl. Spec.*, **35**(1990)137-140.

[200] S. Hofmann, In: Practical Surface Analysis by Auger and X-ray Photoelectron Spectroscopy, D. Briggs and M. P. Seah, eds. J. Wiley & Sons. New York. (1983)141.

[201] N. Khalil, A. Bowen, and J.S.L. Leach, "The anodic oxidation of valve metals -II. The influence of the anodizing conditions on the transport processes during the anodic oxidation of zirconium", *Electrochim. Acta*, **33**(1988)1721-1727.

[202] J.J. Noël, M.G. Bailey, J.P. Crosthwaite, B.M. Ikeda, S.R. Ryan, and D.W. Shoesmith, "Hydrogen absorption by Grade-2 titanium", Atomic Energy of Canada Limited Report, AECL-11608, COG-96-2:1-32. AECL. Pinawa, MB. 1996.

[203] D.W. Shoesmith, F. King, and B.M. Ikeda, "An assessment of the feasibility of indefinite containment of Canadian nuclear wastes",Atomic Energy of Canada Limited Report, AECL-10972, COG-94-5. AECL. Pinawa, MB 1994.